MODELLING DISPERSAL AND CONNECTIVITY OF ANTARCTIC KRILL IN THE LAZAREV SEA AND ADJACENT SEAS

A THESIS SUBMITTED TO
THE INSTITUTE OF MARINE SCIENCES OF
MIDDLE EAST TECHNICAL UNIVERSITY

BY

BULUT ÇAĞDAŞ

IN PARTIAL FULFILLMENT OF THE REQUIREMENTS
FOR
THE DEGREE OF DOCTOR OF PHILOSOPHY
IN
OCEANOGRAPHY

SEPTEMBER 2025

Approval of the thesis:

MODELLING DISPERSAL AND CONNECTIVITY OF ANTARCTIC KRILL IN THE LAZAREV SEA AND ADJACENT SEAS

Submitted by **BULUT ÇAĞDAŞ** in partial fulfillment of the requirements for the degree of **Doctor of Philosophy** i**n Oceanography, Middle East Technical University** by,

Prof. Dr. Barış Salihoğlu
Director, **Institute of Marine Sciences, METU** _____

Prof. Dr. Bettina Fach Salihoğlu
Head of the Department,
Oceanography Department, METU _____

Prof. Dr. Bettina Fach Salihoğlu
Supervisor, **Oceanography Department, METU** _____

Examining Committee Members:

Prof. Dr. Bettina Fach Salihoğlu
Oceanography Department, METU _____

Prof. Dr. Zahit Uysal
Marine Biology and Fisheries, METU _____

Asst. Prof. Dr. Berkay Nüvit Başdurak
Oceanography Department, METU _____

Assoc. Dr. Bilge Tutak
Ship and Ocean Technology Engineering,
İstanbul Technical University _____

Assoc. Prof. Fuat Dursun
Physical Oceanography and Marine Biology,
İstanbul University _____

Date: 01.09.2025

I hereby declare that all information in this document has been obtained and presented in accordance with academic rules and ethical conduct. I also declare that, as required by these rules and conduct, I have fully cited and referenced all material and results that are not original to this work.

Name Last name : Bulut Çağdaş

Signature :

ABSTRACT

MODELLING DISPERSAL AND CONNECTIVITY OF ANTARCTIC KRILL IN THE LAZAREV SEA AND ADJACENT SEAS

Çağdaş, Bulut
Doctor of Philosophy, Oceanography
Supervisor : Prof. Dr. Bettina Fach Salihoğlu

September 2025, 243 pages

The zooplankton species Antarctic krill, *Euphausia superba*, is a key organism in the Southern Ocean ecosystem that is recognized as a main component of the Antarctic marine food web. Antarctic krill is distributed all around Antarctica predominantly south of the Polar Front, including the Lazarev Sea the focus of this study.

In this study a complex modeling system consisting of output from the global, coupled physical-biochemical model FESOM-REcoM2 and a Lagrangian Particle Tracking model is used to simulate the connectivity of the Lazarev Sea krill population with populations from surrounding seas. The survival and growth of different krill developmental stages along transport paths are simulated extracting food concentrations from the coupled model as inputs to an Individual Based Model of krill.

Simulations show that Lazarev Sea krill may be supplied largely by krill from the Riiser-Larsen Sea (60%) while 39% of the population may be retained to recruit to the local Lazarev Sea population. Further, connectivity of krill originating in the Lazarev Sea with different regions in the Weddell Sea and the transport into the ACC is shown, as well as retention areas located in the southeastern Lazarev Sea and near Maud Rise. Krill growth simulations show the importance of sea ice algae as a food source for larval growth, the effect of spatial and seasonal variances on survival and growth. The study shows the interconnectivity of the Lazarev Sea with adjacent seas of the Southern Ocean but at the same time points to a high potential for part of the population being self-recruiting.

Keywords: Antarctic krill, Lazarev Sea, Lagrangian Particle Transport, Connectivity, Numerical modeling.

ÖZ

ANTARKTİK KRİLLERİN LAZAREV DENİZİ VE BİTİŞİK DENİZLERDE DAĞILIM VE BAĞLILIKLARINI MODELLEME

Çağdaş, Bulut
Doktora, Oşinografi
Tez Yöneticisi: Prof. Dr. Bettina Fach Salihoğlu

Eylül 2025, 243 sayfa

Zooplankton türü Antarktika krili (Euphausia superba), Güney Okyanusu ekosisteminde kilit bir organizma olup, Antarktik denizi besin ağının temel bileşeni olarak kabul edilmektedir. Antarktika krili, ağırlıklı olarak Kutup Cephesi'nin güneyinde, bu çalışmanın odak noktası olan Lazarev Denizi de dahil olmak üzere, Antarktika'nın her yerine bulunmaktadır.

Bu çalışmada, küresel, birleşik fiziksel-biyokimyasal model FESOM-REcoM2 ve bir Lagranç Parçacık İzleme modelinden elde edilen çıktılardan oluşan komplike modelleme sistemi, Lazarev Denizi krili popülasyonunun çevre denizlerdeki popülasyonlarla bağlantısını simüle etmek için kullanılmıştır. Taşıma yolları boyunca farklı kril gelişim evrelerinin hayatta kalma ve büyüme süreçleri simüle edilmiş ve birleşik modelden elde edilen besin konsantrasyonları, kril Birey Bazlı Modeli'nde girdi olarak kullanılmıştır.

Simülasyonlar, Lazarev Denizi krilinin büyük ölçüde Riiser-Larsen Denizi'nden gelen kril ile (%60) karşılanabileceğini ve popülasyonun %39'unun yerel Lazarev Denizi popülasyonuna katılarak muhafaza olabileceğini göstermektedir. Lazarev Denizi'nden gelen krillerin Weddell Denizi'ndeki farklı bölgelerle bağlantısı ve ACC'ye taşınması, ayrıca Lazarev Denizi'nin güneydoğusunda ve Maud Yükseltisi etrafındaki muhafaza alanları da gösterilmektedir. Kril büyüme simülasyonları, deniz buzu alglerinin larval büyüme için bir besin kaynağı olarak önemini, mekansal ve mevsimsel farklılıkların hayatta kalma ve büyüme üzerindeki etkisini göstermektedir. Çalışma, Lazarev Denizi'nin Güney Okyanusu'nun komşu denizleriyle olan bağlantısını göstermekle birlikte, kril popülasyonun bir kısmının kendi kendine çoğalma potansiyelinin yüksek olduğunu da göstermektedir.

Anahtar Kelimeler: Antarktik krill, Lazarev Denizi, Lagranç Parçacık Taşınması, Bağlılık, Sayısal modelleme

Dedicated to my family, friends, and friends who passed away. [Max 2 lines]

ACKNOWLEDGMENTS

I would like to thank my supervisor Prof. Dr. Bettina Fach Salihoğlu for her support and guidance at all points of this study. I thank Prof. Dr. Zahit Uysal, Asst. Prof. Dr. Berkay Nüvit Başdurak, Assoc. Dr. Bilge Tutak and Assoc. Prof. Fuat Dursun for their valuable insights and suggestions as my thesis jury members.

I thank Dr. Judith Hauck, Dr. Claudia Wekerle, Dr. Ralph Timmermann and Dr. Özgür Gürses from Alfred Wegener Institute for allowing the use of their FESOM-REcoM2 and Lagrangian Particle Tracking models and their support, as well as their hospitality. I also would like to thank Prof. Dr. Bettina Fach Salihoğlu again for allowing the use of her Antarctic krill individual based model.

I would like to thank Dr. Ehsan Sadighrad and Dr. Ceren Gürarslan Başduvar for their insights and support with my analysis, as well as sharing their office space with me for many years.

I thank Mehmet Selim Keçeci and Mehmet Beklen for their invaluable technical support regarding use of the Unix server and networking. I also would like to thank Ali Osman Acar for his invaluable help with setting up various programming languages on the Unix server.

Finally I extend my thanks all my family and friends who supported me and kept me company through all these years.

This thesis study has been supported by TÜBİTAK 1001 project 118Y325, DEKOSİM (BAP-08-11-DPT2012K120880), and YÖK 100/2000 PhD Scholarship program.

TABLE OF CONTENTS

ABSTRACT v

ÖZ vi

ACKNOWLEDGMENTS viii

TABLE OF CONTENTS ix

LIST OF TABLES xii

LIST OF FIGURES xiii

LIST OF ABBREVIATIONS xvi

1 INTRODUCTION 1

1.1 Lazarev Sea 1

1.2 Antarctic krill 3

1.3 Antarctic krill life cycle 4

1.4 Connectivity in marine populations 6

1.5 Aims of this study 8

2 MATERIALS AND METHODS 11

2.1 Modeling system 11

2.1.1 FESOM 12

2.1.2 REcoM2 14

2.1.3 Model implementation scenarios 15

2.2 Model validation 17

2.2.1 Physical parameters 18

2.2.2 Biochemical parameters 19

2.3 Parameterization of sea ice algae 24

2.4 Lagrangian particle tracking model 27

2.4.1 Particle tracking simulations 28
2.4.2 Preferred transport pathways 31
2.5 Krill Individual Based Model 31
2.6 Inclusion of reproduction into the krill IBM 34
2.6.1 Adult krill growth success 36
3 RESULTS 37
3.1 Krill connectivity in entire Lazarev Sea 37
3.1.1 Transport and retention in the Lazarev Sea 45
3.1.2 Source regions for krill in the Lazarev Sea 49
3.1.3 Fate of krill released at selected stations in the Lazarev Sea 53
3.1.4 200m release results vs surface release results 64
3.2 Ice algae results 65
3.3 Krill growth and survival along transport pathways from selected release point 71
3.3.1 Austral summer/spring release at station 92 71
3.3.2 Austral fall release at station 634 84
3.3.3 Austral winter release at station 516 96
3.3.4 Recruitment success 107
3.4 Simulations of adult krill growth success and reproduction in the entire Lazarev Sea 108
3.4.1 Adult krill growth 109
3.4.2 Spatial distribution of spawning 121
3.4.3 Growth success of adult krill 124
4 DISCUSSION 125

4.1 Connectivity vs retention of Lazarev Sea krill 126
4.1.1 Fate of krill originating in the Lazarev Sea 126
4.1.2 Source of Krill found in the Lazarev Sea 127
4.1.3 Importance of Maud Rise 128
4.1.4 Influence of vertical migration 130
4.1.5 Population structure of Lazarev Sea krill 130
4.2 Larvae and juvenile growth and recruitment during long-distance transport 131
4.2.1 Importance of sea ice algae food 135
4.3 Adult krill IBM reproduction discussion 136
4.4 Model uncertainties 139
4.5 Possible impact of Climate change 141
4.6 Implications for marine protected areas 145
5 CONCLUSION 147
REFERENCES 151
APPENDICES 177
A. Lagrangian particle tracking results 177
B. Larvae and juvenile IBM results 197
C. Adult krill IBM results 235
CURRICULUM VITAE 243

LIST OF TABLES

Table 1 Transmittance values of thickness intervals 25
Table 2 Chlorophyll a values assigned to ice thickness intervals 26
Table 3 Percentage (%) distribution of 2041 drifters released in the Lazarev Sea according to sink regions. 47
Table 4 Percentage (%) distribution of 2041 drifters released in the Lazarev Sea according to source regions 51
Table 5 Percentage (%) distribution of growth success of particles including reproduction for each simulation 124

LIST OF FIGURES

Figure 1 Study region..... 2
Figure 2 Schematic of the early life cycle of Antarctic krill..... 5
Figure 3 Global resolution of the BOLD FESOM mesh 14
Figure 4 Schematic of the basic pathways resolved in the biochemical model REcoM2. 15
Figure 5 Data-model comparison of surface chlorophyll concentration..... 20
Figure 6 Taylor diagram of surface chlorophyll model data comparison in the Southern Hemisphere..... 21
Figure 7 Model output of net primary production. (mg C m^{-2} d^{-1}) 22
Figure 8 Model output of heterotrophic biomass (mmol C m^{-3})..... 23
Figure 9 The probability of Chlorophyll a concentration versus the normalized depth of ice cores 26
Figure 10 Map of the study region with station inset. 30
Figure 11 Concept of the processes included in the biochemical, individual based model (IBM) of Antarctic krill..... 32
Figure 12 Particle trajectories and source/sink regions. 38
Figure 13 The average surface circulation of the years 2004, 2005 and 2006. 39
Figure 14 Surface circulation velocities of 2005 January to March. 40
Figure 15 Surface circulation velocities of 2005 April to June. 41
Figure 16 Surface circulation velocities of 2005 July to September. 43
Figure 17 Surface circulation velocities of 2005 October to December..... 44
Figure 18 Release locations of 2041 drifters for the spawning seasons of 2004/2005 and 2005/2006 color coded for sink regions..... 45
Figure 19 Percentage of forward tracked particles reaching different sink regions 49
Figure 20 Source locations of 2041 drifters that reach Lazarev Sea in the spawning season of 2005/2006 color coded for source regions..... 50
Figure 21 Percentage of backwards tracked particles originating in different source regions..... 52

Figure 22 Lagrangian Particle tracking results of station 92 54
Figure 23 Lagrangian Particle tracking results of station 634 56
Figure 24 Lagrangian Particle tracking results of station 516 58
Figure 25 Trajectories of all particles released at twelve LAKRIS stations in the Lazarev Sea 60
Figure 26 Distance metrics of simulation starting at all 12 stations 61
Figure 27 Distribution of sink regions that particles released at the Lazarev Sea stations 64
Figure 28: Comparison of simulation results between surface layer (left column) and 200m (right column) releases of Station 92 65
Figure 29 Modeled mean monthly sea ice thickness (m) for 2006 66
Figure 30 Mean monthly short-wave radiation as output by the FESOM model for the year 2010 68
Figure 31 Mean monthly sea ice algae concentration 70
Figure 32 Year-long Lagrangian particle trajectories of particles released from station 92 72
Figure 33 Concentrations of food for krill encountered by all drifters released from station 92 in November 2005 74
Figure 34 Concentrations of food for krill encountered by all drifters from station 92 in December 2005 76
Figure 35 Concentrations of food for krill encountered by all drifters from station 92 in January 2006 78
Figure 36 Krill growth over time for krill originating at station 92 80
Figure 37 Year-long Lagrangian particle trajectories of particles released from station 634 84
Figure 38 Concentrations of food for krill encountered by all drifters from station 634 in March 2004 86
Figure 39 Concentrations of food for krill encountered by all particles released from station 634 in April 2004. 88

Figure 40 Concentrations of food for krill encountered by all particles released from station 634 in May 2004. 90
Figure 41 Krill growth over time for krill originating at station 634..... 92
Figure 42 The one year-long Lagrangian particle trajectories of particles released from station 516. 96
Figure 43 The food extracted along the drifter paths of particles released from Station 516 in June 2006. 98
Figure 44 The food extracted along the drifter paths of particles released from Station 516 in July 2006. 100
Figure 45 The food extracted along the drifter paths of particles released from Station 516 in August 2006. 102
Figure 46 Krill growth figures for station 516 104
Figure 47 Simulated krill recruitment per season without sea ice algae. 107
Figure 48 Simulated krill recruitment per season with sea ice algae. 108
Figure 49 Adult krill growth (mm) of particles released on November 16, 2004. 110
Figure 50 Adult krill growth (mm) of particles released on December 16, 2004. 112
Figure 51 Adult krill growth (mm) of particles released on January 16, 2005..... 114
Figure 52 Adult krill growth (mm) of particles released on November 16, 2005. 116
Figure 53 Adult krill growth (mm) of particles released on December 16, 2005. 118
Figure 54 Adult krill growth (mm) of particles released on January 16, 2006..... 120
Figure 55 Starting locations of krill relative growth success. 122
Figure 56 Average surface circulation in the study area for 2005 produced by FESOM 127
Figure 57 Circumpolar distribution of *Euphausia superba* based on standardized data from KRILLBASE 134
Figure 58 The mean spatial distribution of all 12 forward time tracked simulation particles. 138
Figure 59 Planning phases of the Weddell Sea Marine Protected Area 146

LIST OF ABBREVIATIONS

ACC	Antarctic Circumpolar Current
ASF	Antarctic Slope Front
AWI	Alfred Wegener Institute
CCAMLR	Commission for the Conservation of Antarctic Marine Living Resources
Chla	Chlorophyll a
DEKOSİM	Deniz Ekosistem ve İklim Araştırmaları Merkezi (Marine Ecosystem and Climate Research Center)
DIC	Dissolved Inorganic Carbon
ESA	European Space Agency
EVP	Elastic viscous plastic
FESOM	Finite Element Sea Ice Ocean Model
GLOBEC	Global Ocean Ecosystem Dynamics
GLODAPv2	Global Ocean Data Analysis Project Version 2
IBM	Individual Based Model
IPCC	Intergovernmental Panel on Climate Change
JRA-55	Japanese 55-year Reanalysis
LAKRIS	Lazarev Sea Krill Survey
MLD	Mixed layer depth
MPA	Marine Protected Areas
NEMO-OPA	Nucleus for European Modelling of the Ocean - Océan PArallélisé
NPP	Net primary production
NSIDC	National Snow and Ice Data Center
OC-CCI	Ocean Colour Climate Change Initiative
PAR	Photosynthetically available radiation
PF	Polar Front
PISCES/OPA	Pelagic Interactions Scheme for Carbon and Ecosystem Studies - Océan PArallélisé
REcoM2	Regulated Ecosystem Model 2
SACCF	Southern Antarctic Circumpolar Current Front
SAF	Subantarctic Front
TÜBİTAK	Türkiye Bilimsel ve Teknolojik Araştırma Kurumu (Scientific and Technological Research Council of Türkiye)
WOA	World Ocean Atlas
YÖK	Yükseköğretim Kurulu (Council of Higher Education)

CHAPTER 1

INTRODUCTION

1.1 Lazarev Sea

The Southern Ocean is also known as the Antarctic Ocean and encompasses the southernmost waters of the world ocean, extending from the Antarctic continent to 60°S, encircling Antarctica without any land boundary. The Lazarev Sea is located east of the Weddell Sea and west of the Riiser-Larsen Sea between ~12°W and 12°E, extending from the coast of the Antarctic continent to ~ 60°S.

The Lazarev Sea is characterized by a narrow continental shelf and an extensive deep-sea ocean basin with average water depth exceeding 3000 m (Figure 1). The most prominent bathymetric feature in this region is Maud Rise, a seamount situated at 3°E between 64°S and 66°S, where the seafloor rises to 1500 m. The general circulation in the northern Lazarev Sea is dominated by the eastward-flowing Antarctic Circumpolar Current (ACC) and its associated fronts (Orsi et al., 1995). In contrast, south of 62°S, the circulation in the southern Lazarev Sea is dominated by the westward-flowing water associated with the southern limb of the Weddell Gyre. It transports Warm Deep Water of circumpolar origin into the area and enters the inner Weddell Sea. Part of it is forming the Antarctic Slope Front (ASF) near 69°S, that transports colder and fresher water associated with the Antarctic Coastal Current into the Weddell Sea (Cisewski et al., 2011). The Antarctic Slope Front continues its westward flow along the entire Weddell Sea coastline, ultimately reaching the Antarctic Peninsula, where it follows the continental shelf into the Bellingshausen Sea. In the Weddell Sea the Weddell Gyre circulates in a clockwise direction, spanning from approximately 60°W to nearly 10°E.

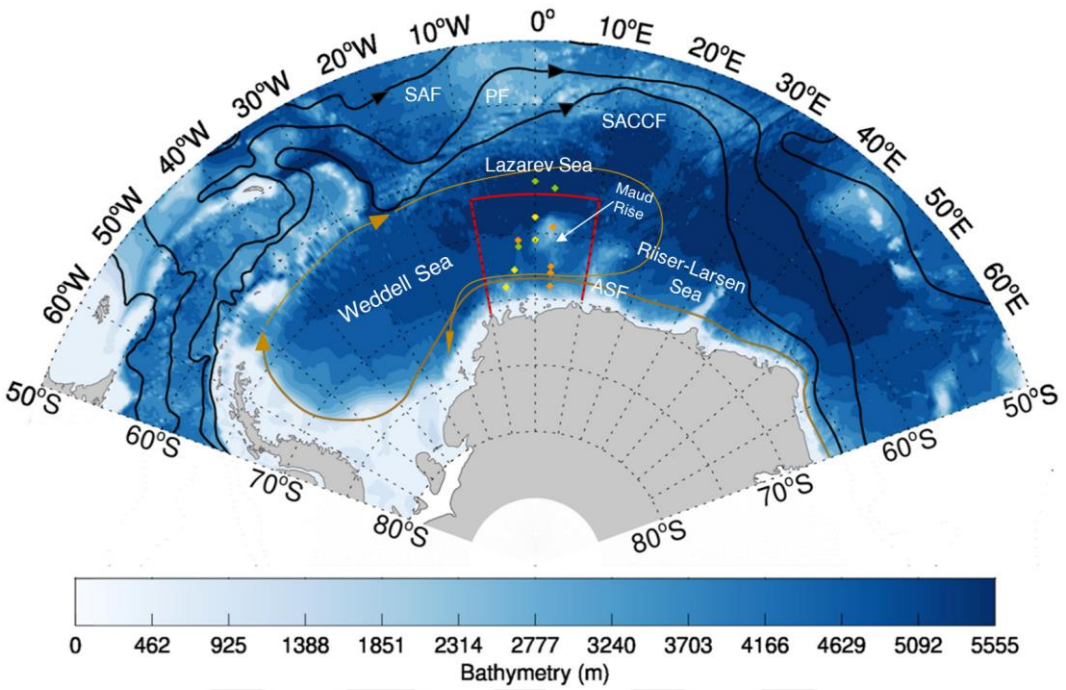


Figure 1 Study region. Black Lines indicate the Fronts of the Antarctic Circumpolar Current with arrows indicating the flow direction (SAF-Subantarctic Front, PF-Polar Front, SACCF-Southern Antarctic Circumpolar Current Front). Orange line marks the Antarctic Slope Front (ASF). The red rectangle marks the release area of 2041 drifters. The orange dots mark the LAKRIS cruise austral summer stations, yellow dots mark austral fall stations, green dots mark austral winter stations.

The neighboring regions of the Lazarev Sea are the Weddell Sea to its west, the Riiser-Larsen Sea to the east, and further east of the Riiser-Larsen is the Cosmonauts Sea. To the north the Lazarev Sea is bound by the eastward flowing Antarctic Circumpolar Current (ACC) that circles the continent. Due to its geographical position, the Lazarev Sea has been widely considered as a transit region for water flowing in from its east and towards west. Marine organisms and populations are similarly exposed to the ocean currents and are inevitably influenced by the circulation dynamics. One such organism that is the focus of this study is the Antarctic krill.

1.2 Antarctic krill

Antarctic krill, *Euphausia superba*, (hereafter krill) has long been recognized as a key component of the Antarctic marine food web (Marr, 1962; Murphy et al., 2017) playing a fundamental role in nutrient cycling that impacts primary production (Cavan et al., 2019) and its transfer to higher predators and is theorized to have small contributions to the global carbon cycle (Smith et al., 2025) with its vertical migration behavior. Krill has been found capable of grazing as much as 55% of the net primary (Atkinson et al., 2001) production and many of the top predator populations are dependent on krill as a food source, such as whales, seals, seabirds, penguins and fish (Marr, 1962; Knox, 1970; Osman et al., 2004; Lynnes et al, 2004; Flores et al., 2004). In addition, it is a growing, globally important fisheries resource (Nicol and Foster 2016; Trathan and Hill 2016; Johnston et al., 2022; Hill et al., 2024; Kawaguchi et al., 2024, Meyer et al., 2020; Gallagher et al., 2023; Lancraft et al., 2004; Nicol et al., 2011; Kaur et al., 2022) that has in recent years started focusing also on the Lazarev Sea region. The focus of recent international programs, such as the Southern Ocean GLOBEC (Global Ocean Ecosystem Dynamics) program on this species is a clear indication of its biological and ecological importance.

Krill inhabits the Southern Ocean predominantly south of the Polar Front, with an estimated total stock biomass ranging between 169 and 379 million metric tons (Siegel, 2005; Atkinson et al., 2009). The Lazarev Sea supports a substantial krill population (Meyer et al., 2010; Siegel, 2012) with biomass compared less to the highly productive Antarctic Peninsula but similar to other regions in East Antarctica (Atkinson et al., 2008; Siegel, 2012). Studies in the Lazarev Sea have concluded that this region does not support a single self-maintaining krill population but represents a complex transition zone of stocks with different origins (Siegel, 2012).

Krill recruitment has been shown to be influenced by environmental conditions in upstream spawning areas as krill is subject to large-scale transport by ocean currents (Hofmann et al., 1998; Fach et al., 2006, Thorpe et al., 2007; Pinones and Fedorov, 2016) and a constantly changing seascape that provides changing food environments

during this transport. Previous studies showed that the different spawning and nursery grounds along the western Antarctic Peninsula are connected via ocean currents (Pinones et al, 2013a; Gallagher et al., 2023) and are even connected to the krill population found at South Georgia (Fach et al., 2006; Thorpe et al., 2007). Similar transport pathways have been shown for krill in the Ross Sea (Pinones et al., 2016). The Lazarev Sea is a known spawning region for Antarctic Krill (Atkinson et al., 2008; Meyer, 2011) that is connected to the neighboring Weddell Sea and the Riiser Larsen Sea via the current dynamics of the Southern Ocean and hence krill population dynamics are expected to be influenced by them.

1.3 Antarctic krill life cycle

Antarctic krill spawning occurs between December and February in austral summer (Ross and Quetin, 1986). After spawning, when gravid females lay their eggs in the upper ocean water column (Marr, 1962; Siegel, 2005), the embryonal and early larval stages of krill undergo a descent-ascent cycle in which embryos sink rapidly through the water column to depths of 700 to 1000 m (Figure 2), and after hatching larvae ascend to the surface where they begin feeding (Marr, 1962; Hempel and Hempel, 1986; Hofmann et al.,1992). While ascending, the larvae develop through two non-feeding (Nauplius, Metanauplius) and several feeding developmental stages (Calyptopis, C1-C3). Afterwards, larvae develop through three Calyptopis stages and six Furcilia stages before reaching the juvenile stage during the next spring or summer (Figure 2). Denys et al., (1982) showed that adult krill can molt into an earlier subadult stage after spawning. In addition, krill have been observed to shrink by molting if starved of food sources (Ikeda and Dixon, 1982; Nicol et al., 1992). Thus, a given age group of krill can include krill that may have shrunk to that size, thereby overlapping separate age groups. As a result, krill age cannot be predicted solely from length.

Studies showed that during the early life cycle of krill there are periods of critical importance to krill survival (Ross and Quetin, 1991; Meyer, 2011. One of them is

the time when krill larvae develop into the first feeding stage (Calyptopis 1, C1). Larvae have only a short time frame of ~10 days to find food before reaching a starvation threshold (a point of no return) after which they do not survive even if food becomes available (Ross and Quetin, 1989). Krill larvae then need to have accumulated sufficient lipid reserves by late austral summer/fall, that they need to survive austral winter when food is scarce (Fach et al., 2008; Meyer et al., 2010). During the winter, larvae also are in need to find biota associated with sea ice for additional food and shelter (Ross and Quetin, 1991; Daly, 1990; Meyer et al., 2002; Meyer et al., 2017). Consequently, a retreat of winter sea ice may be a dominant driver of krill population decline (Flores et al., 2012).

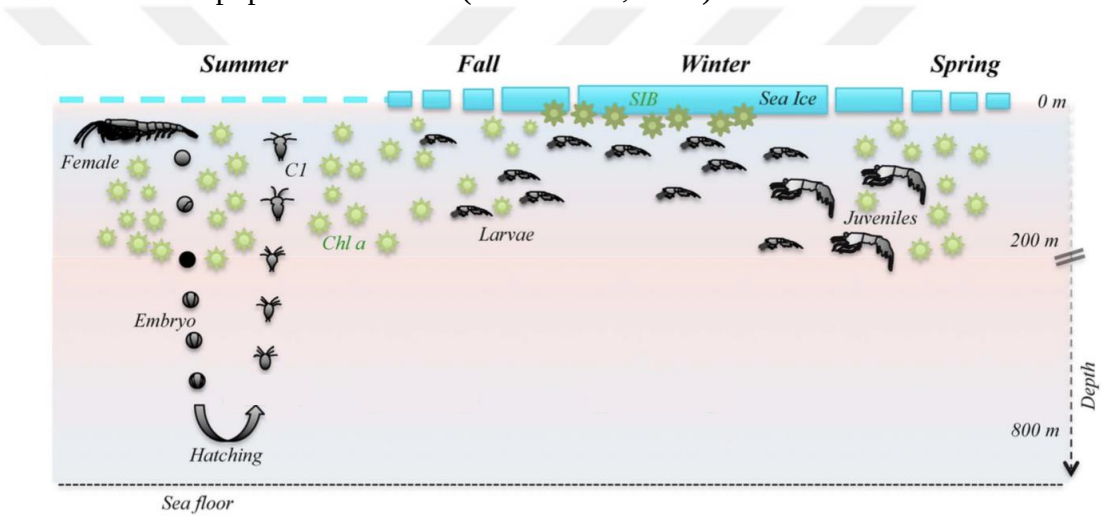


Figure 2 Schematic of the early life cycle of Antarctic krill. Reproduction begins during austral summer; after hatching, the embryos develop into nauplii stages and to the first feeding stage Calyptopis 1 (C1) and after completing the descent-ascent cycle feed on the available chlorophyll a during the rest of austral summer and early austral fall. Krill overwinter underneath sea ice and molt into juveniles during the following austral spring and austral summer. Phytoplankton food (Chl a) and sea ice biota are available for winter-feeding by krill larvae. Reproduced from Pinones and Fedorov (2016).

Chlorophyll concentrations in the Lazarev Sea are highly variable during austral summer, ranging from 0.2 to 4.8 mg m^{-3} in 5 to 30 m depth with an average of 1.0 mg m^{-3}. But in austral fall, after krill spawning has occurred, the chlorophyll concentrations range from only 0.06 to 0.5 mg m^{-3}, diminishing to only 0.01 - 0.04 mg m^{-3} in winter (Meyer et al., 2010). Therefore, transport during and after the

spawning season places larval and juvenile krill in a low food environment during a time when their potential food supply is declining even further. However, krill are omnivores and exploitation of food sources other than pelagic phytoplankton, such as zooplankton, is possible (Kawaguchi et al., 1986; Daly, 1990; Nordhausen et al., 1992), as is feeding on sea ice biota (Marschall, 1988; Daly and Macaulay, 1991, Meyer et al. 2017), which has been observed for larval and juvenile krill, as well as detritus feeding (Holm-Hansen and Huntley, 1984; Kawaguchi et al., 1986; Daly, 1990; Nordhausen et al., 1992). Also, the temperature gradient that krill experience while moving across large distances may affect metabolic processes and thus growth (Quetin et al., 1994; Atkinson et al., 2008).

1.4 Connectivity in marine populations

Many marine populations, including krill or other zooplankton and fish stocks, are structured by their physical environment. As a result, the spatial relationships between physical and biological processes are potentially key to understanding their distribution and abundance. Dispersal occurs mostly during early life through advection by ocean currents, when young individuals are not yet capable of active movement. Older life stages often exhibit behavior and active movement and may therefore be able to move on different spatial scales.

Larval dispersal by ocean currents and the resulting connectivity between different oceanic regions have been identified as crucial factors for structuring marine populations (Cowen et al., 2006; Condie et al., 2011; Wood et al., 2014; Torri et al., 2018; Legrand et al., 2019; Patti et al., 2020) and managing fisheries today (Rossi et al., 2014; Dubois et al., 2016; Di Stefano et al., 2022). It is also of great use for designing networks of Marine Protected Areas (MPAs) (Lester et al., 2009; Moffitt et al., 2009; Moffitt et al., 2011; Clavel-Henry et al., 2024), or even understanding the spread of marine pests (Glasby and Lobb, 2008; Jaspers et al., 2018; Johnston and Purkis, 2011; Johnston and Purkis, 2014a; Johnston and Purkis, 2014b).

Marine population connectivity depends on a variety of factors such as habitat availability, spawning efficiency, retention versus dispersal, trophic interactions and adult movements (Cowen and Sponaugle, 2009; Game et al., 2009). To understand the level of dispersal and hence connectivity between different areas, tagging of animals is often not possible because of the small size of the individuals in their early life stages, and the large numbers of tagged animals needed to be able to recapture enough of them. An alternative approach is to test connectivity using particle simulations (Cowen et al., 2006, Fach and Klinck, 2006; Ashford et al., 2010, Fach, 2014), which is performed in this study.

The ocean currents in the Southern Ocean associated with the Antarctic Circumpolar Currents (ACC), the major, eastward flowing current system circling the continent, are rather strong (up to 50 cm s^{-1}). These strong currents are connecting different regions that may be spatially far apart, with each other. The physical environment of the ocean is of great importance for Antarctic krill, because temperature and salinity distributions facilitate suitable habitats and the currents transport pelagic eggs, larval and juvenile krill long distances downstream of suitable marine environments. The resulting connectivity between these regions can be calculated with models and the probability of krill that have been transported these distances can be estimated depending on the environmental conditions, including food availability.

Transport and connectivity of krill between regions spatially far apart have been demonstrated for the western Antarctic Peninsula and South Georgia regions (Hofmann et al., 1998; Fach and Klinck, 2006; Fach et al, 2006), with Antarctic krill spawned at the Antarctic Peninsula and the Weddell Sea supplying the South Georgia krill population. It was found that food availability and the length of time needed for transport together favor juveniles as the stage most likely to survive transport to South Georgia (Fach et al., 2006). Similarly, long transport pathways have been shown for to shape the krill population in the Ross Sea (Pinones et al., 2016) as well as connect spawning and nursery grounds along the western Antarctic Peninsula (Pinones et al, 2013a; Gallagher et al., 2023).

1.5 Aims of this study

Previous studies of krill in the Lazarev Sea suggested that this region does not support a single, self-maintaining population, but represents a complex transition zone of stocks with different origins (Siegel, 2012), which are hypothesized to originate from other adjacent seas, possibly the Scotia Sea, location of the Turkish Antarctic Station, or Cosmonaut Sea in the south-west Indian Ocean and to its west, neighboring Riiser-Larsen Sea. The aim of this study is therefore to investigate investigating the hypothesis that krill in the Lazarev Sea is not a single self-maintaining population but influenced by different krill populations from the Scotia Sea and even the Cosmonaut Sea via ocean currents and find the population(s) supplying input the Lazarev Sea krill population. And further, to investigate if environmental and biological parameters such as the timing of spawning, food availability and reproduction influence the survival of different developmental stages of krill (from larvae to adult krill) during such a long-distance transport as well as assess the impact of interannual variability on krill transport and survival dynamics.

This is achieved by using the output of an innovative modeling system including high-resolution, circumpolar, hydrodynamic-ecosystem model (FESOM-REcoM2) run for 10 years, together with a Lagrangian Particle Tracking model and a sophisticated individual-based model of Antarctic krill.

Given the global significance of krill, maintaining their population levels and their ecological relationships with other krill populations in the Southern Ocean is important for the sustainable management of this species. The results on connectivity of Antarctic krill originating in the Lazarev Sea with other regions is further of interest for the Commission for the Conservation of Antarctic Marine Living Resources (CCAMLR), the organization that regulates commercial krill catch quotas, as it may demonstrate that fishable krill swarms widely separated in space can belong to the same population. Hence krill fishing quotas need to be adjusted accordingly to ensure future stocks. In addition, CCAMLR is currently working on establishing a network of Marine Protected Areas (MPA) around the Antarctic

continent (Teschke et al., 2016; Teschke et al., 2021). Specifically, a MPA in the Weddell Sea is being planned and the information on connectivity between regions is of value for supporting the proposed MPA boundaries.

CHAPTER 2

MATERIALS AND METHODS

2.1 Modeling system

When talking about modeling in oceanography, the term modeling stands for the theoretical description of the ocean, solving sets of differential equations which describe certain ecosystem dynamics (Fennel and Neumann, 2006) on the computer. Models are simplified forms of the real world and hence include certain levels of uncertainties in reproducing the natural dynamics. They use in situ observation data for a specific species and its habitat in a known/limited area and apply it to larger /unknown areas. The complex modeling system FESOM-REcoM2 used in this study integrates the physical oceanography conditions of the Southern Ocean, such as surface current speed and direction, temperature and salinity together with biological conditions, such as phytoplankton and zooplankton abundance to model the connectivity of different regions between the Lazarev Sea and its adjacent seas for the commercially important Antarctic krill.

To be able to achieve the aims of this study, assessing connectivity between areas separated by large distances, information on the current speeds and direction in the Lazarev Sea is required. In addition, information on temperature, which influences krill metabolism, and on sea-ice cover of the study area is needed, as it potentially provides an additional food source for krill. This information is provided by the circumpolar version of the Finite Element Sea Ice-Ocean Model (FESOM) (Wang et al., 2014; Sidorenko et al., 2015; Rackow et al., 2017 Danilov et al., 2017). The simulation of particle dispersal is achieved using a Lagrangian Particle Tracking model specifically developed for FESOM current outputs (Wekerle et al., 2018). The particle tracking simulations are used to assess the effect of circulation patterns on

krill distribution in the Lazarev Sea and investigate long-distance transport vs retention patterns.

The other information vital for the study is information on food supply for krill such as phytoplankton, particularly diatoms, and zooplankton biomass, as well as detritus concentrations in the study region. This information is supplied by the ecosystem model REcoM2 (Regulated Ecosystem Model 2) (Hauck et al., 2013; Schourup-Kristensen et al., 2014) coupled to FESOM. Model runs of FESOM coupled to REcoM2 have proven to be well suited for studies on the global and regional scale (Schourup-Kristensen et al., 2014, Schourup-Kristensen et al., 2018; Karakus et al, 2021, Karakus et al, 2022).

Further, the growth and survival of Antarctic krill during transport and under the specific environmental conditions of the Lazarev Sea is simulated with an Individual Based Model (IBM) of krill (Fach et al., 2002; Fach et al., 2008).

2.1.1 FESOM

FESOM (Finite Element Sea Ice–Ocean Model) is a finite element model that solves the hydrostatic primitive equations under the Boussinesq approximations (Danilov et al., 2004; Wang et al., 2008). FESOM is the first mature, global sea-ice ocean model that employs unstructured-mesh methods and has been developed and run at the Alfred Wegener Institute, Helmholtz Centre for Polar and Marine Research (AWI) over the last 15 years (Danilov et al., 2004; Wang et al., 2008; Timmermann et al., 2009). It is used for simulations of the three-dimensional global ocean with special focus on the Antarctic (Timmermann et al., 2012; Timmermann and Hellmer 2013, Haid and Timmermann, 2013). It includes elastic-viscous-plastic sea ice dynamics together with the thermo-dynamics adopted from Parkinson and Washington (1979) as described in detail by Timmermann et al. (2009). The model uses an Arakawa A-grid with vertical z coordinates for simplicity. The bottom topography of FESOM's grid south of 60^{o}S, is constructed using the bottom

topography from Timmermann et al. (2010) with a resolution of 1 min (Rtopo-1). The version of FESOM used utilizes a linear representation on tetrahedrals (in 3-D) for all model variables such as temperature and salinity but also the biological tracers. The BOLD mesh as described in Sein et al. (2016) was used where the finest horizontal resolution is 10 km and includes 47 vertical layers. In this mesh regions with high sea surface height variability, such as pass ways of main currents, such as the Antarctic Circumpolar Current (ACC) are resolved at 10 km. This means the horizontal resolution in the Lazarev Sea is 15-20 km, even though the model is not eddy permitting. in the horizontal dimension. It still guaranteed adequate resolution of eddies in the Antarctic Circumpolar Current (Figure 3). In this study, further simulations were undertaken with the CORE mesh (Sidorenko et al., 2011; Sidorenko et al., 2015; Danilov et al., 2017; Wang et al., 2014) which is coarser in spatial resolution than the BOLD mesh.

The sea ice implementation of FESOM is based on the elastic–viscous–plastic (EVP) rheology (Hunke and Dukowicz, 1997), adapted to operate on unstructured triangular meshes to accommodate local mesh refinement in polar and marginal ice zones (Timmermann et al., 2009; Wang et al., 2014). This approach helps simulate how sea ice moves and deforms under wind, ocean currents, internal stresses and Coriolis force. The model can represent sea ice as a range of thickness categories simulating both ice dynamics and ice thermodynamics (Timmermann et al., 2012). Thermodynamics are treated using a multi-layer representation of sea ice and snow, solving energy balance equations for temperature evolution, with parameterizations for surface melt, basal growth/melt, and snow–ice conversion. (Timmermann et al., 2012). The model accounts for sea ice salinity, brine rejection during freezing, and freshwater input during melting, thereby influencing ocean stratification and mixed-layer processes. Surface albedo varies dynamically based on snow and melt pond conditions, and ice–ocean heat fluxes are computed interactively, enabling realistic coupling of ocean and sea ice processes in climate and regional simulations (Timmermann and Hellmer, 2013; Wang et al., 2014). The results of the

implementation show that, for the Weddell Sea, FESOM can simulate the ice shelf processes in agreement with field observations (Timmermann et al., 2012).

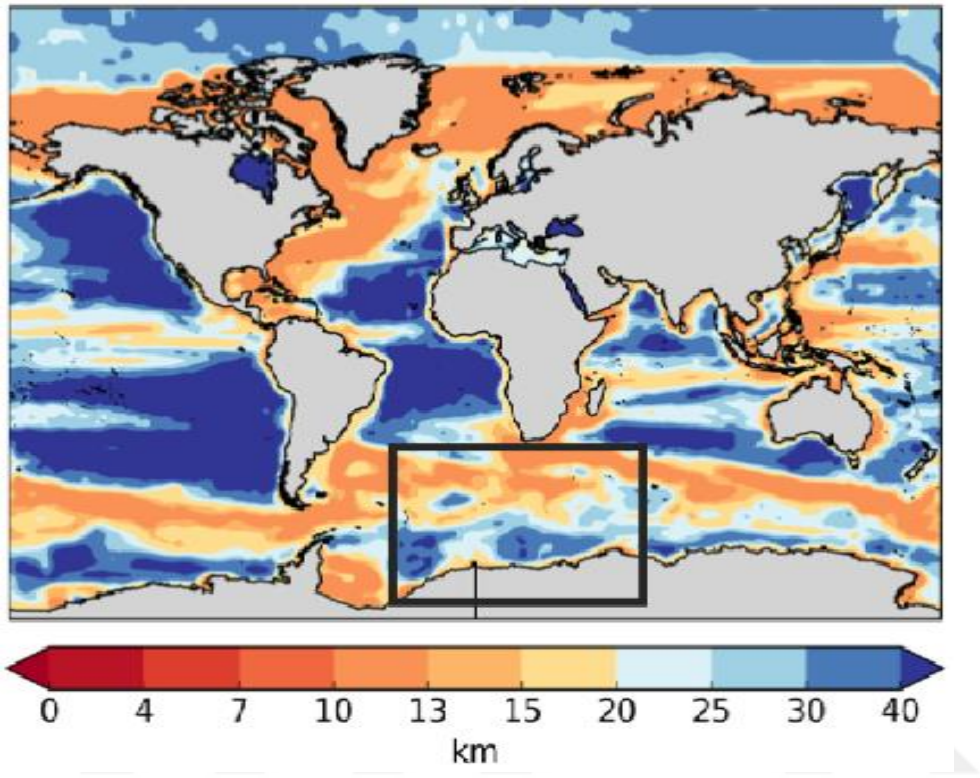


Figure 3 Global resolution of the BOLD FESOM mesh (reproduced from https://fesom.de/models/meshessetups/). The black box marks the greater Lazarev Sea area for which this mesh provided a higher resolution mesh than the CORE mesh.

2.1.2 REcoM2

REcoM2 (Regulated Ecosystem Model 2) is an ecosystem model including 21 state variables that are representing two classes of phytoplankton: nanophytoplankton and diatoms, zooplankton and detritus, as well as benthos (Figure 4). The model is employing the cell quota approach, meaning the internal nutrient ratios of phytoplankton cells vary depending on light, temperature and nutrient conditions and are not set to Redfield ratio. The model simulates the nutrients nitrogen, silicon and iron, as well as the carbon cycle, including calcium carbonate. Carbon chemistry follows the guidelines provided by the Ocean Carbon Model Intercomparison Project

(Orr et al., 1999), and the air–sea flux of CO_2 is parameterized after Wanninkhof (1992). Uptake of nutrients in the model is controlled by the internal concentrations, as well as the external nutrient concentrations, while phytoplankton growth depends only on the internal nutrient concentrations (Droop, 1973; Droop, 1983). Iron uptake in the model is controlled by Michaelis-Menten kinetics.

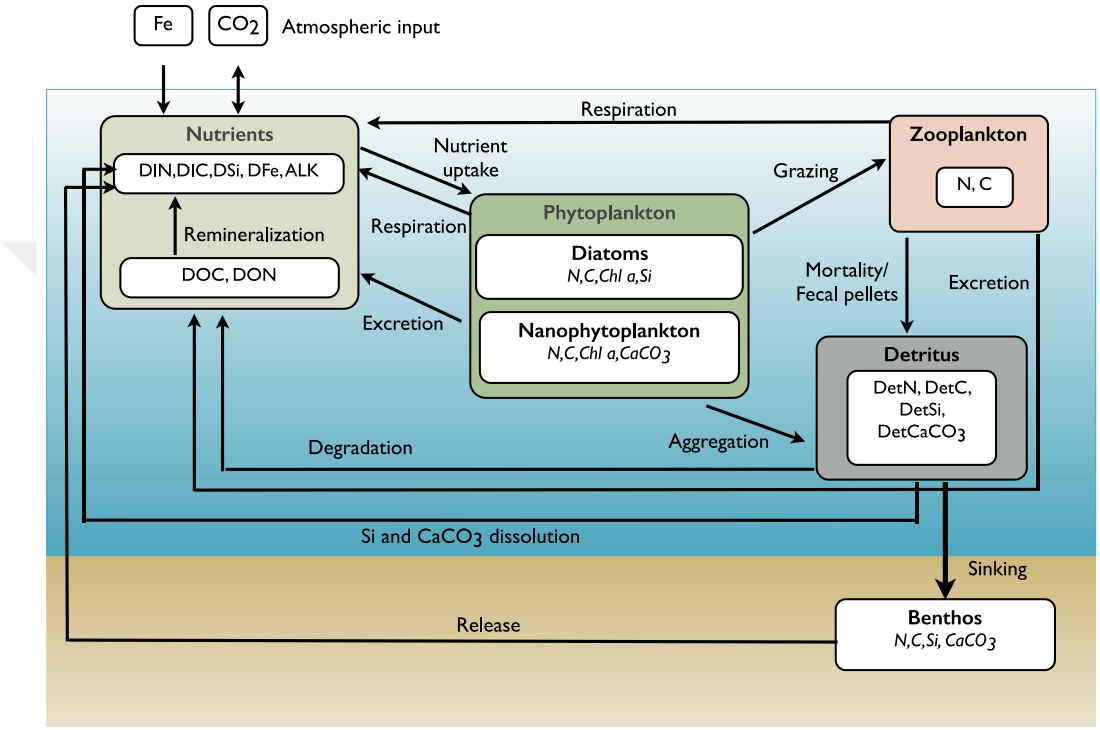


Figure 4 Schematic of the basic pathways resolved in the biochemical model REcoM2. The model tracks 21 state variables that can be grouped (indicated by boxes) into dissolved nutrients (upper left) together with dissolved organic material) and carbonate system parameters, phytoplankton (center), zooplankton (upper right), detritus (middle right), and benthos (lower right). Source and sink terms are depicted by arrows.

2.1.3 Model implementation scenarios

The FESOM-REcoM2 model used in the study started with a 52 year-long simulation starting in 1958 using a global setup with of the BOLD mesh setup. An analysis of only the last 10 years for the time 2000–2009 is presented in this study. The 10-year simulation is following a 42-year spin up from 1958-1999 that was performed to

reach model equilibrium. The simulation is forced with the atmospheric data obtained from the Japanese 55-year Reanalysis (JRA-55) compiled by Kobayashi et al. (2015), which is a comprehensive climate dataset covering the period from 1958, when regular radiosonde observations began on a global basis. Initial conditions for temperature, salinity, nutrients, dissolved inorganic nitrogen and dissolved silicic acid were taken from the World Ocean Atlas (WOA) 2013 products (Garcia et al., 2014), and dissolved inorganic carbon (DIC) and alkalinity from GLODAPv2 (Lauvset et al., 2016).

It should be noted that the model simulations of FESOM-REcoM2 were undertaken in collaboration with colleagues at the Alfred Wegener Institute (AWI) in Bremerhaven, Germany. Within the framework of the TÜBİTAK 1001 project 118Y325 (TÜBİTAK, 2022) this collaboration was established and entailed the use of the German National High Performance Computing computer to run the necessary simulations. My colleague Dr. Ehsan Sadighrad performed and validated two 10year simulations of the three-dimensional global ocean and ecosystem from 2000-2009 with special focus on the Southern Ocean. The output of these simulations are used in this study.

The transport of larval and juvenile krill was simulated using Lagrangian particle tracking in the three-dimensional velocity fields of the FESOM model. Of the 10-year simulation of particle trajectories results from simulations starting in three years (2004-2006) are presented here. They are chosen to coincide with three cruises that were performed in the LAKRIS project that provide a comprehensive data set on krill distribution (Meyer et al., 2010; Siegel, 2012). Another Lagrangian particle tracking simulation series was also set up where 2041 particles are placed with equal spacing within the study area (Figure 1).

The REcoM2 outputs used for this modeling study are derived using the older CORE mesh (Danilov et al., 2017; Sidorenko et al., 2011) with a coarser resolution instead of the BOLD mesh setup used for FESOM. The reason for this change in mesh was that biochemical tracer output values were becoming unstable for the study region

when using the BOLD mesh. Instead the older stable CORE mesh biochemical output values are interpolated on top of the BOLD mesh points and extracted separately to be used as food inputs for the krill IBM.

2.2 Model validation

To validate the FESOM-REcoM-2 model results with observations, it was necessary to collate all available data from many different data sources and interpolate the available data onto the same grid as the FESOM-REcoM2 model to do an in-depth model-data comparison. The following available data sets have been used for this purpose: The World Ocean Atlas 2013 data sets were used for the validation of temperature (Locarnini et al., 2013), salinity (Zweng et al., 2013) and nutrient distributions (Garcia et al., 2014); Sea ice extent from satellite data available from the National Snow and Ice Data Center (NSIDC); satellite data on chlorophyll concentration and its seasonal cycle available from The ESA (European Space Agency) Ocean Colour Climate Change Initiative (OC-CCI) version 3.1 (http://www.esa-oceancolour-cci.org). Because of a lack of global data set for dissolved iron, the model dissolved iron concentrations output of FESOM-REcoM2 are compared to concentrations from a different global hydrodynamic model called NEMO-OPA coupled with PISCES, a biochemical model, assuming that this PISCES/OPA model data is a good approximation to the actual global dissolved iron concentrations (Aumont et al., 2015). An extensive model validation was conducted by my colleague Dr. Ehsan Sadighrad by comparing simulation results achieved by the FESOM-REcoM2 model simulation on the BOLD mesh over 10 years from 2000-2009 and to data. Only a small fraction of validation results is presented in the results section with his permission. The full validation is available in the final TÜBİTAK report for project 118Y325 (TÜBİTAK, 2022) and here only the chlorophyll concentration result presented, as it is a proxy for the main food for krill.

2.2.1 Physical parameters

The temperature and salinity distribution around Antarctica is modelled very well by the FESOM model (TÜBİTAK, 2022). The average temperature around the Antarctic continent is close to 0°C, increasing slowly zonally past 60°S to about 14°C when reaching 40°S. This spatial distribution is produced by the model and matches the WOA data (TÜBİTAK, 2022). The difference between both is minor (maximum of +-0.8°C) in the Southern Ocean, below 60°S. The salinity in the Southern Ocean ranges between 33.6 psu and 34.2 psu with fresher water located in areas near ice sheets such as in the Weddell Sea and Ross Sea and the model matches this distribution. The difference between both is again minor (maximum of +-0.36psu) (TÜBİTAK, 2022).

The very good fit between the spatial distributions of modelled and observed surface temperature and salinity is further demonstrated correlation coefficients higher than 0.99 for temperature and higher than 0.95 for salinity. The standard deviations of 6 and 1, translating to normalized standard deviation of close to 1 for both fields.

The simulated maximum mixed layer depth in the Southern Ocean is between 10-100 m with maximum mixed layer depths being deeper (down to 400m) again at the ice shelfs of the Weddell and Ross Sea due to the melting ice there (not shown here). The mean mixed layer depth shows four bands of deep and shallow mixed layers with again shallow mixed layer depths between 50-100m near the continent but deep mean mixed layers reaching 300m directly at the edge of the permanent ice sheets of the Mixed layer depth (MLD) is important for the ecosystem of the ocean as it marks the depth down to which the upper ocean is completely mixed and uniform in temperature, salinity and therefore also density.

Further, the seasonal variability of the MLD leads to entrainment of water with high nutrient concentrations to the surface water during winter, and the maximum depth of the mixed layer during the year is therefore especially important from a biological point of view. Overall, the modelled maximum fits well with the observations, but it

is generally too deep in the Southern Ocean, with the consequence that limiting nutrients are frequently replenished during winter. This may lead to increased nutrient supply and increased net primary production (NPP) in the area.

2.2.2 Biochemical parameters

Chlorophyll concentrations in the Southern Ocean are low despite the relatively high nutrient concentrations (Figure 5A) and highest concentrations are found close to the continent and landmasses. This is generally due to the higher iron concentration in those regions. There are chlorophyll hotspots located at the coast of the Antarctic Peninsula, the Ross Sea and other coastal regions. The region downstream of the Antarctic Peninsula, the Weddell Sea and also the Lazarev Sea show moderate chlorophyll concentrations around 1 mg Chl m^{-3}.

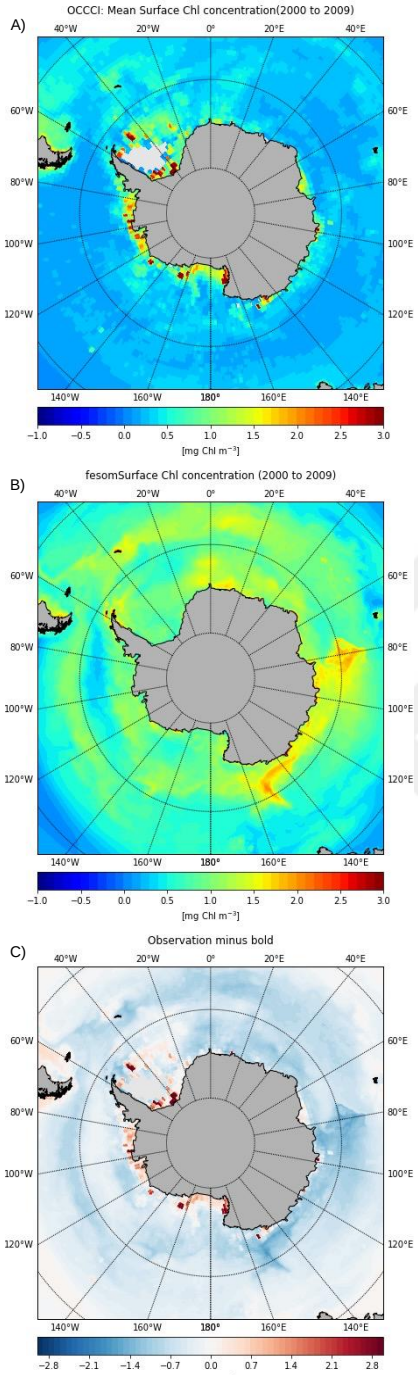


Figure 5 Data-model comparison of surface chlorophyll concentration (mg Chla m^{-3}) from 2000-2009. Top image: Surface chlorophyll data from the OC-CCI data set. Middle image: mean surface chlorophyll output from the 10-year FESOM model run. Bottom image: Difference between data and model results (chlorophyll data minus the model chlorophyll output). Reproduced with permission of Dr. Ehsan Sadighrad.

The model simulation produces overall higher values than observed on the circumpolar scale (Figure 5B), particularly off western Antarctica. This is despite the fact that iron concentrations are generally underestimated by the model (not shown here). The difference between model and data displays this general overestimation by the model of up to 1.4 mg Chl m^{-3} in the Lazarev Sea (Figure 5) and even more in other regions. However, the model grossly underestimates the hotspots along continental margins. Overall, this leads to a correlation coefficient of 0.517 (Figure 6).

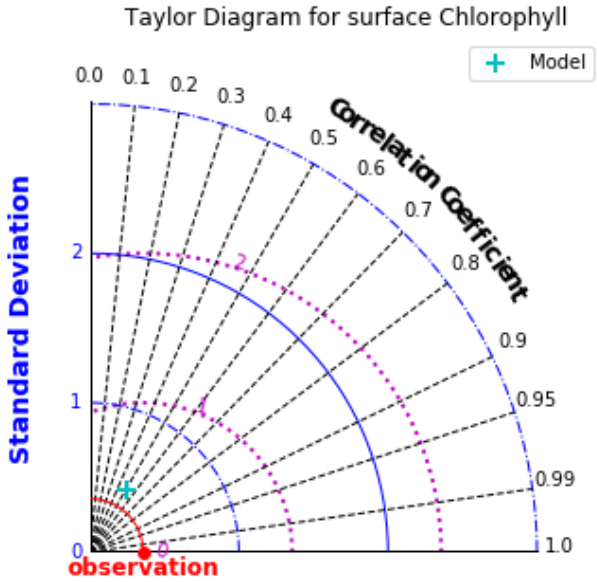


Figure 6 Taylor diagram of surface chlorophyll model data comparison in the Southern Hemisphere

Further the model gives information about the net primary production (Figure 7A) (TÜBİTAK, 2022) also split into the two phytoplankton groups represented in the model. Diatoms (Figure 7B) thereby dominate the primary production from the continent to 46°S while Nanoplankton (Figure 7C) dominates north of this area. The fraction of the total biomass comprised by diatoms in the Southern Ocean differs between studies (Alvain et al., 2005; Hirata et al., 2011).

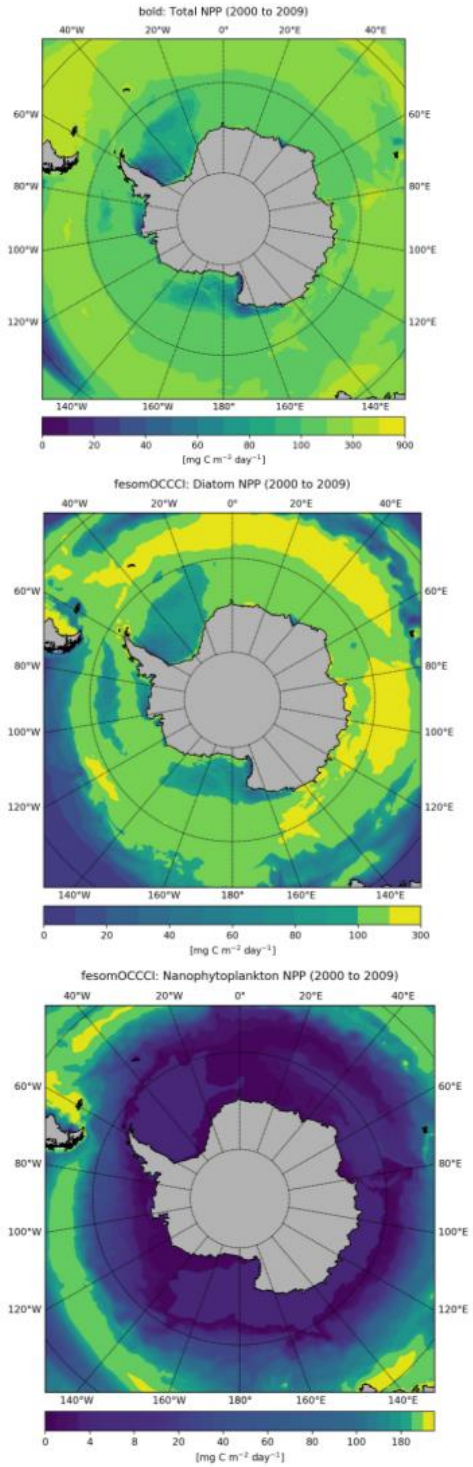


Figure 7 Model output of net primary production. (mg C m^{-2} d^{-1}) Top image image (NPP) from a 10-year FESOM model run encompassing the years 2000-2009: Mean NPP. Middle image: mean diatom NPP. Bottom image: mean nanophytoplankton NPP.

In the present study, diatoms are responsible for most of the NPP south of 50°S, varying from 0 % in the very iron limited waters of the South Pacific to 100 % in the iron replete regions of the Weddell Sea and on the Patagonian shelf. Vogt et al. (2013) compared the results of four ecosystem models and showed that the percentage of diatom biomass in the Southern Ocean differed significantly between them, ranging from 20 to 100 %. The diatom percentage is therefore within the spread of other models.

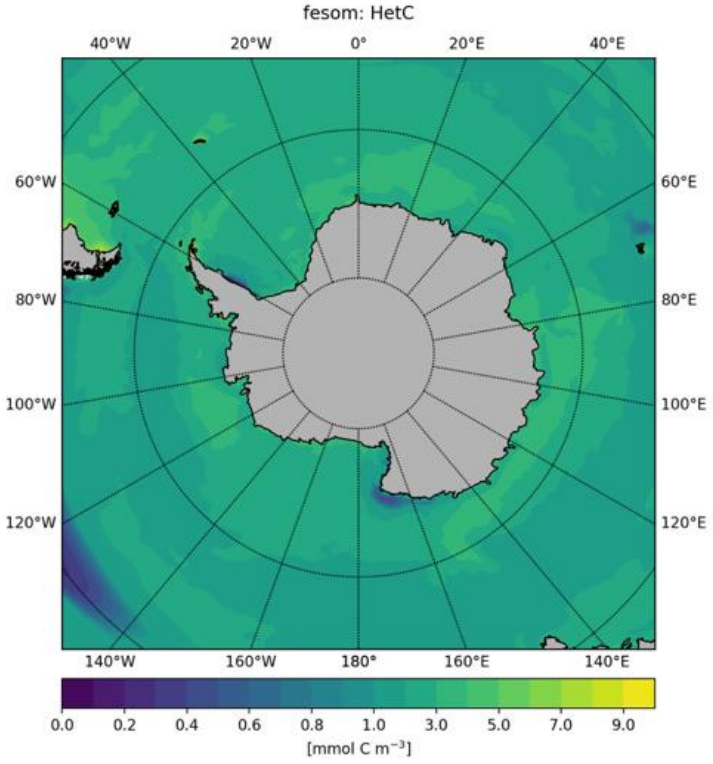


Figure 8 Model output of heterotrophic biomass (mmol C m^{-3}) representing copepods

Heterotrophs, representing a general copepod group, is also include in the model. Because krill do feed on copepods and it is an important food in terms of lipid source for krill it is of particular interest to this study. The distribution of copepod biomass around the Antarctic is modeled as between 1 and 3 mmol C m^{-3} (Figure 8) with some patchiness indicating a band of low copepod concentration starting at 50°S and lower biomass in the Weddell Sea and Ross Sea areas (TÜBİTAK, 2022).

The FESOM-REcoM2 model has been used in other studies and has been extensively validated for the Southern Ocean over the years (Schourup-Kristensen et al. 2014, 2018), and particularly the REcoM2 model assessment outlines the global NPP distribution overall as 25.9% dominated by the diatoms and that the surface distribution of Chlorphyll-a is somewhat exaggerated by the model compared to satellite data at the higher latitudes, such as the Southern Ocean and the Artic regions.

2.3 Parameterization of sea ice algae

One of the important food items for krill in winter is sea ice algae. It has been shown that during winter krill, especially larval krill, rely on sea ice biota as food resource and use sea ice for shelter (Ross and Quetin, 1991; Daly, 1990; Meyer et al., 2011). The FESOM-REcoM2 modeling system does not include explicitly sea ice biota, however it does include sea ice dynamics and hence the percent ice cover, ice cover duration and ice thickness. The biomass and distribution of sea ice biota under the sea ice was therefore calculated based on light availability, thickness of the ice and how much of the ocean is covered for how long a time following the approach by Meiners et al. (2012) and Melbourne-Thomas et al (2016), which has shown that bottom algal communities have the highest probability of forming with ice thickness between 0.4 m and 1 m owing to favorable brine salinities, nutrient availability, temperature conditions and irradiance.

The amount of photosynthetically available radiation (PAR) transmitted through the ice is linked to the thickness of the ice itself. Experiments done with Antarctic Sea ice by Perovich (1993) makes it possible to assign transmittance values to certain thickness of ice. Assuming that the ice is non snow covered white Antarctic Sea ice, the transmittance values for 400 nm wavelength was split to 7 intervals of ice thickness with distinct transmittance values (Table 1).

Table 1 Transmittance values of thickness intervals

Thickness (m)	Transmittance
0.00000 – 0.10624	1.000
0.10625 – 0.31249	0.750
0.31250 – 0.74999	0.500
0.75000 – 1.42499	0.250
1.42500 – 1.97499	0.100
1.97500 – 2.99999	0.050
3.00000 – 3.50000	0.025

Using the shortwave radiation model outputs of FESOM in conjunction with the ice thickness outputs, the estimated amount of PAR transmitted to the bottom of varying thickness of ice was calculated by multiplying with the appropriate transmittance value for the given thickness. Since krill only has access to the bottom of the sea ice, only the transmittance through the entire ice needed to be calculated.

Bottom algal communities are only available to larval krill if there is sufficient light for algal growth and the light compensation point for sea-ice biota growth during winter is 1 µmol photons m^{-2} s^{-1} (Morgan-Kiss et al., 2006) which is equal to 0.45 W m^{-2} per week (Melbourne-Thomas et al., 2016). Therefore, the transmitted light values at grid points were averaged over 52 weeks per year and if a point had less than 0.45 W m^{-2} for a given week, it was filtered out from the sea ice algae calculation for the given week.

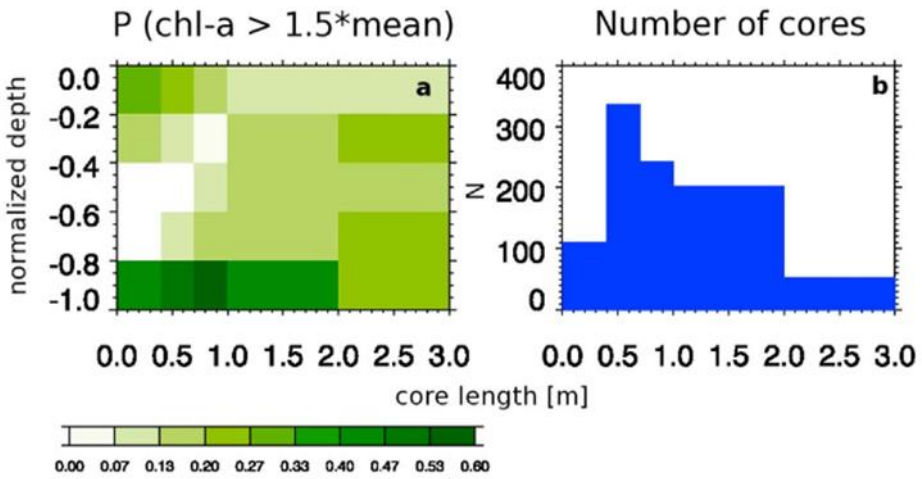


Figure 9 The probability of Chlorophyll a concentration versus the normalized depth of ice cores taken in the Antarctic a) and the number of ice cores used for each length class used for the normalization b). Plots are taken from Meiners et al. (2012).

Availability of sea ice algae is based on the normalized distribution of chlorophyll a from ice cores (Figure 9) taken from the Antarctic ice (Meiners et al., 2012). Using the 1300 ice cores as a base, 5 intervals of ice thickness are assigned a base chlorophyll a value (Table 2).

Table 2 Chlorophyll a values assigned to ice thickness intervals (from Meiners et al., 2012)

Thickness (m)	**mgChla m^{-3}**
0.000 – 0.004	0.0000
0.005 – 0.399	0.6525
0.400 – 0.999	1.2000
1.000 – 1.999	0.6525
2.000 – 3.500	0.3525

This base value is then further multiplied with the integrated chlorophyll a mean of the given season, which is 12.9 mg chla m^{-3} for austral summer, 8.9 mg chla m^{-3} for austral fall, 3.2 mg chla m^{-3} for austral winter and 6.9 mg chla m^{-3} for austral spring. This sea ice algae parameterization in this study was applied to all years of the simulation 2000 – 2009.

2.4 Lagrangian particle tracking model

To simulate the drifting of krill larvae and juveniles with the ocean currents a Lagragian particle tracking model was used (Wekerle et al., 2018). Particles were placed in the study region and tracked over time for one year. Particles were tracked both forwards and backwards in time to determine both the fate of krill originating in the Lazarev Sea and the origin of the krill found In the Lazarev Sea.

The equation governing the Lagrangian Particle Tracking calculation (Wekerle et al., 2018) follows:

$$\frac{d\vec{X}}{dt} = \vec{U}(\vec{X}, t)$$

Where $\vec{X}$ is the position of the particle in three dimensions that changes with time ($\frac{d\vec{X}}{dt}$) and is modified by the three-dimensional velocity field ($\vec{U}(\vec{X}, t)$) obtained from. The Lagrangian drifter code is using the Euler method for numerical integration with a one-hour time step and particle locations are recorded every 24 hours.

Antarctic krill larvae undergo diurnal vertical migration over the top 200 m of the water column feeding in surface waters at night and spending daylight hours at depth (Fraser 1936; Nast 1978; Demer and Hewitt 1995; Meyer et al., 2017). The effect of this vertical migration was evaluated in different modeling studies (Alonzo and Mangel 2001, Alonzo et al., 2003; Murphy et al., 2004; Cresswell et al., 2007, Cresswell et al., 2009), and it has been found that vertical movement does not strongly influence krill location (Cresswell et al. 2007; Murphy et al., 2004; Pinones et al. 2013a). Hence vertical migration behavior of krill was not included in this study.

2.4.1 Particle tracking simulations

2.4.1.1 Particle release in the entire Lazarev Sea during spawning season

Lagrangian particles representing larval krill were released at grid points throughout the Lazarev Sea in the months November, December, and January of each year (2004-2006), coinciding with krill spawning season (Ross and Quetin, 1986). A total of 2041 particles were released across the entire Lazarev region placed between 10°W-10°E and 62°S-72°S at a distance of 10 km between particles (Figure 10, red square). To cover the entire spawning season and variability over that time frame, particles were released at 6 times on the 1st of November, 16th of November, 1st of December, 16th of December, 1st of January and 16th of January, and were tracked for 365 days in each simulation. This way larval dispersal during two consecutive spawning seasons, austral summer of 2004/2005 and 2005/2006, were simulated. That is twelve separate simulations tracking a total of 22,142 particles, using the circulation model output of the years 2004-2006. In addition, particles starting at these locations were also backtracked in time for one year to investigate where the krill present in the Lazarev Sea region originates from. Due to the computational time cost required, only a total of 3 backtracking simulations were performed compared to the twelve performed forward in time. The starting dates of the backtracked simulations are on 1st of November 2005, 1st of December 2005 and 1st of January 2006.

2.4.1.2 Particle release at selected stations during three different seasons

To investigate the variability of transport and retention spatially and temporally, one year long particle tracking simulations were performed where particles representing krill were released at the stations of the LAKRIS expeditions (Meyer et al., 2010) Starting point for the particle tracking simulations are all stations at which during three Antarctic expeditions (2004, ANT XXI-4 and XXII-2; 2006, ANT XXIII-6)

with the German research icebreaker R/V Polarstern called Lazarev Sea Krill Surveys (LAKRIS) detailed in Meyer et al. (2010) found Antarctic krill (Figure 10). There were a total of 12 stations where krill were caught (Figure 10, inset for station locations) during the research cruises conducted in austral fall 2004, austral summer 2005, and winter 2006. Stations 44, 46, 47, 53, 92 represent the austral summer of 2005. The Lagrangian drifter simulations used these as starting points for particles released in austral summer which translates to particles were released particles there in November, December and January (January is technically in 2006 but for sake of simplicity it is included in 2005). Representing the austral fall season of 2004 are stations 621, 634, 678 and 683, and served as starting points for particles released in austral fall in the months of March, April and May. Finally, for the austral winter season of 2006, drifter simulations were started in the months of June, July and August at stations 474, 508 and 516. For each station, these simulations have been conducted tracking particles first forward in time for one year and then backwards in time for one year. Release depths were chosen to be surface (10m) and 200m.

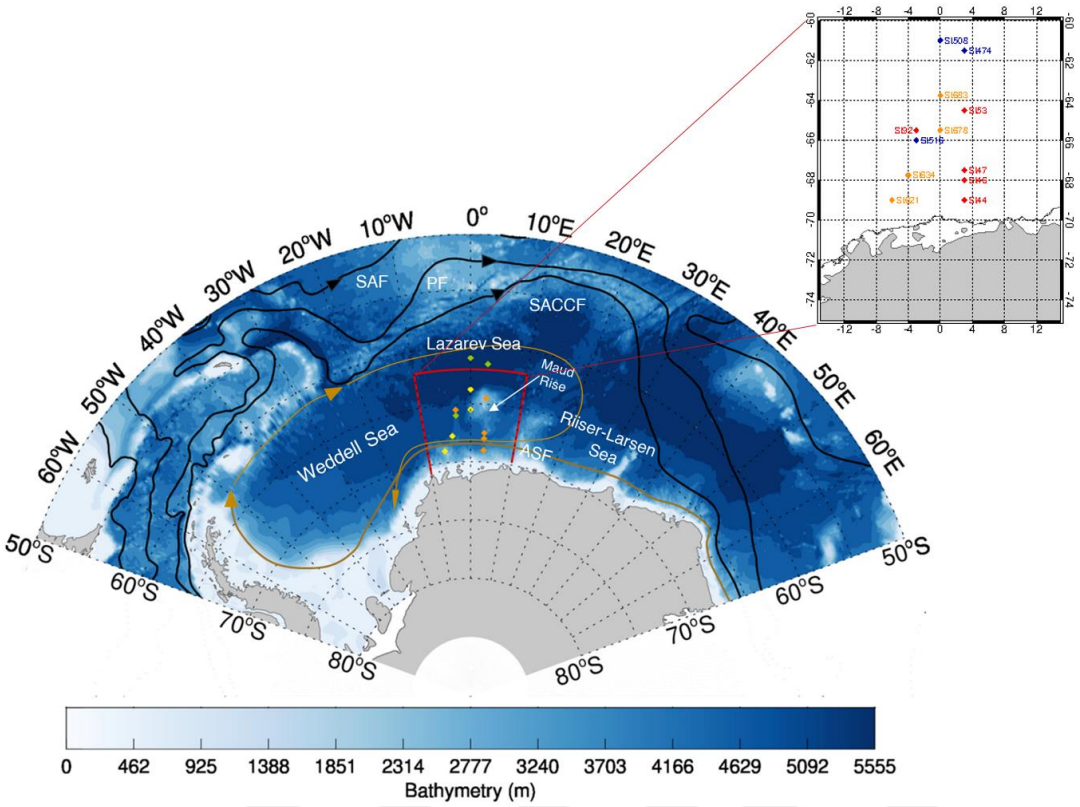


Figure 10 Map of the study region with station inset. Black Lines indicate the Fronts of the Antarctic Circumpolar Current with arrows indicating the flow direction (SAF-Subantarctic Front, PF-Polar Front, SACCF-Southern Antarctic Circumpolar Current Front). Orange line marks the Antarctic Slope Front (ASF). The red rectangle marks the release area of 2041 drifters. The orange dots mark the LAKRIS cruise austral summer stations, yellow dots mark austral fall stations, green dots mark austral winter stations. Inset in the top right corner shows the LAKRIS cruise station locations and station numbers.

To investigate the temporal variability of particle trajectories in each season, particles were released from at each respective station on every day of the respective season. For example, at station 53 particles were released starting from the 1st of November every single day until the 31st of January. This makes for a total of 92 particles that are tracked over one year. Therefore, the overall total number of particles used for the twelve stations amounts to 1104 particles.

2.4.2 Preferred transport pathways

To visualize the temporal variation of the particle pathways depending on release time, preferred transport pathways and retention areas were calculated. This was achieved by dividing the study area into a structured 0.5 x 0.5-degree grid and calculated determining how many particles are located in each grid cell at every time step over the total number of active particles at each time step. With $n_{(g,t)}$ being the number of particles located at grid g at timestep t and N_t the total number of active particles at timestep t the particle accumulation $T_{(g,t)}$ at grid g at timestep t is calculated by:

$$T_{(g,t)} = \frac{n_{(g,t)}}{N_{(t)}}$$

The value for each grid cell is then obtained by taking the mean of all the drifters for every timestep for every given grid cell.

2.5 Krill Individual Based Model

The individual based model (IBM) used to simulate the growth of krill in this study was originally developed by Fach et al. (2008). The krill IBM includes a detailed bioenergetics component that calculates the ingestion of food available to krill, respiration, assimilation, and growth of krill depending on the life stage of the krill and the current season. (Figure 11).

In this study, the food input into the IBM model is extracted along particles trajectories from the ecosystem model REcoM2 results, specifically diatoms, nanophytoplankton, copepods and detritus (mg C m^{-3}). In addition, sea ice algae calculated from the physical components of ice thickness and shortwave radiation is extracted as food source (mg Chla m^{-3}). The sea ice algae component is converted from Chla to C using the conversion constant of 0.040, which is an appropriate for lower light conditions (Arrigo et al., 1993; Johnsen and Hegseth., 1991).

The food inputs are divided into their contribution to the protein, polar lipid, neutral lipid, and carbohydrates pools defined the model. The average phytoplankton, which krill primarily feeds on (Holm-Hansen and Huntley., 1984; Quentin and Ross., 1985; Schnack., 1985) is considered as 3 parts protein, 0.6 parts polar lipid, 0.4 parts neutral lipid and 2.5 parts carbohydrate (Lee et al., 1971; Roman., 1983). The constituents to energy conversions use the ratios of 39.55 J/mg for lipids, 23.65 J mg^{-1} for protein and 17.16 J mg^{-1} for carbohydrates (Brody., 1945; Clarke., 1980).

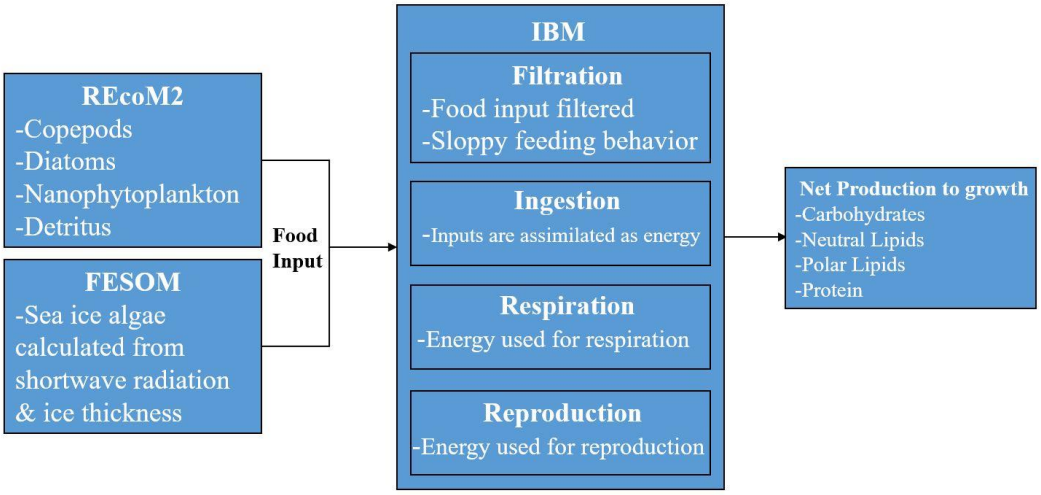


Figure 11 Concept of the processes included in the biochemical, individual based model (IBM) of Antarctic krill and the changes made to it in in this study. Output from the FESOM-REcoM2 simulation (left boxes) serves as krill food in the IBM model and is split into its basic components: carbohydrates, proteins, neutral and polar lipids (right box). Growth of krill in the model is based on formulations that allow differential metabolism of these components ingested by krill represented in the middle box. Net production of krill is calculated by subtracting energy used for respiration from assimilated food, and then translates into building the structural body of krill. Unassimilated food is assumed to be lost as fecal pellets.

The food inputs eaten by krill via filtration are then assimilated by the modeled krill (for a detailed model description see Fach et al., 2002; Fach et al 2008). Assimilated ingestion of food is calculated with the following equation:

$$AI_i = AE_i \,.\gamma\,.F^{cf}\,.food_i(t)$$

The food assimilated by the krill is dependent on the assimilation efficiency (AE_i), feeding fraction (γ), compression filtration rate (F^{cf}), which itself depends on the size

of the krill (Hofmann and Lascara, 2000; Fach et al., 2002). The assimilation efficiency for protein is 100%, for lipid is 100% and for carbohydrate is 20% (Handa, 1969). The feeding fraction is taken as 0.9 for larvae and 0.75 for krill that are other juveniles and adult. Any unassimilated food is lost as fecal pellets.

After this, krill respiration is taken into account calculated as:

$$R = R^s(1 + \zeta + \varepsilon)$$

Where R^s is the standard metabolic rate, which itself is tied to the size of the krill, ε is the feeding activity and finally ζ is the reduced winter activity (Hofmann and Lascara., 2000; Fach et al., 2002). Calculation of the standard metabolic rate indirectly includes the molting energy cost of the krill.

The equation governing net production is calculated as:

$$NP_i = AI_i - R_i$$

Where NP is net production, AI is the assimilated ingestion of food, R is the total respiration and where i stands for the index of the six components proteins, polar lipids, neutral lipids, carbohydrates, chitin and ash. When net production is positive and all biochemical ratios are met, the krill's overall length is increased. Conversely, when the net production is less than the respiration requirements, the existing reserves on the krill are used and afterwards the krill's body length can shrink.

The model assumes that polar lipid represents somatic tissue, and neutral lipids represents any form of lipid reserves and the krill growth is governed by the formation of structural components, therefore neutral lipids act as storage component for krill and do not contribute to the krill length (Fach et al., 2008). The assimilated protein is stored in the somatic tissue protein pool, the assimilated carbohydrates in the carbohydrate pool and is also used to produce chitin, any excess carbohydrates go to the neutral lipid pool, assimilated polar lipids go to the somatic tissue polar lipid pool and any excess is stored in the neutral lipid pool.

Before the addition of reproduction was made to the model, the respiration requirements of the krill were the only metabolic loss of energy. The first energy

reservoir to be used by the model is the assimilated carbohydrate pool, the assimilated carbohydrates are removed from the model with the protein to carbohydrate ratio checked. If krill has not assimilated enough carbohydrates to meet the required energy, then the remainder of the required energy is taken from the remaining assimilated food pools. If the energy requirements are still not met, then the neutral lipid pool is used until the neutral lipid to polar lipid ratio minimum (Hagen, 1988) is reached. Further remaining energy requirements afterwards are taken from the structural components, which can lead to shrinkage to the size of the krill. If the krill is unable to maintain any of the biochemical constituent ratios, or any of the pools are used up and are not replenished, krill is assumed to be dead by the model.

If krill do not encounter food and start starving, the model appropriately starts shrinking their size. The model assumes that the loss of wet weight of 45% to be equivalent to death (Ikeda and Dixon., 1982), furthermore larvae class krill are more susceptible to starvation and are assumed dead if they are unable to feed for 6 days (Ikeda., 1984; Meyer and Oettel., 2005). The larvae krill have an extra condition regarding starvation, where if a larvae class krill is unable to feed for 6 days, then it is presumed have reached a point of no return (Ikeda., 1984; Meyer and Oettl, 2005) and are assumed to be dead by the model.

2.6 Inclusion of reproduction into the krill IBM

Reproduction was included for only adult krill who can invest lipid reserves from austral spring to fall into reproduction. While larvae and juveniles invest no energy into this. That means that only adult krill in the model allocate energy for reproduction as they are the ones using most energy reserves for reproduction (Clarke, 1980; Quetin et al.,1994). Further, adult krill in the model are assumed to be only female as they are the ones using most energy reserves for reproduction (Clarke, 1980; Quetin et al.,1994) and only invest in lipids for reproduction, specifically in gonad production, from austral spring to fall, but not in winter

(Kawaguchi et al, 2007), which is assumed to be the regression period. Multiple surveys and experiments in the field have shown that female krill are able to start spawning from late October/early November through the Austral Spring period if the food availability is favorable (Kawaguchi, 2016). Kawaguchi (2016) shows that the spawning period of krill in the Lazarev sector is from November until the end of January. Therefore, the starting date of spawning in the krill IBM model has been set as November 1st and the ending date has been set as January 31st, giving krill in the model 92 days for reproduction.

As a second step, the actual use of structural components for reproduction was incorporated into the model following the observations detailed in Clarke (1980), Quetin et al. (1994), Nicol et al. (1995), Torres et al. (1994), Hagen et al. (2001) that show adult krill may use 80-95% of their reserves to invest into gonad production. Gonads that grow to be bigger than a critical mass are converted to eggs and experiments performed on groups of gravid and spent krill (Nicol et al., 1995) have shown the mean difference of 150 mg of dry weight between the two groups and this was the amount of loss defined for reproduction in the krill model. This means that during an average 92 day spawning season a 150 mg body dry weight loss results in a use of 19.88 mg of polar lipids, 38.93 mg neutral lipids and 53.96 mg of protein.

The reproduction is therefore implemented into the IBM model as follows:

1. Only adult krill can reproduce, they are defined in the model as krill larger than 40 mm in size.

2. All adult krill in the model are assumed to be females.

3. Reproduction occurs from the November 1st until January 31st in which krill and is considered to be a continuous process.

4. During a simulation with 10 time steps per day, krill uses 0.0599 mg of protein, 0.022 mg of polar lipids and 0.043 mg of neutral lipids per spawning day.

2.6.1 Adult krill growth success

To be able to measure the relative growth success of adult krill after a yearlong simulation, the surviving number of krill are analyzed in each simulation. The average length of the whole simulation is calculated, as are the maximum length and minimum length of krill at any given timestep throughout the simulation. Afterwards the midpoint between the average length of the simulation and the maximum/minimum is calculated to define the above average, below average and average length range the krill grow to.

Krill that end the simulation between the maximum length and the midpoint between average length and maximum length are considered experiencing above average growth, the ones that end at between minimum length and the midpoint between average and minimum length are considered to have developed to below average sizes and the ones that end between the two midpoints are considered average. This information is then analyzed to visualize the relative growth success spatially, depending on the release points.

RESULTS

3.1 Krill connectivity in entire Lazarev Sea

The pathways of drifters representing krill released in the entire Lazarev Sea (see red rectangle in Figure 10) at 10m depth show extensive transport into different directions over one year (Figure 12A). This is expected due to the very large release area and the different current effecting different parts of the Lazarev Sea (see Figure 10). Drifters end up in different sink regions that are largely separated in space (Figure 12A). Further, the source of krill reaching the Lazarev Sea particles released in the entire Lazarev Sea at 10m depth was assessed backtracking drifter in time for one year (Figure 12B). To better differentiate the extend of krill transport, as well as the possible source and sink regions, seven distinct regions were defined in the study area as North Weddell Sea, South Weddell Sea, South Lazarev Sea, North Lazarev Sea, Northwest Region, the entrainment into the ACC and the Riiser Larsen Sea (Figure 12C).

To understand the transport pattern of Lagrangian drifters between regions, below the FESOM simulated currents that are used to produce the drifter transport are analyzed for the year 2005 month by month (Figure 14, Figure 15, Figure 16, Figure 17) and additionally the average surface circulation of the years 2004, 2005 and 2006 (Figure 13) are presented to compare annual variability between the years.

The average surface circulation of the study area for the years of 2004, 2005 and 2006 (Figure 13) show similar characteristics, the ASF is the strongest current in the area after the ACC. Currents entering the Southern Lazarev area via the ASF are stronger in 2004 compared to 2005 and 2006. The Western arm of the Weddell Gyre has a higher velocity circulation at 68°S and 42°E in 2006 compared to 2004 and 2005. The Southern Weddell area has variable differences in circulation velocities and pathways inside the area for each year, but apart from these differences, the average surface circulation of these three years is consistent over the years.

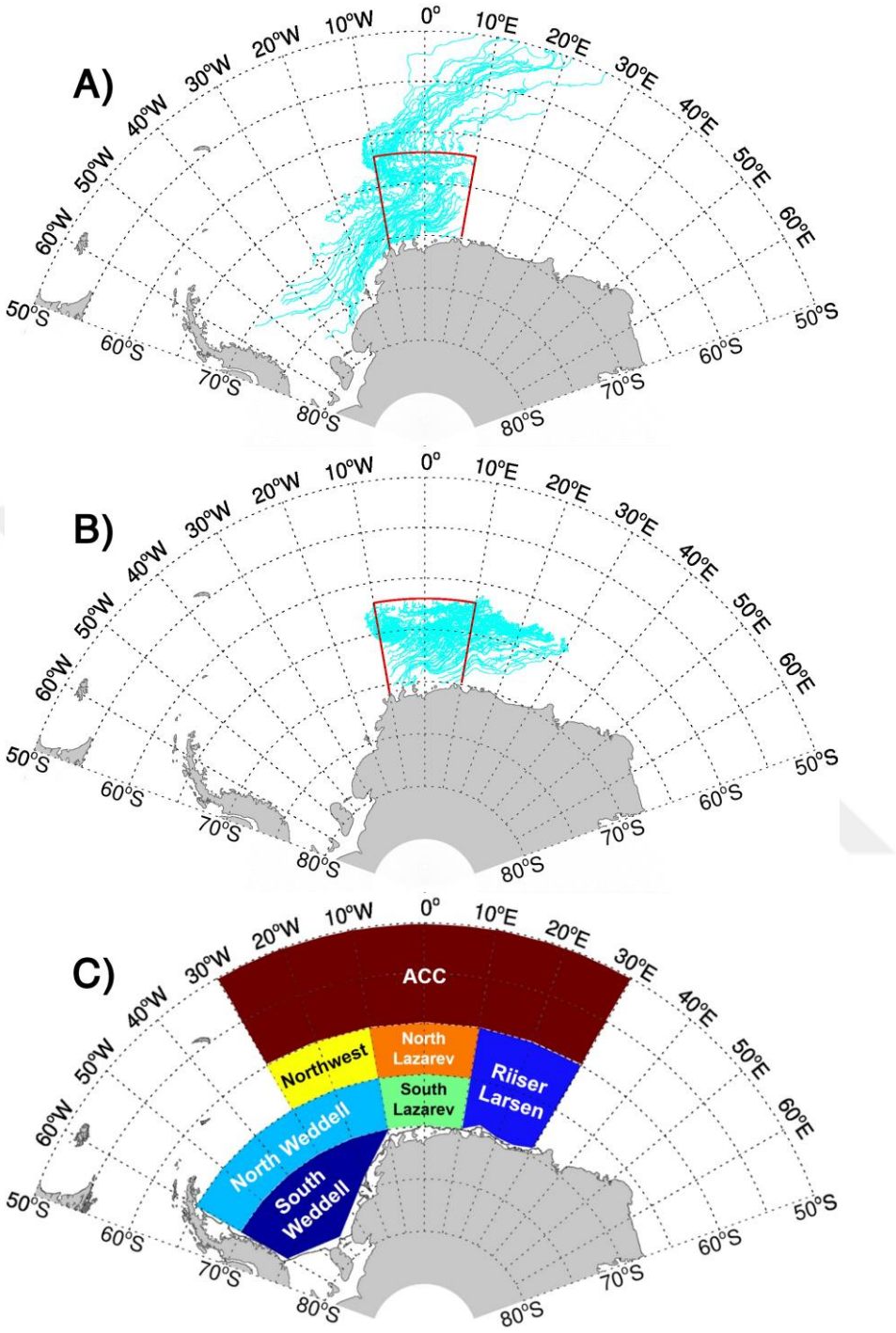


Figure 12 Particle trajectories and source/sink regions. A) Particle trajectories of all 2041 drifters released at 10km distance between 62°S-72°S and 10°W-10°E on January 1, 2005 and tracked for one year. B) Particle trajectories of all 2041 drifters released at 10km distance between 62°S-72°S and 10°W-10°E on January 1, 2005 and backtracked in time for one year. C) Color coded sink and source regions for the drifters simulated above.

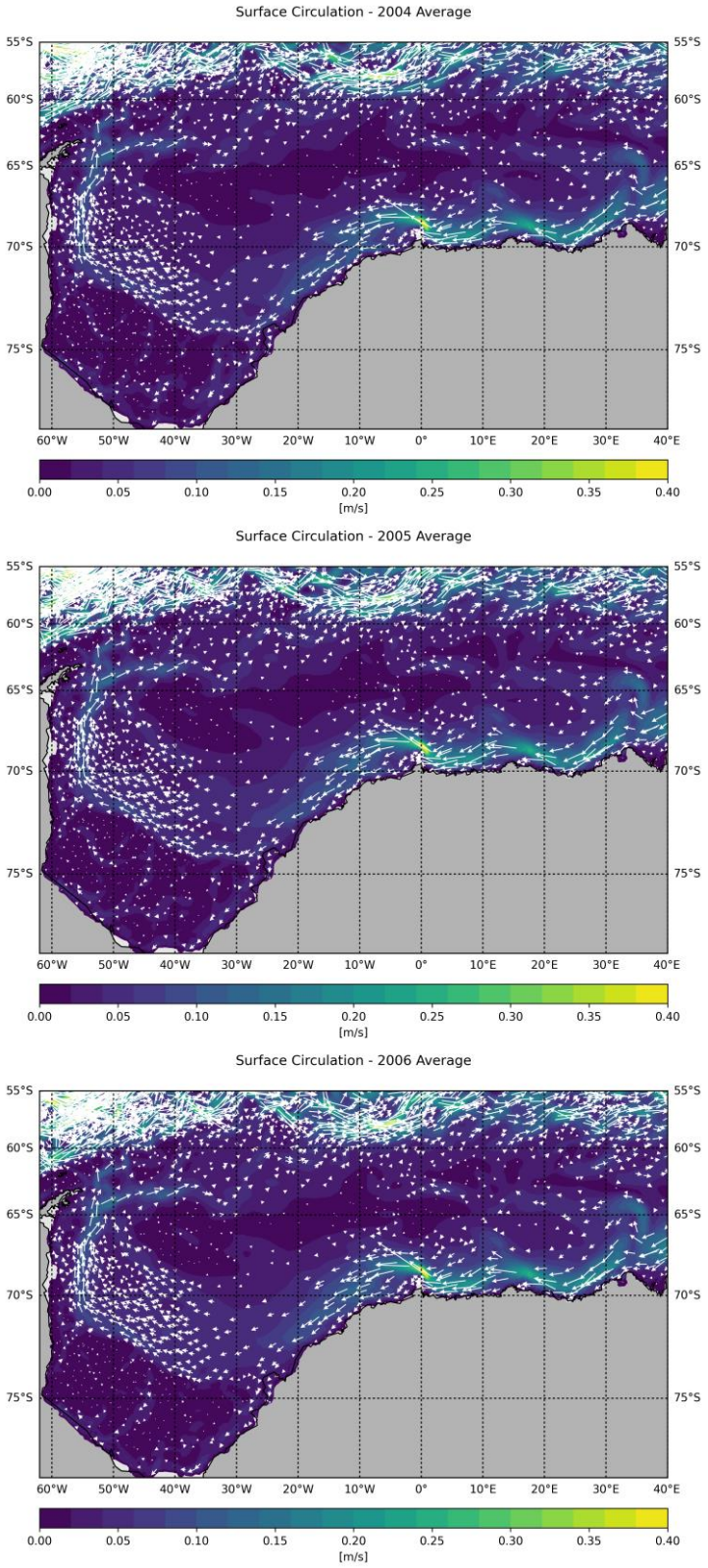


Figure 13 The average surface circulation of the years 2004, 2005 and 2006.

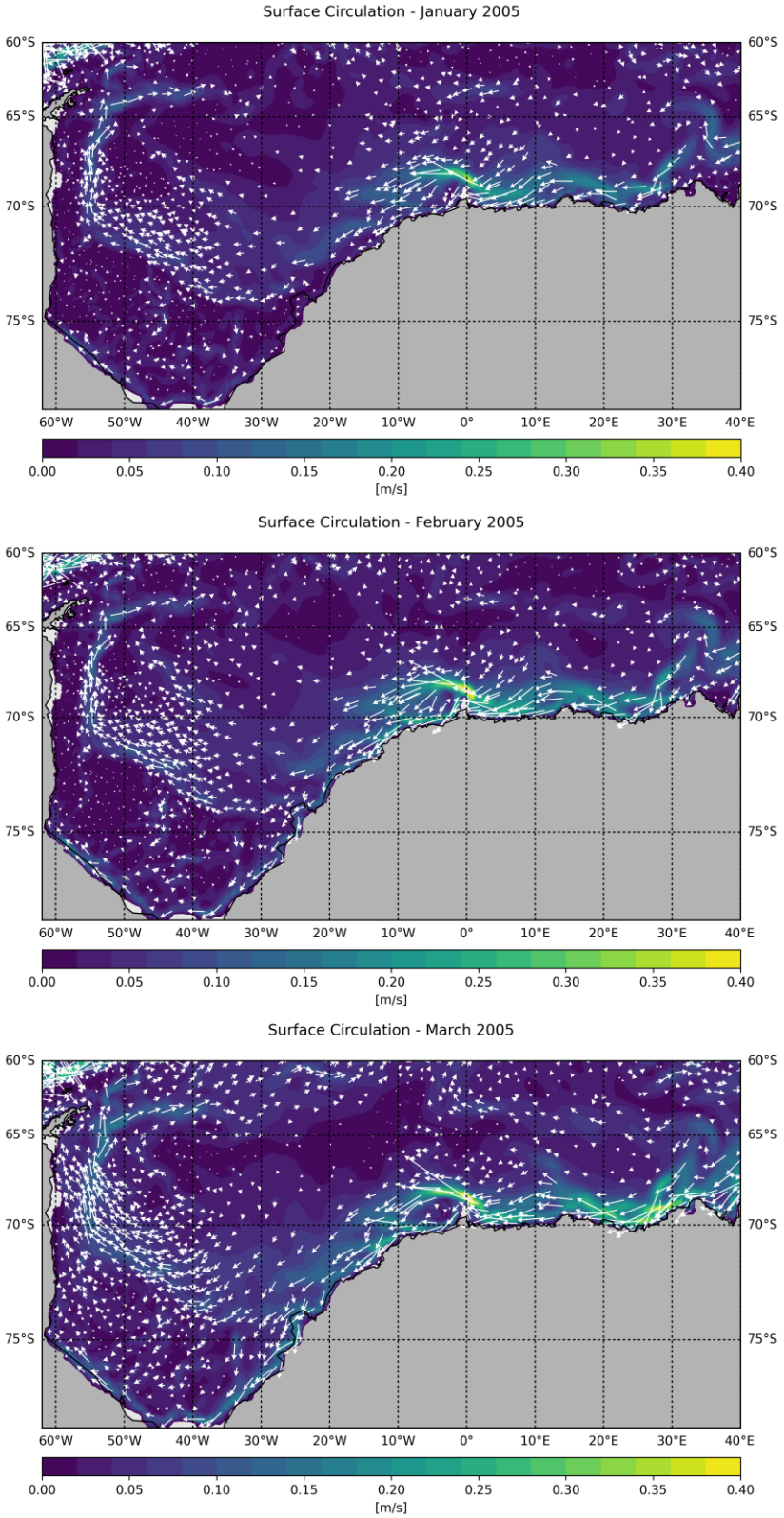


Figure 14 Surface circulation velocities of 2005 January to March.

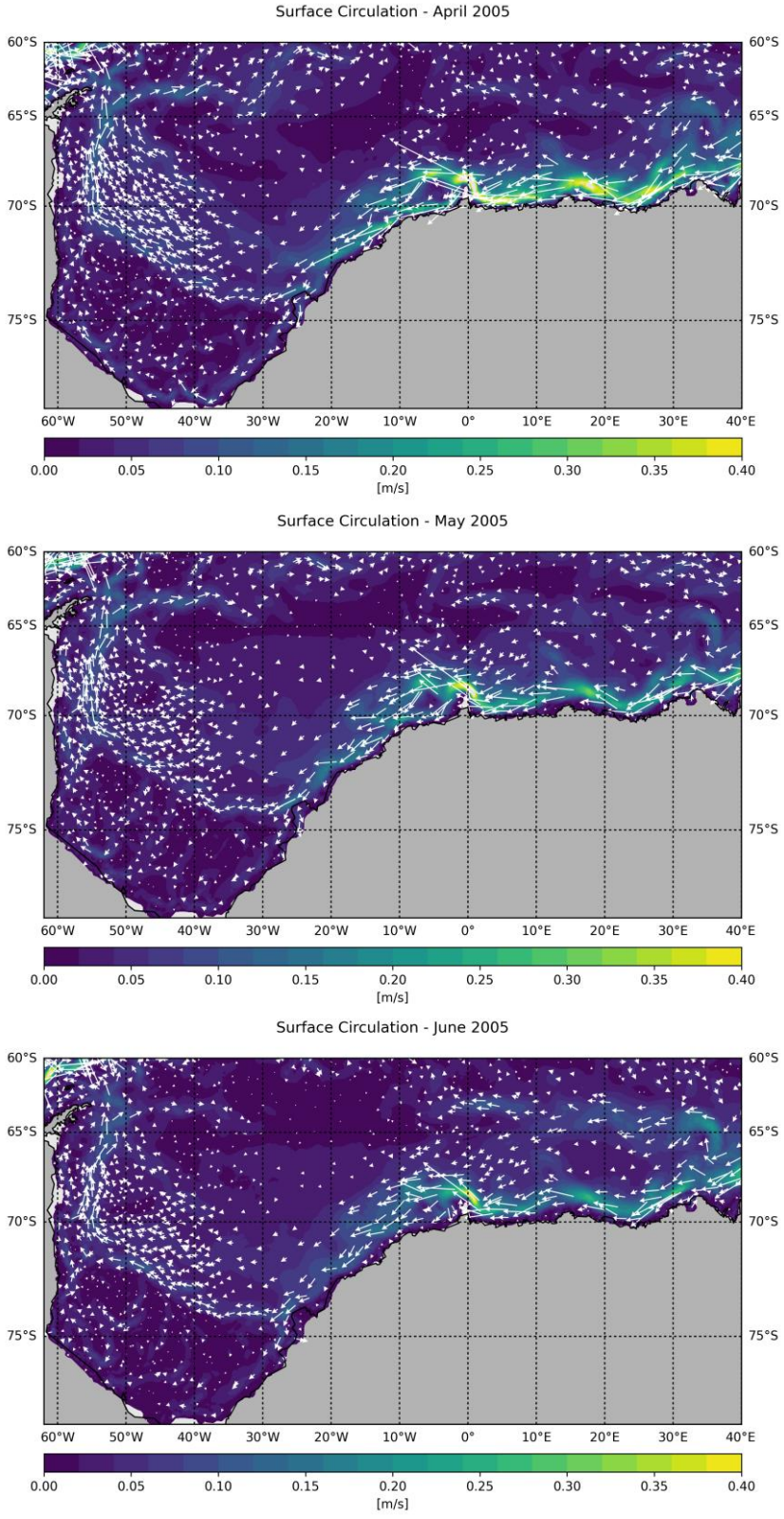


Figure 15 Surface circulation velocities of 2005 April to June.

The circulation features of the study region from January to December (Figure 14, Figure 15, Figure 16 and Figure 17) for the year 2005 show that the Antarctic Slope Front (ASF), becomes more intensified from January to May. The winter period from July to August shows the ASF weakens slightly, but the velocities stay overall similar to the month of May. It is from September to November that the ASF shows the slowest current in terms of velocity, and only in December the velocity starts to increase again.

The western portion of the Weddell Gyre that moves up to the Antarctic Peninsula shows steady current velocities through the year, however during the month of March, it shows intensification compared to the other months. The southern limb of the Weddell Gyre does show variability during the year, increasing in terms of velocity during the same months as the ASF, which can be seen from January to May.

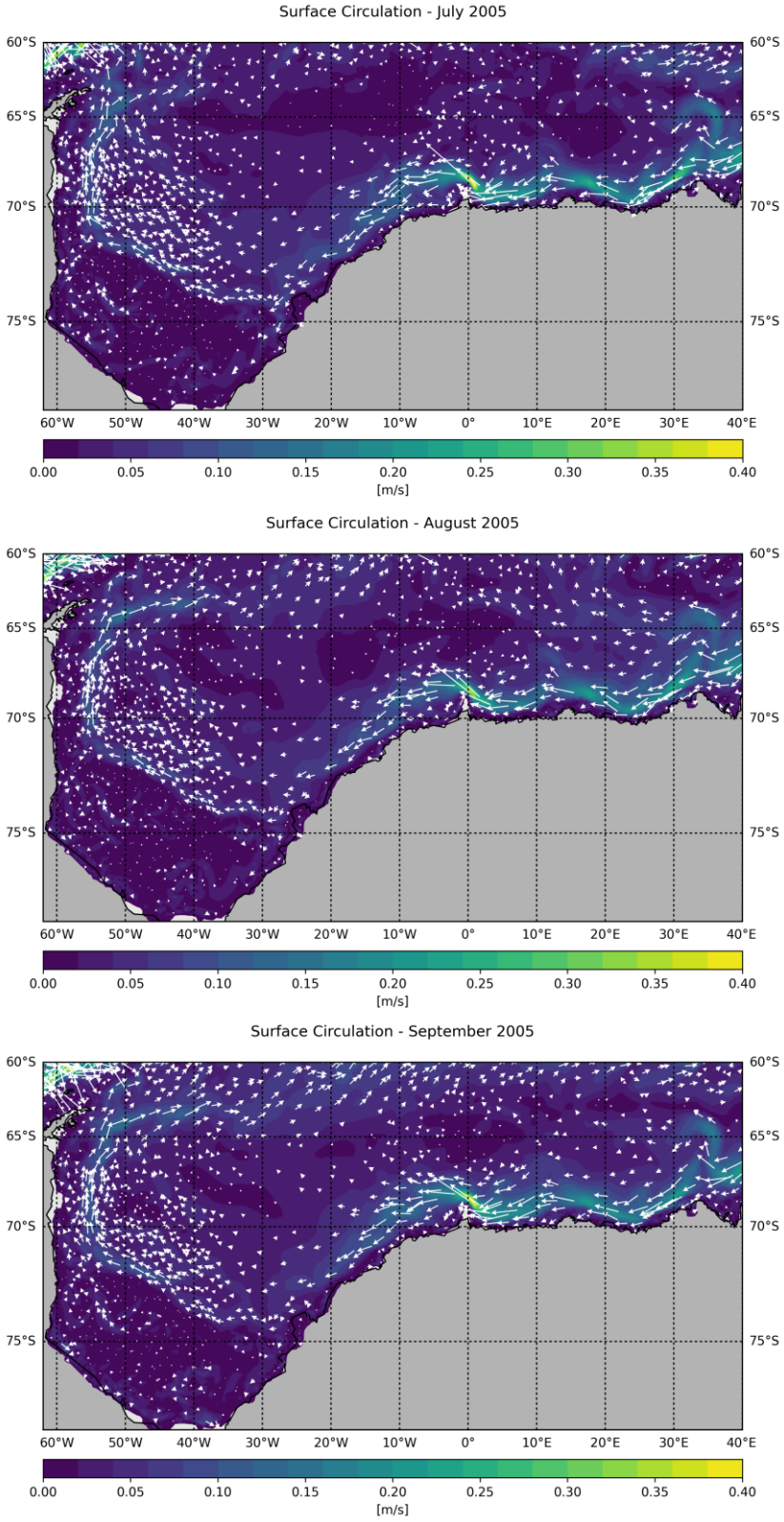


Figure 16 Surface circulation velocities of 2005 July to September.

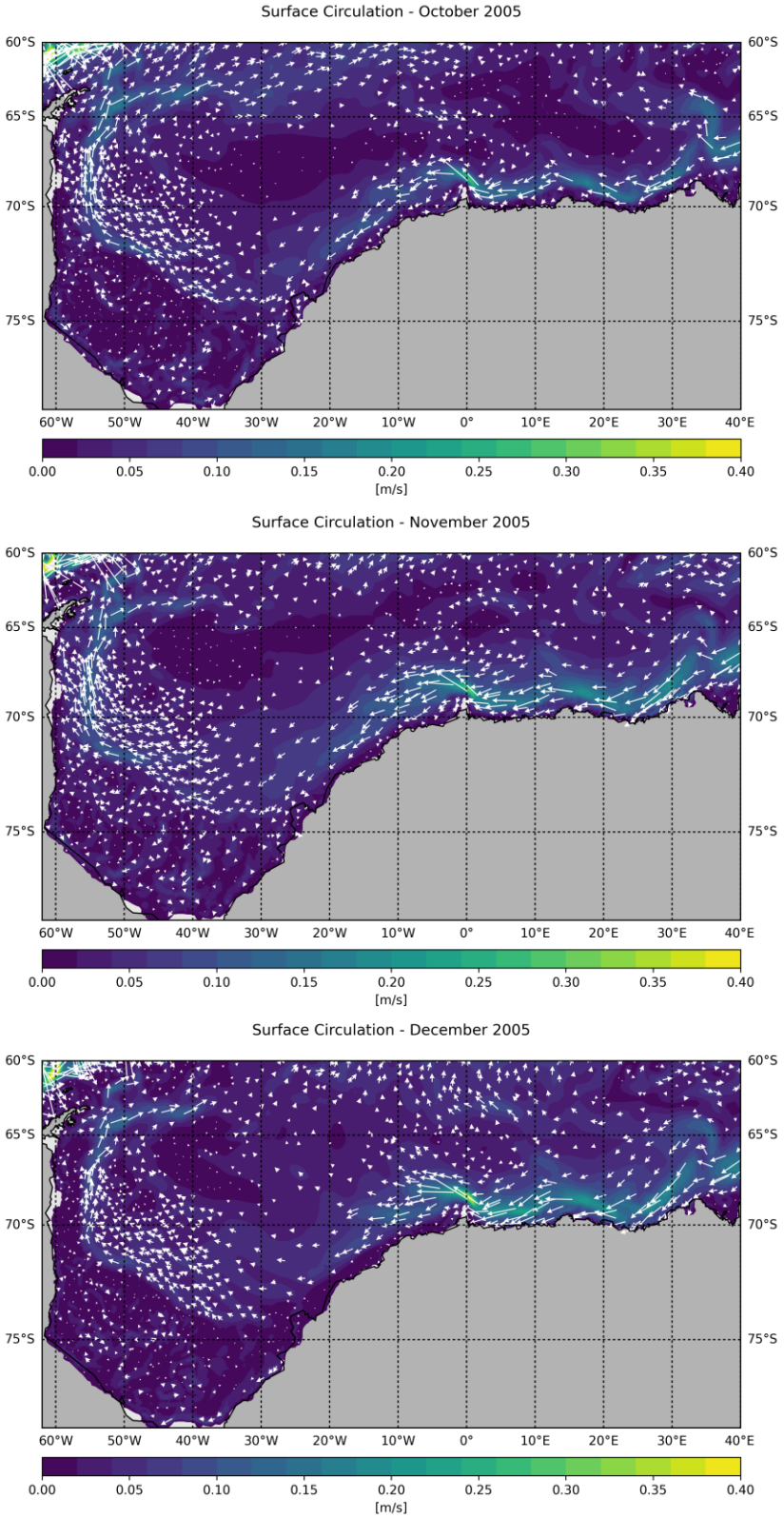


Figure 17 Surface circulation velocities of 2005 October to December.

Eddies and other circulation features in the South Weddell Sea area show the highest velocities between the months of January and May. From July to August some of the eddies and fronts remain as more dominant features in the area. Then, from September to December, the overall velocities begin to increase again.

The South Lazarev Sea area is primarily affected by the ASF current system, however there is a small pocket created by the protrusion of the Antarctic continent at 0° longitude which creates a persistent eddy feature seen from January to July. The North Lazarev Sea area has variable velocities from month to month with lower velocities when compared to the Southern Lazarev Sea area. The velocities increase from January to July, briefly slow down at August, then increase back up in September and remain steady until December.

3.1.1 Transport and retention in the Lazarev Sea

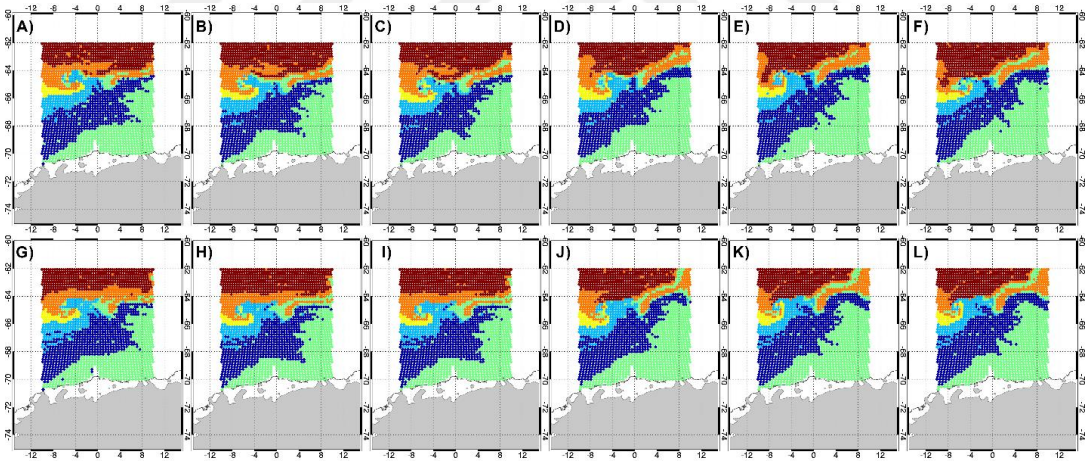


Figure 18 Release locations of 2041 drifters for the spawning seasons of 2004/2005 and 2005/2006 color coded for sink regions the particles reached after a one-year simulation as define in Figure 12. Simulation results start in the top row with A) release on 1st of November 2004 to F) 16th of January 2005, each month is represented with the 1st day and 16th day in the simulation. Similarly results continue in the bottom row with G) release on 1st of November 2005 to F) 16th of January 2006. Each dot represents a single particle start point and colors mark the sink region reached: red - entrained in the ACC, orange - North Lazarev Sea, yellow - Northwest region, light blue - North Weddell Sea, dark blue - South Weddell Sea, and green – South Lazarev Sea.

Using these regions, the end point distributions or sink regions for krill released in the Lazarev Sea (red rectangle Figure 1) show a distinct general pattern where the northernmost released krill particles are transported into in the ACC and those starting slightly further south below 63.5°S move into the North Lazarev Sea in all 12 forward simulations (Figure 18). Below this a small patch of drifters originating west of 2°W is located that reach the Northwest region (Figure 18, marked in yellow) while below a diagonal band of particles end up in the North Weddell Sea (Figure 18, marked in light blue) and South Weddell Sea regions (Figure 18, marked in dark blue). Most particles released close to the Antarctic continent and even particles released as far north as 64°S in the eastern part of the release area exclusively reach the South Lazarev Region (Figure 18, marked in green).

The two spawning seasons of 2004/2005 and 2005/2006 show a repeating spatial pattern in the north. At the onset of the spawning period in November, a distinct band of particles is observed reaching the North Lazarev Sea (Figure 18A, marked in orange). This band effectively separates the particles entrained into the Antarctic Circumpolar Current (ACC) from the diagonal band of particles that subsequently reach both the Northern and Southern Weddell Sea. However, as the season progresses into mid-December (Figure 18D), particles released within the longitudinal range of 4°W and 1°E are increasingly transported into the ACC. Further, a diagonal patch of particles reaching the South Lazarev Sea from the South Lazarev Sea, situated between the ACC and the North Lazarev region, begins to emerge in the northern domain. The bands of particles transported to the South Lazarev Sea and South Weddell Sea are persistent features across all model simulations, with only minor interannual variability associated with the timing of particle release. Occasionally, particles reaching the Southern Weddell Sea intrude into the patch associated with the South Lazarev Sea. Similar variability is observed in the particle patch transported to the Northwestern region and its interaction with the North Lazarev Sea patch that are both consistent features reproduced across simulations.

The percentage of drifters reaching each sink region as a function of spawning time (Table 3) shows little temporal variability. Most regions receive a stable inflow of particles such as the South Weddell Sea, which receives between 24.11% and 27.14% (mean 25.27%) while the Northwest region receives between 1.71% and 2.50% (mean 2.14%). The North Weddell region shows a consistent decline in numbers arriving from November through January, whereas the South Lazarev Sea shows a consistent increase over the same period. The North Lazarev Sea maintains consistent inflow of particles until the end of December, when numbers decrease by 2%. Finally, particles are increasingly entrained in the ACC from November to December, followed by a marked reduction in January, apart from the January 16, 2006 simulation.

Table 3 Percentage (%) distribution of 2041 drifters released in the Lazarev Sea according to sink regions. (see Figure 10, red rectangle) with each spawning time transported to different sink regions defined in Figure 12C.

	South Weddell Sea	**North Weddell Sea**	**South Lazarev Sea**	**North Lazarev Sea**	**Northwest Region**	**ACC**
2004 Nov 01	25.67	8.72	28.03	12.30	2.40	22.88
2004 Nov 16	24.30	8.23	28.03	12.15	2.20	25.09
2004 Dec 01	24.11	7.45	29.40	12.40	2.30	24.35
2004 Dec 16	24.15	7.45	33.66	12.20	2.50	20.04
2005 Jan 01	27.14	7.94	32.93	11.27	2.16	18.57
2005 Jan 16	26.95	7.79	34.79	10.04	2.01	18.42
2005 Nov 01	25.92	9.26	28.03	13.38	2.25	21.17
2005 Nov 16	24.60	9.21	28.56	12.00	1.81	23.81
2005 Dec 01	24.20	9.06	29.15	11.51	2.06	24.01
2005 Dec 16	24.50	7.94	34.25	10.98	2.20	20.14
2006 Jan 01	26.95	7.79	34.79	10.04	2.01	18.42
2006 Jan 16	24.74	6.76	33.95	10.98	1.71	21.85

The distribution of the total number of 24,492 particles released across sink regions (Figure 19, left) indicates that 43% are retained within the Lazarev Sea (North and South) region after a one year simulation, identifying it as the primary sink for

simulated krill. Of these, 31% reach the South Lazarev Sea and 12% reach the North Lazarev Sea. The Weddell Sea region accounts for 33% of particles destinations, with 25% reaching the South Weddell Sea and 8% the North Weddell Sea. In total, 22% of the particles are entrained into the ACC and transported downstream, effectively removing them from contributing to recruitment within the Lazarev Sea. Only 2% of all particles are transported to the Northwest region. The spatial patterns (Figure 19, right) displays a diagonal band associated with the South Lazarev Sea and South Weddell Sea region as dominating the southern release points in the west and reaching approximately 64°S in the eastern release points. These two regions together account for 56% of all particles. In the north, across all longitudes entrainment into the ACC dominates.

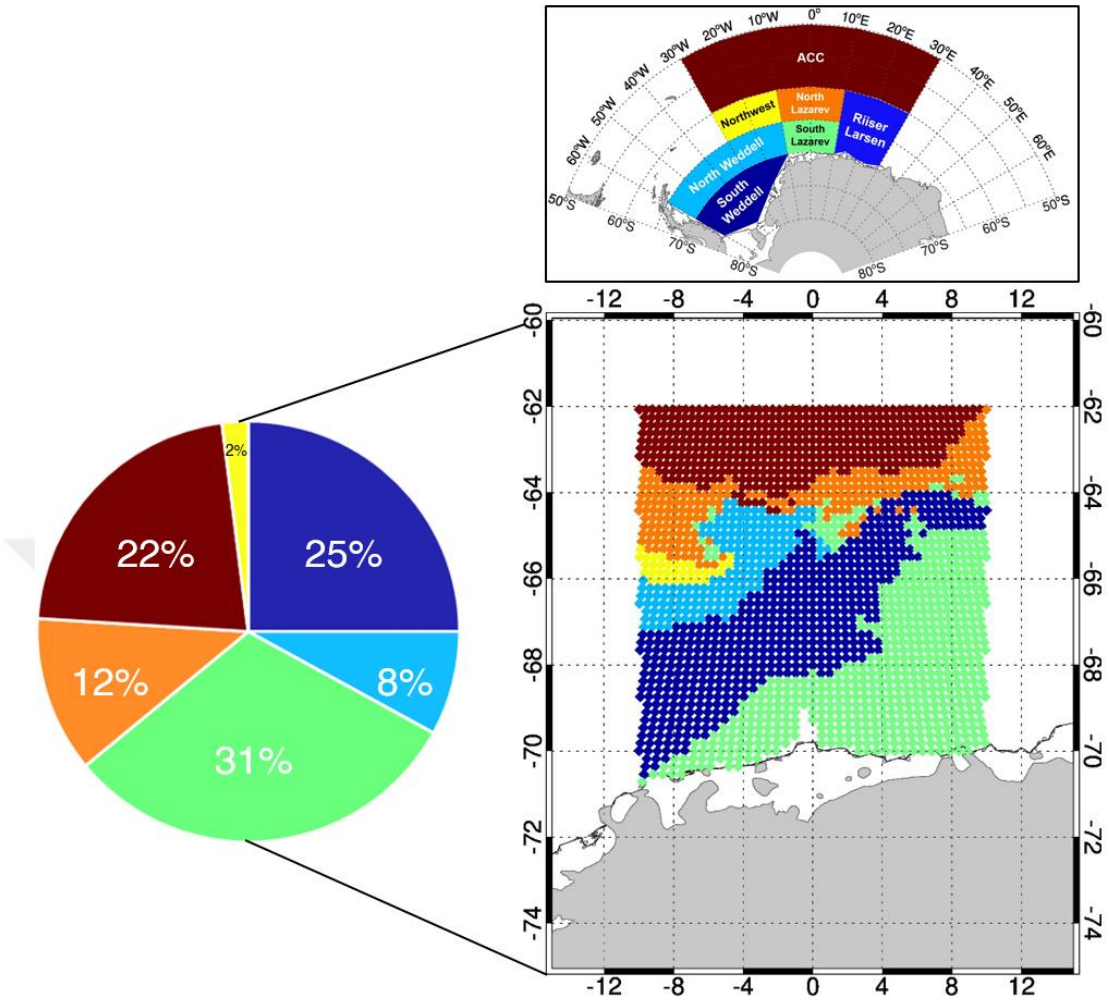


Figure 19 Percentage of forward tracked particles reaching different sink regions (see Figure 12A) for all 12 spawning times comprising 24,492 particles (bottom left) and the mean spatial distribution of this distribution (bottom right). Top right inset shows the regions which each color belongs to.

3.1.2 Source regions for krill in the Lazarev Sea

To investigate the source regions of the 2041 Lagrangian particles released in the entire Lazarev Sea at different spawning times (see Figure 10, red rectangle), in a separate set of simulation these drifters were backtracked in time over one year. This means they were released on the same spatial grid but transport was calculated backwards in time for one year reversing the time stepping in the Lagrangian particle

tracking algorithm, allowing to locate the region of origin for each particle starting November 1st 2005, December 1st, 2005 and January 1st, 2006 (Figure 21).

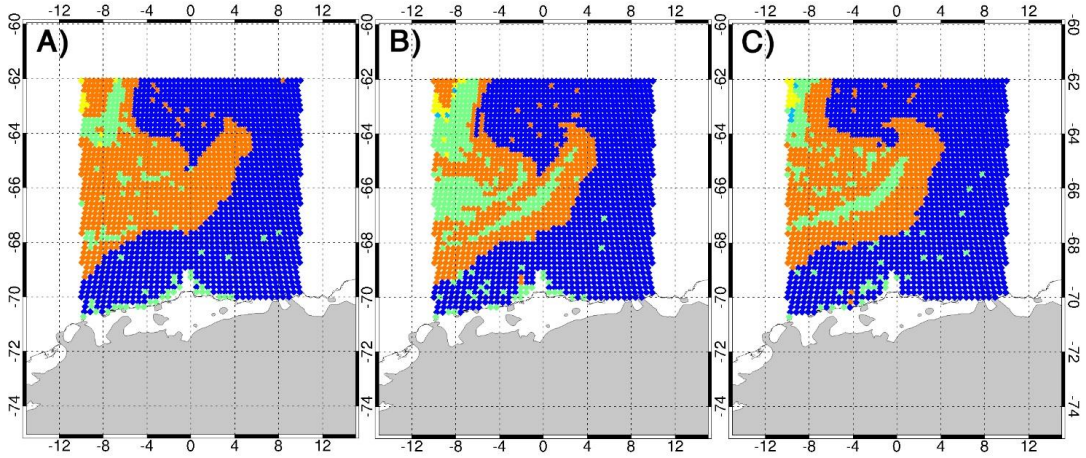


Figure 20 Source locations of 2041 drifters that reach Lazarev Sea in the spawning season of 2005/2006 color coded for source regions the particles originated from in a one-year backtracking simulation as defined in Figure 12. A) 1st of November 2005 B) 1st of December 2005 and C) 1st of January 2006. Each dot represents a single particle start point and colors mark the source region: orange - North Lazarev Sea, light blue – North Weddell Sea, yellow - Northwest region, dark blue – Riiser Larsen Sea, and green – South Lazarev

Backtracked particle trajectories reveal a symmetrical swirl-like source distribution centered within the Lazarev Sea (Figure 20). The eastern portion of the release area is predominantly sourced by the Riiser Larsen region extending from the southern coastline to the northern boundary of the release area, only interrupted by the swirl pattern. The western part of the release area is dominated by the Northern Lazarev and Southern Lazarev region origin regions almost equally that form the distinctive swirl pattern in the center. Minimal contributions are observed from the Middle Region and North Weddell Sea.

Table 4 Percentage (%) distribution of 2041 drifters released in the Lazarev Sea according to source regions (see Figure 1, red rectangle) with each spawning time originating from different source regions defined in Figure 12C.

	South Weddell	North Weddell	South Lazarev	North Lazarev	Northwest Region	ACC	Riiser Larsen
2005 Nov 01	0	0	7.16	33.17	0.44	0	59.22
2005 Dec 01	0	0.15	15.10	24.26	0.78	0	59.70
2006 Jan 01	0	0.20	9.12	30.29	0.54	0	59.85

Across all three backtracking simulations, the Riiser-Larsen Sea consistently emerges as the primary source region, followed by the North Lazarev and South Lazarev Seas (Figure 20). Other regions contribute less than 1% of total particle origins, while no particles are traced back to the South Weddell Sea or the ACC, reflecting the influence of dominant current structures that inhibit upstream connectivity from these areas.

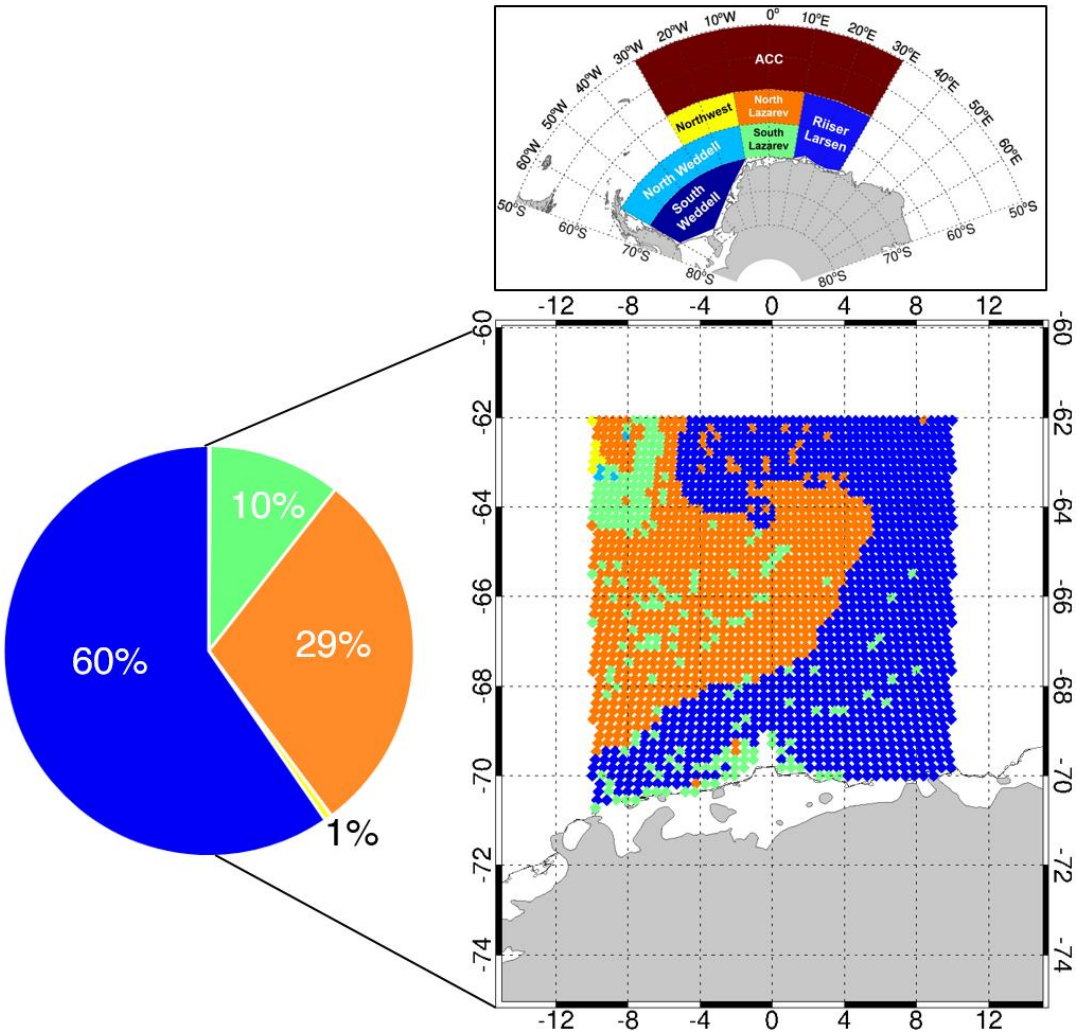


Figure 21 Percentage of backwards tracked particles originating in different source regions as defined above (see Figure 12B) for all 6 spawning times comprising 6123 particles (bottom left) and the mean spatial distribution of this distribution (bottom right). Top right inset shows the regions which each color belongs to.

The above analysis of particles released across the larger Lazarev Sea area at different spawning times and tracked forward and backward in time revealed interesting patterns of connectivity with regions in and around the Lazarev Sea. Apart from small seasonal variations, 43% of krill spawned in the Lazarev Sea region stay in the Lazarev Sea when tracked for one year, with a larger number (31%) reaching the South Lazarev Sea and 12% the North Lazarev Sea. Further, most krill found in the greater Lazarev Sea area (60%) originate in the Riiser Larsen Sea,

followed by 39% originating in the Lazarev Sea itself, and only 1% making up Northwest and North Weddell Sea regions.

3.1.3 Fate of krill released at selected stations in the Lazarev Sea

To gain more detailed insight into the dynamics within the Lazarev Sea itself simulations at station locations where krill was found during the LAKRIS cruises that took place in (2004-2006) Meyer et al. (2010) are presented in the following results section. The simulations were started on November 2005, December 2005 and January 2006.

3.1.3.1 Austral summer/spring release at station 92

Meyer et al. (2010) reported that in the austral spring months cruise of 2005/2006 five stations found krill and station 92 is used here to represent the fate of krill spawned in this season (Figure 22).Particles were released daily for 3 months starting in November 2005 over a three month period, totaling 92 drifters that were tracked for one year.

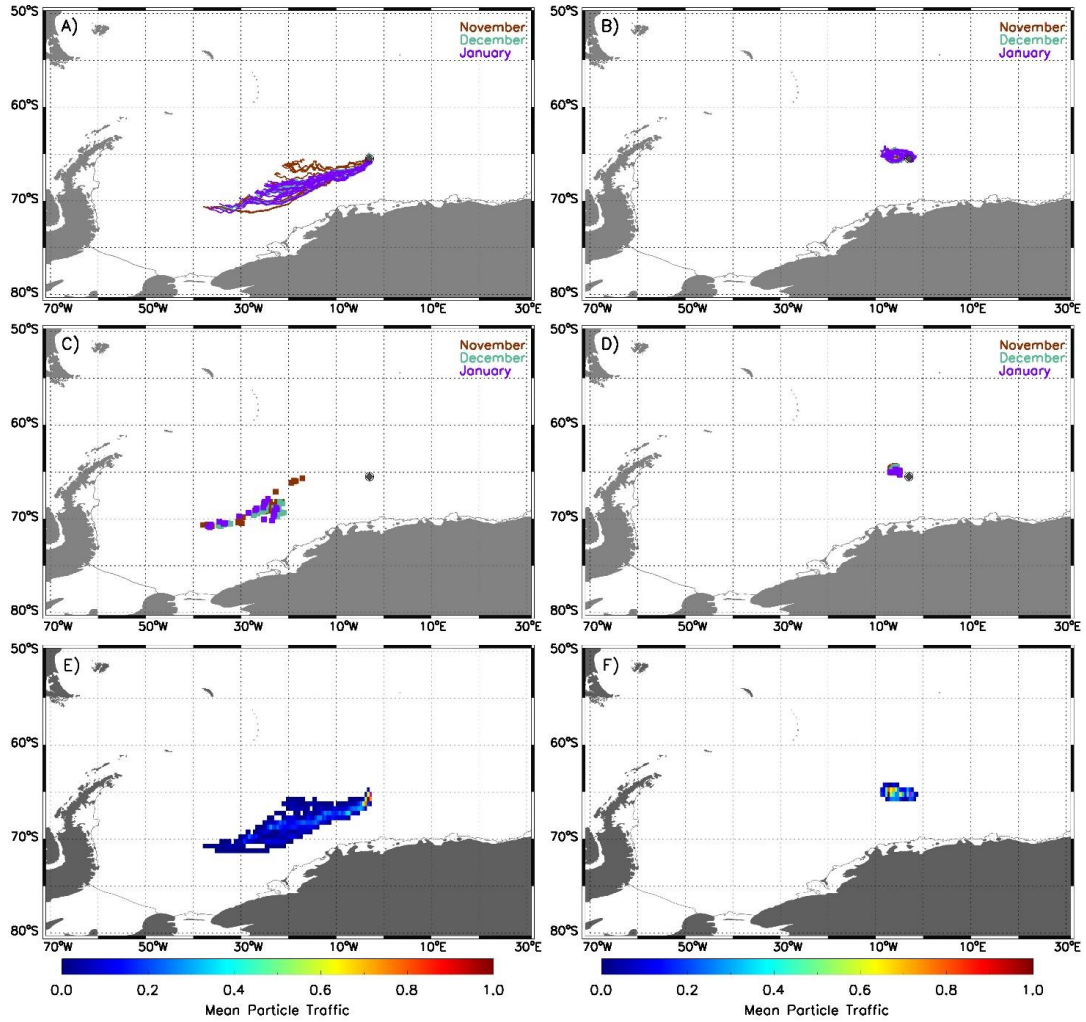


Figure 22 Lagrangian Particle tracking results of station 92. particles released in austral spring and summer 2005. A) Trajectory of all particles tracked forward in time from 2005 to 2006, black diamond denotes the release point of particles. B) Trajectory of all particles tracked backwards in time from 2005 to 2004, black diamond denotes the release point of particles. C) End points of particles tracked forwards in time are denoted by squares, black diamond inside the circle denotes the release point of particles. D) End points of particles tracked backwards in time are denoted by squares, black diamond inside the circle denotes the release point of particles. E) Mean particle traffic map of particles tracked forwards in time, purple rectangle denotes the release cell. F) Mean particle traffic map of particles tracked backwards in time, purple rectangle denotes the release cell.

All forward-tracked particles follow a westward path with slight southward deflection toward the Weddell Sea with some variation in their meandering behavior at the beginning of their simulation, with November showing the greatest deviation

from the main path (Figure 22A). In contrast, backward-tracked particles exhibit persistent local meandering centered around the release station, with limited displacement (Figure 22B). Forward-tracked particle dispersal varies notably across months and even within monthly cohorts, indicating variability in downstream connectivity (Figure 22C). Whereas the dispersal pattern of the backwards time tracked particles (Figure 22D) show a much tighter spread indicating the potential origin point to be very close to the station itself with little to no monthly variation. Particle traffic maps reinforce these findings. Forward-tracked trajectories show a dominant transport pathway extending southwestward from the station into the Weddell Sea (Figure 22E). Meanwhile the backtracked particle traffic map (Figure 22F) show the most activity to be the meandering pattern northwest of the station. To see the results of particles released from other stations in this season please refer to Appendix A.

3.1.3.2 Austral fall release at station 634

To test the effect of transport during austral fall, simulations beginning in March, April and May of 2004 were started at four different stations where Meyer et al. (2010) reported finding krill in the austral fall cruise. Particles released from the location of station 643 were released daily for three months starting in March 2004 over a three-month period, totaling 92 drifters, and were tracked for one year (Figure 23).

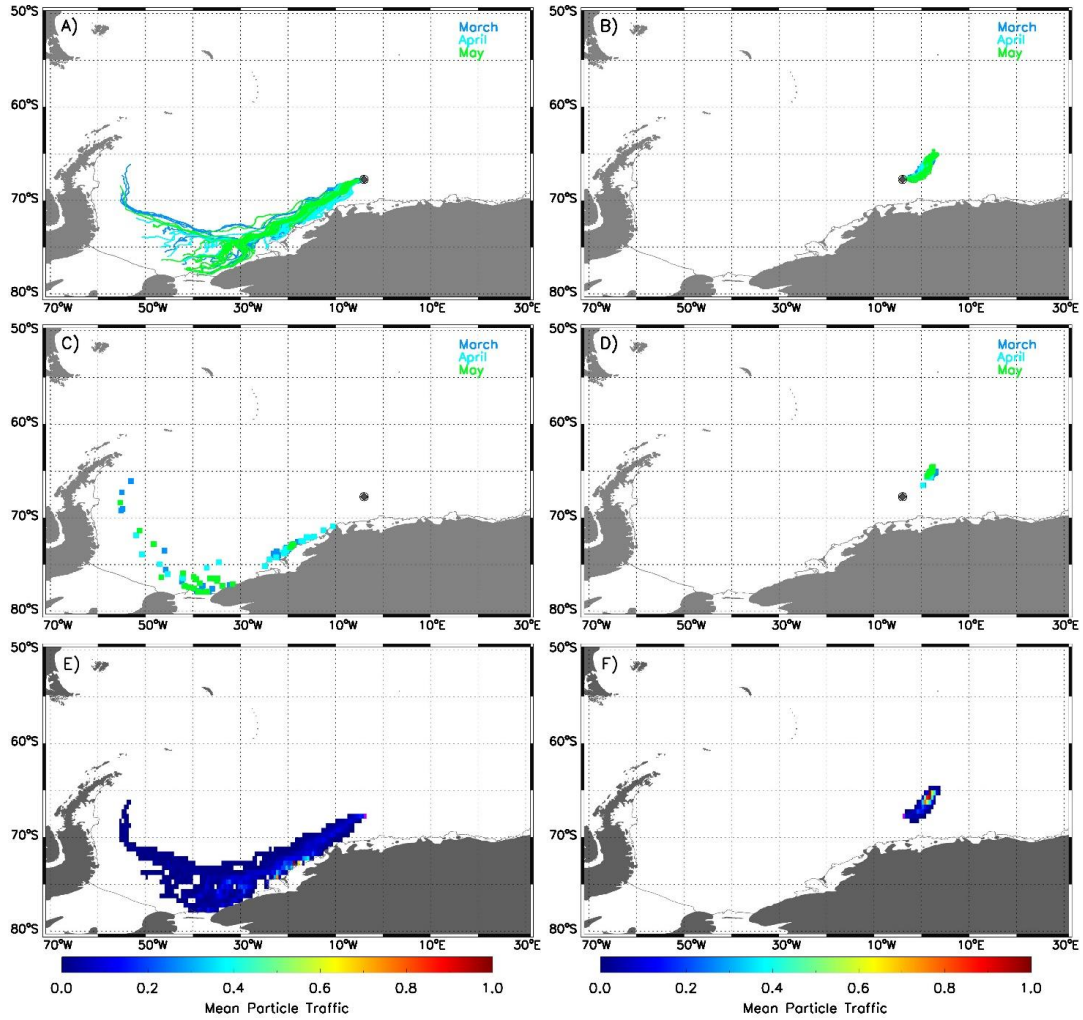


Figure 23 Lagrangian Particle tracking results of station 634 particles released at station 634 in austral fall 2004. A) Trajectory of all particles tracked forwards in time from 2004 to 2005, black diamond denotes the release point of particles. B) Trajectory of all particles tracked backwards in time from 2004 to 2003, black diamond denotes the release point of particles. C) End points of particles tracked forwards in time are denoted by squares, black diamond inside the circle denotes the release point of particles. D) End points of particles tracked backwards in are denoted by squares, black diamond inside the circle denotes the release point of particles. E) Mean particle traffic map of particles tracked forwards in time, purple rectangle denotes the release cell. F) Mean particle traffic map of particles tracked backwards in time, purple rectangle denotes the release cell.

The trajectories of particles released at station 634 (Figure 23A) tracked forward in time indicate that the particles move southwestward through the Weddell Sea following the currents associated with the Antarctic Slope Front and later continue

turning northward with some particles reaching to near the tip of the Antarctic peninsula at 66°S. The dispersal pattern shows that particles from all three months make their way along this trajectory with little spatial spread. Only after passing 30°W the spatial spread of the particles increases. The backwards time tracked trajectories (Figure 23B) meanwhile show the particles moving slowly northeast of the station location while meandering, with no discernible differences between the monthly releases. The ending points for forward time tracked particles indicate that some particles stay close to the coast while the rest move well into the Weddell Sea and along the coast of the Antarctic Peninsula (Figure 23C). The backwards time tracked particle ending points (Figure 23D) indicate a particles originate northeast of the station point .The particle traffic map for the forwards time tracked particles (Figure 23E) indicate that the most travelled pathway is close to the Antarctic coast along the 25°W-10°W longitudes. Backwards time tracked traffic map (Figure 23F) shows a uniform movement towards the northeast from where particles originate. For the results of particles released from other stations in this season please refer to Appendix A.

3.1.3.3 Austral winter release at station 516

To test the effect of transport during austral winter season particles were released in the months of June, July and August of 2006, at stations 474, 508 and 516 where Meyer et al, (2010) found krill during this season. Here only station 516 results are shown below (Figure 24), the remaining stations can be found in the Appendix A.

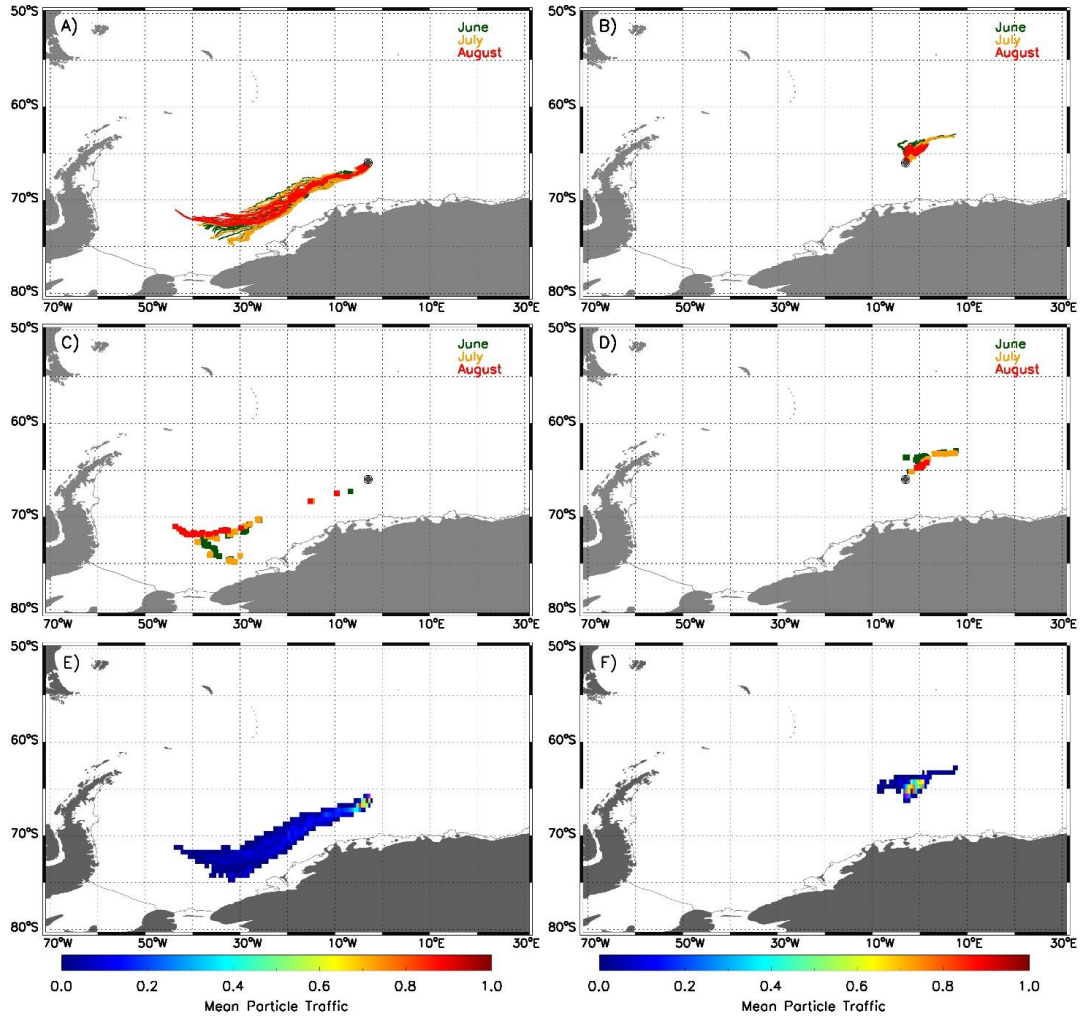


Figure 24 Lagrangian Particle tracking results of station 516 released in austral winter 2006. A) Trajectory of particles tracked forwards in time from 2006 to 2007, black diamond denotes the release point of particles. B) Trajectory of particles tracked backwards in time from 2006 to 2005, black diamond denotes the release point of particles. C) End points of particles tracked forwards in time are denoted by squares, black diamond inside the circle denotes the release point of particles. D) End points of particles tracked backwards in are denoted by squares, black diamond inside the circle denotes the release point of particles. E) Mean particle traffic map of particles tracked forwards in time, purple rectangle denotes the release cell. F) Mean particle traffic map of particles tracked backwards in time, purple rectangle denotes the release cell

The trajectory of the forward tracked particles (Figure 24A) show all particles moving southwestward into the Weddell Sea following currents associated with the Antarctic Slope Front. After passing 30°W longitude, the spatial separation between

particle paths increases. The trajectories of particles backtracked in time (Figure 24B) show slow movement, including meandering, towards the north and northeast of the release station with biggest spatial variation most evident with June particles. The ending points for the forward tracked particles (Figure 24C) show a spatial spread associated with the release month of the particles, with majority of the particles going past the 30°W longitude. Trajectories of particles released in June and July are spread out in a diagonal pattern whereas the August particles trajectories are horizontally spread. The backtracking simulation ending points (Figure 24D) also show the monthly variability with June and July with a horizontal pattern and August with a diagonal pattern, however these endpoints are located closer together compared to their forward tracked counterparts. The particle traffic map for the forward tracked particles (Figure 24E) show the majority of the traffic near the station itself where the particles first leave, after that there doesn't appear to be a dominant pathway with almost all different pathways showing similar traffic values. Similarly, the backwards simulation tracking traffic map (Figure 24F) shows most traffic near the station itself with low traffic areas spread around horizontally and towards the north.

3.1.3.4 Results for all stations

A summary of all particle tracking simulation results that are tracked forward in time (Figure 25A) for the LAKRIS cruise stations, shows the stations located below 65°S and west of 0° longitude are predominantly moving west and southwest into the Weddell Sea following currents associated with the Antarctic Slope Front. While stations below 65°S and east of 0° longitude show meandering behavior in the Lazarev Sea area before start moving into the Weddell Sea. Stations located above 65°S latitude line show north and northeastern movement towards the Antarctic Circumpolar Current.

The particles that are tracked backwards in time (Figure 25B) show that the particles meander inside the Lazarev Sea and depending on the station end the simulation still

inside the Lazarev Sea while the other stations move east towards the Riiser-Larsen Sea, particularly towards 63°S and 25°E.

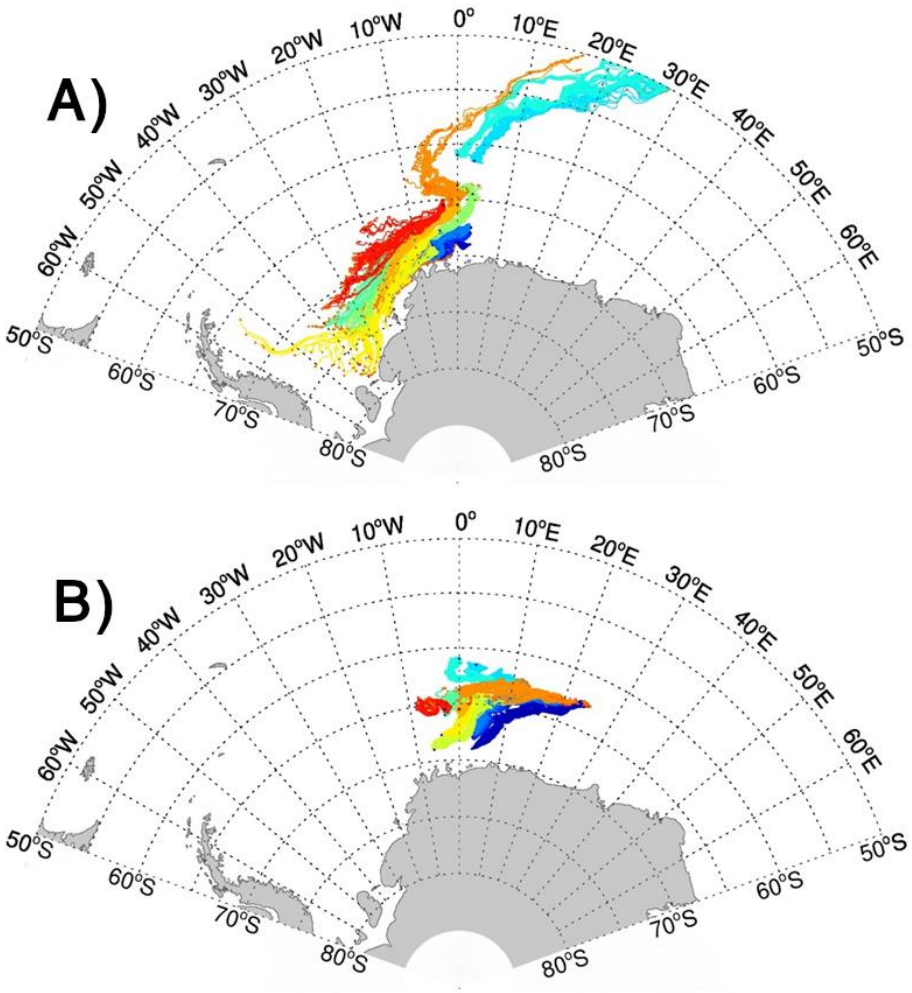


Figure 25 Trajectories of all particles released at twelve LAKRIS stations in the Lazarev Sea (see Figure 1). A) Trajectories tracked forward in time for 365 days. B) Trajectories tracked backward in time for 365 days. Colors differentiate the trajectories originating at the 12 different stations.

The mean total distance traveled by forward tracked particles (Figure 26A) shows the average of all the austral spring stations to be 1050 km with a minimum of 329 km for station 44 and a maximum of 1752 km for station 53. Austral fall stations average at 1360 km distance traveled with a minimum of 395 km for station 621 and 1847 km for station 678 as a maximum. The average total distance traveled for

austral winter stations is 2985 km with station 516's 1876 km minimum and station 474's 3509 km maximum.

3.1.3.4.1 Distance travelled

For the particles that are tracked backwards in time, the mean total distance travelled (Figure 26B) by the austral spring stations average at 1546 km with a minimum of 1340 km for station 53 and a maximum of 1753 km for station 44. The average for austral fall stations is 1441 km with a minimum of 1121 km by station 678 and a maximum of 1690 km by station 683. The austral winter stations have an average of 1541 km with a minimum of 1199 km for station 516 and a maximum of 1784 km for station 508.

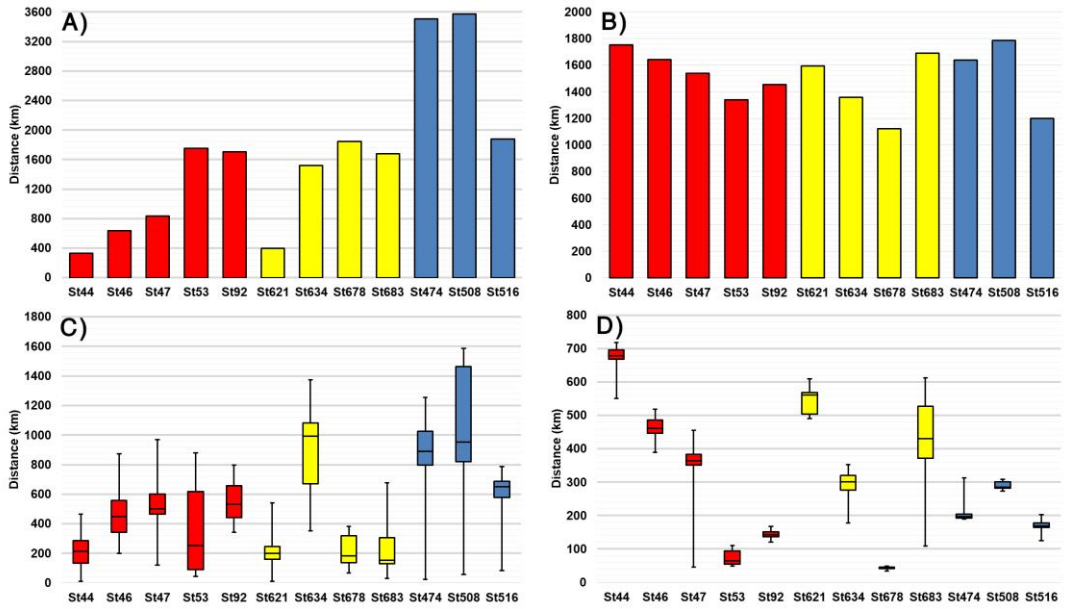


Figure 26 Distance metrics of simulation starting at all 12 stations A) The mean of total distance travelled by all forward tracked particles released per station. B) The mean of total distance travelled by all backward tracked particles released per station. C) Mean distance of all the particles to their origin, tracked forward in time per station. D) Mean distance of all the particles to their origin, tracked backward in time per station. Stations marked red are austral spring, yellow are austral fall and blue are austral winter stations.

The lowest median distance to a station origin observed in forward tracked (Figure 26C) austral spring particles is 211 km at station 44, while the highest median distance to a station origin is station 92 with 531 km distance. The largest quartile 1 and quartile 3 variance is with station 53 at 216 km, while the lowest variance is with station 47 at 136 km. The maximum mean distance of a given particle is at 968 km from the origin at station 47, while the minimum mean distance of a given particle is 10 km at station 44. For austral fall the lowest median distance to a station origin is station 683 with 153 km, and the highest median distance is at station 634 with 991 km. Station 634 has the largest quartile 1 to quartile 3 variance with 411 km, and station 621 has the smallest variance at 87 km. The maximum mean distance is 1374 km at station 634 and the minimum is 11 km at station 621. The austral winter stations have the highest median at 951 km with station 508 and the lowest median at 649 km with station 516. The highest interquartile range is at station 508 with 646 km and the lowest range is station 516 at 110 km. The maximum mean distance is 1587 km for station 508 and the minimum mean distance is 25 km at station 474.

The median for backwards tracked particles (Figure 26D) has an austral spring maximum of 678 km at station 44 and minimum of 65 km for station 53. The largest interquartile variance is for tied for stations 53 and 46 at 39 km, while the smallest variance is station 92 at 14 km. The maximum mean distance is at station 44 at 718 km and the minimum mean distance is at station 47 at 45 km. The austral fall maximum median is at station 621 at 560 km while the minimum median is at station 678 with 43 km. The largest interquartile variance is with station 683 at 156 km and the minimum is at station 678 with 5 km. The maximum mean distance is 612 km at station 683 and the minimum is 33 km at station 678. For austral winter, the maximum median is 285 km at station 508 and the minimum is 169 km at station 516. The largest interquartile variance is 18 km at station 508 and the minimum is tied between stations 474 and 516 at 12 km. The maximum mean distance is at station 474 with 313 km and the minimum is at station 516 with 125 km.

Overall, the total distance travelled by forward tracked particles varies from season to season, and for station to station within the season. The winter stations particles

have the highest total distance travelled with also the highest distance to their starting location. The total distance travelled by spring and fall stations appear similar, but fall stations tend to be closer to their release point, except station 634, whereas spring station particles tend to be further away from their release point, except station 44. Some of the stations like station 53, station 634 and station 508 have a higher interquartile range compared to other stations, meaning the particles in this station have a high variety of displacement compared to each other in their simulation.

The backwards tracked particles per station all have similar total distance travelled with smaller seasonal variances, however even with variance, forward tracked total distance travelled is still higher considering winter results. The distance to station release origin however is quite varied, where spring shows a large variance from station to station with the difference between station 53s distance to its origin and station 44s distance to its origin being 600 km. Similarly for fall, the difference between station 678 and station 621 500 km. The winter stations however, are consistent with their distance to their station release points. This means that even though nearly all particles travel the same distance on their backtracked trajectory, there is a spatial variance depending on the station release point, where stations such as 53 and 678 are within 100 km to their origin, and stations such as 44 and 621 are 680 and 550 km away respectively.

3.1.3.4.2 Sink regions

The sink regions reached by the particles according to their season indicate that the largest sink region for austral spring (Figure 27A) is the South Lazarev (44%) followed by South Weddell (34%), while the North Weddell (14%) and North Lazarev (7%) make up the remaining sink regions.

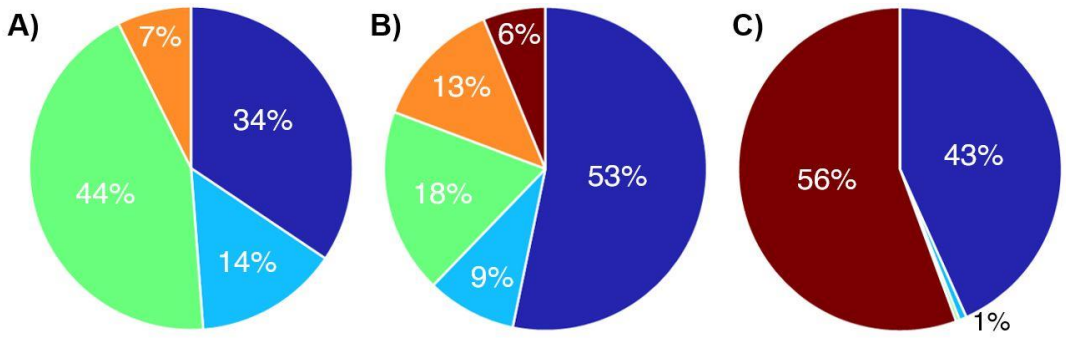


Figure 27 Distribution of sink regions that particles released at the Lazarev Sea stations reach during forward simulation for 365 days depending on seasons: A) austral spring B) austral fall, and C) austral winter. Colors mark the sink region as defined in Figure 12C: red - entrained in the ACC, orange - North Lazarev Sea, yellow - Northwest region, light blue - North Weddell Sea, dark blue - South Weddell Sea, and green - South Lazarev Sea.

The largest sink region for austral fall (Figure 27B) is South Weddell (54%) while the South Lazarev (18%) and North Lazarev(13%) follow as the second and third. Finally North Weddell (9%) and ACC (6%) make up the remainder.

For austral winter (Figure 27C) the two largest sink regions are ACC (56%) and South Weddell (43%), the remaining sink regions, Northwest region and South Weddell, make up 1%.

3.1.4 200m release results vs surface release results

The comparison between particles released at 200m depth versus the particles released at the surface is shown for stations 92 below (Figure 28). For the remaining stations please see the Appendix A.

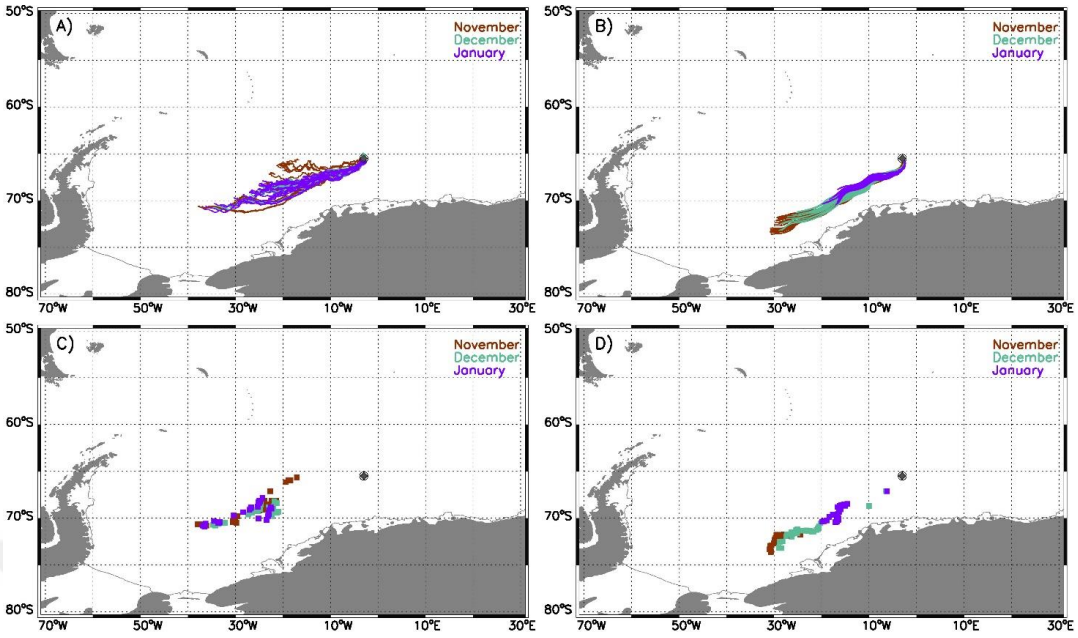


Figure 28: Comparison of simulation results between surface layer (left column) and 200m (right column) releases of Station 92 . A) Trajectories of surface release, B) Trajectories of 200m release, C) End points of surface release, D) End points of 200m release.

Both releases show westward trajectories into the Weddell Sea region. The 200m depth results show a more consistent and tight spatial spread between the particles with different month releases whereas the surface layer results show a wider spread. The 200m results overall show a more consistent pattern of ending points compared to the 0m results. This pattern is consistent with the results from other stations (Appendix A) and hence this study only focuses on surface drifters.

3.2 Ice algae results

The FESOM-REcoM2 modeling system did not include explicitly sea ice biota, however it included sea ice dynamics and hence the percent ice cover, ice cover duration and ice thickness. The biomass and distribution of sea ice biota under the sea ice was therefore calculated based on light availability, thickness of the ice and how much of the ocean is covered for how long a time following the approach by

Meiners et al. (2012) and Melbourne-Thomas et al (2016) as described in detail above in the Methods section.

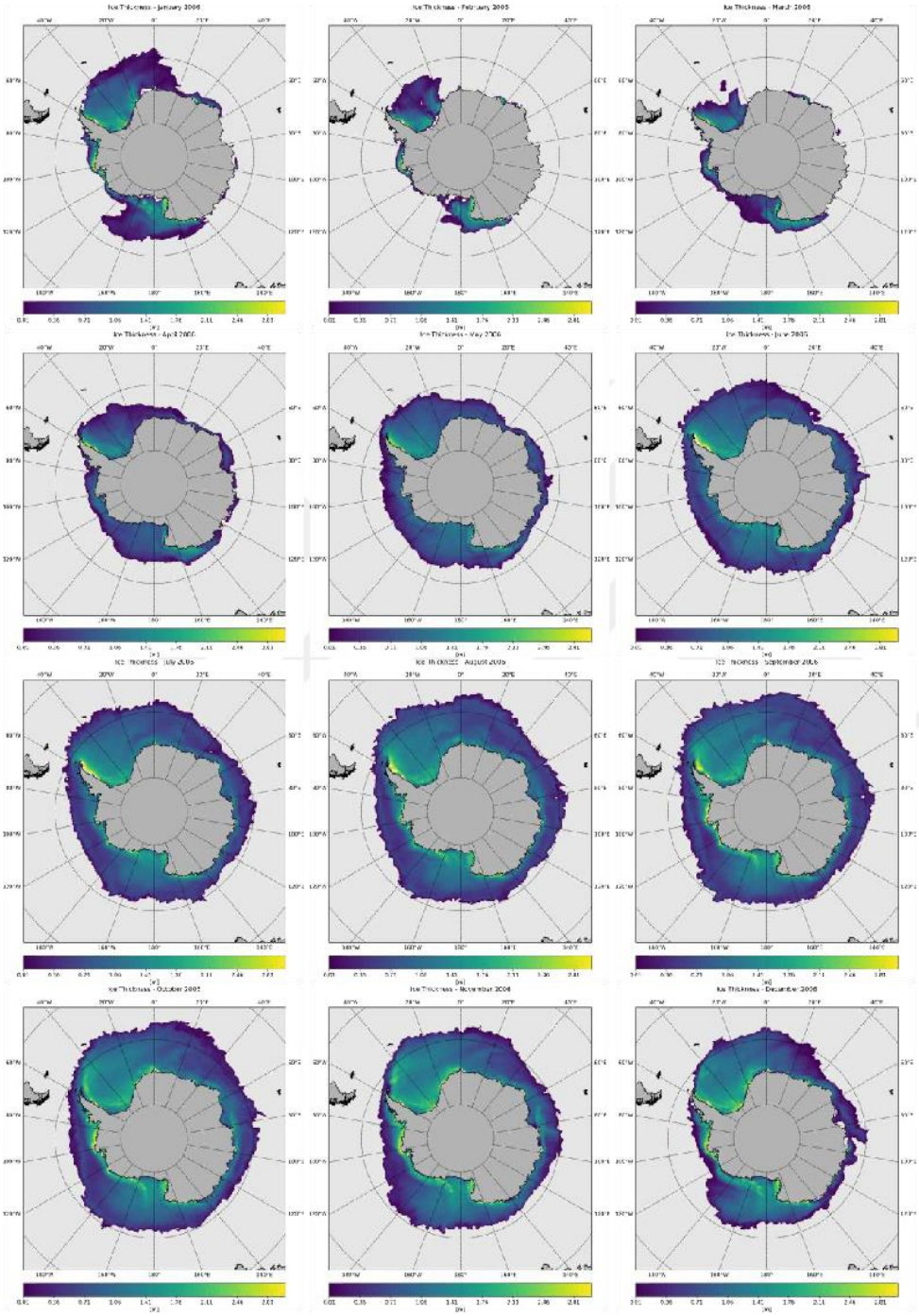


Figure 29 Modeled mean monthly sea ice thickness (m) for 2006 from the 10-year FESOM model starting in January (top left).

As a first step the model distribution sea ice thickness at each grid cell was computed (Figure 29). Sea ice extent reaches it's the maximum during the months of June to October, which is to be expected as this is the austral winter, and ice forms and accumulates during these months. The minimum extent is observed in March. Ice thickness is particularly high in the Weddell Sea and Ross Sea areas (Figure 29), which are also the regions with the thickest ice. The pattern of extending and shrinking ice extend follows observations from satellite well. In the Lazarev Sea, the region of interest for this study some ice can be found in January but starting February until April barely any ice is found there. After April ice continues to grow and thickness reaches a maximum of > 1m but below 1.5m (Figure 29).

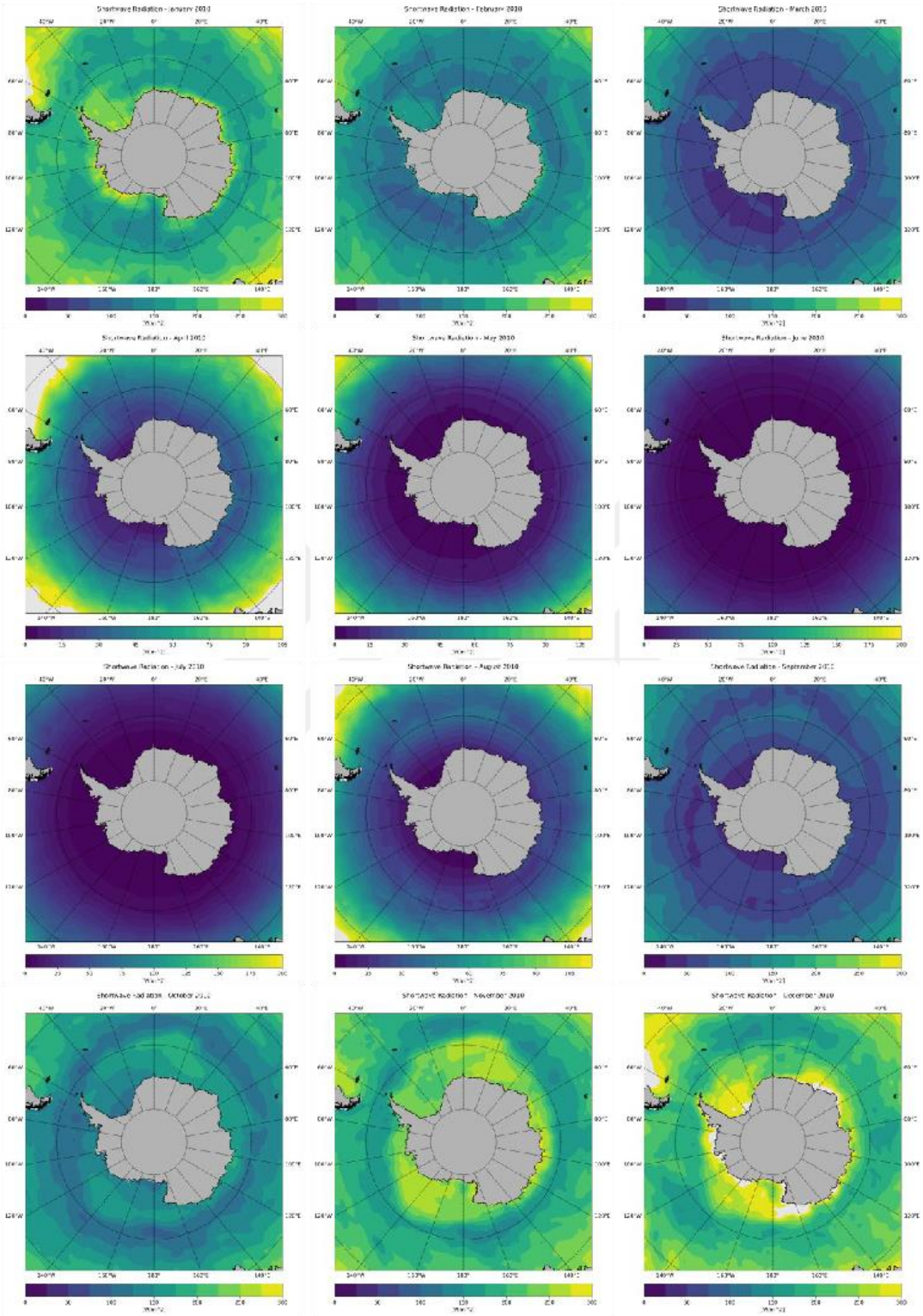


Figure 30 Mean monthly short-wave radiation as output by the FESOM model for the year 2010 starting in January (top left).

At the same time the short-wave radiation from the FESOM model (Figure 30) was checked if a minimum of 0.45 W m^{-2} light was present, which is the threshold for algal growth (Melbourne-Thomas et al, 2016). Further, incoming solar radiation from FESOM is multiplied with the light transmittance value 0.002 to calculate the amount of light that can be transmitted through all the ice and snow above. Radiation is highly variable over the course of the year following the different seasons (Figure 30). Radiation of 200-300 W m^{-2} is present all-around Antarctica in January but decreases to almost no radiation (< 25 W m^{-2}) in the austral winter months and only starts increasing after August again.

Sea ice algae are mostly abundant at times when sea ice cover is not too thick, and enough radiation is present and hence the highest values of sea ice algae in the Lazarev Sea can be found from September to January (Figure 31). In April to July the lack of radiation does not allow for algal growth, while in February and March the lack of ice in the Lazarev Sea hinders the growth of ice algae.

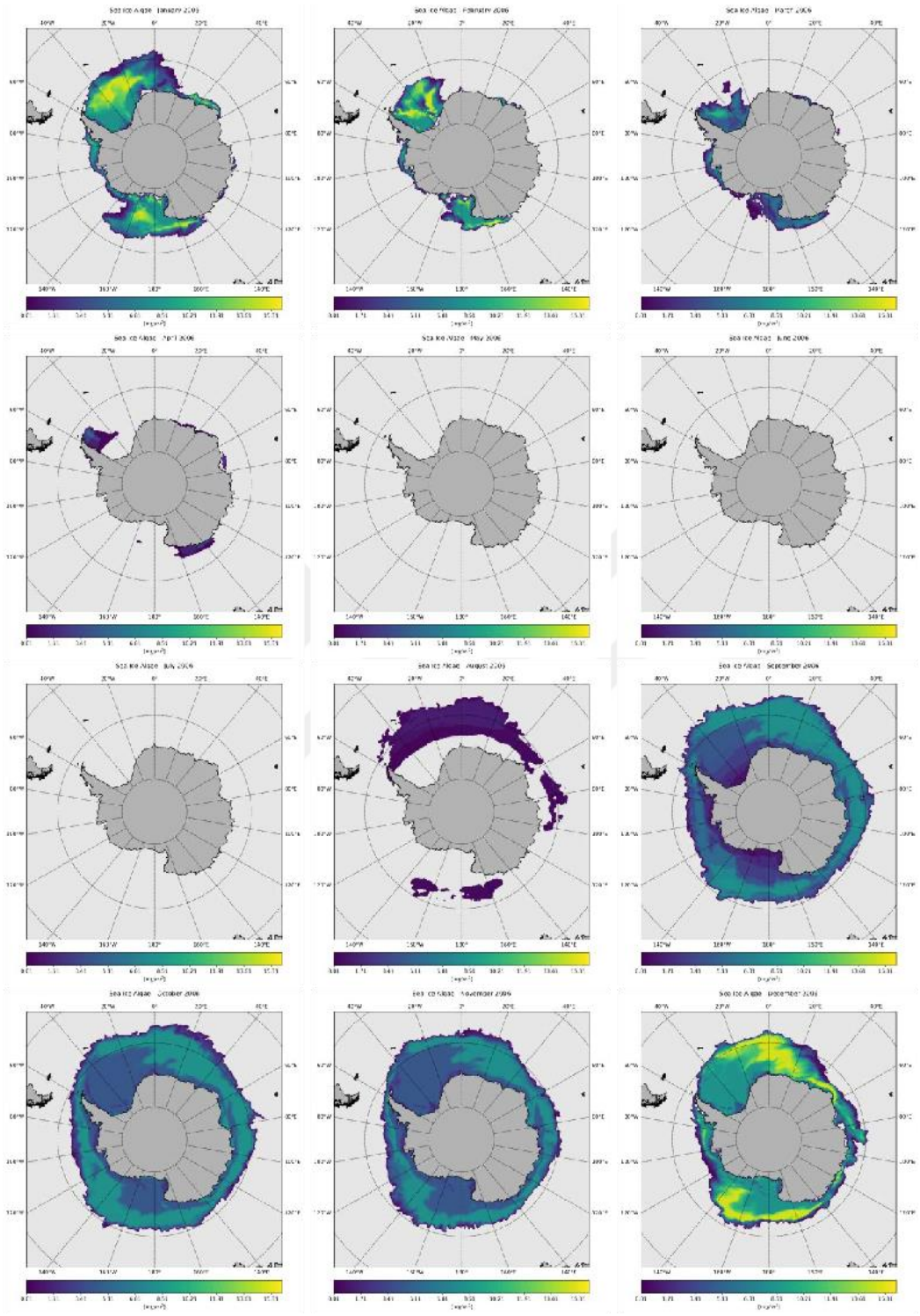


Figure 31 Mean monthly sea ice algae concentration in mg chl m^{-2} as calculated from the 10-year FESOM model following the approach of Meiners et al. (2012) and Melbourne-Thomas et al (2016) for the year 2010 starting in January on the top left.

3.3 Krill growth and survival along transport pathways from selected release point

In this results section it was investigated if larvae and juvenile krill that start transport at the different LAKRIS station can survive this transport and how well they will grow. This was accomplished by extracting food from the REcoM2 model along transport pathways particles and using it with the krill IBM described above. In this section the specific transport pathways, the available food extracted along the pathways of each of the particle, and the IBM simulation results are presented. Out of the original twelve LAKRIS station, three stations were chosen to represent the three respective seasons. Station 92 represents austral spring and spawning season for Antarctic krill, station 634 represents the austral fall and station 516 represents the austral winter. For each of the three stations/seasons the 92 particle trajectories are presented with three particles marked red, green and blue to better show the differences between transport pathways. The remaining results are presented in Appendix B.

3.3.1 Austral summer/spring release at station 92

The particles released at station 92 in austral summer from the Lazarev region move westward and south into the Weddell Sea region. Over the entire three months, the majority of the particles do not cross the 72°S latitude during their journey and none of the particles get close to the Antarctic coast. The furthest West that any of the particles can reach is 38°W.

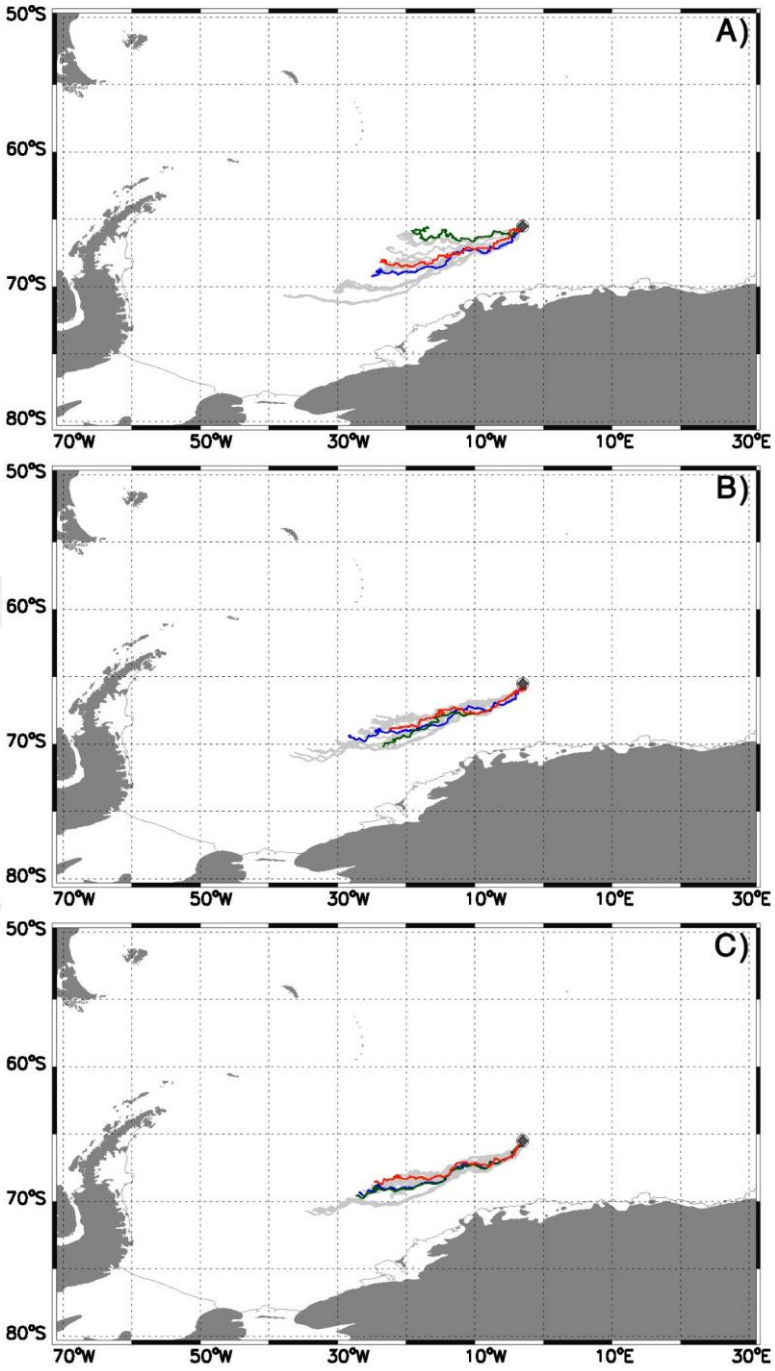


Figure 32 Year-long Lagrangian particle trajectories of particles released from station 92 are marked in grey. A) Particles released in November of 2005, B) December of 2005, C) January of 2006. Selected particles marked in red, green and blue.

Particles released in November (Figure 32A) have the widest north to south distribution pattern between 65°S and 72°S latitudes, and the furthest longitude in the west reached by the particles is 38°W, making the longitudinal distribution of the November particles between the 38°W and 16°W longitudes. Particles released in December (Figure 32B) and January (Figure 32C) have a similar latitudinal spread moving between the 66°S and 72°S latitudes, where particles released in January end closer together compared to December. The farthest longitude both December and January particles can reach is 37°W and 35°W respectively, placing the longitudinal distribution of particles between 37°W and 20°W longitudes for December, and 35°W to 20°W for January releases.

The red, green and blue particles follow similar trajectories during December and January releases, placing them between 66°S and 71°S latitudes in the Northern Weddell Sea region. The green particle released in November is one exception that ends at 66°S latitude and 16°W longitude, still inside the Northern Weddell region, making it the furthest drifter compared other selected drifters.

Station 92 drifters show the most variability in their trajectory and ending points during the November particle release and show the most consistency in the January release, with December being very similar to January with less consistency.

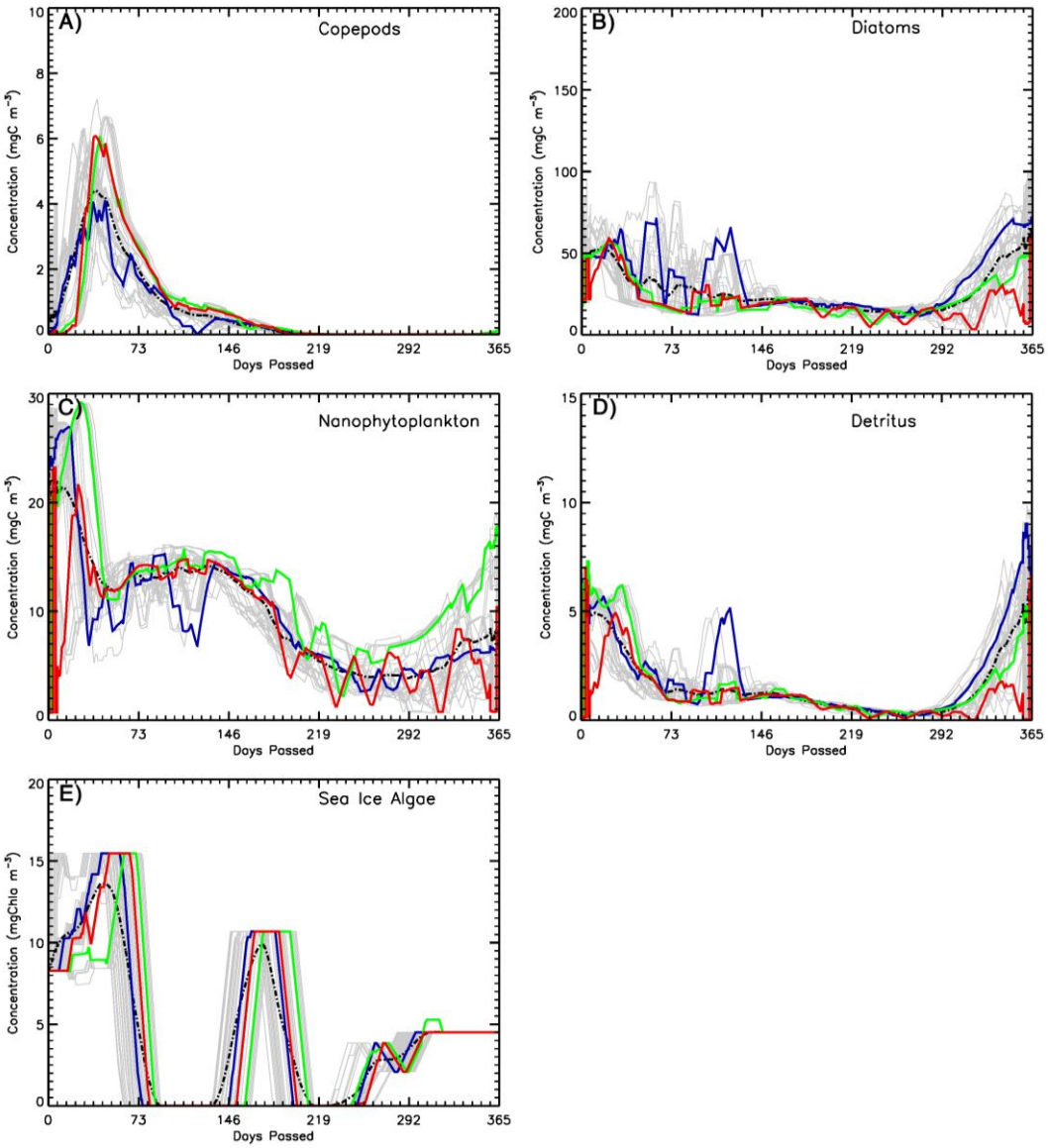


Figure 33 Concentrations of food for krill encountered by all drifters released from station 92 in November 2005 in grey. A) Copepod concentration (mgC m^{-3}), B) Diatom concentration (mgC m^{-3}), C) Nanophytoplankton concentration (mgC m^{-3}), D) Detritus concentration (mgC m^{-3}), E) Sea ice algae concentration (mg Chla m^{-3}). The red, green, blue marked lines correspond to the food concentrations along the same particle trajectories as marked Figure 32A.

The station 92 particles, released starting from November 1st until November 30th, start their journey during austral spring, which also is the spawning season for krill. The copepod availability (Figure 33A) at the beginning of transport is just above 0 mgC m^{-3} and increases to an average of 4.2 mgC m^{-3} on day 40. After day 40 the

copepod concentrations start to decline with availability ranging from 0.5 mgC m^{-3} to 1 mgC m^{-3} between days 110 and 200. After day 200 availability declines to 0 mgC m^{-3} during the austral winter period. By day 365, the next austral spring approaches, and a concentration 0.1 mgC m^{-3} is observed with the green particle.

The average diatom concentrations (Figure 33B) at the beginning of transport is 50 mgC m^{-3}. The average concentration decreases to 25 mgC m^{-3} by day 73. The concentration keeps declining by day 292 but does not decrease below an average of 20 mgC m^{-3}. After day 292, the values start increasing again and reach their peak of 135 mgC m^{-3} with the average showing an increase trend up to 70 mgC m^{-3} by day 365.

Nanopyhtoplankton concentrations (Figure 33C) begin with an average of 20 mgC m^{-3} then dropping to an average of 12 mgC m^{-3} by day 73. By day 146 another peak of 15 mgC m^{-3} occurs after which the average concentrations start to drop for the austral winter months down to 5 mgC m^{-3} by day 219. After day 292 the average concentration start increasing to 8 mgC m^{-3} before day 365.

Detritus concentrations (Figure 33D) starts with an average concentration of 5 mgC m^{-3} then starts to decline down to 1.5 mgC m^{-3} by day 73. Afterwards apart from some peaks up to 5 mgC m^{-3}, the average steadily drops below 1 mgC m^{-3} until day 292. As austral spring approaches, the average values increase again reaching 5 mgC m^{-3} between days 292 and 365.

Sea ice algae average concentrations (Figure 33 E) range from 7 mgChla m^{-3} to 15 mgChla m^{-3} until day 73, then decrease to zero. By day 146 the average concentration increases again to 10 mgChla m^{-3} only to drop down to zero by day 219. The concentrations reach an average of 2.5 mgChla m^{-3} by day 292 and further increase up to 4.5 mgChla m^{-3} by the end of the 365 day simulation. It should be noted that the reason that the sea ice algae values appear to jump between certain values is due to how the parameterization is made using set predefined values for ice thickness and seasonal multipliers. Therefore only certain constant values of ice algae can be encountered on particle paths in some seasons.

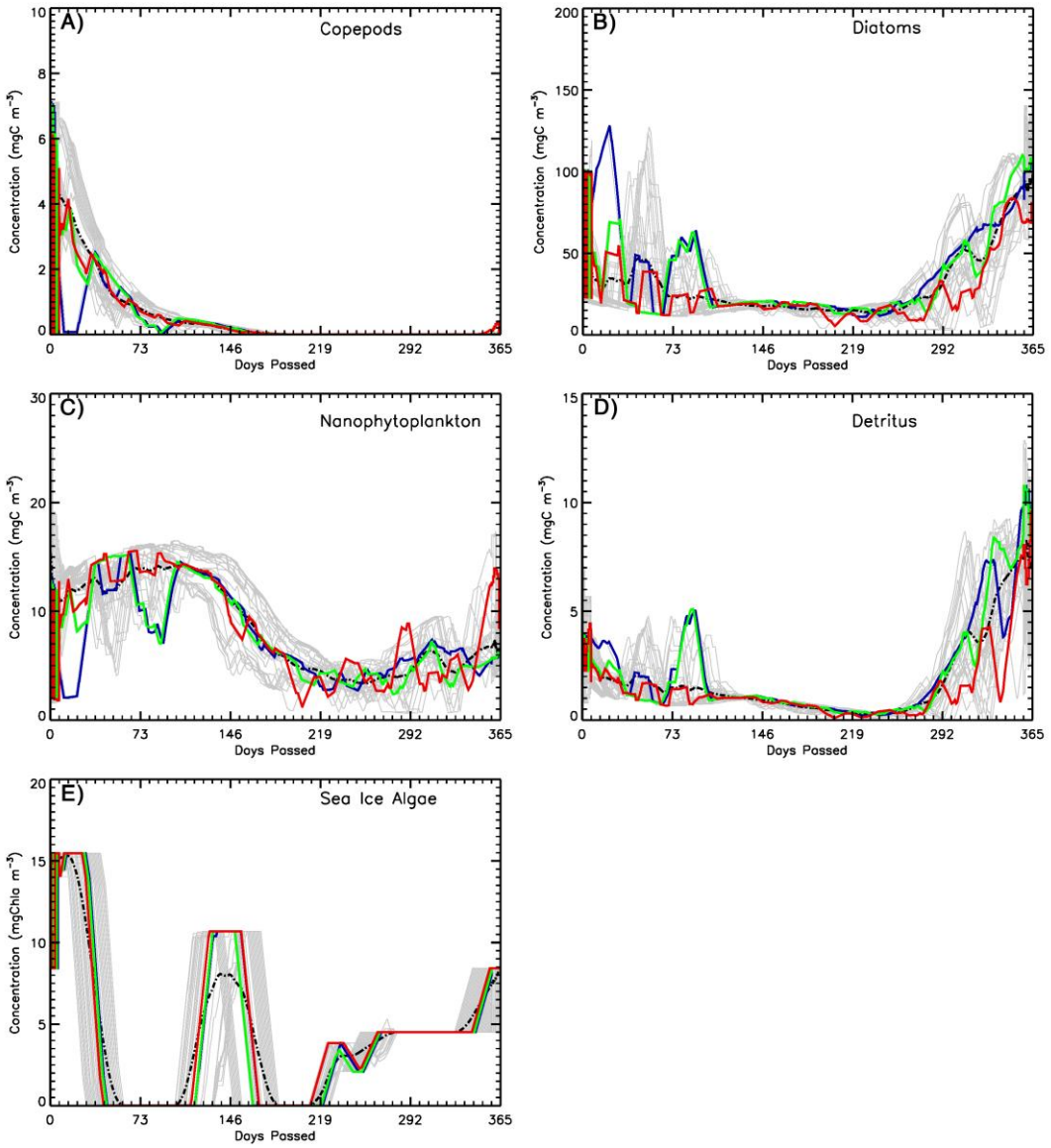


Figure 34 Concentrations of food for krill encountered by all drifters from station 92 in December 2005 . A) Copepod concentration (mgC m^{-3}), B) Diatom concentration (mgC m^{-3}), C) Nanophytoplankton concentration (mgC m^{-3}), D) Detritus concentration (mgC m^{-3}), E) Sea ice algae concentration (mg Chla m^{-3}). The red, green, blue marked lines correspond to the food concentrations along the same particle trajectories as marked Figure 32B.

The station 92 particles, released starting December 1st until December 31st, start their transport in austral summer and in the middle of the spawning season. The copepod concentrations (Figure 34A) starting with an average of 4.2 mgC m^{-3} show a decreasing trend until day 146 where the average reaches 0.2 mgC m^{-3}. The

concentrations keep decreasing until reaching zero by day 180 and only start to increase towards the end of the simulation around day 360 to 0.5 mgC m^{-3} with the red particle.

The average diatom concentrations (Figure 34B) starts at 30 mgC m^{-3} and increases to 50 mgC m^{-3} before day 73 and drop down to 25 mgC m^{-3} by day 73 and remains at this level until day 219. Afterwards the average shows an increasing trend starting day 292 and manages to reach an average of 100 mgC m^{-3} by day 365.

Nanophytoplankton concentrations (Figure 34C) averages around 12 mgC m^{-3} until day 73. Afterwards the average shows decreasing trend until day 219, decreasing to 4 mgC m^{-3}. Between days 292 and 365 the average fluctuates between 4 and 7 mgC m^{-3}.

Detritus concentrations (Figure 34D) start with an average of 2.5 mgC $m^{-3}$and show a decreasing trend down to 0.2 until day 292. Afterwards the average has an increase trend and manages to increase to 6 mgC m^{-3} by day 365.

The sea ice algae concentrations (Figure 34E) averages at 15 mgChla m^{-3} during the beginning of the simulation then sharply drops to zero by day 36. By day 128 an increase in average concentrations to 11 mgChla m^{-3} occurs and decreases again to zero on day 182. An increase to 4 mgChla m^{-3} occurs at day 283, followed by an increase to 8 mgChla m^{-3} by the end of the year in December.

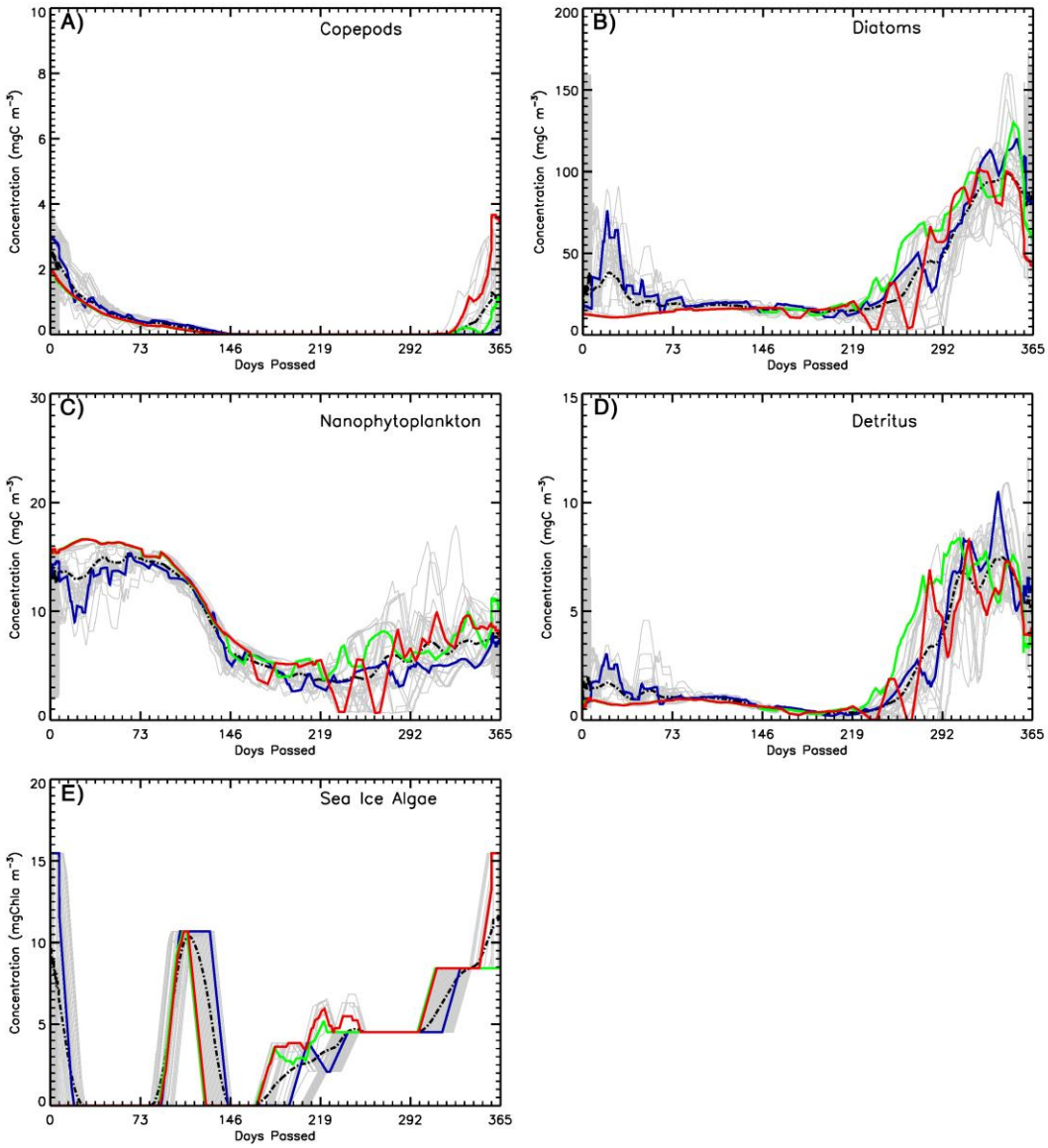


Figure 35 Concentrations of food for krill encountered by all drifters from station 92 in January 2006. A) Copepod concentration (mgC m^{-3}), B) Diatom concentration (mgC m^{-3}), C) Nanophytoplankton concentration (mgC m^{-3}), D) Detritus concentration (mgC m^{-3}), E) Sea ice algae concentration (mg Chla m^{-3}). The red, green, blue marked lines correspond to the food concentrations along the same particle trajectories as marked Figure 32C.

Station 92 January particles released from January 1st until January 31st in austral summer and towards the end of the spawning season encounter copepod concentrations (Figure 35A) with average values of 2.6 mgC m^{-3}. The average gradually decreases to zero by day 146 and concentrations only increase again by

day 320, and towards the end of the simulation the average concentration increases to 1 mgC m^{-3}.

Diatom concentrations (Figure 35B) start with average values of 25 mgC m^{-3} in the beginning and decrease to 20 mgC m^{-3} by day 73 and remains at that value until day 219. The concentrations start to increase by day 292 and eventually reaches an average peak of 100 mgC m^{-3} by the end of the simulation.

The Nanophytoplankton concentrations (Figure 35C) average at 14 mgC m^{-3}, the concentrations start decreasing by day 146, and reaches an average of 5 mgC m^{-3}. After day 292, the maximum concentrations increase to 18 mgC m^{-3}, however the average stays at 7 mgC m^{-3} with lows of 1 mgC m^{-3}.

Detritus concentrations (Figure 35D) average at 1.5 mgC m^{-3} at the beginning with maximums values of 8 mgC m^{-3}. The average gradually drops to 1 mgC m^{-3} by day 146, and then further decreases to 0.5 mgC m^{-3} by day 219. The concentrations start increasing in by day 292 with maximum values 12 mgC m^{-3} and averages 7 mgC m^{-3}.

Sea ice algae concentrations (Figure 35E) start with maximum values of 15 mgChla m^{-3} with an average of 9 mgChla m^{-3}, and drop to zero on day 18. Later at day 91, the average concentration increases again to 11 mgChla m^{-3} and goes back to zero around day 146. By day 164, the values increase to an average of 4 mgChla m^{-3} and steadily increase up to 10 mgChla m^{-3} and further to 15 mgChla m^{-3} by day 365.

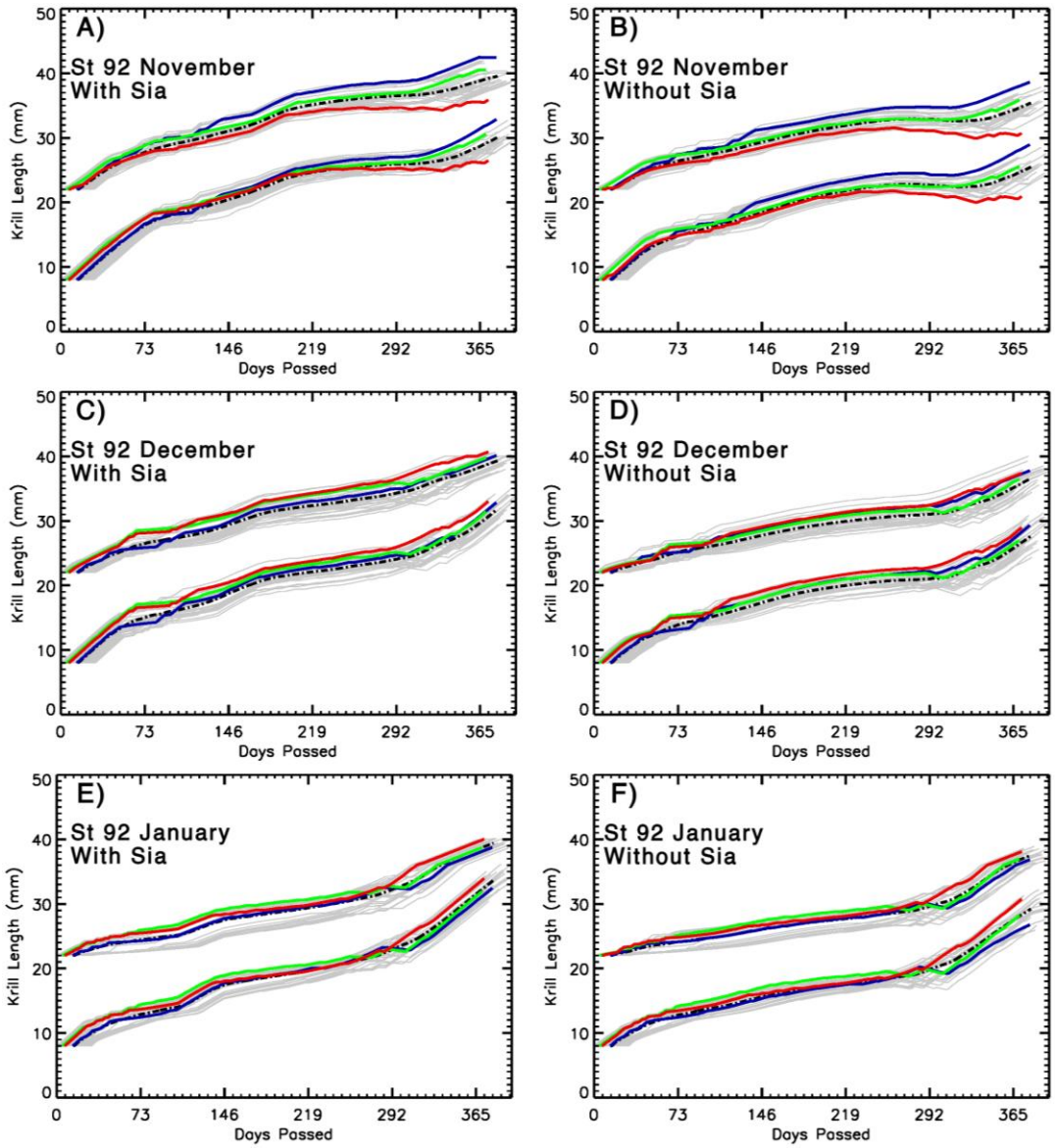


Figure 36 Krill growth over time for krill originating at station 92 starting A) November of 2005 feeding on sea ice algae, B) November of 2005 without feeding on sea ice algae, C) December of 2005 feeding on sea ice algae, D) December of 2005 without feeding sea ice algae, E) January of 2006 feeding on sea ice algae, F) January of 2006 without feeding sea ice algae. Juveniles start at 22mm, larvae start at 8mm. The red, green, blue marked lines mark growth of krill feeding on the food extracted along the same colored particle trajectories in Figure 32 and the black dash dot dash line indicates the average of all the surviving krill. Particles representing krill were released on consecutive days seen by the offset on the x-axis month and the average growth line corresponds to day 15 day.

In the next step, the growth of larval and juvenile krill feeding on the food encountered along drifter path is simulated with the krill IBM. Larval krill is thereby

starts at 8 mm length and juveniles at 22 mm. Simulations that include sea ice algae as food for krill show that, for November (Figure 36A) both larvae and juveniles have an average increasing growth trend as soon as the simulation starts, the trend slows down by day 100 however after day 292 the growth rate starts increasing towards the end of the simulation. The larvae reach an average size of 30 mm and juveniles 39.5 mm by the end of the simulation. The green and blue particles diverge in their sizes towards the middle of the simulation and end at nearly the same size for larvae, and produce a 1 mm difference for juveniles. The red particle starts below the average and stays 1.5 mm below all through the simulation, however towards the end its growth rate increases and it reaches average size.

December simulations with krill feeding on sea ice algae (Figure 36C) show a higher increase in average size for larvae compared to juveniles, the larvae growth slows down by day 73 whereas the juvenile growth remains similar to the initial starting rate. After day 292 the growth rates increase towards the end of the simulation and larvae reach an average size of 32 mm and juveniles reach 39 mm. The colored particles for both classes of krill show that the blue particle starts the simulation ahead of the average size by 1.5 mm, however around day 292 it decreases to the average size for the juvenile simulation and 0.5 mm below the average for larvae simulation. The green particle follows the average size in both size classes and towards the end of the simulation grows 0.5 mm larger. The red particle is 1 mm smaller than the average but manages to catch up to the average size and grows 0.5 mm larger as larvae.

January krill growth with feeding on sea ice algae (Figure 36E) shows that for larvae, there is an initial growth until about day 50, when it slows down and then increases again until day 146 and afterwards it is once again slowed down. Day 292 shows another growth increase until the end of the simulation. The juveniles have a steadier average growth with one jump at day 80 and a second one at day 292. The larvae can grow on average to 33.5 mm and juveniles to 39.5 mm length. The blue particle shows a consistent 1 mm larger size compared to the average, the green particle

follows the average closely and only falls below it by 1 mm, and the red particle starts 2 mm below and by the end is 0.5 mm smaller than the average.

Krill growth of particles released at station 92 for November without feeding sea ice algae (Figure 36B) have an increase of average length for the first 73 days. Larvae grow from 8 mm to 14 mm and the juveniles grow from 22 mm to 26 mm in size. The increasing trend continues slower until day 219, where larvae reach to 23 mm and juveniles reach 33 mm. From day 219 to 292 there is a slight decrease trend of 0.5 mm in size for both classes of krill. After day 292 the average length starts to increase and by day 365 larvae reach an average 25 mm in size and juveniles reach an average 36 mm in size. The red particle starts the simulation close to the average trend line, only around day 219 starts deviating and falls below the average and finishes day 365 at 21 mm for larvae and 31 mm for juveniles respectively. The green particle starts higher than the average trend but by day 219 falls to the average trend and finishes 26 mm and 36 mm in size. The blue particle starts the same as the average but after day 73 grows higher than the average and by day 146 surpasses the average by 2.5 mm in size. By day 365 it manages to reach 29 mm and 38.5 mm in size as the largest particle.

Krill originating from station 92 in December feeding on no sea ice algae (Figure 36D) has an increasing trend of average length throughout the simulation. The average starts from 8 mm and 22 mm for larvae and juveniles respectively, the average reaches 14 mm and 24 mm, at 146 reaches 16 mm and 26 mm, by day 219 reaches 21 mm and 31 mm and by day 365 reaches 27.5 mm and 36.5 mm. The red particle follows the trend line average but by day 292 falls 1.5 mm below and finishes the simulation with 24.5 mm and 34 mm in length. The green particle follows the average closely but by day 146 grows 1.5 mm above the average and finishes the simulation 29.5 mm and 38 mm in length. The blue particle follows the trend in larvae simulation and after day 73 the larvae grows 2 mm larger, while the juvenile krill on the blue pathway grows 3.5 mm larger than the average 30 days into the simulation. After day 73, the blue particle keeps growing and finishes the simulation

as the 2nd largest particle at 29 mm in the larvae simulation and 40 mm as the largest particle in the juvenile simulation.

The January krill not feeing on sea ice algae (Figure 36F) have a steady average growth trend from the start until day 292 where the average growth trend increases. The average length of larvae starts from 8mm and reaches 20 mm and juveniles start from 22 mm and reaches 30 mm. From day 292 to 365, the average length of larvae reaches 29.5 mm and the average length of juveniles reach 37.5 mm.

The difference between simulations of krill feeding on ice algae and not having access to ice algae is 4 mm for larvae and 3.5 mm for juveniles in November. For December the difference are 4 mm and 3 mm, and for January the differences are 4 mm and 2 mm for larvae and juveniles respectively.

3.3.2 Austral fall release at station 634

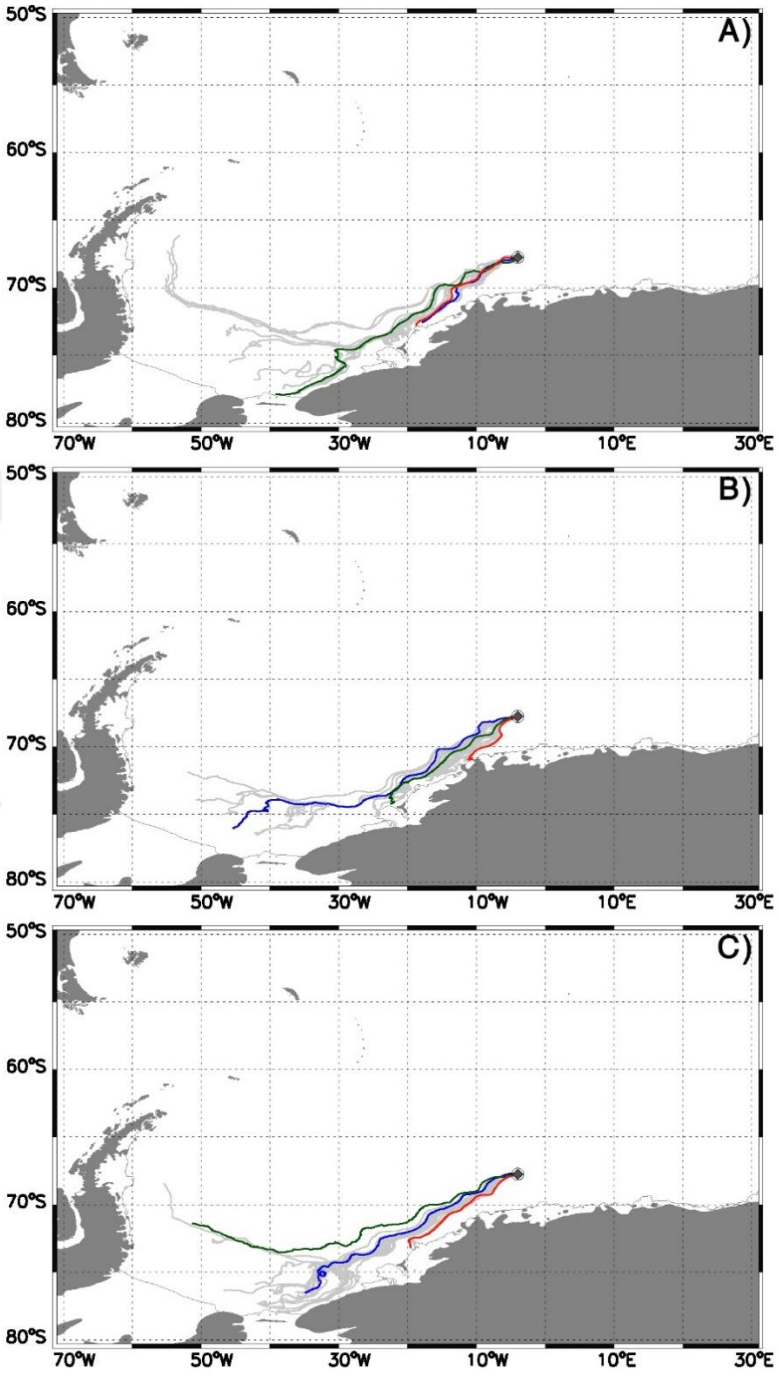


Figure 37 Year-long Lagrangian particle trajectories of particles released from station 634 are marked in grey. A) Particles released in March, B) April, C) May of 2004. Selected particles marked in red, green and blue.

Station 634 drifters (Figure 37) released from the Lazarev Sea in austral fall, follow the Antarctic coast to the West and flow into the Weddell Sea. Release during all three months feature particles that stay at the Antarctic Coast, but many particles are transported west of the 30°W longitude. The particles released in March (Figure 37A) manage to reach as far as the tip of the Antarctic Peninsula around 66°S latitude and 55°W longitude. Some of the particles flow close to the Antarctic Coast and end up between 25°W and 15°W longitudes. The other particles that are able to continue their journey are spread between 72°S and 77°S latitudes and 46°W and 36°W longitudes.

April particles (Figure 37B) can cross the 50°W longitude with particles remaining between 68°S and 77°S latitudes. Some of the particles are retained along the Antarctic coast between 25°W and 10°W longitudes. The remainder of the particles are distributed between 46°W and 35°W longitudes and 74°S and 76°S latitudes.

The particles released in May (Figure 37C) are capable of reaching close to the tip of the Antarctic Peninsula with one particle reaching as far as 68°S latitude and 55°W longitude with two others reaching 72°S latitude and 50°W longitude. Only one particle is retained near the Antarctic Coast at 20°W longitude (red particle). The remaining particles are distributed between 46°W and 34°W longitudes and 76°S and 78°S latitudes.

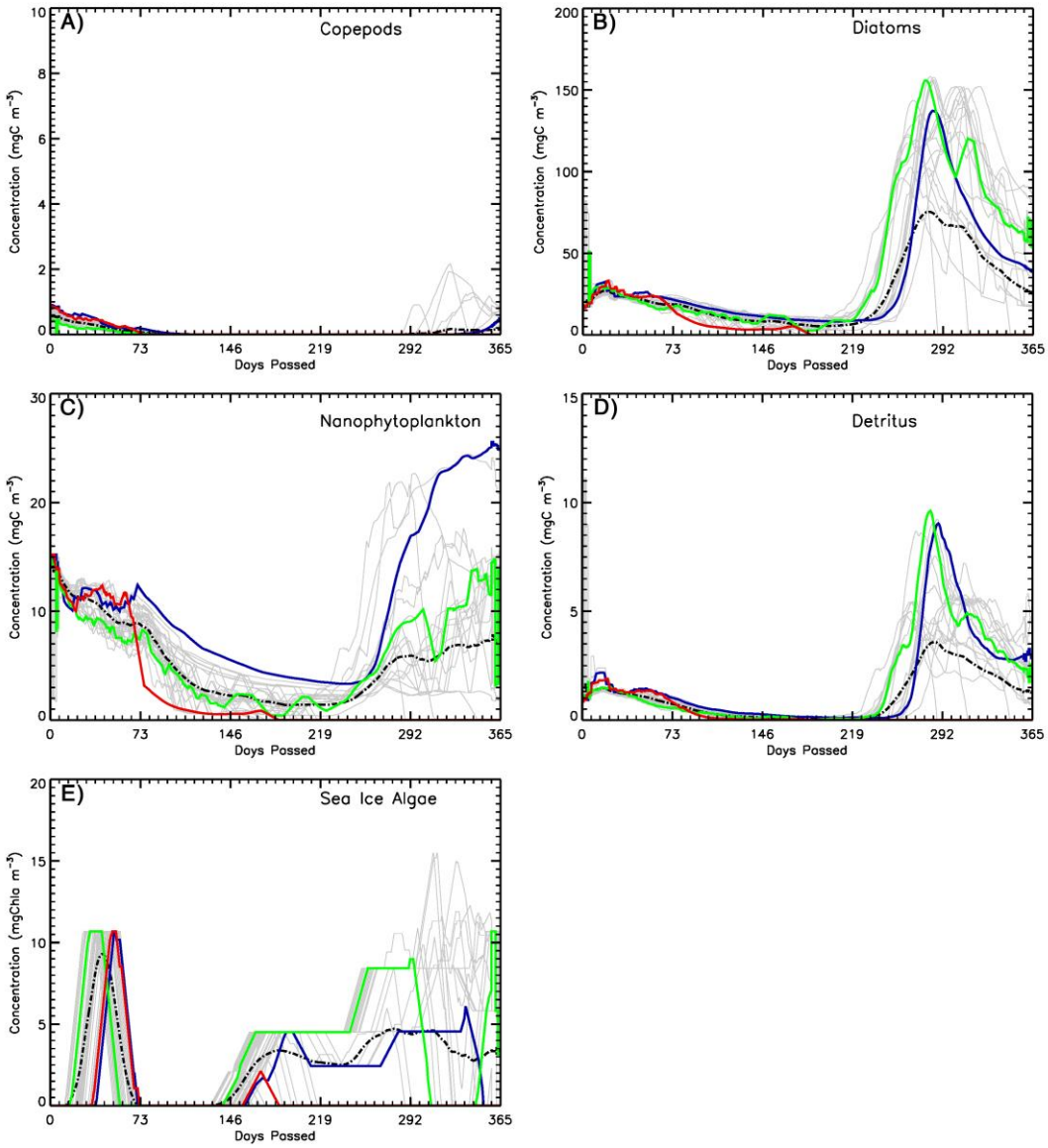


Figure 38 Concentrations of food for krill encountered by all drifters from station 634 in March 2004. A) Copepod concentration (mgC m^{-3}), B) Diatom concentration (mgC m^{-3}), C) Nanophytoplankton concentration (mgC m^{-3}), D) Detritus concentration (mgC m^{-3}), E) Sea ice algae concentration (mg Chl m^{-3}). The red, green, blue marked lines are the food extracted along the same colored particle trajectories in Figure 37A

Station 634 March particles, released from the 1st of March until the 31st of March, encounter during the first 73 days a declining amount of copepods food (Figure 38A) starting from 0.6 mgC m^{-3} that reaches zero. By day 292 the average slowly increases to 0.2 mgC m^{-3} by the end of 365 days.

The diatom concentration (Figure 38B) starts with an average of 20 mgC m^{-3}, increases to 25 mgC m^{-3} then slowly declines to 10 mgC m^{-3} by day 219. Afterwards the average shows an increasing trend and reaches 75 mgC m^{-3} then starts declining down to 25 mgC m^{-3} by day 365.

Nanophytoplanton average concentration (Figure 38C) starts with an average of 15 mgC m^{-3} and slowly declines down to 2 mgC m^{-3}. After day 219, the average starts to increase and manages to reach 7.5 mgC m^{-3} by day 365.

The detritus concentration (Figure 38D) starts with 1.5 mgC m^{-3} average and decreases down to zero by day 219. Afterwards an increase trend shows that the average reach 3.5 mgC m^{-3} peak and decrease down to 1.25 mgC m^{-3} by day 365.

No sea ice algae (Figure 38E) is initially encountered at the start, only after day 40 the average concentration of sea ice algae increases to 9.0 mgChla m^{-3} and drops back to zero by day 73. After day 146 the average starts to increase and hovers between 3.5 and 4 mgChla m^{-3}, and before day 292 the average is at 4.5 mgChla m^{-3}. After day 292 the trend starts to decline and is between 3 and 3.5 mgChla m^{-3} by the end of the simulation.

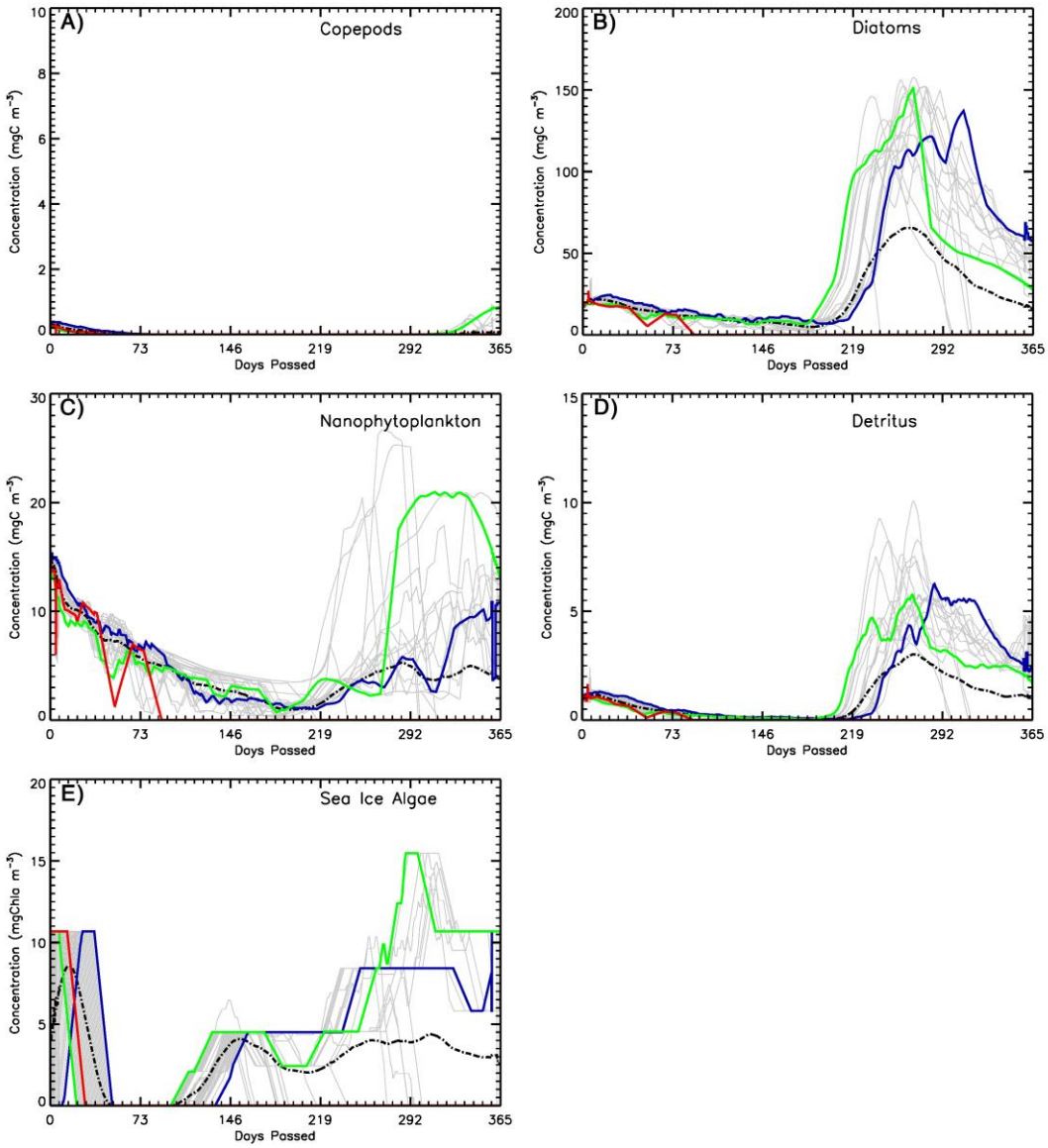


Figure 39 Concentrations of food for krill encountered by all particles released from station 634 in April 2004. A) Copepod concentration (mgC m^{-3}), B) Diatom concentration (mgC m^{-3}), C) Nanophytoplankton concentration (mgC m^{-3}), D) Detritus concentration (mgC m^{-3}), E) Sea ice algae concentration (mgChla m^{-3}). The red, green, blue marked lines are the food extracted along the same colored particle trajectories in Figure 37B.

Station 634 April particles are released from April 1st until April 30th, which encounter a decreasing copepod concentration (Figure 39A) with an average of 0.5 mgC m^{-3} that reaches zero by day 73. Only after day 292 that the average increases from zero to 0.1 mgC m^{-3} before day 365.

The diatom concentration (Figure 39B) starts with an average of 20 mgC m^{-3} and slowly decreases down to 5 mgC m^{-3}. By day 219 the average trend increases and reaches a peak average of 65 mgC $m^{-3}$and slowly trends back down to 15 mgC m^{-3} before the end of the simulation.

The nanophytoplankton concentration (Figure 39C) starts from an average of 15 mgC m^{-3} and trends downwards to 1 mgC m^{-3} until day 219. After day 219 the trend increases and fluctuates between 5.5 and 4 mgC m^{-3} by day 365.

Detritus concentration (Figure 39D) has a starting average of 1 mgC m^{-3} that decreases to zero until day 219. Afterwards the trend shows an increase and the average reaches a peak of 4.5 mgC m^{-3} and slowly goes back to 1 mgC m^{-3} by day 365.

Sea ice algae concentration (Figure 39E) average starts from 4 mgChla m^{-3} and reaches a peak average of 8.5 mgChla m^{-3} and drops to zero by day 40. The trend increases after day 146 where the average climbs back to 4.5 mgChla m^{-3} and fluctuates down 2.0 mgChla m^{-3} and back to 4.5 mgChla m^{-3}.

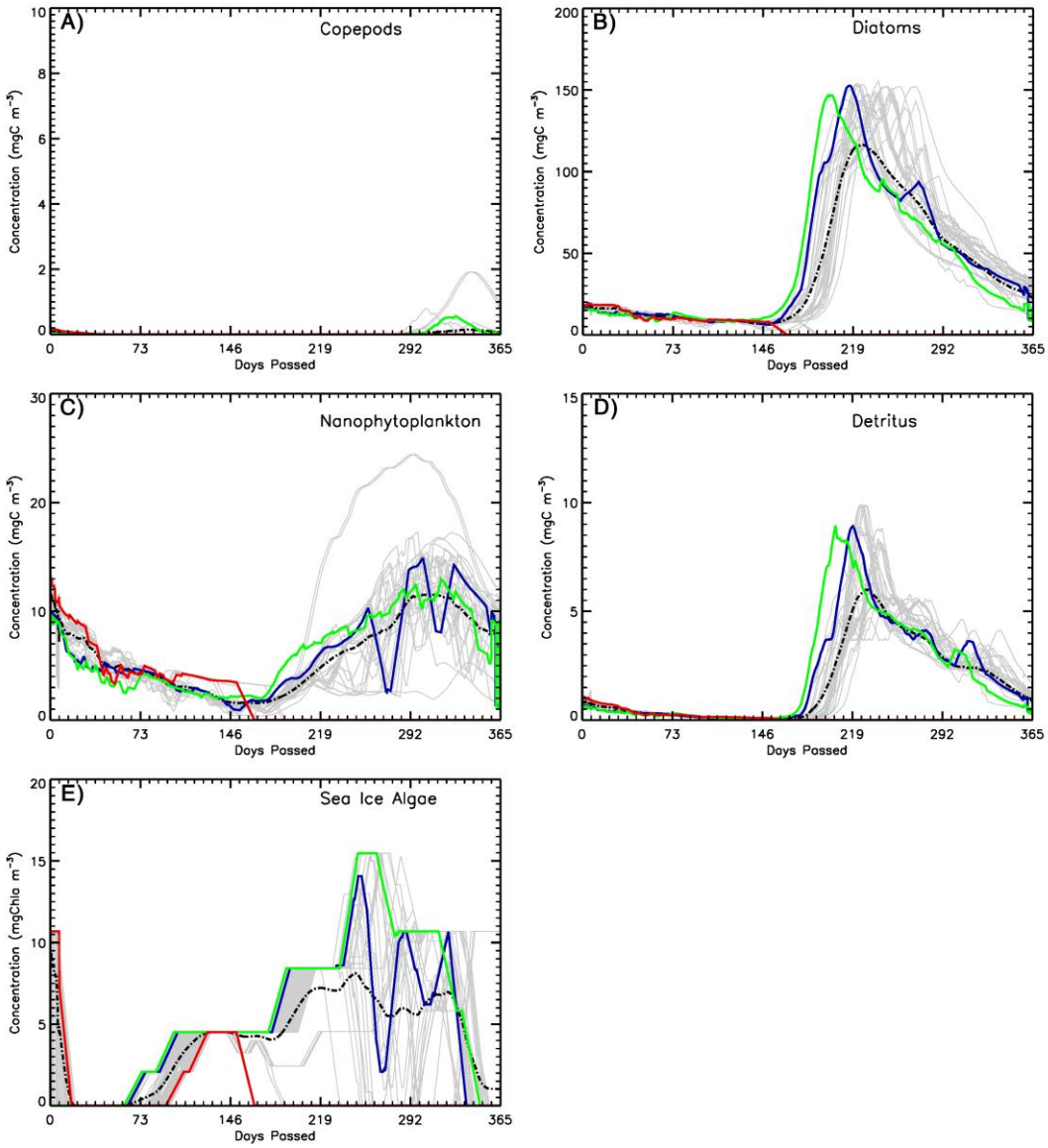


Figure 40 Concentrations of food for krill encountered by all particles released from station 634 in May 2004. A) Copepod concentration (mgC m^{-3}), B) Diatom concentration (mgC m^{-3}), C) Nanophytoplankton concentration (mgC m^{-3}), D) Detritus concentration (mgC m^{-3}), E) Sea ice algae concentration (mgChla m^{-3}). The red, green, blue marked lines are the food extracted along the same colored particle trajectories in Figure 37C.

Station 634 May particles are released from May 1st until May 31st, shows zero average copepod concentration (Figure 40A) at the start and only goes up to 0.3 mgC m^{-3} between days 292 and 365 with some individual particles ranging from 1 and 2 mgC m^{-3}.

The diatom concentration (Figure 40B) starts with an average of 15 mgC m^{-3} and decreases down to 10 mgC m^{-3} by day 146. After day 146 the average trend increases and reaches 110 mgC m^{-3} peak and starts to decline to 25 mgC m^{-3} by day 365.

Nanophytoplankton average (Figure 40C) starts with an average of 11.5 mgC m^{-3} and shows a decreasing trend that drops to 2 mgC m^{-3} by day 146. After day 146 the average starts to increase and reaches 11.5 mgC m^{-3} again, before dropping to 7 mgC m^{-3} by day 365.

Detritus average (Figure 40D) starts at 0.75 mgC m^{-3} and slowly declines to zero by day 146. Then the average starts to increase and reaches 6 mgC m^{-3} and declines again down to 1 mgC m^{-3} by day 365.

The sea ice algae (Figure 40E) average concentration starts from 9 mgChla m^{-3} and drops to zero at day 25. The average starts to increase after day 73 and reaches 4.5 mgChla m^{-3} by day 146 and 8 mgChla m^{-3} after day 219. After day 292 the trend starts to decrease and drops to 1 mgChla m^{-3} by day 365.

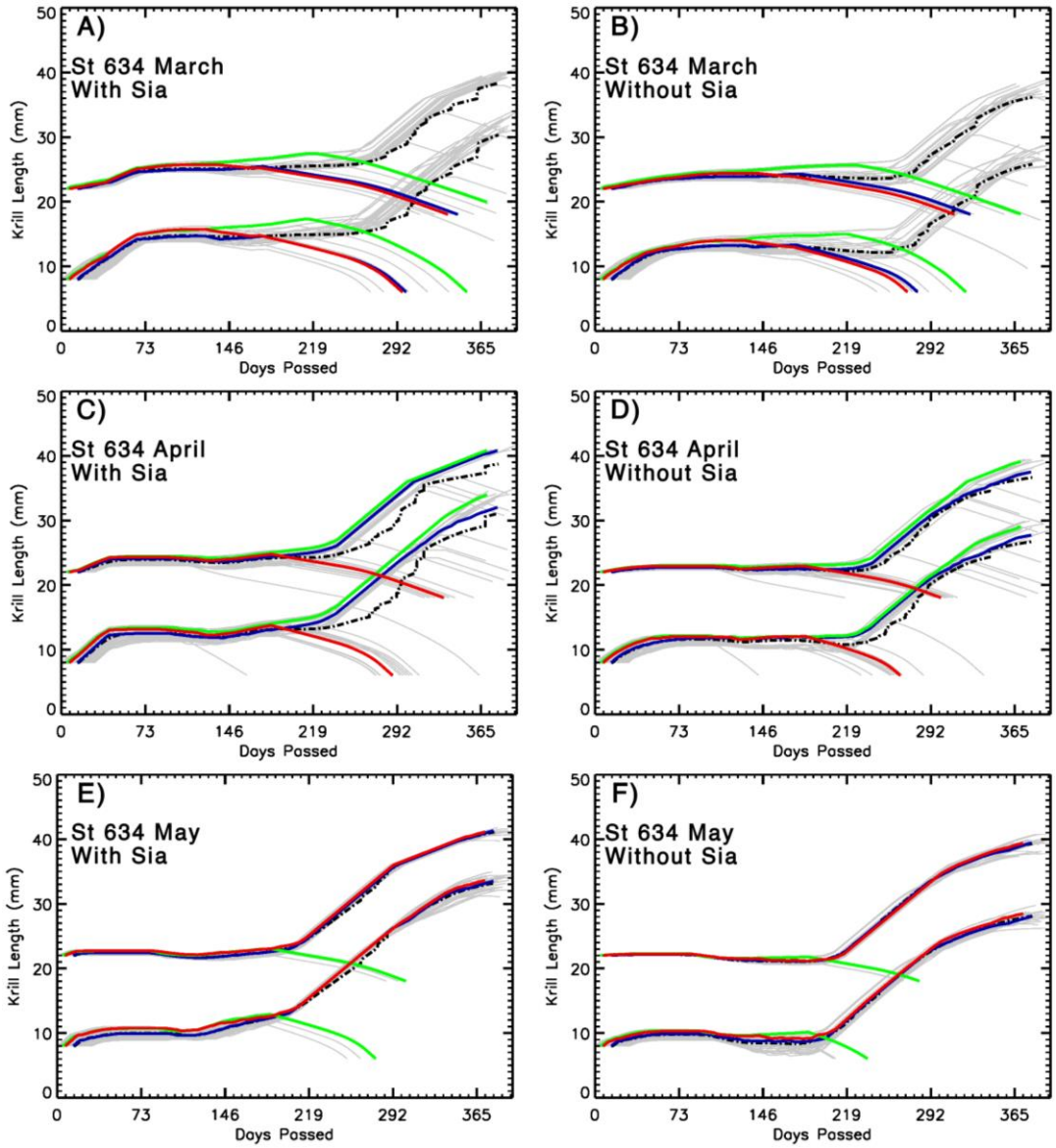


Figure 41 Krill growth over time for krill originating at station 634 starting A) March of 2004 with feeding on sea ice algae, B) March of 2004 without sea ice algae, C) April of 2004 with sea ice algae, D) April of 2004 without sea ice algae, E) May of 2004 with sea ice algae, F) May of 2004 without sea ice algae. Juveniles start at 22mm, larvae start at 8mm. The red, green, blue marked lines mark growth of krill feeding on food extracted along the same-colored particle trajectories in Figure 37.and the black dash dot dash line indicates the average of all the surviving krill. Particles representing krill were released on consecutive days seen by the offset on the x-axis month and the average growth line corresponds to day 15 day.

Simulations of krill growth for particles representing krill larvae and juveniles released from station 634 in March (Figure 41A) show that there is an initial growth

of the average length in both larvae and juveniles up until day 73 when the growth reaches a plateau. Larvae grow to 14 mm and juveniles grow to 25 mm. The average trend only starts to increase at day 292 and the average length by the end of the simulation reaches 30.5 mm for larvae and 38.5 for juveniles. During the larvae simulation the red particle stays mostly below the average initially but after day 73 manages to reach and then pass the average reaching 2 mm higher length at the end. The green particle starts nearly identical to the average and around day 170 falls below the average and is deceased by day 300. The blue particle shortly after the simulation starts, surpasses the average by 1 mm and finishes the simulation consistently 1 mm larger. The colored particles in the juvenile simulation are grouped closer to the average initially, with the blue particle being 0.5 mm larger than the average. The green particle again starts to shrink and is deceased, but by day 350. Compared to the average, the red particle manages to grow 1 mm larger in size, and the blue particle 0.5 mm larger in size.

For the particles released in April (Figure 41C) the growth curve increases and plateaus by day 40 and only starts increasing again after day 219. The average length of larvae reaches 31 mm, and the average length of juveniles reaches 38.5 mm in size by the end of the simulation. The colored particles in larvae simulation show that green stays near the average and is only 1 mm larger by the end, red starts below the average but by the end overtakes green and is 3 mm larger than the average, and blue starts higher than the average but is the same size as red by the end. For the juvenile simulation the colored particles are within 0.5 mm range with one another and closely follow the average at the start of the simulation, but after day 219 all of them surpass the average and reach the same size by the end.

The particle simulations for the month of May (Figure 41E) show that the larvae has an increase of growth initially in the first 20 days and then their size reaches a plateau, whereas the juveniles start with the plateauing behavior. By day 100 both classes of krill show shrinking in their size but recover and start to increase by day 146. After day 219 the average size of the krill shows an increasing trend reaches 33.5 mm in size for larvae and 41 mm in size for juveniles. The colored particles in

both larvae and juveniles show that the blue particle starts larger in size initially 1.5 to 0.5 mm larger, and after day 170 start shrinking in size and is deceased by day 270 and 300 respectively. The red and green particles very closely follows the average trend line and finishes nearly identical in size in both simulations.

Simulations for krill released in March from station 634 not feeding on sea ice algae (Figure 41B) show an initial growth trend on the first 73 days for larvae where the average length of larvae grows to 13 mm, the average length of the juveniles only grow to 23 mm. By day 146, some particles show a decrease trend, notably the red particle, where their length drops to 11 mm for larvae and 21 for juvenile, and some particles, notably the blue particle, grow to 14.5 mm and 24 mm surpassing the average. After day 219 mortalities for larvae start occurring, however the average remains steady for both larvae and juveniles. After day 292 mortalities start occurring with juveniles, the average for surviving particles shows an increasing trend, reaching 26 mm and 36 mm by the end of the simulation. While the blue particle remains higher than the average and the green particle remains close to the average, at the end of the simulation the green particle manages to grow longer than the blue particle.

Particles released on April (Figure 41D) have an increase trend of the average for larvae, reaching 11 mm in length, whereas the average for juveniles only reach 22.5 mm. Between day 73 and 219 the average length remains constant, however the red particle during the larvae simulation shrinks rapidly and deceases by day 146, in the juvenile simulation the red particle deceases by day 219. After day 219 other particles start shrinking and decease, the surviving particle's average length has an increasing trend that reaches 27 mm for larvae and 37 mm for juveniles. The blue particle starts the simulation about 1 mm bigger than average for larvae and 0.5 mm higher in juveniles, whereas the green particle starts about 2 mm smaller for larvae and 0.5 mm smaller for juveniles. By the end of the simulation, both green and blue particles reach 29 mm in length for larvae, and 39 mm for juveniles.

The May release of particles (Figure 41F) for the larvae simulation show an initial average growth to 9 mm length, then a decrease down to 8 mm by day 146. A second growth trend occurs by day 219, where the average length ends up as 28 mm at the end of the simulation. For the juvenile simulation, the average starts and remains at 22 mm and by day 146 decreases to 21.5 mm. After day 219 the average starts to increase, where it reaches 29 mm in length. The red particle in larvae simulation start 1 mm higher than the average, however after day 146 a sharp decrease trend occurs and the particle is deceased before day 219. For juvenile simulation the red particle is the same as the average until day 146. A decrease trend occurs and the particle is deceased before day 292. The blue and green particles in the larvae simulation have a similar growth trend where they start 1 mm smaller than the average but by day 292 they catch the average and in the case of the blue particle surpass it by 1 mm becoming the 2nd largest in length. For the juvenile simulation both blue and green particles follow the average trend line and only after day 292 start surpassing the average, where the blue reaches 41 mm in length becoming the largest particle.

Comparison of both the March release simulations with and without ice algae as food available to juvenile and larvae krill shows that when sea ice algae is included in the simulation, krill are on average 4.5 mm and 2 mm larger for larvae and juveniles respectively. April simulations show that inclusion of sea ice algae makes larvae on average 4 mm larger and juveniles 2 mm larger. The difference becomes 5 mm for larvae and 1.5 mm for juveniles during the May simulation.

3.3.3 Austral winter release at station 516

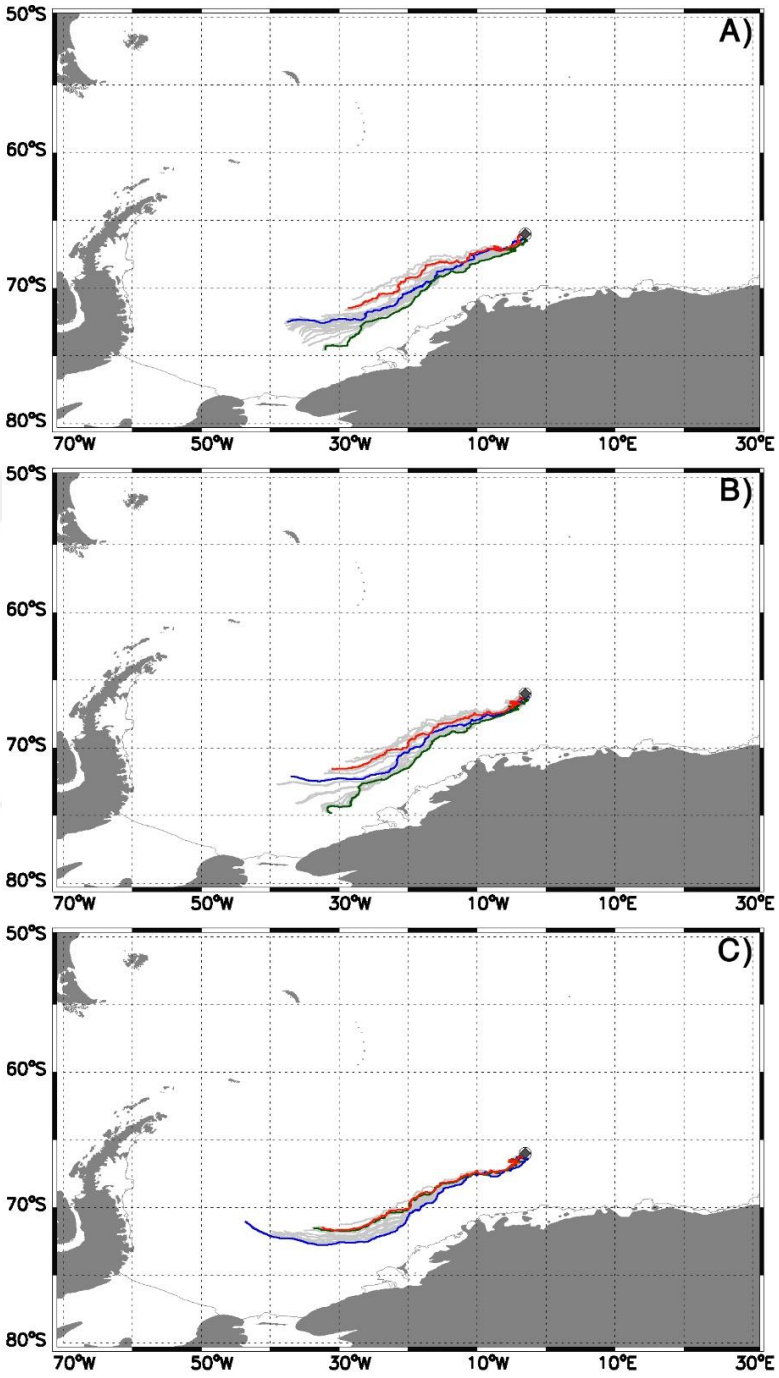


Figure 42 The one year-long Lagrangian particle trajectories of particles released from station 516. A) Particles released in June, B) July, C) August of 2006. The red, green and blue trajectories are the selected particles and represent the same particles in their respective food and IBM growth figures.

The Station 516 drifters (Figure 42) are released in austral winter from the Lazarev Sea. Particles flow westward and into the Weddell Sea, ending roughly between the 70S°S to 75°S latitudes, and 40°W to 30°W longitudes. Particles released on March (Figure 42A) and April (Figure 42B) have a similar dispersal pattern, while following the Antarctic Coast into the Weddell Sea, some of the particles flow from 68°S latitude away from the other particles, and other particles, such as the red particle, meander in the Lazarev Sea near the release point and thus remain in the Lazarev region (Figure 42A).

The particles released in May (Figure 42C) have a tight dispersal pattern, some particles, like the red particle, still meander and remain in the Lazarev region. Other particles that follow the Antarctic coast and flow into the Weddell Sea reach 49°W longitude and in the case of the blue particle, pass it.

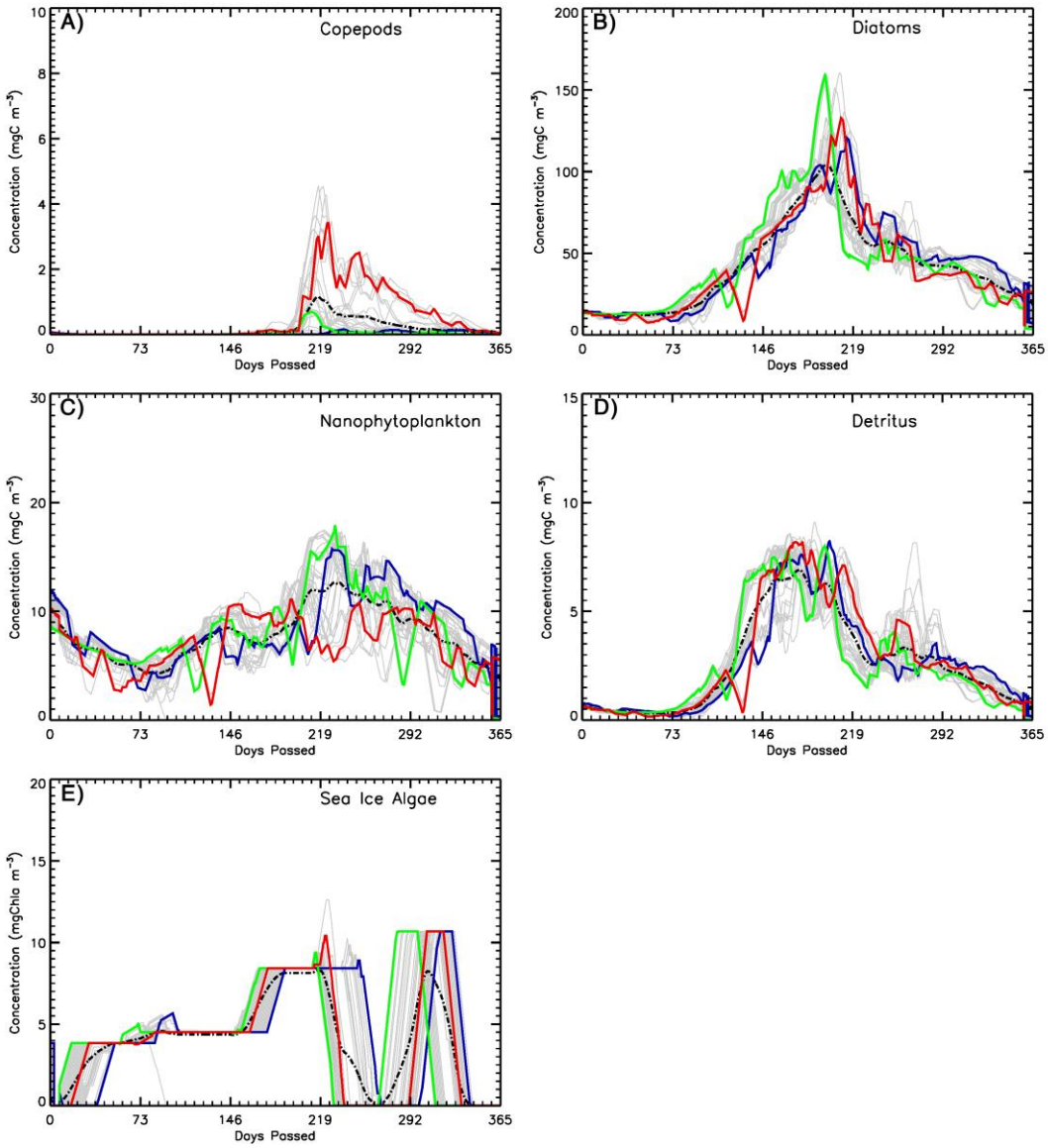


Figure 43 The food extracted along the drifter paths of particles released from Station 516 in June 2006. A) Copepod concentration (mgC m^{-3}), B) Diatom concentration (mgC m^{-3}), C) Nanophytoplankton concentration (mgC m^{-3}), D) Detritus concentration (mgC m^{-3}), E) Sea ice algae concentration (mgChla m^{-3}). The red, green, blue marked lines are the food extracted along the same colored particle trajectories in Figure 42A.

Station 516 June particles are released from June 1st until June 30th, day 73 marks August, day 146 marks October and day 219 Marks January. The copepod concentration (Figure 43A) starts with a zero average concentration until day 219, where the average concentration increases to 0.5 mgC m^{-3}. By day 292 the average

copepod concentration shows a decreasing trend down to 0.1 mgC m^{-3} by day 292, afterwards the average reaches zero on day 365.

The diatom concentration (Figure 43B) starts with 30 mgC m^{-3} average and has an increasing trend until day 219 where the average reaches 100 mgC m^{-3}. The diatom concentration has a steady declining trend down to an average of 40 mgC m^{-3} by day 292 then down to 20 mgC $m^{-3}2$ at day 365.

The nanophytoplankton concentration (Figure 43C) starts with an average of 10 mgC m^{-3} and decreases down to 4 mgC m^{-3} by day 73, then the trend starts increasing with fluctuations until day 219 where the average reaches 13 mgC m^{-3}. The concentration averages at 9 mgC m^{-3} until day 292 then starts declining towards 4 mgC m^{-3} at day 365.

Detritus concentration (Figure 43D) starts with an average of 0.5 mgC m^{-3} then has an increasing trend, by day 146 the trend fluctuates with an average of 5.5 mgC m^{-3} then starts decreasing down to 3 mgC m^{-3} by day 219. The average concentration drops to 2.5 mgC m^{-3} around day 219 then continues the decreasing trend to 0.5 mgC m^{-3} by day 365.

The sea ice algae concentration (Figure 43E) starts at zero average but has an increasing trend and reaches 4.5 mgChla m^{-3} by day 73 and holds this average until day 146, after that average increases to 8.5 mgChla m^{-3} and remains at this value until day 219. The average drops to zero after day 219 and then briefly increases back to 8 mgChla m^{-3} at day 292 after which the average drops to zero before day 365.

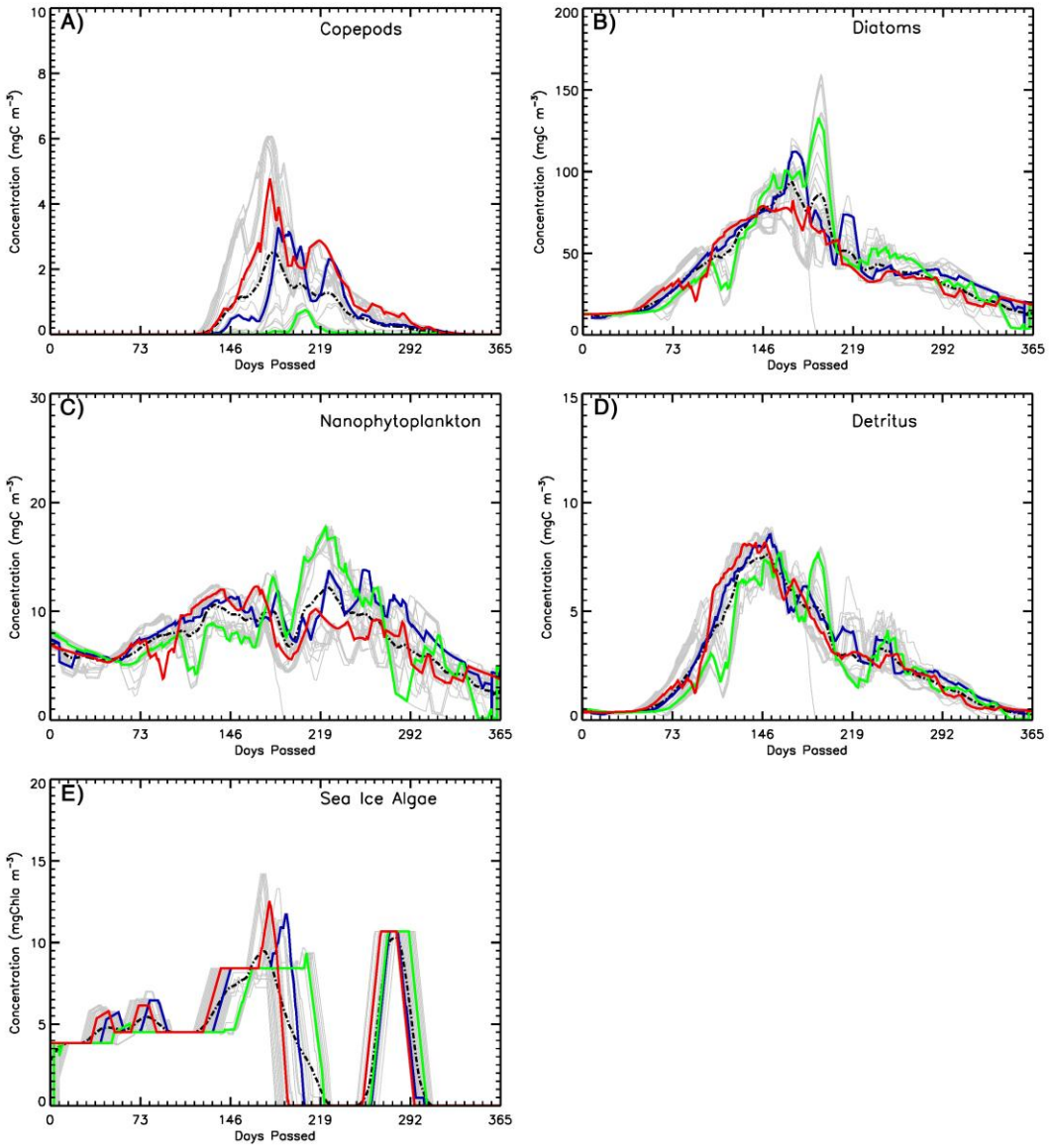


Figure 44 The food extracted along the drifter paths of particles released from Station 516 in July 2006. A) Copepod concentration (mgC m^{-3}), B) Diatom concentration (mgC m^{-3}), C) Nanophytoplankton concentration (mgC m^{-3}), D) Detritus concentration (mgC m^{-3}), E) Sea ice algae concentration (mgChla m^{-3}). The red, green, blue marked lines are the food extracted along the same colored particle trajectories in Figure 42B.

The station 516 July particles are released from July 1st until July 30th, day 73 marks September, day 146 marks September, day 219 marks February and day 292 marks April. Copepod concentration (Figure 44A) starts with an average of zero, which starts to increase after day 146, reaching 2.6 mgC m^{-3} then decreases down to 1 mgC

m^{-3} by day 219 and keeps decreasing down to 0.2 mgC m^{-3} at day 292 and eventually reaches zero again before day 365.

The diatom concentration (Figure 44B) average starts at 12 mgC m^{-3} and has a steady increase trend until after day 146 where it reaches 90 mgC m^{-3} and starts a decrease trend until day 365 where the value once again drops to 12 mgC m^{-3}.

Nanophytoplankton concentrations (Figure 44C) average at 7 mgC m^{-3} at the start and shows a slight increase trend until day 146 where the value reaches 10 mgC m^{-3}, the average fluctuates between days 146 and 219 reaching as high as 11 mgC m^{-3}, afterwards the trend starts to decrease and drops to 2.5 mgC m^{-3} at day 365.

The detritus concentration (Figure 44D) average starts with 0.5 mgC $m^{-3}$and remains steady until day 73, where the trend starts to increase, by day 146 the trend reaches 7.5 mgC m^{-3}, afterwards the trend starts decreasing back down to 0.5 mgC m^{-3} by day 365.

The sea ice algae (Figure 44E) is encountered with an average of 3.5 mgChla m^{-3} and steadily increases to 5.5 mgChla m^{-3} by day 73, the concentrations fluctuates down to 4 mgChla m^{-3} but by day 146 starts to show an increasing trend and reaches 9.5 mgChla m^{-3} then declines sharply down to zero by day 219. A brief concentration averaging at 11 mgChla m^{-3} is encountered by day 292, afterwards the average drops to zero by day 365.

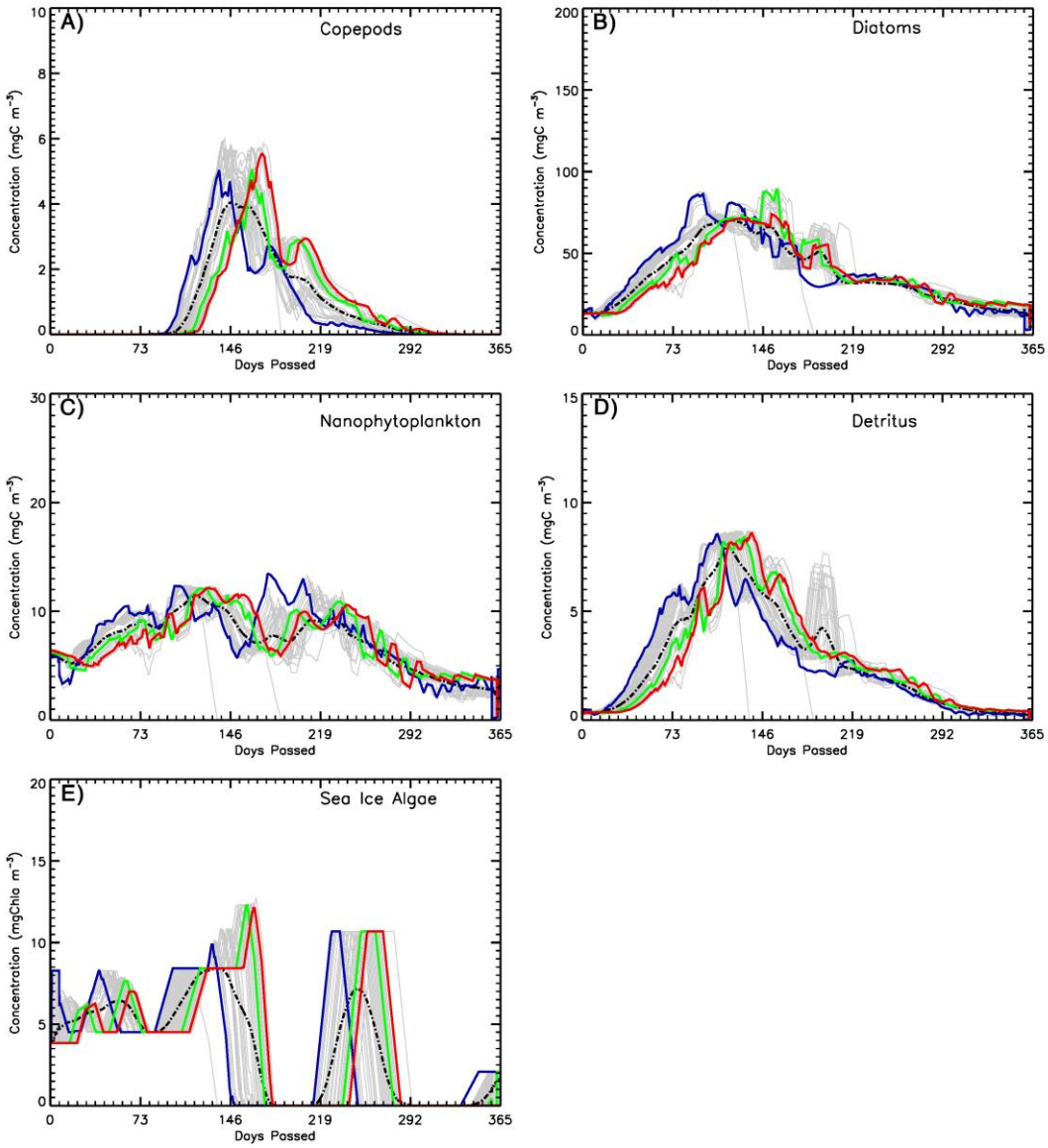


Figure 45 The food extracted along the drifter paths of particles released from Station 516 in August 2006. A) Copepod concentration (mgC m^{-3}), B) Diatom concentration (mgC m^{-3}), C) Nanophytoplankton concentration (mgC m^{-3}), D) Detritus concentration (mgC m^{-3}), E) Sea ice algae concentration (mg Chla m^{-3}). The red, green, blue marked lines are the food extracted along the same colored particle trajectories in Figure 42C.

Station 516 August particles are released from August 1st until August 31st. Day 73 corresponds to October, 146 to December, 219 to March and 292 to May. The copepod concentration (Figure 45A) average starts from zero and after day 73 starts

increasing and reaches 3.8 mgC m^{-3} peak by day 146, then the trend starts to decrease and drops to zero again after day 292.

Diatom concentrations (Figure 45B) start with an average of 15 mgC m^{-3} and shows an increasing trend until day 146 with a peak of about 65 mgC m^{-3}, the trend starts to decrease afterwards back down to 15 mgC m^{-3} by day 365.

The nanophytoplankton concentration (Figure 45C) averages at 6 mgC m^{-3} and shows an increasing trend up to 11 mgC m^{-3} then the trend fluctuates until day 219, afterwards a decrease trend drops the average to 3 mgC m^{-3}.

The detritus concentration (Figure 45D) starts with an average of 0.5 mgC m^{-3} increasing to 8 mgC m^{-3} between days 73 and 146. After the peak the trend decreases steadily with brief fluctuations until day 365 where it drops back down to 0.5 mgC m^{-3}.

Sea ice algae concentrations (Figure 45E) start at 4 mgChla m^{-3} average, fluctuating to 6.5 mgChla m^{-3} by day 73 then down to 4.5 mgChla m^{-3}. The trend starts increasing by day 146 and it peaks to 8.5 mgChla m^{-3}, afterwards it starts decreasing and reaches zero. After day 219 a brief concentration averaging at 7 mgChla m^{-3} is encountered then drops to zero afterwards. By day 365 the concentration starts to increase again to a 1.5 mgChla m^{-3} average.

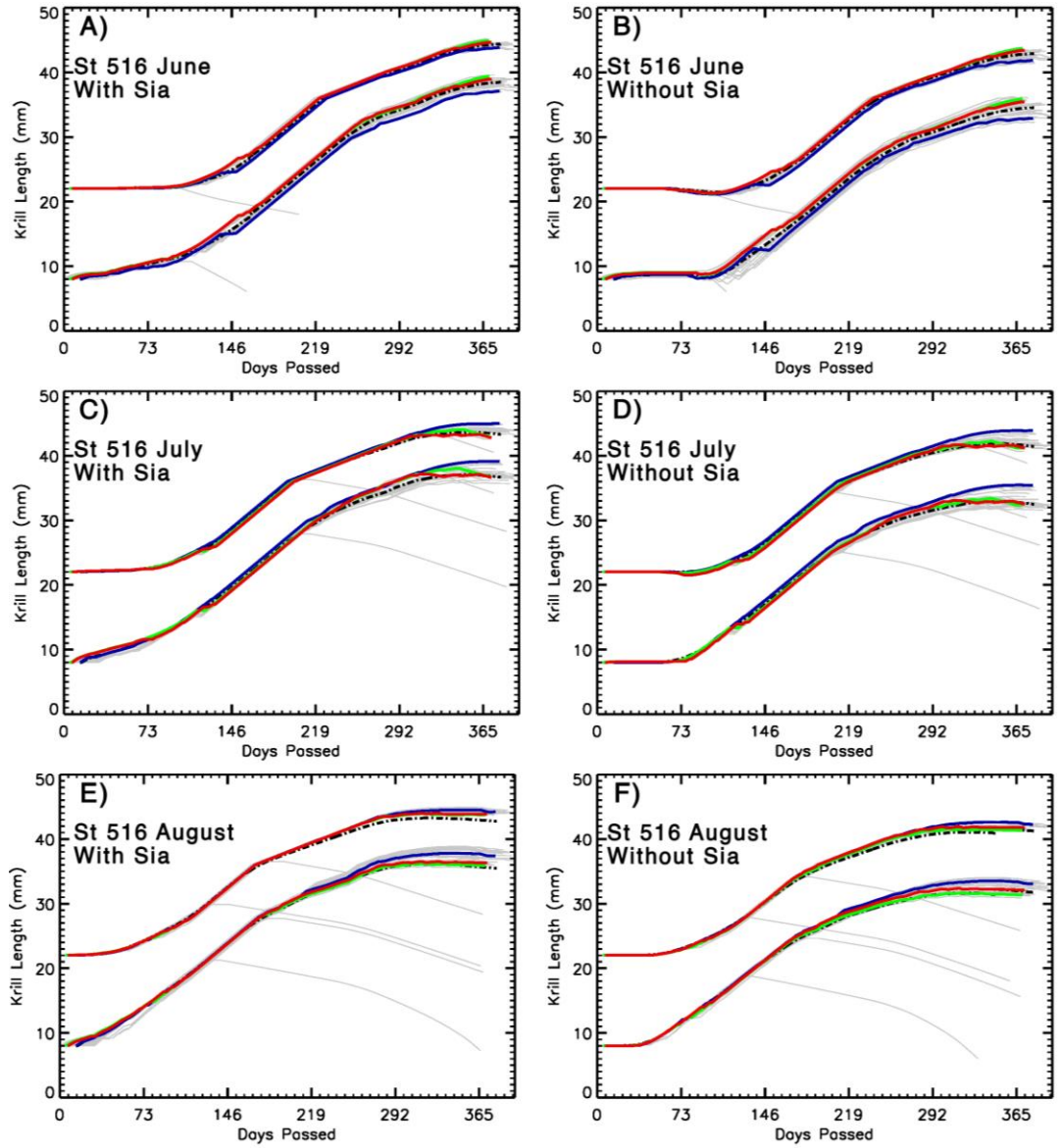


Figure 46 Krill growth figures for station 516 A) June of 2006 with sea ice algae, B) June of 2006 without sea ice algae, C) July of 2006 with sea ice algae, D) July of 2006 without sea ice algae, E) August of 2006 with sea ice algae, F) August of 2006 without sea ice algae. Juveniles start growth from 22mm, larvae start growth from 8mm. The red, green, blue marked lines are the food extracted along the same colored particle trajectories in Figure 42 and the black dash dot dash line indicates the average of all the surviving particles. Every particle has been given the day offset on the x-axis to their respective starting date on the month and the average line has been given a 15 day offset.

Simulations that are run with the inclusion of sea ice algae starting in June (Figure 46A) initially start with an increasing growth trend for larvae, reaching 20 mm of length by day 146, meanwhile the juveniles start with very little initial growth but the trend starts to increase by day 100 and the average juvenile length reaches 30 mm of length. Afterwards the trend of increase slows down, from day 219 the larvae reach from 25 mm to 38.5 mm until day 365, and the juveniles grow from 35 mm to 44.5 mm in length. The blue particle in the larvae simulation manages to surpass the average growth by 1 mm, the red particle grows nearly identical to the average trend and the green particle drops below the average by 1.5 mm. During the juvenile simulations, the red, green and blue particles mostly follow the average krill length and all end up 1 mm within each other in terms of length.

For simulations started in July (Figure 46B), the larvae show an initial increasing growth trend whereas the juvenile growth is steadier. Both classes of krill show a faster growth after day 73, and by day 219 the trend slows down. The larvae manage to grow from 8 mm to 27 mm by day 219 and juveniles grow from 22 mm to 37 mm. By day 365 the larvae reach an average length of 36.5 mm and juveniles reach 43.5 mm. The larvae simulations show the red, green and blue particles mostly following the average trend but start diverging after by day 292 where the green particle grows 2 mm above the average, the red particle nearly identical to the average and the blue about 1 mm below the average. The juvenile simulations have a similar pattern, the three particles follow the average length and by day 292 start to diverge with green particle staying 2 mm above the average, red particle 1 mm above and the blue particle 1 mm below the average.

The August simulations (Figure 46E) for both larvae and juvenile show an increasing trend by day 73. Both classes of krill show the trend slow down by day 219 where the larvae are at 30 mm and juveniles are at 38 mm in length. By the end of the simulation the average growth slows down and larvae reach 35.5 mm and juveniles reach 42.5 mm in length. The larvae simulation shows the red, green and blue particles starting to diverge from the average by day 292 and at the end of simulation all remain above the average with 1 mm divergence from each other. The juvenile

simulation also has the colored particles diverge by day 292 with all three above the average with 0.5 mm divergence of length from each other.

The simulations done without sea ice algae show that krill growth for June particles (Figure 46B) initially show an average of 0.5 mm growth in length for larvae while juveniles remain at 22 mm average length. By day 146 the average length starts to increase and reaches 35 mm for larvae and 43 mm for juveniles by day 365. The red particle starts following the average but after day 73 starts shrinking and deceases. The green particle follows the and finishes 1 mm smaller than the average for larvae and 0.5 mm smaller for juveniles, whereas the blue particle, grows larger than the average by 1 mm for larvae and 0.5 mm for juveniles.

The July particles (Figure 46D) start with a steady average of 8 mm and 22 mm, after day 73 the average trend starts increasing and reaches 32.5 mm and 41.5 mm in length. The red particle in both cases starts declining around day 219 and is deceased before day 365. The blue and green particles both follow the average, where the blue particle ends up 3 mm larger and green particle 0.1 mm smaller than the average at the end.

August particles (Figure 46F) remain at their starting length until day 73 and show an average increasing trend where they reach 31.5 mm and 41 mm at the end. The red particle starts shrinking by day 146 and is deceased before day 365. The green and blue particle follow the average and by the end the green particle for larvae is 0.5 mm smaller, for juveniles is the same as the average and the blue particle for larvae is 0.5 mm larger, while the blue particle for juveniles is 1 mm larger than the average.

Comparing the simulations done with and without sea ice algae, shows that each month has a similar growth curve shape in both with and without sea ice algae cases. However the averages at the end show that in June larvae grows 4 mm and juveniles grows 1.5 mm larger when using sea ice algae. July averages show larvae growth increase by 3.5 mm and juvenile growth increase by 2 mm. Finally the August averages show that larvae length increases by 4 mm and juveniles by 2.5 mm.

3.3.4 Recruitment success

The recruitment success of larval and juvenile krill transported in the Lazarev Sea is investigated calculating the percent of krill that survives the year-long transport (Figure 47). This also gives an indication of the seasonal mortality of larvae and juveniles.

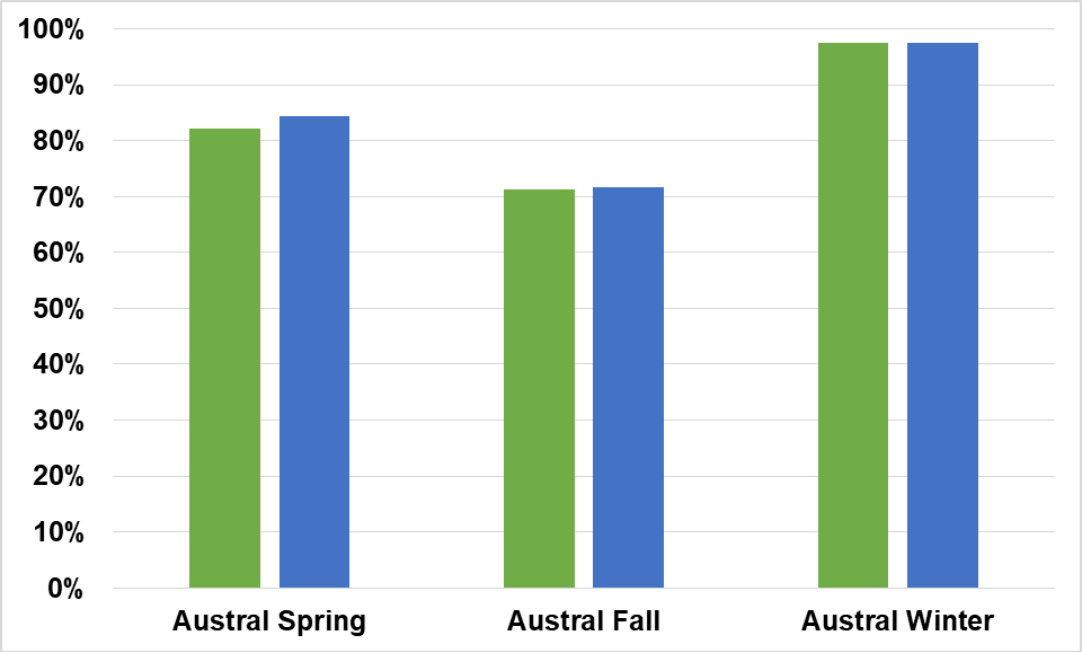


Figure 47 Simulated krill recruitment per season without sea ice algae. The green bar indicates the recruited larvae and the blue bar the recruited juvenile krill.

The seasons are corresponding to the stations as detailed above in (Figure 10), as well as in Chapter 3.1.3 Fate of krill released at selected stations in the Lazarev Sea. In total, for austral spring 460 particles, for austral fall 368 and for austral winter 276 particles were used to simulate krill survival. Highest survival rates for the IBM simulations without krill feeding on sea ice algae (Figure 47) were in austral spring when a total of 82.2% of larvae survived to recruit into the population and only 17.8% larvae died. For juvenile krill 84.3% krill survived the transport and only 15.7% died. In austral fall larvae recruitment of was 71.2% and mortality 28.8%, the juvenile recruitment was slightly higher with 71.3% and mortality is of 28.7%.

Finally in austral winter larvae and juvenile recruitment both is at 97.5%, which is rather surprising.

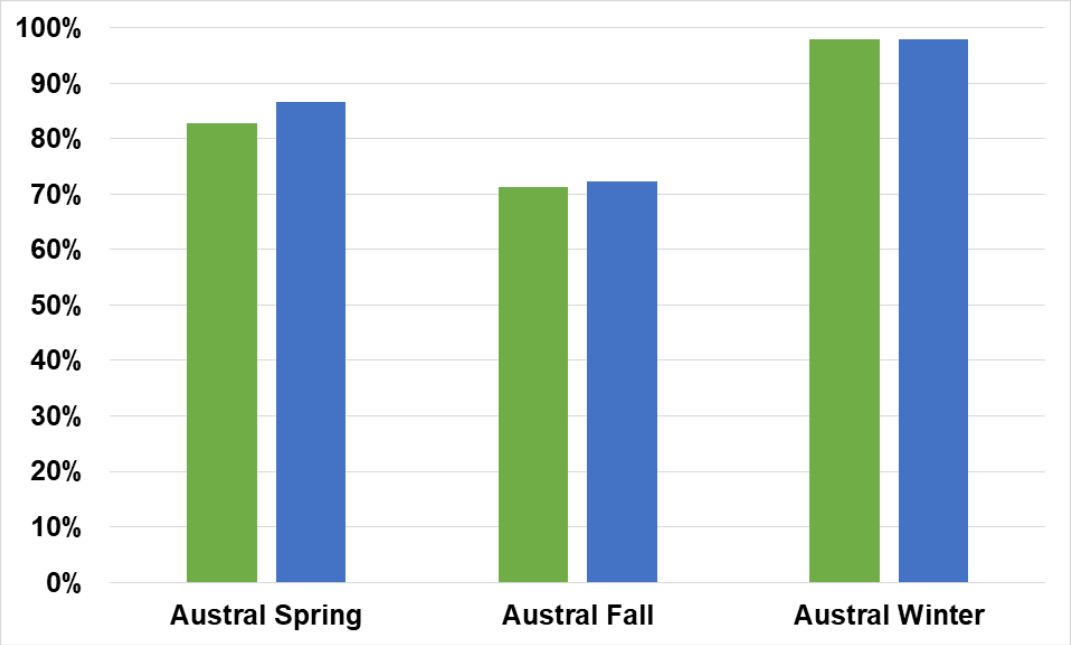


Figure 48 Simulated krill recruitment per season with sea ice algae. The green bar indicates the recruited larvae and the blue bar the recruited juvenile krill.

With sea ice algae food is made available for krill larvae and juveniles, the recruitment rates (Figure 48) in austral spring increase to 82.8% for larvae and 86.5% for juveniles. In austral fall larvae recruitment remains at 71.2% while the juvenile recruitment increases to 72.3%. Finally, austral winter recruitment success is increased to 97.8% for both larvae and juveniles, showing that feeding on sea ice algae is an important factor influencing growth and survival of both larval and juvenile krill, with larval krill benefitting slightly more from this food.

3.4 Simulations of adult krill growth success and reproduction in the entire Lazarev Sea

The drifter paths of the twelve separate Lagrangian particle tracking simulations performed on 2041 particles each, released in the entire Lazarev Sea as described in section 2.4.1.1, have been used to now simulate the growth of adult krill and their

ability to successfully spawn in the Lazarev Sea. The growth of krill in terms of length is plotted, and the relative growth success of each particle analyzed.

Any Lagrangian particle tracking results that ended before 200 days of simulation were filtered out of the analysis, as the inclusion of particles with less simulation days may include additional mortality to the results. This filtering process filtered 2716 of the total 24,492 particles, leaving 21,776 particles to be analyzed. Not all twelve simulations are shown here, but rather six simulations of krill released in the middle of November 2004 and 2005, the middle of December 2004 and 2005, and the middle of January 2005 and 2006 were chosen to represent the difference in spawning time during one entire spawning season. The results of the remaining simulations can be found in the Appendix C.

3.4.1 Adult krill growth

The simulations are once conducted with turning off the capacity to reproduce in the krill IBM mode and then another time with enabling reproduction. This is to elucidate the effect the energy expenditure of spawning has on the adult krill in the Lazarev Sea and in which region most successful spawning could be observed. To be able to measure the relative growth success of adult krill after a yearlong simulation, the surviving number of krill are compared within the same simulation. The average length of the whole simulation is calculated and plotted as a black dash dot dash line on the simulation growth results (Figure 49). The maximum length and minimum length at any given timestep through the simulation are also calculated and then plotted as blue and red dotted lines respectively. Further, the midpoint between the average length of the simulation and the maximum/minimum is calculated (green dotted lines) marking the areas of above average, average and below average success. The analysis determines that krill length at the end of each simulation that are above the upper middle point line are considered as experiencing above average growth, the ones that end between the upper and lower middle point lines are experiencing

average growth, while the adults that end below the lower middle point line are considered to grow below average.

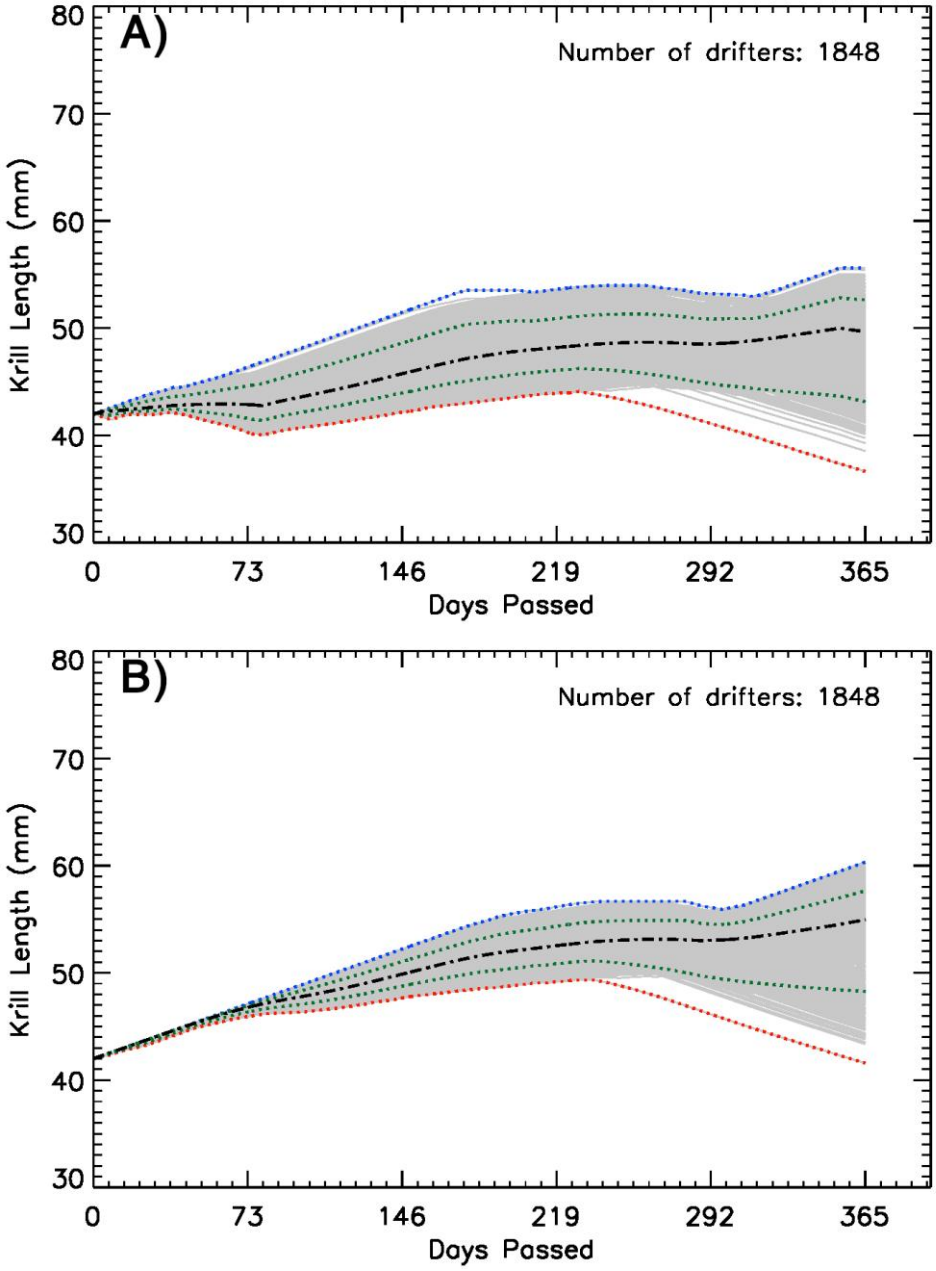


Figure 49 Adult krill growth (mm) of particles released on November 16, 2004. A) Simulation with reproduction enabled and B) with reproduction disabled. Black dash dot dash line represents the total average length of all krill, red dotted line represents the minimum length at a given timestep, blue dotted line represents the maximum length at a given timestep, green dotted lines are the middle point between the average and the maximum/minimum length at a given timestep.

The growth of adult krill released on November 16, 2004 with reproduction enabled (Figure 49A) shows the average length of krill remains 40 mm until day 80 as this is when the spawning season ends. Afterwards the average length starts increasing and reaches 47 mm by day 219. The increase trend slows down after day 219 then starts increasing again after day 292 and finally starts declining before day 365 with a final average length of 49.5 mm. The maximum length particle reaches 55.5 mm and the minimum length particle on reaches to 36.5 mm by the end of the simulation, meaning it decreased in size compared to its original adult size.

The comparison with the simulation where reproduction is disabled (Figure 49B), shows that the average length increases from the beginning of the simulation on because no resources are used for spawning. The average length reaches 47 mm by day 80, and keeps increasing until day 219 where the trend slows down but after day 292 it increases again 55 mm by the end of the simulation, 5.5 mm higher than in the reproduction enabled simulation. The maximum length is at 60.5 mm, 5 mm higher, and the minimum length is at 41 mm, which is 3.5 mm higher in comparison.

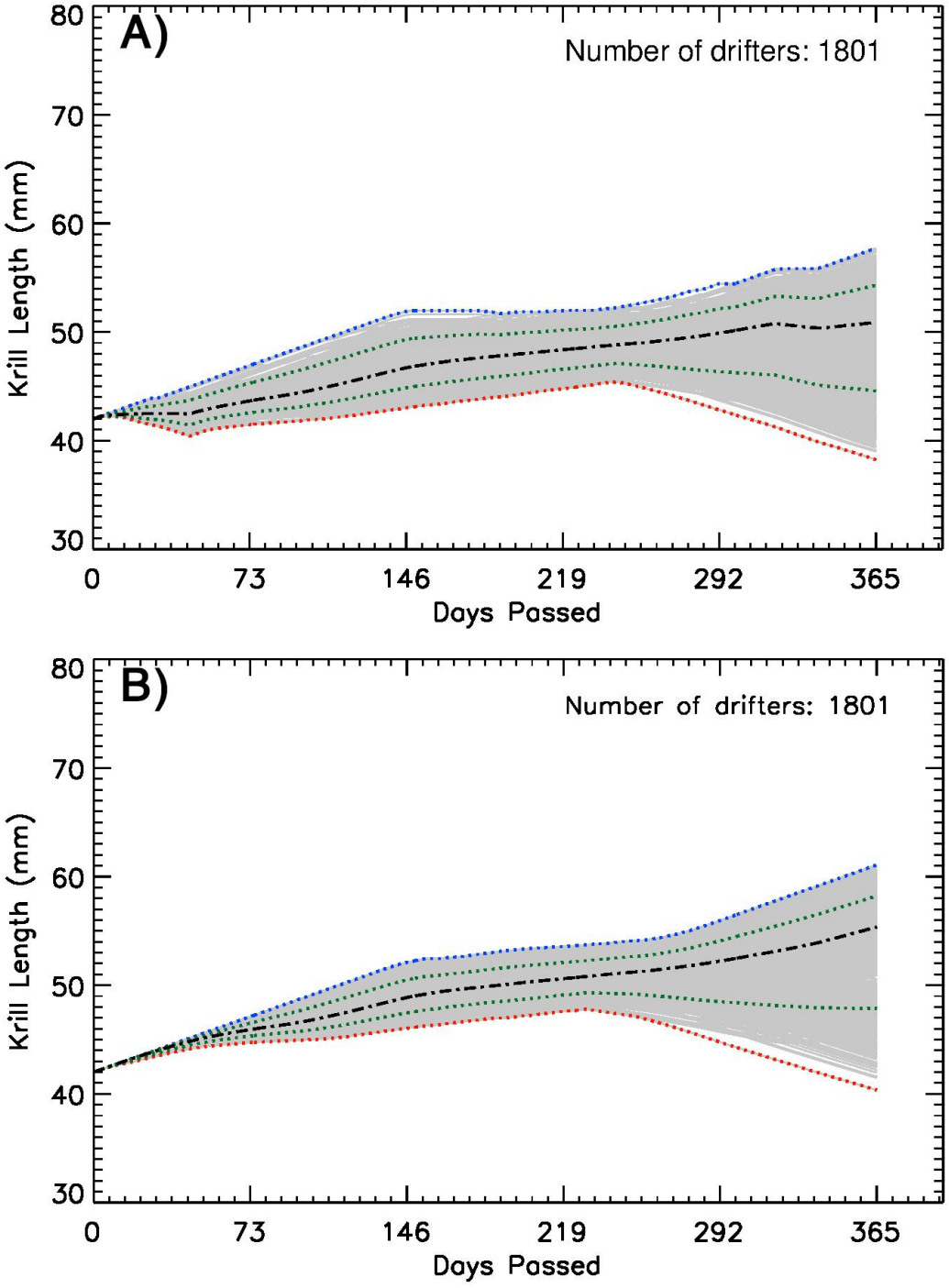


Figure 50 Adult krill growth (mm) of particles released on December 16, 2004. A) Simulation with reproduction enabled and B) with reproduction disabled. Black dash dot dash line represents the total average length of all krill, red dotted line represents the minimum length at a given timestep, blue dotted line represents the maximum length at a given timestep, green dotted lines are the middle point between the average and the maximum/minimum length at a given timestep.

December 16, 2004 that include reproduction (Figure 50A) shows the average length remain at 42 mm until day 50, afterwards an increase starts as then the energy of krill is not used up by reproduction anymore. Krill length continues to increase until day 320 after which the trend decreases then starts to increase back again before day 365. The average length reaches 51 mm, the maximum reaches 58 mm and the minimum drops to 38 mm at the end of the simulation.

The length development without reproduction (Figure 50B) shows average length to increase without slowing down throughout the simulation where the average length reaches 55.5 mm which is 4.5 mm higher, the maximum reaches 61 mm, 3 mm higher, and the minimum is 40 mm, 2 mm higher than in the simulation with reproduction.

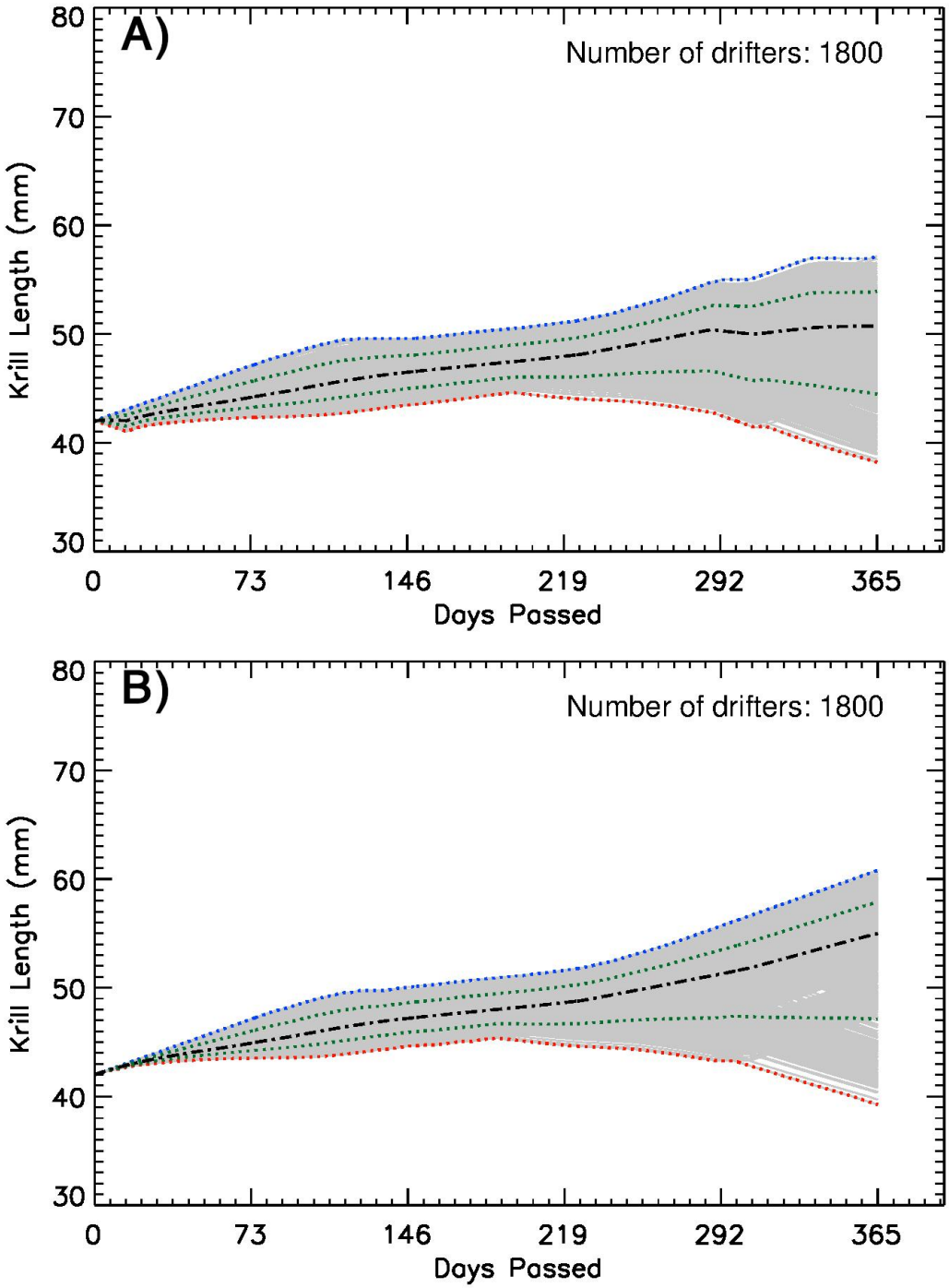


Figure 51 Adult krill growth (mm) of particles released on January 16, 2005. A) Simulation with reproduction enabled and B) with reproduction disabled. Black dash dot dash line represents the total average length of all krill, red dotted line represents the minimum length at a given timestep, blue dotted line represents the maximum length at a given timestep, green dotted lines are the middle point between the average and the maximum/minimum length at a given timestep.

The average length of krill within the January 1, 2005 simulation with reproduction enabled (Figure 51A) starts increasing at the start of the simulation until day 292 where the trend plateaus and reaches 51 mm of length. The maximum length reached is 57 mm, while the minimum length is 38 mm.

The simulation without reproduction enabled (Figure 51B) also shows an increasing trend of average length which gets stronger after day 292. The final average length is 55 mm, 2 mm higher, the maximum is 61 mm, 4 mm higher, and the minimum length is 39 mm, which is 1 mm higher compared to the simulation with reproduction enabled.

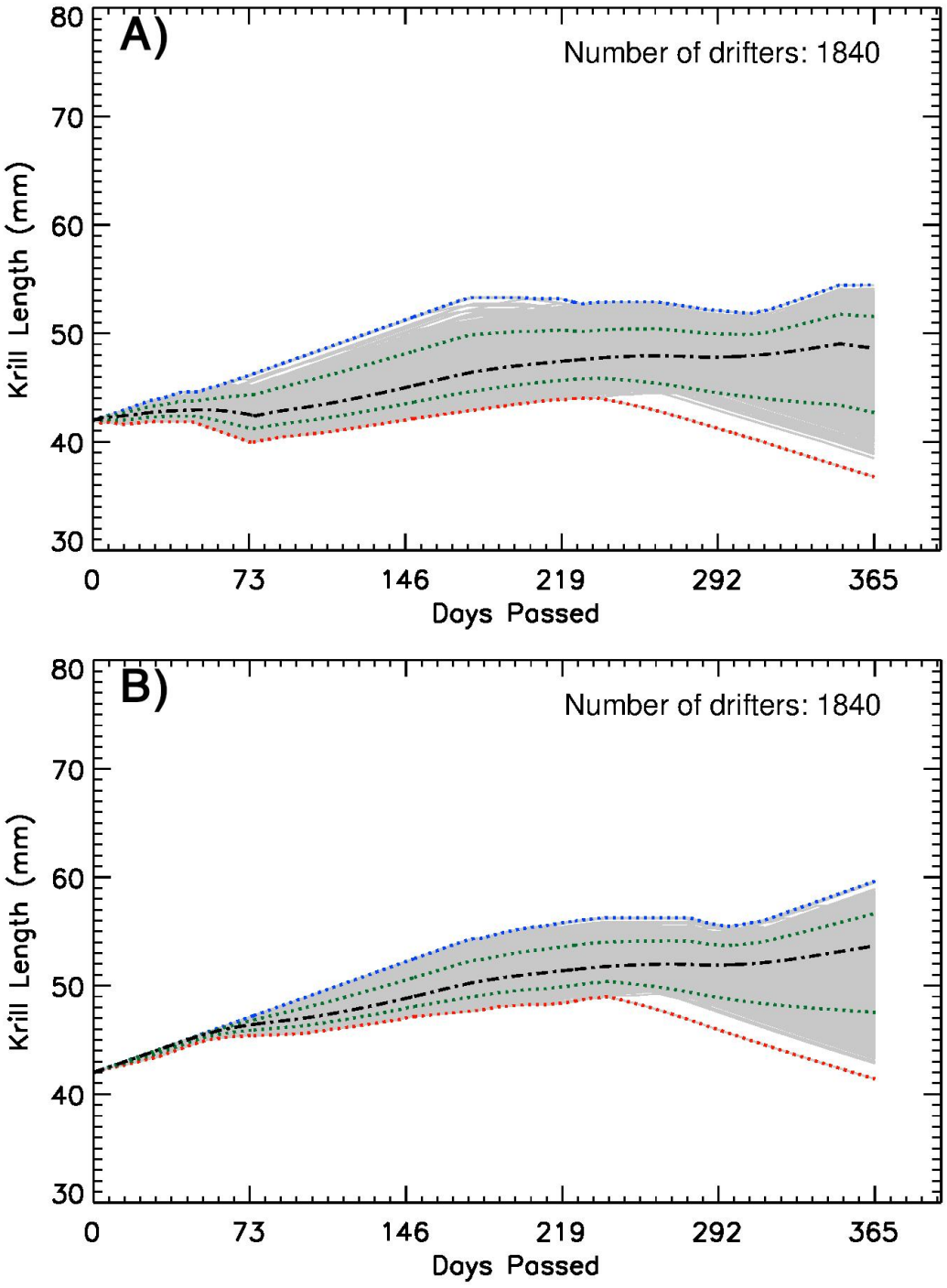


Figure 52 Adult krill growth (mm) of particles released on November 16, 2005. A) Simulation with reproduction enabled and B) with reproduction disabled. Black dash dot dash line represents the total average length of all krill, red dotted line represents the minimum length at a given timestep, blue dotted line represents the maximum length at a given timestep, green dotted lines are the middle point between the average and the maximum/minimum length at a given timestep.

The particles released on November 16 2005 with reproduction enabled (Figure 52A) show an initial average length at 42 mm until day 73 where it drops to 41.5 mm then starts increasing again. Just before day 365 length starts to decrease with the final average length at 49 mm, the maximum at 54.5 mm, and the minimum at 37 mm.

With reproduction disabled (Figure 52B) krill average length increases through the simulation and the final average length is 54 mm, 5 mm larger compared to reproduction enabled. The maximum value is at 60 mm, 5.5 mm larger, and the minimum is at 41 mm, 4 mm larger in comparison.

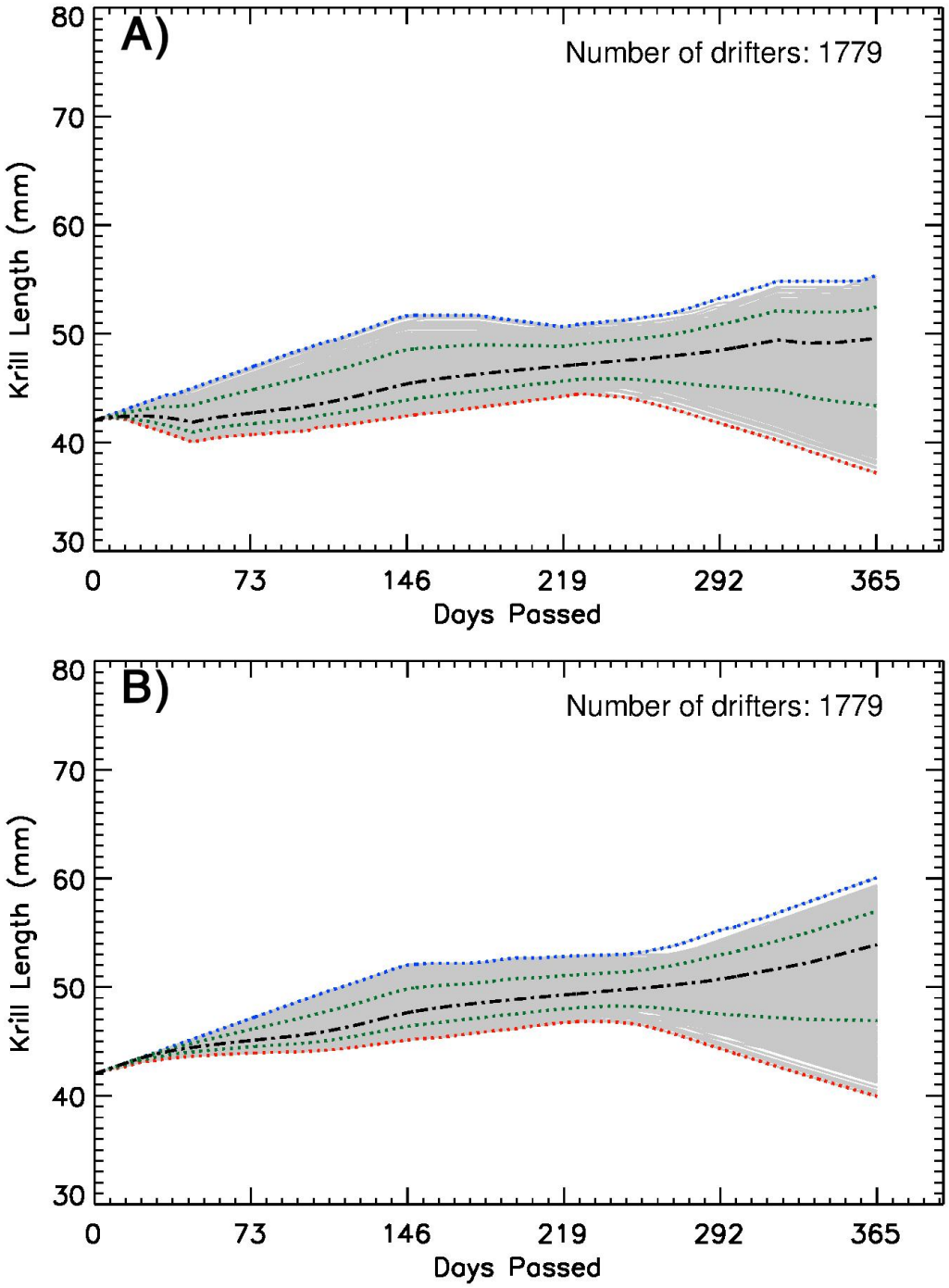


Figure 53 Adult krill growth (mm) of particles released on December 16, 2005. A) Simulation with reproduction enabled and B) with reproduction disabled. Black dash dot dash line represents the total average length of all krill, red dotted line represents the minimum length at a given timestep, blue dotted line represents the maximum length at a given timestep, green dotted lines are the middle point between the average and the maximum/minimum length at a given timestep.

The growth of the adult krill with reproduction enabled (Figure 53A) shows that the average length starts to decrease until day 60 in the simulation starting December 16, 2005, afterwards length starts to increase again. By day 310 the average krill length plateaus and the final average length is 49.5 mm, the maximum is 55.5 mm, and the minimum is 37 mm.

With reproduction disabled (Figure 53B) the average length starts with an immediate increase that lasts the entire simulation with a final average length of 54 mm, 4.5 mm higher in comparison. While the maximum is 60 mm, and the minimum is at 40 mm, 4.5 and 3 mm higher respectively.

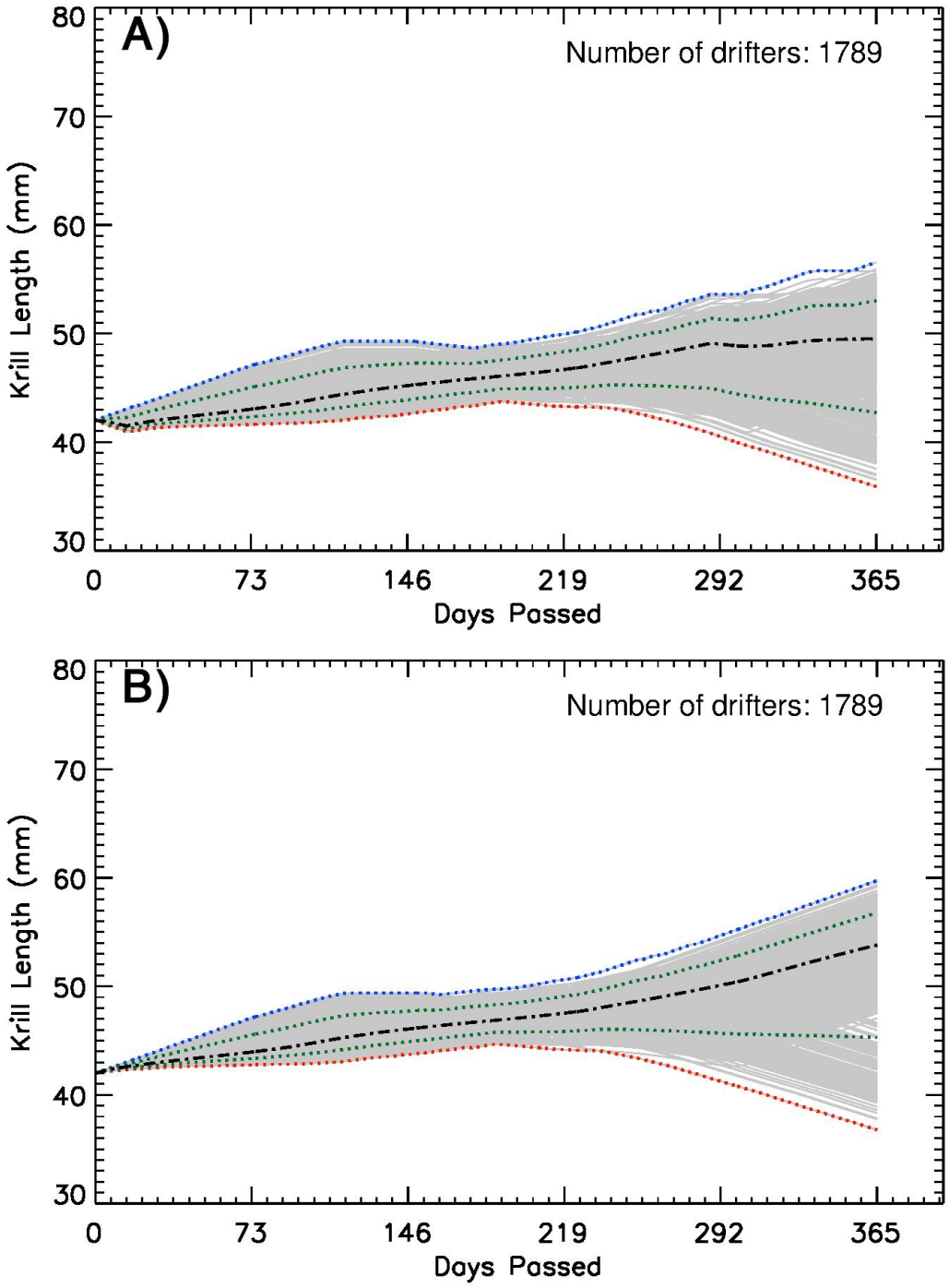


Figure 54 Adult krill growth (mm) of particles released on January 16, 2006. A) Simulation with reproduction enabled and B) with reproduction disabled. Black dash dot dash line represents the total average length of all krill, red dotted line represents the minimum length at a given timestep, blue dotted line represents the maximum length at a given timestep, green dotted lines are the middle point between the average and the maximum/minimum length at a given timestep.

Krill length is simulated to decrease slightly for the first 30 days in the January 2006 simulation including reproduction (Figure 54A) with the average dropping to 41 mm, after which length starts increasing until day 292 after which it only slightly increases more. At the end of the simulation the average length is 49.5 mm, the maximum 56.5 mm, and the minimum is 35.5 mm.

Without reproduction (Figure 54B), the average length of krill increases slightly and starts increasing more by day 73. The simulation ends with the average reaching 54 mm, 3 mm higher, the maximum at 60 mm, 3.5 mm higher, the minimum 37 mm, 1.5 mm higher than with reproduction enabled.

3.4.2 Spatial distribution of spawning

The above analysis showed great variability in the growth of krill length over the time frame of one year transport across the Lazarev Sea depending on the amount of food encountered by krill. The food encountered varies greatly spatially and to better understand which of the krill are doing better than other and if there is some form of spatial pattern in terms of where particles originate, the growth of krill were displayed in maps, marking each drifter release point to display which type of growth success was experienced. Hereby above average growth was marked in blue, average growth in green and below average growth in red, following the definition above.

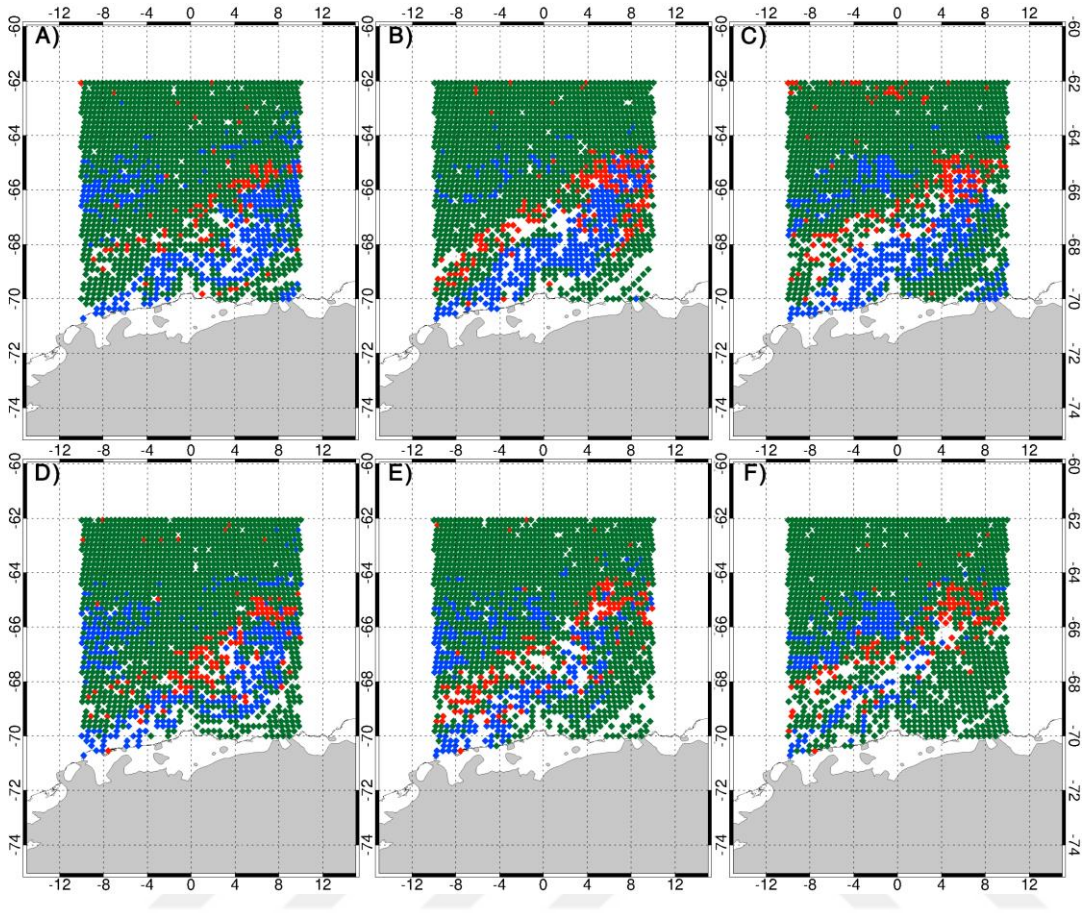


Figure 55 Starting locations of krill relative growth success. Krill experiencing above average growth in length (blue), average growth (green) and below average growth (red) in simulations starting in A) November 16 2004, B) December 16 2004, C) January 16 2005, D) November 16 2005, E) December 16 2005, and F) January 16 2006 For the November 16, 2004 simulation, the starting locations of particles encountering enough food to grow above average in length are distributed first a diagonal band from 10°W to 10°E and 72°S to 66°S with a patch located at 71°S and 9°E (Figure 55A). An additional patch is centered at 66°S and 8°W, and another band can be found at 64°S from 0° to 10°E. The below average particles are located on a band from 8°W to 10°E and 69°S to 65°S, the remaining below average particles are heterogeneously distributed amongst the other particles.

The distribution of the starting locations of particles released in mid-December 2004 (Figure 55B) show that above average growth particles are distributed again on a diagonal band, this time extending from 10°W to 10°E and 72°S to 66°S. The below

average particles are on a diagonal band from 69°S to 65°S and 10°W to 10°E, and on a vertical band from 69°S to 65°S at 8.5°E.

A similar pattern is seen for the particle distribution of the mid-January 2005 simulation (Figure 55C) showing that the above average distribution is on a diagonal band from 10°W to 10°E and 72°S to 66°S, with a crescent shaped distribution at 66°S and 6°W and also another patch located at 70°S and 8°E. The below average particles are distributed along the diagonal line from 68°S to 65°S and 8°W to 8°E and another line located at 62°S from 10°W to 0°.

Looking at the above average length particle distribution for the November 16, 2005 simulation (Figure 55D) again a diagonal band from 10°W to 10°E and 72°S to 66°S is seen, with a patch located at 67°S and 8°W and a line at 64.5°S and 4°E to 10°E. The below average particles are located on a diagonal band from 68°S to 65°S and 1°W to 9°E. The remaining above average and below average particles are found heterogeneously scattered in the region.

The December 16, 2005 particle distribution (Figure 55E) shows the above average growth particles on a diagonal band from 10°W to 5°E and 72°S to 66°S, with a patch located at 67°S and 8°W. A diagonal band from 68°S to 65°S and 1°W to 9°E contains the majority of the below average particles. Any remaining particles are found heterogeneously scattered on the area.

In the January 16, 2006 simulation (Figure 55F) the above average growth particles are starting from patches located at 70.5°S and 9°W, at 67°S and 8°W, and a third one at 66°S and 2°W. There is a diagonal band from 71°S to 68°S and 10°W to 0°. The below average particles are located along a diagonal band 68°S to 65°S and 10°W to 10°E. The other above average and below average particles are distributed heterogeneously.

Overall, the particles experiencing above average growth in all simulations are mostly starting simulations in this diagonal band stretching from the Antarctic

continent towards the northeast. Similarly, the below average growth are also found in locations that do not change dramatically from simulation to simulation.

3.4.3 Growth success of adult krill

Table 5 Percentage (%) distribution of growth success of particles including reproduction for each simulation

	Above Average	Average	Below Average
2004 Nov 1	16.52	79.75	3.73
2004 Nov 16	18.67	76.46	4.87
2004 Dec 1	13.86	79.02	7.12
2004 Dec 16	17.05	74.18	8.77
2005 Jan 1	18.26	74.82	6.92
2005 Jan 16	19.44	72.72	7.83
2005 Nov 1	13.23	81.94	4.83
2005 Nov 16	17.55	75.76	6.68
2005 Dec 1	18.25	75.62	6.12
2005 Dec 16	15.85	76.39	7.76
2006 Jan 1	17.64	74.67	7.69
2006 Jan 16	11.01	82.34	6.65

The distribution of growth success of particles from all simulations including reproduction shows that the November simulations contain above average length particles ranging from 13.23 % to 17.55 %, and below average particles from 3.73% to 6.68%. The above average particles for December simulations range from 13.86% to 18.25%, while the below average particles range from 6.12% to 8.77%. Finally, the January simulations show an above average length particles ranging from 11.01% to 19.44%. Simulations show there is no large variability between growth of krill between the different release months during the spawning season.

DISCUSSION

In this study, Antarctic krill dispersal and connectivity was studied in the Lazarev Sea and adjacent seas. The Lazarev Sea was chosen specifically, because previous studies in the Lazarev Sea concluded that this region does not support a single self-maintaining population but represents a complex transition zone of stocks with different origins, which are hypothesized to originate from other adjacent seas, possibly the Scotia Sea, where the Turkish Antarctic Station is located, or Cosmonaut Sea (Siegel, 2012). The motivation of this study was therefore to investigate the possible connection of Lazarev Sea krill with other Southern Ocean krill populations via ocean currents and find the population(s) supplying input the Lazarev Sea krill population.

The results produced by the FESOM-REcoM2 simulations were compared to and validated with a wide variety of data sets available on sea ice extend, chlorophyll concentration and its seasonal cycle, iron, copepod and plankton functional types distribution. The validation revealed that the FESOM-REcoM2 modeling system has some problems with accurately representing the mixed layer depth, which influences net primary production, however despite of that is well suited to model the Southern Ocean and does particularly well in resolving the region of the Scotia Sea, Weddell Sea and adjacent Lazarev Sea. The FESOM model has previously been applied and evaluated in various Southern Ocean studies (e.g., Downes et al. 2015; Downes et al. 2018; Farneti et al. 2015; Naughten et al. 2018) that have found its performance to be equally satisfying. The findings concerning the biochemical model Regulated Ecosystem Model (REcoM2) (Hauck et al., 2013; Schourup-Kristensen et al., 2014) agree with previous studies that have shown it is an ecosystem model that is suitable for large scale studies in the Southern Ocean (Schourup- Kristensen et al., 2014) as well as the Arctic (Schourup- Kristensen et al., 2018).

In the following sections the results of the three different analyses undertaken above in the Results section are discussed.

4.1 Connectivity vs retention of Lazarev Sea krill

The output of the FESOM-RecoM2 modeling system was used in this study as a tool to investigate krill connectivity with a Lagrangian particle tracking model and it was found that the currents in the Lazarev Sea are such that they facilitate connectivity with krill in the surrounding seas. However, the Lazarev Sea represents indeed a complex transition zone that can be explained as follows.

4.1.1 Fate of krill originating in the Lazarev Sea

Simulations of krill originating in the entire Lazarev Sea, from 10°W to 10°E and extending from the continent to 62°S (see section 3.1.1, Figure 18, Figure 19), show that after a one-year simulation 43% of the krill are retained within the Lazarev Sea region after a one year simulation. Specifically, 31% end up in the South Lazarev Sea and 12% reach the North Lazarev Sea, while only 2% of all particles are transported to the Northwest region. That means the remaining 55% of krill originating in the Lazarev Sea are transported to regions outside the Sea and are lost for the krill population recruiting in the Lazarev Sea. These krill mainly reach the Weddell Sea region (33%) of which 25% reach the South Weddell Sea via currents associated with the Antarctic Slope Front flowing westward along the Antarctic continent and 8% reach the North Weddell Sea, most likely with the currents associated with the easternmost part of the Weddell Gyre located north of the ASF. Overall, 22% of the particles are transported from the northern Lazarev Sea towards the north-west and are entrained into the ACC and then transported downstream towards the east in the direction of the Cosmonaut Sea in the south-west Indian Ocean. The percentage of drifters ending in each of the sink regions depending on spawning month (from November to January) show very little variation between spawning times for all regions.

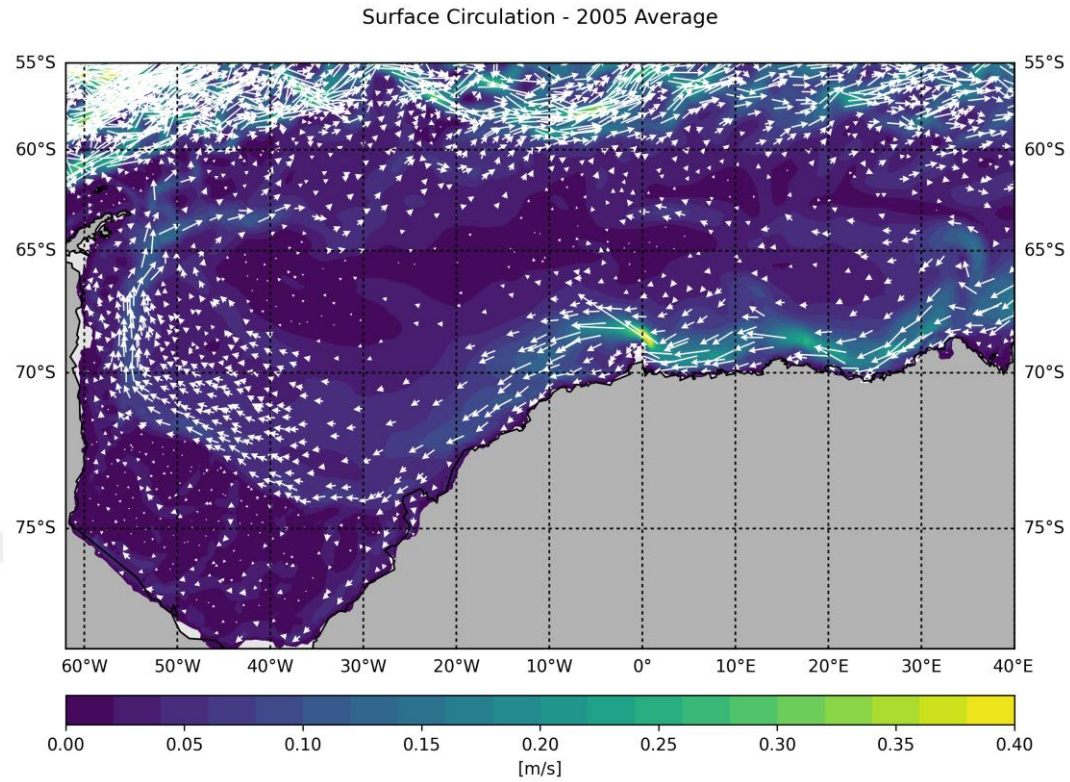


Figure 56 Average surface circulation in the study area for 2005 produced by FESOM

Overall, the Lazarev Sea displays a distinct spatial pattern where krill released in the northernmost region are transported north-eastward and are eventually entrained into the ACC and those released slightly further south below 63.5°S move into the North Lazarev Sea. Below this a small patch of drifters originating west of 2W is located that reach the Northwest region while below a diagonal band of particles end up in the North Weddell Sea and South Weddell Sea regions. Most particles released close to the Antarctic continent and even particles released as far north as 64°S in the eastern part of the release area are exclusively retained in the South Lazarev Region.

4.1.2 Source of Krill found in the Lazarev Sea

When looking at the source region for krill found in the entire Lazarev Sea, it is interesting to note that 60% of all drifters that end up in the eastern Lazarev Sea are

transported into the area from the Riiser Larsen Sea on currents associated with the eastern Weddell Gyre as well as the Antarctic Slope Front, while 39% originate from the North and South Lazarev Sea regions, and only 1% from Northwest and North Weddell Sea.

When investigating release of krill in different season at selected stations (section 3.1.3 Fate of krill released at selected stations in the Lazarev Sea) the results support above observations. As most of the stations are in the southern Lazarev Sea results show a common pathway of krill from the Lazarev Sea into the Weddell Sea, following currents associated with the ASF. But the further a particle is originating in the southeastern release zone of the region, the more likely it is to stay inside the Lazarev Sea.

4.1.3 Importance of Maud Rise

The calculated travel distances of simulated krill released in the Lazarev Sea at selected stations shows high variability in regard to the distance to station origin, where the austral winter release simulations show higher variance, travel furthest from their origin and have the highest mean total distance traveled exceeding 3200 km. The austral spring and austral fall release simulations show krill to stay closer to their station origins and have an overall less mean total distance traveled (1200 km). This combined with the trajectory, ending points and traffic data points towards frequent meandering near the station release points before flowing into their respective sink regions.

The analysis of the source of krill found at the selected stations simulations show krill move a maximum of 700 km distance to their point of origin, less than in the forward tracking simulations, and on average manage to travel more than 1000 km on their journey. This indicates increase meandering movement in the region near the sink station and consistently shows that particles arriving at these stations must have originated from within the Lazarev Sea itself. This increase retention in the area

is an aspect that is of specific interest in the context of this study and may be cause by the most prominent bathymetric feature in this region, Maud Rise. Maud Rise is a seamount situated at 3°E between 64°S and 66°S, where the seafloor rises to 1500 m. The interaction between the eastern extend of the Weddell Gyre and this topographic feature influences the regional circulation giving rise to mesoscale and submesoscale features that have implications for water mass transformation, biogeochemistry, sea ice dynamics, and connectivity (Holland, 2001; de Steur et al., 2007; Campbell et al., 2019;Våge et al., 2020). The obstruction of the eastward-flowing Weddell Gyre leads to the formation of both warm-core anticyclonic eddies and cold-core cyclonic eddies (Holland, 2001). These processes contribute to localized vertical mixing and enhance the vertical exchange between the deep and surface layers but also promotes the development of hydrographic fronts that are often associated with enhanced biological productivity due to localized nutrient enrichment (Campbell et al., 2019). Importantly, Maud Rise is also a zone of physical and biological retention. Warm-core anticyclonic eddies generated near the seamount can retain water parcels for weeks to months (Holland, 2001; Våge et al., 2020), creating favorable conditions for the persistence and growth of phytoplankton and potentially enhancing survival of planktonic larvae and krill. Regions of reduced mean current in the lee of the seamount further extend residence times, reinforcing retention effects. Krill have been found on the southern slope of the Maud Rise under thick ice formations (Brandt et al., 2011) along with a rich biota. Finally, Maud Rise is also causing Maud Rise Polynya events, that are large, recurring openings in the sea ice cover, which were observed extensively in the mid-1970s and during 2016-2017. These events are thought to result from the combined influence of topographically induced eddy activity, wind-driven ice divergence, and the breakdown of stratification, enabling deep convection in this region (Campbell et al., 2019).

4.1.4 Influence of vertical migration

The release depth of the particles were compared and trajectories were not identical but similar in pathways and the extent of drift, hence it is concluded that the release depth does not make a significant difference in investigating krill source and sink regions. This supports previous studies that the concluded daily vertical migration has minimal effect on the dispersal of the krill (Cresswell et al. 2007; Murphy et al., 2004; Pinones et al. 2013a) and can be neglected in connectivity studies of Antarctic krill.

4.1.5 Population structure of Lazarev Sea krill

Previous studies of krill in the Lazarev Sea suggested that this region does not support a single, self-maintaining population, but represents a complex transition zone of stocks with different origins (Meyer et al., 2010; Siegel, 2012), which are hypothesized to originate from other adjacent seas, possibly the Scotia Sea or Cosmonaut Sea in the south-west Indian Ocean. The analysis of Lagrangian particle simulations revealed that krill found in the Lazarev Sea originated 39% from the Lazarev Sea and 60% of krill are transported there from neighboring Riiser-Larsen Sea (Figure 1). This indicates that krill in the Lazarev Sea is indeed in part supplied by regions upstream from it though the transport takes place on a smaller scale, not from as far as the Cosmonaut Sea as suggested by Siegel (2012), at least not within one year. Particles from the Scotia Sea do not reach the Lazarev Sea in these simulations, as krill originating there are entrained into the ACC and transported eastward (Fach and Klinck, 2006; Fach et al., 2002) and the ACC moves along the north of the Lazarev Sea. At the same time a surprisingly high retention rate has been observed in the Lazarev Sea that is mainly facilitated by the interaction of Maud Rise with the eastern Weddell Gyre (Figure 1). It can be concluded that the hypothesis that krill in the Lazarev Sea is not a single self-maintaining population but influenced by different krill populations upstream should be revised to state that the Lazarev

Sea krill population is in part influenced by the Riiser Larsen Sea krill population while it is also able to maintain part of its population via retention in the area. It can be expected that interannual variability in currents structure may influence which of the two is more dominant in any given year.

These results complement previous Lagrangian studies in the Scotia Sea (Hofmann et al., 1998; Fach et al, 2002; Fach et al., 2006; Thorpe et al, 2007; Pinones et al., 2013a, 2013b) and the Ross Sea (Pinones et al., 2016), where similar transport distances were calculated as in this study. However, this study is the first to focus on the Lazarev Sea and the effect of current dynamics there. It also confirms the results of other studies that the Southern Ocean is a very dynamic environment where strong currents facilitate high exchange rates between areas far apart. The fact that krill in the Lazarev Sea is connected to the Weddell Sea in the west and the Riiser-Larsen Sea in the east, supports the idea that this is an area of transition for the Antarctic coastal region in this sector and mainly a gateway into the Weddell region. It also supports the theory that is possible that krill is in fact connected all around the continent of Antarctica (Thorpe et al, 2007; Pinones and Fedorov, 2016) Genetic study by Shao et al., (2023) also states that krill in the Southern Ocean has no clear genetic population structure, which supports the notion of high circumpolar connectivity. However, the Lazarev Sea is special in that its dynamic current structure also facilitates a high amount of retention, even though the idea that an endemic krill population exists in the area was considered unlikely (Siegel et al., 2013a; Siegel et al., 2013b).

4.2 Larvae and juvenile growth and recruitment during long-distance transport

After investigating the connectivity of the Lazarev Sea krill population with other regions and establishing that long-distance transport of krill via ocean currents is indeed occurring, the next aim of this study was to investigate how environment and biological parameters, such as the food availability, and timing of transport influence

the growth and survival of krill during such a long-distance transport. To this end the krill IBM described above (Chapter 2.5 Krill Individual Based Model) was used to simulate the growth and survival of krill larvae and juveniles using the biochemical REcoM2 outputs extracted along simulated particle trajectories from selected statin locations as food sources, as well as the sea ice algae estimates derived from the FESOM outputs.

Food availability in the region differs from season-to-season, but is high enough to ensure the survival of the larvae and juvenile krill under most scenarios simulated in this study. Diatoms are the most dominant food for krill and are an abundant food source in the FESOM-REcoM2 simulations. They are likely to be over estimated by the model for the Lazarev and Weddell Sea regions as discussed in the validation section above by up to 1.4 mg m^{-3} depending on the region (Figure 5). A simulation with a more realistic diatom concentration would account for less survival of krill during simulations. Still, the release month of particles plays an important role in its survival. Particles representing krill that are released in March and April have the highest mortality rates while particles released in austral spring have better survival chances. There is variability in mortality depending on station location. For example, station 44, from which particles are released in spring, has higher mortality rates compared to the rest of the spring release stations (see Appendix B). In addition, mortality is also dependent on the release month such as in the case of the January particle release at Station 47 where this month has much higher mortality compared to particles released in other months at the same station (see Appendix B).

The surprisingly high winter survival for both classes of krill can be explained due to the high amount of food availability by the REcoM2 outputs. Population dynamics model study performed by Ryabov et al., (2023) has found that larval and juvenile losses decreases as the ice cover is increased which strongly suggest that both larvae and juveniles benefit from the cold winter seasons.

These simulations were undertaken for the release of krill at all of the 12 station locations in the Lazarev Sea and hence relate to the results discussed above.

To recall, all krill found during all seasons at those stations were shown to have originated within the Lazarev Sea itself, most likely influenced by the eddy dynamics observed in the greater Maud Rise area. However, the krill starting simulations from these stations were transported to the Weddell Sea (48%) or retained in the Lazarev Sea (51%) during a spring release, to the Weddell Sea (62%) or retained (31%) in fall release and transported entirely out of the Lazarev Sea in winter with 56% being entrained in the ACC and 43% transported to the South Weddell Sea.

During the long-distance transport towards the south-west Indian Ocean and when being retained in the Lazarev Sea, krill encounters sufficient food to survive and recruit into the population downstream of the Lazarev Sea. This is in agreement with data on the circumpolar distribution of Antarctic krill as compiled in KRILLBASE (Atkinson et al., 2009; Atkinson et al., 2019) that shows existing krill populations downstream of the Lazarev Sea, as well as a hotspot of krill in the Riiser Larsen Sea (Figure 57). However, krill moving towards the Weddell Sea encounter environmental conditions that make survival difficult for juvenile krill and larval krill to survive. Therefore, retention in the Lazarev Sea results in best growth rates for krill larvae, while long-distance transport in the currents of the ACC results in best growth rates for juvenile krill. Not much is known about the krill population in the Southern Weddell Sea due to the difficulty access the region (Figure 57), but krill are found in the Weddell Sea throughout the year, with seasonal shifts in distribution (Atkinson et al. 2009; Atkinson et al., 2019).

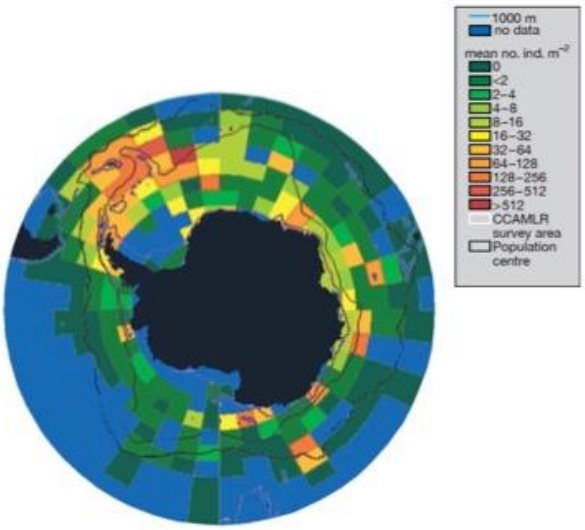


Figure 57 Circumpolar distribution of *Euphausia superba* based on standardized data from KRILLBASE plotted as arithmetic mean krill densities (individuals m^{-2}) of all stations within each 3° latitude by 9° longitude grid cell. Fronts shown in thin black lines (north to south) are the Antarctic Polar Front and the Southern Boundary of the Antarctic Circumpolar Current (Orsi et al. 1995). Reproduced from Atkinson et al. (2009)

It should be noted that as shown by Bahlburg et al. (2023), the selection of an individual-based growth model for Antarctic krill is critical, as each model type incorporates distinct assumptions, structural constraints, and sensitivities that directly affect growth projections. Their comparative analysis of eight models, including the Fach et al. (2002) IBM on which the IBM used in this study is based —ranging from empirical formulations based on observed chlorophyll and temperature relationships, to mechanistic models (Fach et al, 2002), Dynamic Energy Budget frameworks, and fully process-based physiological models— demonstrated that under identical environmental forcing, simulated growth trajectories can diverge in both magnitude and timing. Much of this variability stemmed from differences in how food availability was represented (e.g., satellite-derived versus in situ chlorophyll estimates), in combination with varying temperature dependencies and bioenergetic allocation schemes. This is the main reason why the current IBM was chosen for this study, as it is based on detailed observation from krill in the entire Southern Ocean and has been validated

extensively. This is particularly relevant in the context of the simulations results presented here, which show that food availability in the study region varies seasonally but is generally sufficient to sustain larval and juvenile krill under most scenarios. Model choice may therefore influence the magnitude of predicted growth and the inferred resilience of early life stages to seasonal variability in food supply. Applying multiple models, as recommended by Bahlburg et al. (2023), may foster a more robust assessment of how such seasonal changes translate into survival potential, thereby strengthening ecological inferences that link simulated krill transport and retention patterns to recruitment success. However, this kind of study is outside the scope of this thesis work.

4.2.1 Importance of sea ice algae food

The addition of the ice algae to the model has a noticeable effect on the krill growth rather than survival. When feeding on ice algae, the larvae benefit more than juveniles and grow about 4 mm larger, and juveniles benefit slightly less and grow about 2 mm larger in general. The observation that juveniles benefiting less from ice algae food than larvae is in agreement with other studies (Bernard et al., 2022; Walsh et al, 2020). Grazing on ice algae enables larvae to maintain metabolic activity, avoid depletion of lipid reserves, and increase survival until the onset of the spring phytoplankton bloom (Meyer et al., 2010). The timing and magnitude of sea ice algal production are therefore linked to krill recruitment success; years with extensive, long-lasting sea ice typically support higher overwinter survival of larvae and juveniles, whereas reduced ice extent or early break-up can result in food limitation and elevated mortality (Quetin and Ross, 2001; Flores et al., 2012). One drawback of the model used in the study is that it always assumes that the krill is constantly moving with the currents. Whereas in reality krill can attach to the underside of ice and keep feeding on an existing sea ice algae source. The extensive ice sheet located along the coast, especially in the Weddell Sea (Mueller and Timmermann, 2017), may provide an overwintering advantage to an existing krill population in the region.

The circulation pattern of the Weddell Region, with its cyclonic gyre along the coast flowing from the Lazarev Sea region (Muench and Gordon, 1992), supports a krill population inside the Weddell region itself in a full 365-day transport.

Given the krill's central role in Southern Ocean food web as a primary energy source for top predators such as baleen whales, seals, penguins and sea birds, and its contribution to vertical carbon flux through fecal pellet export (Belcher et al., 2019), the Lazarev Sea population's stability is critical for ecosystem functioning. However, recent trends in sea ice variability linked to climate-driven changes in atmospheric and oceanic circulation (Hattermann and Levermann 2009; Sylvester et al., 2025) pose significant threats to krill recruitment and larval survival in this region (Atkinson et al., 2019). Modelling studies and empirical observations suggest that reduced winter sea ice may lead to trophic mismatches and long-term biomass declines, emphasizing the need for enhanced monitoring and inclusion of the Lazarev Sea in integrated ecosystem management frameworks under the Convention for the Conservation of Antarctic Marine Living Resources (CCAMLR).

4.3 Adult krill IBM reproduction discussion

Across most simulations, the spatial pattern of growth success shows a distinct diagonal band of optimal conditions, bordered by adjacent regions where growth was consistently lowest. White areas, patches, or bands in the results correspond to particles excluded from the analysis due to tracking durations of less than 200 days. Such particles frequently entered or attempted to cross the model mesh boundaries, which encompass the Antarctic coastline. Although the Lagrangian particle tracking framework included a corrective algorithm to prevent boundary-crossing errors, this was limited to 150 iterations per particle to reduce computational cost. Once this threshold was exceeded, the particle was removed from the simulation.

When simulated in the individual-based model (IBM), these prematurely terminated trajectories would have represented individuals experiencing early mortality, mainly

due to the absence of food sources. Retaining them in the analysis would have biased growth estimates and hence were excluded. It was decided to exclude these particles because in reality adult krill can actively swim away from areas of persistent food scarcity and remaining stationary without feeding for extended periods would constitute unrealistic behavior.

These limitations highlight a potential shortcoming of this Lagrangian approach for simulating krill movement and survival. In nature, adult krill exhibit active swimming behavior that enables them to respond adaptively to environmental variability, including gradients in food availability, temperature, and predator presence (Murphy et al., 2004; Tarling and Thorpe, 2014). Incorporating such behavioral components into Lagrangian particle tracking frameworks—by coupling physical advection with movement rules based on both physical and biogeochemical cues—could reduce boundary artefacts, better capture avoidance of low-food areas, and more realistically reproduce observed spatial dynamics of krill populations (Fach et al., 2006; Hill et al., 2013). Behaviorally coupled Lagrangian models have been shown in other zooplankton studies to improve predictions of distribution and survival by allowing individuals to navigate toward favorable feeding habitats and away from unsuitable conditions, and similar implementations for krill could enhance ecological realism and predictive skill in future simulations (Thorpe et al., 2007; Bahlburg et al., 2023). However, including behavior in such models has also been proven to be rather complicated and computationally expensive.

The lack of mortality can be attributed to the filtering process of the particles mentioned above, however looking at the below average growth particles of the simulations shows that another 6 months of simulation would have most likely resulted in their mortality. Therefore the below average particles should be considered as at risk of mortality.

Implementation of the krill reproduction into the model enables the seasonal variation in krill growth. Any comparison to the simulations without reproduction

show that the average growth is always trending upwards, whereas the reproduction does add a seasonal decline and plateau effect.

There is a distinct diagonal shape in the release area where the above average growth particles are consistently located, and the below average particles located around those areas. Referring to the mean sink region of particles (Figure 58) where the diagonal pattern is located, shows the South Weddell and South Lazarev as the most likely sink regions for the above average and below average growth krill. The above average particle line at 66.5S° and 8°W has the likely sink area as in the North Weddell, and the patch located at 70°S and 9°E has the most likely sink area in the South Lazarev.

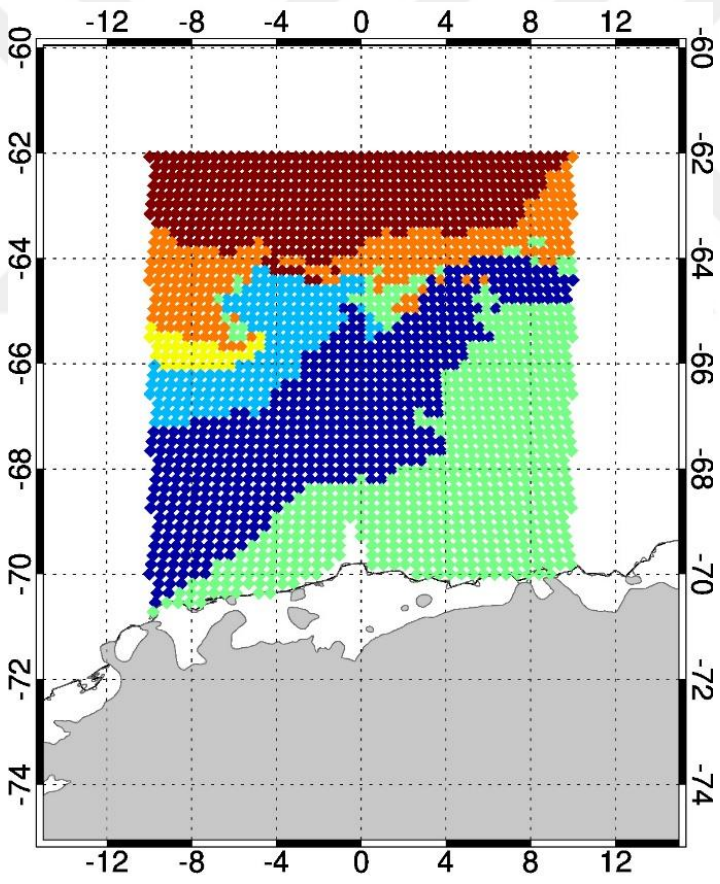


Figure 58 The mean spatial distribution of all 12 forward time tracked simulation particles. Colors mark the sink region: red - entrained in the ACC, orange - North Lazarev Sea, yellow - Northwest region, light blue - North Weddell Sea, dark blue - South Weddell Sea, and green - South Lazarev Sea.

It should also be noted that the area from 64°S to 66°S at 3°E where the Maud Rise is located, had the tendency to have a patch of below average particles located in its proximity.

Conroy et al., (2020) has found that female krill are more abundant on the continental shelf compared to the open coastal water, following with the implications for any spawned recruits and their interactions with the circulation and connectivity of the region.

4.4 Model uncertainties

The FESOM-REcoM2 version 1.4 model used in the study has been developed specifically for the Southern Ocean and has been validated extensively (Wang et al., 2014; Wang et al., 2018; Schourup-Kristensen et al., 2018), however there are some limitations of the FESOM model that are discussed here. One is the resolution of the mesh, which influences model performance. Even with a resolution of 4.5 km, a relatively high resolution for a global model, the model is not always eddy-resolving (Wang et al., 2014; Wang et al., 2018; Schourup-Kristensen et al., 2018) especially when the Rossby radius is small, between 1 to 15 km, such as in basins. FESOM can be configured to be eddy-resolving at ~0.1° or higher resolutions, but with increased computational cost (Wang et al., 2014), and also Sein et al. (2017) explore increasing the resolution with the FESOM model in order to ensure eddy are resolved and show that the ACC and most parts of the Southern Ocean are eddy resolved. Since eddies and fronts are one of the main transport and also retention mechanisms for krill, a lack of eddy reolution may lead to underestimated retention in certain areas,

The baratrophic stream function of the model causes weaker transport for the Weddell Sea ranging from 4 Sv to 20 Sv (Wang et al., 2014) compared to observations which can reach up to 29.5 Sv at the tip of the Antarctic Peninsula (Fahrbach et al., 1994) and 60 Sv at 0° longitude (Schröeder and Fahrbach, 1999). The relatively coarse mesh, thus coarser bottom topography, used in the region is the

reason for weaker transport (Wang et al., 2014). The diffusivity of the model is reported to be the highest in the Southern Ocean at 60°S and 130°W, reaching up to 1300 m^2s^{-1} of a 10 year mean at 300 m depth. This may be due to setting the lower bound of diffusivity to 0.2, which causes higher resolution areas with intense eddy activity to have higher diffusivity values (Wang et al., 2014). However the diffusivity for the study area, which contains the Weddell Sea and the Lazarev Sea, have low diffusivity, ranging from 100 to 200 m^2s^{-1} of a 10 year mean at 300 m depth and with zonal mean thickness diffusivity between the 80°S and 60°S ranging from 100 to 300 m^2s^{-1} (Wang et al., 2014). The Meridional Overturning Circulation (MOC) as simulated by the model slightly underestimates the strength of bottom water and intermediate waters compared toMazloff et al. (2010) with a maximum eddy MOC of 10 Sv (Wang et al., 2014).

Further, the Southern Ocean in FESOM version 1.4 has weak mixed layer depths (MLD) and shallow vertical mixing (Wang et al., 2014; Schourup- Kristensen et al., 2014) when compared to the observed data (de Boyer Montegut et al., 2004). The general MLD maximum difference can be up to 150 m shallower, with the exception of the Weddell Sea, which shows values of up to 450 m deeper but this is also a feature present in other Southern Ocean models such as Griffies et al. (2009). The overall Southern Ocean MLD has a 0.63 correlation compared to observational estimates. Shallower MLD can have the effect of less nutrient replenishment in winter by REcoM2 which can lead to the dominance of nanophytoplankton over diatoms in certain areas (Schourup- Kristensen et al., 2014). The surface chl a distribution of REcoM2 compared to satellite esimations (Schneider et al., 2008), show that for the Southern Ocean in general and in the study region, there is an overestimation of chlorophyll a of up to 0.7 mg chl a m^{-3} which results in a correlation coefficient of 0.57 with data (Schourup- Kristensen et al., 2014). The REcoM2 net primary production in the Southern Ocean is equal to 3.1 Pg C yr^{-1} with a correlation coefficient of 0.75 to available data (Schourup- Kristensen et al., 2014), these values are higher than the estimates of 2.6 Pg C yr^{-1} reported by Carr et al. (2006). Diatoms are reported to be responsible for 25% of the net primary production

in the Southern Ocean varying according to the iron distribution as simulated by REcoM2, for our specific study region, net primary production contribution of diatoms in the Weddell Sea range from 50% to 100% and in the Lazarev Sea range from 25% to 75%, overestimating the diatom values in the area (Schourup-Kristensen et al., 2014).

The Lagrangian Particle Tracking model was used to represent larvae as well as juveniles and adults' drifting behavior. While such drifting is feasible for larvae and juveniles, but adults are capabke of swimming in any direction they are able to choose, furthermore some of the mesh border interactions with the particles and computational time constraints led to some particles remaining stationary near the Antarctic coast mesh boundary. This indirectly led to these particles receiving less food compared to their moving counterparts and that led in some instances to eliminating those particles from at least the adult simulations. The amount of eliminated particles was 11.1% of the total particles simulated, in order to reduce or eliminate this percentage, the Lagrangian Particle Tracking code needs to be modified to resolve the mesh border interactions in a more accurate manner. Furthermore, the current model system is also incapable of simulating some of the sea ice and krill interactions such krill deciding to remain under a particular ice sheet for feeding purposes for an extended period of time.

4.5 Possible impact of Climate change

Cavanagh et al. (2021) states the risks to the Southern Ocean due to long term climate change includes, apart from rising water temperatures, the weakening of carbon uptake, changes in the circulation, acidification as well as retreating sea ice, reduced krill biomass related to the ice retreat and subsequent dangers to biodiversity with the reduction of krill, as it is the primary food source for many species in the region.

The effect of rising water temperatures on Antartic krill have been tested with controlled experiments (Brown et al., 2010) show that the the best temperatures for

growth were -1°C and 1°C, where 1°C had shorter time between moulting periods. The results at 3°C reduced growth rates, indicating the sensitivity of krill to rising water temperatures. The overall yearly average temperature for the model simulations used in this study were surface temperature around 0°C (TÜBİTAK, 2022), and the krill IBM used in the study (Fach et al., 2008) includes krill sensitiviy to temperature variations in the model itself. Any future increases in the surface temperature in the region however would negatively effect the growth period of the Antarctic krill if the averages rise above 1°C. Temperature is further of importance for the descent-ascent cycle of krill embryos developing into larvae (Hofmann et al., 1992). Modeling studies have shown that the cycle can vary dramatically with region depending on if and at what depth krill encounter suitable water masses, the Circumpolar Deep Water (CDW), a relatively warm (> 1.0°C) water mass at deep depths for hatching (Hofmann et al., 1992, Hofmann and Hüsrevoğlu 2003). Hofmann and Hüsrevoğlu (2003) show that in the Weddell Sea, the embryo hatching depth is likely deeper, at 805 m with an average 0°C, compared to other regions simulated which averaged at a depth of 570 m and 0.5°C. The time required for the embryo to hatch was also longer in the Weddell Sea, about 8 days, compared to the 6.5 days average for the rest of the Antarctic regions simulated (Hofmann and Hüsrevoğlu 2003). Changes in water temperature are likely to affect water masses and their distribution and therefore may have a profound impact on krill reproduction and recruitment success.

While this study does not directly investigate the affects of climate change on Antarctic Krill in the region, particular attention should be heeded on this subject nontheless. The Intergovernmental Panel on Climate Change (IPCC) 6th report regarding polar regions (Constable et al., 2022), states that the sea ice extent in the Antarctic does not have a circumpolar trend, but rather regional losses are occuring such as the Antarctic Peninsula. Projections for the next 100 years predict a circumpolar loss of ice coverage with low confidence. The observed warming and sea ice retreat is already causing changes in the marine ecosystem of the Southern Ocean. It has been observed that the Antarctic krill has been shifting poleward,

towards the south (Constable et al., 2022). They state that the recruitment and survival of Antarctic krill is dependent on the availability of sea ice, with the predicted loss of sea ice cover, the Antarctic krill is projected to lose its habitats and population is expected to shrink. Other factors such as warmer temperatures and shortening of the suitable spawning season as well as ocean acidification are expected to negatively effect the recruitment of krill. The report also states that the westerly winds are strengthening and shifting polewards, which in turn strengthens the ACC. This in turn may cause increased upwelling of nutrients along the continent and may influence the sites of primary production, carbon uptake and ice melting. Such changes could influence where sea ice formations and blooms can occur in the Southern Ocean and directly alter the krill habitat locations. The report also projects the krill habitat for the Weddell Sea to be in danger of decline due to the sea ice loss, warming and the decline in primary production (Constable et al., 2022), which implicates similar habitat loss predictions for Lazarev Sea krill.

A quantitative modeling study regarding the effects of climate change on sea ice and krill larvae (Sylvester et al., 2025) simulated three different habitats located on low latitude shelf (67°S to 62°S of the Antartic Peninsula), high latitude shelf (from the Antarctic coast up to 67°S) and open ocean (remaining open ocean in the area) of the region from 100°W to 20°W and up to 55°S, which also includes the Weddell Sea. Our results showed that under baseline conditions, the low latitude shelf habitat is the most favorable for krill growth and survival due to high nutrient availability from the shallow depth and habitat accessibility. The open ocean habitat was found to be the least favorable due to deeper depths that had less nutrient availability because of the absence of glacial melt and less habitat accessibility. The high latitude shelf habitat had intermediate sustainability due to glacial melt, nutrient access from shallower depths balanced out by limited light availability. With climate change scenarios applied to the model, the results showed that the most negative impacts on krill growth and larval survival occurred in the low latitude shelf habitat due to the decrease of primary production in Austral Fall, and changes in temperature and wind stress. Open ocean habitat had varied mixed results to the multiple climate change

scenarios applied by the model, where growth was impacted less but survival was positively effected by increase of primary production but was also negatively effected by the loss of sea ice. The high latitude habitat was generally negatively effected by all scenarios with particular emphasis on temperature driven glacial melt directly reducing the habitat suitability for larval krill growth.

Another study concerning long term effects of climate change in the Southern Ocean within the Marine Ecosystem Assessment for the Southern Ocean (MEASO) framework (Pinkerton et al., 2021), used satellite data, in situ measurments and a Vertically Generalised Production Model (VGPM) (Behrenfeld and Falkowski, 1997) as well as Carbon Based Production Model (CBPM) (Behrenfeld et al., 2005; Westberry et al., 2008), to measure the impacts of climate change on primary producers. The satellite observations showed that there was elevated primary production south of the PF and the southern limit of the ACC observed as higher chlorophyll a values. The trend of increasing chlorophyll a by satellite time series data (1997 - 2019) was seen in Northern and Subantarctic zones, conversely a decreasing trend was observed continental shelf areas, including the Weddell Sea. Overall the study suggests an increase in primary production in the Southern Ocean for the next 100 years with the caveat that the primary production will occur more in the water column and less so under the sea ice cover with the predicted retreat of sea ice. The current community of microbial life is expected to also shift from phytoplankton dominated to smaller flagellated species with the endemic Southern Ocean species being replaced by other temperate species (Deppeler and Davidson, 2017).

While the long term effects of climate change on Antarctic Krill is difficult to model, the studies done so far point towards the retreat of krill towards the higher latitudes mostly associated with the retreating sea ice cover and the reduction of favorable spawning environments on the lower latitudes. Under the current predicted climate change scenarios, the growth of an individual krill may be easier with access to more food via increased primary production in the Southern Ocean, but the spawning and

recruitment of krill overall may become more difficult with the loss of sea ice habitats.

4.6 Implications for marine protected areas

Marine Protected Areas (MPA) around the Antarctic continent (Teschke et al., 2016; Teschke et al., 2021). Specifically, Weddell Sea MPAs are being planned in two stages, phase 1 proposal and phase 2 (CCAMLR-38/23, Teschke et al., 2021), and the study area of this project in the Lazarev Sea is located mostly in the phase 2 area (Figure 59). Hence, the results from this connectivity study are of interest to CCMLAR as it is of great importance for MPA planning to understand the connectivity between regions separated by large distance to be able to assess population separation and establish meaningful krill fishing quotas. The establishment of MPA's will set the stage for restricting Antarctic krill and other fishing quotas and has therefore been discussed for many years by CCMLAR member states. While there are studies on connectivity of krill in other regions of the Southern Ocean such as the Antarctic Peninsula, Scotia Sea, Kerguelen Plateau, and Ross Sea there is so far no other study providing information on the greater Lazarev Sea region.

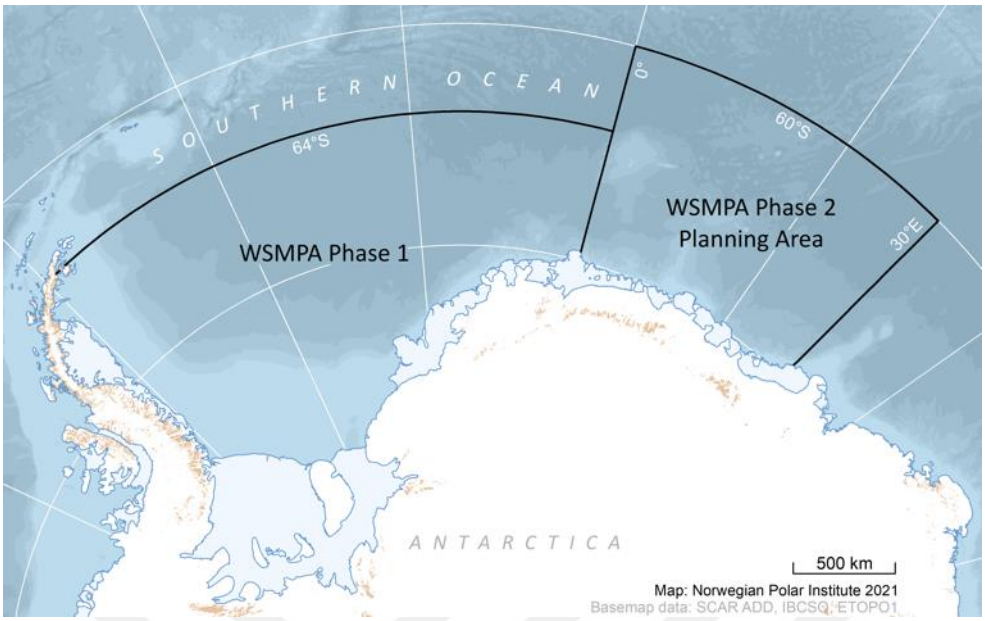


Figure 59 Planning phases of the Weddell Sea Marine Protected Area (WSMPA) as designated in phase 1 and phase 2. Adopted from Gary Griffith, Norwegian Polar Institute (personal communication)

With increasing concerns regarding the effects of climate change on the habitat of krill, and the projections saying that krill is going to retreat to higher latitudes (Veytia et al., 2020; McBride et al., 2021; Kawaguchi et al., 2023), the decisions for declaring MPA should be taken into account with scientific findings such as this thesis and other studies (Trathan, 2023).

CONCLUSION

This study aimed to research the transport and conncetivity of antarctic krill in the region which has historically been thought to be a transport site for the Southern Ocean population. Specifically to investigate the hypothesis that krill in the Lazarev Sea is not a single self-maintaining population but supplied by different krill populations from the Scotia Sea and even the Cosmonaut Sea via ocean currents. This was accomplished by using a complex system of models including the output of a high-resolution, circumpolar, hydrodynamic-ecosystem model (FESOM-REcoM2) run for 10 years, together with a Lagrangian Particle Tracking model and a sophisticated individual-based model of Antarctic krill. The modeling approach taken in the study makes the assessment of a large area like the Lazarev Sea much more feasible compared to a field study. Furthermore, it allows for the exploration of the field data collected in the region and the chance to evaluate the data in a larger spatial context.

One of primary goals was to find the source and sink regions of the krill that were found during the field studies. With the use of the Lagrangian particle tracking model it was found that the neighboring Riiser Larsen Sea (60%) and the Lazarev Sea itself (39%) was the most likely source of origin for the Lazarev Sea population. As for the sink regions, the results of the particle tracking simulations indicate that, krill originating in the Lazarev Sea most likely get transported downstream along the Antarctic continent into the Weddell Sea or are entrained into currents associated with the ACC and transported eastward. This transport experiences seasonal and spatial variability. However, particles origination in the south eastern part of the study region are more likely be retained inside the Lazarev region, which agrees with the source region simulation results. These findings, first agree with the notion that the Lazarev Sea is indeed a trasnitional region (Siegel 2012) for krill in the broader Southern Ocean environment, especially the area north of the 10°W to 10°E and 65°S to 64°S . However these findings also point to a surprisingly high potential for

retention area compared to other regions in the Southern Ocean and the possibility for the Lazarev Sea krill population to be self-sustaining.

Using the krill IBM the growth and survival of larvae and juvenile krill during the long-distance transport was assessed and that was rather variable depending on what season transport started. The austral spring release, which falls into the krill spawning season, was shown to increase growth and survival compared to the austral fall release. Interestingly, the winter release resulted in a very high survival, most likely related to the high food availability in the region that was known to be overestimated in the FESOM-REcoM2 simulations. Krill larvae showed a higher chance for mortality compared to juveniles, mostly visible during the austral spring simulations. Including sea ice agae as food showed a visible increase in growth, especially with larvae compared to juveniles, and a small decrease in mortality, indicating the importance of ice algae food for larval krill.

Implementation of reproduction in the krill IBM has been successfull at replicating the energy loss incurred on the adult females during spawning season. Simulations including the ability of adult krill to reproduce during the transport starting during the spawning season in the entire Lazarev Sea show that a high rate of average (76.97%) and above average growth (16.44%) success for the majority of the particles, with an average minority (6.58%) of below average particles that are risk of mortality. The spatial distribution of particles highlight that 10°W to 10°E and 65°S to 64°S diagonal line mentioned above is the starting location for the majority of particles that are marked below average, however just south of that is another diagonal from 10°W to 10°E and 72°S to 66°S that is starting location for the majority of the above average particles.

Overall, this study shows the Lazarev Sea's connectivity with the neighboring Weddell Sea, Riiser Larsen Sea and currents associated with the ACC, as well as retention inside the Lazarev Sea itself through the use of spatial and temporal Lagrangian particle tracking. The potential tranport routes for krill larvae were outlined, and growth, survival and success of larvae, juvenile and adult krill are

assessed using a krill IBM. Furthermore the effects of sea ice algae and reproduction are explored on larvae/juveniles and adult krill respectively.

REFERENCES

Alonzo, S. H., Switzer, P. V., & Mangel, M. (2003). Ecological games in space and time: the distribution and abundance of Antarctic krill and penguins. Ecology, 84(6), 1598-1607.

Alonzo, S., & Mangel, M. (2001). Survival strategies and growth of krill: Avoiding predators in space and time. Marine Ecology Progress Series, 209, 203–217. https://doi.org/10.3354/meps209203

Alvain, S., Moulin, C., Dandonneau, Y., & Bréon, F. M. (2005). Remote Sensing of phytoplankton groups in case 1 waters from Global SeaWiFS imagery. Deep Sea Research Part I: Oceanographic Research Papers, 52(11), 1989–2004. https://doi.org/10.1016/j.dsr.2005.06.015

Arrigo, K. R., Kremer, J. N., & Sullivan, C. W. (1993). A simulated Antarctic ast ice ecosystem. Journal of Geophysical Research: Oceans, 98(C4), 6929-6946.

Ashford, J.R., La Mesa, M., Fach, B.A., Jones, C. and Everson, I. (2010). Testing early life connectivity using otolith chemistry and particle-tracking simulations. Canadian Journal of Fisheries and Aquatic Sciences, 67: 1303-1315.

Atkinson A, Siegel V, Pakhomov EA, Jessopp MJ, Loeb V (2009) A re-appraisal of the total biomass and annual production of Antarctic krill. Deep-Sea Research Part I: Oceanographic Research Papers 56: 727–740.

Atkinson, A., Siegel, V., Pakhomov, E., Rothery, P., Loeb, V., Ross, R., Quetin, L., Schmidt, K., Fretwell, P., Murphy, E., Tarling, G., & Fleming, A. (2008). Oceanic circumpolar habitats of Antarctic krill. Marine Ecology Progress Series, 362, 1–23. https://doi.org/10.3354/meps07498

Atkinson, A., Whitehouse, M. J., Priddle, J., Cripps, G. C., Ward, P., & Brandon, M. A. (2001). South Georgia, Antarctica: a productive, cold water, pelagic ecosystem. Marine Ecology Progress Series, 216, 279-308.

Atkinson, Angus, Hill, S. L., Pakhomov, E. A., Siegel, V., Reiss, C. S., Loeb, V. J., Steinberg, D. K., Schmidt, K., Tarling, G. A., Gerrish, L., & Sailley, S. F. (2019). Krill (euphausia superba) distribution contracts southward during rapid regional warming. Nature Climate Change, 9(2), 142–147. https://doi.org/10.1038/s41558-018-0370-z

Aumont, O., Ethé, C., Tagliabue, A., Bopp, L., & Gehlen, M. (2015). Pisces-V2: An Ocean biogeochemical model for carbon and Ecosystem Studies. Geoscientific Model Development, 8(8), 2465–2513. https://doi.org/10.5194/gmd-8-2465-2015

Bahlburg, D., Thorpe, S. E., Meyer, B., Berger, U., & Murphy, E. J. (2023). An intercomparison of models predicting growth of Antarctic Krill (Euphausia superba): The importance of recognizing model specificity. PLOS ONE, 18(7). https://doi.org/10.1371/journal.pone.0286036

Behrenfeld, M. J., & Falkowski, P. G. (1997). Photosynthetic rates derived from satellite-based chlorophyll concentration. Limnology and Oceanography, 42(1), 1–20. https://doi.org/10.4319/lo.1997.42.1.0001

Behrenfeld, M. J., Boss, E., Siegel, D. A., & Shea, D. M. (2005). Carbon-based ocean productivity and phytoplankton physiology from space. Global Biogeochemical Cycles, 19(1). https://doi.org/10.1029/2004gb002299

Belcher, A., Henson, S. A., Manno, C., Hill, S. L., Atkinson, A., Thorpe, S. E., Fretwell, P., Ireland, L., & Tarling, G. A. (2019). Krill faecal pellets drive hidden pulses of particulate organic carbon in the Marginal Ice Zone. Nature Communications, 10(1). https://doi.org/10.1038/s41467-019-08847-1

Bernard, K. S., Steinke, K. B., & Fontana, J. M. (2022). Winter condition, physiology, and growth potential of juvenile Antarctic Krill. Frontiers in Marine Science, 9. https://doi.org/10.3389/fmars.2022.990853

Brandt, A., Bathmann, U., Brix, S., Cisewski, B., Flores, H., Göcke, C., Janussen, D., Krägefsky, S., Kruse, S., Leach, H., Linse, K., Pakhomov, E., Peeken, I., Riehl, T., Sauter, E., Sachs, O., Schüller, M., Schrödl, M., Schwabe, E., … Wilmsen, E.

(2011). Maud Rise – a snapshot through the water column. Deep Sea Research Part II: Topical Studies in Oceanography, 58(19–20), 1962–1982. https://doi.org/10.1016/j.dsr2.2011.01.008

Brody, S. (1945). Bioenexgetics and growth, with special reference to the efficiency complex in domestic animals.

Brown, M., Kawaguchi, S., Candy, S., & Virtue, P. (2010). Temperature effects on the growth and maturation of Antarctic Krill (euphausia superba). Deep Sea Research Part II: Topical Studies in Oceanography, 57(7–8), 672–682. https://doi.org/10.1016/j.dsr2.2009.10.016

Campbell, E. C., Wilson, E. A., Moore, G. W. K., Riser, S. C., Brayton, C. E., Mazloff, M. R., & Talley, L. D. (2019). Topographically induced eddies and their role in polynya formation at Maud Rise. Nature Communications, 10, 5020. https://doi.org/10.1038/s41467-019-08541-0

Carr, M.-E., Friedrichs, M. A. M., Schmeltz, M., Noguchi Aita, M., Antoine, D., Arrigo, K. R., Asanuma, I., Aumont, O., Barber, R., Behrenfeld, M., Bidigare, R., Buitenhuis, E. T., Campbell, J., Ciotti, A., Dierssen, H., Dowell, M., Dunne, J., Esaias, W., Gentili, B., … Yamanaka, Y. (2006). A comparison of global estimates of marine primary production from Ocean Color. Deep Sea Research Part II: Topical Studies in Oceanography, 53(5–7), 741–770. https://doi.org/10.1016/j.dsr2.2006.01.028

Cavan, E. L., Belcher, A., Atkinson, A., Hill, S. L., Kawaguchi, S., McCormack, S., Meyer, B., Nicol, S., Ratnarajah, L., Schmidt, K., Steinberg, D. K., Tarling, G. A., & Boyd, P. W. (2019). The importance of Antarctic krill in biogeochemical cycles. Nature Communications, 10(1). https://doi.org/10.1038/s41467-019-12668-7

Cavanagh, R. D., Melbourne-Thomas, J., Grant, S. M., Barnes, D. K., Hughes, K. A., Halfter, S., Meredith, M. P., Murphy, E. J., Trebilco, R., & Hill, S. L. (2021). Future risk for Southern Ocean Ecosystem Services under climate change. Frontiers in Marine Science, 7. https://doi.org/10.3389/fmars.2020.615214

Cisewski, B., Strass, V. H., & Leach, H. (2011). Circulation and transport of Water Masses in the Lazarev Sea, Antarctica, during summer and winter 2006. Deep Sea Research Part I: Oceanographic Research Papers, 58(2), 186–199. https://doi.org/10.1016/j.dsr.2010.12.001

Clarke, A. (1980). The biochemical composition of krill, Euphausia superba Dana, from South Georgia. Journal of Experimental Marine Biology and Ecology, 43(3), 221-236.

Clavel-Henry, M., Bahamon, N., Aguzzi, J., Navarro, J., López, M., & Company, J. B. (2024). Indicators to assess temporal variability in marine connectivity processes: A semi-theoretical approach. PLOS ONE, 19(7). https://doi.org/10.1371/journal.pone.0297730

Condie, S. A., Mansbridge, J. V., & Cahill, M. L. (2011). Contrasting local retention and cross-shore transports of the East Australian current and the Leeuwin current and their relative influences on the life histories of small pelagic fishes. Deep Sea Research Part II: Topical Studies in Oceanography, 58(5), 606–615. https://doi.org/10.1016/j.dsr2.2010.06.003

Conroy, J. A., Reiss, C. S., Gleiber, M. R., & Steinberg, D. K. (2020). Linking Antarctic krill larval supply and recruitment along the Antarctic Peninsula. Integrative and Comparative Biology, 60(6), 1386–1400. https://doi.org/10.1093/icb/icaa111

Constable, A.J., S. Harper, J. Dawson, K. Holsman, T. Mustonen, D. Piepenburg, and B. Rost, 2022: Cross-Chapter Paper 6: Polar Regions. In: Climate Change 2022: Impacts, Adaptation and Vulnerability. Contribution of Working Group II to the Sixth Assessment Report of the Intergovernmental Panel on Climate Change [H.-O. Pörtner, D.C. Roberts, M. Tignor, E.S. Poloczanska, K. Mintenbeck, A. Alegría, M. Craig, S. Langsdorf, S. Löschke, V. Möller, A. Okem, B. Rama (eds.)]. Cambridge University Press, Cambridge, UK and New York, NY, USA, pp. 2319–2368, doi:10.1017/9781009325844.023.

Cowen, R. K., Paris, C. B., & Srinivasan, A. (2006). Scaling of connectivity in marine populations. Science, 311(5760), 522–527. https://doi.org/10.1126/science.1122039

Cowen, Robert K., & Sponaugle, S. (2009). Larval dispersal and marine population connectivity. Annual Review of Marine Science, 1(1), 443–466. https://doi.org/10.1146/annurev.marine.010908.163757

Cresswell, K. A., Tarling, G. A., & Burrows, M. T. (2007). Behaviour affects local-scale distributions of Antarctic krill around South Georgia. Marine Ecology Progress Series, 343, 193-206.

Cresswell, K. A., Tarling, G. A., Thorpe, S. E., Burrows, M. T., Wiedenmann, J., & Mangel, M. (2009). Diel vertical migration of Antarctic krill (Euphausia superba) is flexible during advection across the Scotia Sea. Journal of Plankton Research, 31(10), 1265-1281.

Daly, K.L., (1990). Overwintering development, growth, and feeding of larval Euphausia superba in the Antarctic marginal ice zone. Limnology and Oceanography 35(7), 1564-1576.

Daly, K.L., Macaulay, M.C., (1991). Influence of physical and biological mesoscale dynamics on the seasonal distribution and behavior of Euphausia superba in the Antarctic marginal ice zone. Marine Ecology Progress Series 79, 37-66.

Danilov, S., D. Sidorenko, Q. Wang, and T. Jung (2017), The Finite-volumE Sea ice–Ocean Model (FESOM2), Geoscientific Model Development, 10(2), 765–789, doi:10.5194/gmd-10-765-2017.

Danilov, Sergey, Kivman, G., & Schröter, J. (2004). A finite-element ocean model: Principles and evaluation. Ocean Modelling, 6(2), 125–150. https://doi.org/10.1016/s1463-5003(02)00063-x

de Boyer Montégut, C., Madec, G., Fischer, A. S., Lazar, A., & Iudicone, D. (2004). Mixed layer depth over the global ocean: An examination of profile data and a

profile-based climatology. Journal of Geophysical Research: Oceans, 109(C12). https://doi.org/10.1029/2004jc002378

de Steur, L., Holland, D. M., Muench, R. D., McPhee, M. G., & Steele, M. (2007). The hydrography of the Lazarev Sea: Maud Rise region. Deep-Sea Research Part II: Topical Studies in Oceanography, 54(21–22), 2191–2207. https://doi.org/10.1016/j.dsr2.2007.06.013

Demer, D. A., & Hewitt, R. P. (1995). Bias in acoustic biomass estimates of Euphausia superba due to diel vertical migration. Deep Sea Research Part I: Oceanographic Research Papers, 42(4), 455–475. https://doi.org/10.1016/0967-0637(94)e0005-c

Denys, C. J., & McWhinnie, M. A. (1982). Fecundity and ovarian cycles of the Antarctic Krill euphausia superba (crustacea, euphausiacea). Canadian Journal of Zoology, 60(10), 2414–2423. https://doi.org/10.1139/z82-309

Deppeler, S. L., & Davidson, A. T. (2017). Southern Ocean Phytoplankton in a changing climate. Frontiers in Marine Science, 4. https://doi.org/10.3389/fmars.2017.00040

Di Stefano, M., Legrand, T., Di Franco, A., Nerini, D., & Rossi, V. (2022). Insights into the spatio-temporal variability of spawning in a territorial coastal fish by combining observations, modelling and literature review. Fisheries Oceanography, 32(1), 70–90. https://doi.org/10.1111/fog.12609

Downes, S. M., Farneti, R., Uotila, P., Griffies, S. M., Marsland, S. J., Bailey, D., Behrens, E., Bentsen, M., Bi, D., Biastoch, A., Böning, C., Bozec, A., Canuto, V. M., Chassignet, E., Danabasoglu, G., Danilov, S., Diansky, N., Drange, H., Fogli, P. G., … Yeager, S. G. (2015). An assessment of Southern Ocean Water Masses and sea ice during 1988–2007 in a suite of Interannual Core-II simulations. Ocean Modelling, 94, 67–94. https://doi.org/10.1016/j.ocemod.2015.07.022

Downes, S.M., Spence, P., & Hogg, A. M. (2018). Understanding variability of the Southern Ocean Overturning Circulation in Core-II models. Ocean Modelling, 123, 98–109. https://doi.org/10.1016/j.ocemod.2018.01.005

Droop, M. (1983). 25 Years of Algal Growth Kinetics A Personal View. Botanica Marina, 26(3), 99-112. https://doi.org/10.1515/botm.1983.26.3.99

Droop, M. R. (1973). Some thoughts on nutrient limitation in algae1. Journal of Phycology, 9(3), 264–272. https://doi.org/10.1111/j.1529-8817.1973.tb04092.x

Dubois, M., Rossi, V., Ser-Giacomi, E., Arnaud-Haond, S., López, C., & Hernández-García, E. (2016). Linking basin-scale connectivity, oceanography and population dynamics for the conservation and management of Marine Ecosystems. Global Ecology and Biogeography, 25(5), 503–515. https://doi.org/10.1111/geb.12431

Fach, B. A., & Klinck, J. M. (2006). Transport of antarctic krill (euphausia superba) across the Scotia Sea. part I: Circulation and particle tracking simulations. Deep Sea Research Part I: Oceanographic Research Papers, 53(6), 987–1010. https://doi.org/10.1016/j.dsr.2006.03.006

Fach, B. A., & Klinck, J. M. (2006). Transport of antarctic krill (euphausia superba) across the Scotia Sea. part I: Circulation and particle tracking simulations. Deep Sea Research Part I: Oceanographic Research Papers, 53(6), 987–1010. https://doi.org/10.1016/j.dsr.2006.03.006

Fach, B. A., Hofmann, E. E., & Murphy, E. J. (2002). Modeling studies of antarctic krill Euphausia superba survival during transport across the Scotia Sea. Marine Ecology Progress Series, 231, 187203. https://doi.org/10.3354/meps231187

Fach, B. A., Meyer, B., Wolf-Gladrow, D., & Bathmann, U. (2008). Biochemically based modeling study of Antarctic krill Euphausia superba growth and development. Marine Ecology Progress Series, 360, 147161. https://doi.org/10.3354/meps07366

Fach, B.A. (2014) Modeling the influence of hydrodynamic processes on anchovy distribution and connectivity in the Black Sea. Turkish Journal of Fisheries and Aquatic Sciences 14: 353-365. DOI: 10.4194/1303-2712-v14_2_06

Fahrbach, E., Rohardt, G., Schröder, M., & Strass, V. (1994). Transport and structure of the weddell gyre. Annales Geophysicae, 12(9), 840–855. https://doi.org/10.1007/s00585-994-0840-7

Farneti, R., Downes, S. M., Griffies, S. M., Marsland, S. J., Behrens, E., Bentsen, M., Bi, D., Biastoch, A., Böning, C., Bozec, A., Canuto, V. M., Chassignet, E., Danabasoglu, G., Danilov, S., Diansky, N., Drange, H., Fogli, P. G., Gusev, A., Hallberg, R. W., … Yeager, S. G. (2015). An assessment of Antarctic Circumpolar Current and Southern Ocean Meridional overturning circulation during 1958–2007 in a suite of Interannual Core-II simulations. Ocean Modelling, 93, 84–120. https://doi.org/10.1016/j.ocemod.2015.07.009

Flores, H., Kock, K. H., Wilhelms, S., & Jones, C. D. (2004). Diet of two icefish species from the South Shetland Islands and Elephant Island, Champsocephalus gunnari and Chaenocephalus aceratus. Polar Biology, 27(2), 119-129.

Flores, H., van Franeker, J.A., Siegel, V., Haraldsson, M., Strass, V.H., Meesters, E.H.W.G., Bathmann, U., Wolff, W.J., (2012). The association of Antarctic krill Euphausia superba with the under-ice habitat. Plos One 7 (2), e31775.

Fraser, J. H. (1936). The occurrence, ecology and life history of Tigriopus fulvus (Fischer). Journal of the Marine Biological Association of the United Kingdom, 20(3), 523-536.

Gallagher, K. L., Dinniman, M. S., & Lynch, H. J. (2023). Quantifying antarctic krill connectivity across the West Antarctic Peninsula and its role in large-scale Pygoscelis penguin population dynamics. Scientific Reports, 13(1). https://doi.org/10.1038/s41598-023-39105-6

Game, E.T., Grantham, H.S., Hobday, A.J., Pressey, R.L., Lombard, A.T., Beckley, L.E., and Richardson, A.J. (2009). Pelagic protected areas: the missing dimension in ocean conservation. Trends in ecology & evolution, 24(7): 360-369.

Garcia, H. E., R. A. Locarnini, T. P. Boyer, J. I. Antonov, O.K. Baranova, M.M. Zweng, J.R. Reagan, D.R. Johnson, (2014). World Ocean Atlas 2013, Volume 4: Dissolved Inorganic Nutrients (phosphate, nitrate, silicate). S. Levitus, Ed., A. Mishonov Technical Ed.; NOAA Atlas NESDIS 76, 25 pp.

Glasby, T. M., & Lobb, K. (2008). Assessing the likelihood of marine pest introductions in Sydney estuaries: a transport vector approach. Final Report Series no. X. NSW Department of Primary Industries. Fisheries, 75pp.

Griffies, S. M., Biastoch, A., Böning, C., Bryan, F., Danabasoglu, G., Chassignet, E. P., England, M. H., Gerdes, R., Haak, H., Hallberg, R. W., Hazeleger, W., Jungclaus, J., Large, W. G., Madec, G., Pirani, A., Samuels, B. L., Scheinert, M., Gupta, A. S., Severijns, C. A., … Yin, J. (2009). Coordinated ocean-ice reference experiments (cores). Ocean Modelling, 26(1–2), 1–46. https://doi.org/10.1016/j.ocemod.2008.08.007

Hagen W, Kattner G, Terbrüggen A, Van Vleet ES (2001) Lipid metabolism of the Antarctic krill Euphausia superba and its ecological implications. Mar Biol 139:95–104

Hagen, W., Kattner, G., Terbrüggen, A., & Van Vleet, E. S. (2001). Lipid metabolism of the Antarctic krill Euphausia superba and its ecological implications. Marine Biology, 139(1), 95-104.

Haid, V., & Timmermann, R. (2013). Simulated heat flux and sea ice production at coastal polynyas in the southwestern Weddell Sea. Journal of Geophysical Research: Oceans, 118(5), 2640–2652. https://doi.org/10.1002/jgrc.20133

Hattermann, T., & Levermann, A. (2009). Response of Southern Ocean circulation to global warming may enhance basal ice shelf melting around Antarctica. Climate Dynamics, 35(5), 741–756. https://doi.org/10.1007/s00382-009-0643-3

Hauck, J., C. Völker, T. Wang, M. Hoppema, M. Losch, and D. A. Wolf-Gladrow (2013), Seasonally different carbon flux changes in the Southern Ocean in response to the southern annular mode, Global Biogeochemical Cycles, 27(4), 1236–1245, doi:0.1002/2013GB004600.

Hempel, I., Hempel, G., (1986). Field observations on the developmental ascent of larval Euphausia superba (Crustacea). Polar Biology 6, 121-126.

Hill, S. L., Atkinson, A., Arata, J. A., Belcher, A., Nash, S. B., Bernard, K. S., Cleary, A., Conroy, J. A., Driscoll, R., Fielding, S., Flores, H., Forcada, J., Halfter, S., Hinke, J. T., Hückstädt, L., Johnston, N. M., Kane, M., Kawaguchi, S., Krafft, B. A., … Yang, G. (2024). Observing change in pelagic animals as sampling methods shift: The case of Antarctic Krill. Frontiers in Marine Science, 11. https://doi.org/10.3389/fmars.2024.1307402

Hill, S. L., Phillips, T., & Atkinson, A. (2013). Potential climate change effects on the habitat of Antarctic krill in the Weddell quadrant of the Southern Ocean. PloS one, 8(8), e72246.

Hirata, T., Hardman-Mountford, N. J., Brewin, R. J., Aiken, J., Barlow, R., Suzuki, K., Isada, T., Howell, E., Hashioka, T., Noguchi-Aita, M., & Yamanaka, Y. (2011). Synoptic relationships between surface chlorophyll-a and diagnostic pigments specific to phytoplankton functional types. Biogeosciences, 8(2), 311–327. https://doi.org/10.5194/bg-8-311-2011

Hofmann, E. E., & Hüsrevoğlu, Y. S. (2003). A circumpolar modeling study of habitat control of Antarctic krill (Euphausia Superba) reproductive success. Deep Sea Research Part II: Topical Studies in Oceanography, 50(22–26), 3121–3142. https://doi.org/10.1016/j.dsr2.2003.07.012

Hofmann, E. E., & Lascara, C. M. (2000). Modeling the growth dynamics of Antarctic krill Euphausia superba. Marine Ecology Progress Series, 194, 219-231.

Hofmann, E. E., Capella, J. E., Ross, R. M., & Quetin, L. B. (1992). Models of the early life history of Euphausia superba—part I. Time and temperature dependence

during the descent-ascent cycle. Deep Sea Research Part A. Oceanographic Research Papers, 39(7–8), 1177–1200. https://doi.org/10.1016/0198-0149(92)90063-y

Hofmann, E. E., Klinck, J. M., Locarnini, R. A., Fach, B., & Murphy, E. (1998). Krill transport in the Scotia Sea and Environs. Antarctic Science, 10(4), 406–415. https://doi.org/10.1017/s0954102098000492

Holland, D. M. (2001). Explaining the Weddell Polynya – A large ocean eddy shed at Maud Rise. Science, 292(5522), 1697–1700.

Holm-Hansen, O., & Huntley, M. (1984). Feeding requirements of krill in relation to food sources. Journal of Crustacean Biology, 4(5), 156-173.

Hunke, E. C., & Dukowicz, J. K. (1997). An elastic–viscous–plastic model for sea ice dynamics. Journal of physical oceanography, 27(9), 1849-1867.

Ikeda, T. (1984). Development of the larvae of the Antarctic krill (Euphausia superba Dana) observed in the Laboratory. Journal of Experimental Marine Biology and Ecology, 75(2), 107–117. https://doi.org/10.1016/0022-0981(84)90175-8

Ikeda, T., & Dixon, P. (1982). Observations on moulting in Antarctic krill (Euphausia superba Dana). Marine and Freshwater Research, 33(1), 71-76.

Jaspers, C., Huwer, B., Antajan, E., Hosia, A., Hinrichsen, H., Biastoch, A., Angel, D., Asmus, R., Augustin, C., Bagheri, S., Beggs, S. E., Balsby, T. J., Boersma, M., Bonnet, D., Christensen, J. T., Dänhardt, A., Delpy, F., Falkenhaug, T., Finenko, G., … Woźniczka, A. (2018). Ocean current connectivity propelling the secondary spread of a marine invasive comb jelly across Western Eurasia. Global Ecology and Biogeography, 27(7), 814–827. https://doi.org/10.1111/geb.12742

Johnsen, G., & Hegseth, E. N. (1991). Photoadaptation of sea-ice microalgae in the Barents Sea. Polar Biology, 11(3), 179-184.

Johnston, M. W., & Purkis, S. J. (2011). Spatial analysis of the invasion of lionfish in the western Atlantic and Caribbean. Marine Pollution Bulletin, 62(6), 1218–1226. https://doi.org/10.1016/j.marpolbul.2011.03.028

Johnston, M. W., & Purkis, S. J. (2014a). Are lionfish set for a Mediterranean invasion? modelling explains why this is unlikely to occur. Marine Pollution Bulletin, 88(1–2), 138–147. https://doi.org/10.1016/j.marpolbul.2014.09.013

Johnston, M. W., & Purkis, S. J. (2014b). Lionfish in the Eastern Pacific: A cellular automaton approach to assessing invasion risk. Biological Invasions, 16(12), 2681–2695. https://doi.org/10.1007/s10530-014-0696-z

Johnston, N. M., Murphy, E. J., Atkinson, A., Constable, A. J., Cotté, C., Cox, M., Daly, K. L., Driscoll, R., Flores, H., Halfter, S., Henschke, N., Hill, S. L., Höfer, J., Hunt, B. P., Kawaguchi, S., Lindsay, D., Liszka, C., Loeb, V., Manno, C., … Yang, G. (2022). Status, change, and futures of Zooplankton in the Southern Ocean. Frontiers in Ecology and Evolution, 9. https://doi.org/10.3389/fevo.2021.624692

Karakuş, O., Völker, C., Iversen, M., Hagen, W., & Hauck, J. (2022). The role of zooplankton grazing and nutrient recycling for global ocean biogeochemistry and phytoplankton phenology. Journal of Geophysical Research: Biogeosciences, 127(10). https://doi.org/10.1029/2022jg006798

Karakuş, O., Völker, C., Iversen, M., Hagen, W., Wolf-Gladrow, D., Fach, B., & Hauck, J. (2021). Modeling the impact of Macrozooplankton on carbon export production in the Southern Ocean. Journal of Geophysical Research: Oceans, 126(12). https://doi.org/10.1029/2021jc017315

Kaur, K., Kortner, T. M., Benitez-Santana, T., & Burri, L. (2022). Effects of Antarctic krill products on feed intake, growth performance, fillet quality, and health in Salmonids. Aquaculture Nutrition, 2022, 1–14. https://doi.org/10.1155/2022/3170854

Kawaguchi, K., Matsuda, O., Ishikawa, S., Naito, Y., (1986). The overwintering strategy of Antarctic krill (Euphausia superba) under the coastal fast ice off the Ongul Island in Lutzow-Holm Bay, Antarctica. Memoirs of the National Institute of Polar Research, Tokyo (Special Issue) 44, 67-85.

Kawaguchi, S. (2016). Reproduction and larval development in Antarctic krill (Euphausia superba). In Biology and ecology of Antarctic krill (pp. 225-246). Cham: Springer International Publishing.

Kawaguchi, S., Atkinson, A., Bahlburg, D., Bernard, K. S., Cavan, E. L., Cox, M. J., Hill, S. L., Meyer, B., & Veytia, D. (2023). Climate change impacts on Antarctic krill behaviour and population dynamics. Nature Reviews Earth & Environment, 5(1), 43–58. https://doi.org/10.1038/s43017-023-00504-y

Kawaguchi, S., Bell, E., Bestley, S., Cox, M. J., & Swadling, K. M. (2025). Editorial: Antarctic Krill and interactions in the east Antarctic ecosystem. Frontiers in Marine Science, 12. https://doi.org/10.3389/fmars.2025.1642870

Kawaguchi, S., Yoshida, T., Finley, L., Cramp, P., & Nicol, S. (2007). The krill maturity cycle: a conceptual model of the seasonal cycle in Antarctic krill. Polar Biology, 30(6), 689-698.

Knox, G.A., (1970). Antarctic marine ecosystems. In: Laws, R.M. (Ed.), Antarctic Ecology, Volume 2, Academic Press, London, pp. 69-109.

KOBAYASHI, S., OTA, Y., HARADA, Y., EBITA, A., MORIYA, M., ONODA, H., ONOGI, K., KAMAHORI, H., KOBAYASHI, C., ENDO, H., MIYAOKA, K., & TAKAHASHI, K. (2015). The JRA-55 reanalysis: General specifications and basic characteristics. Journal of the Meteorological Society of Japan. Ser. II, 93(1), 5–48. https://doi.org/10.2151/jmsj.2015-001

Lancraft, T. M., Reisenbichler, K. R., Robison, B. H., Hopkins, T. L., & Torres, J. J. (2004). A krill-dominated micronekton and macrozooplankton community in Croker Passage, Antarctica with an estimate of fish predation. Deep Sea Research Part II: Topical Studies in Oceanography, 51(17-19), 2247-2260.

Lauvset, S. K., Key, R. M., Olsen, A., van Heuven, S., Velo, A., Lin, X., Schirnick, C., Kozyr, A., Tanhua, T., Hoppema, M., Jutterström, S., Steinfeldt, R., Jeansson, E., Ishii, M., Perez, F. F., Suzuki, T., & Watelet, S. (2016). A new global interior

ocean mapped climatology: The 1° × 1° GLODAP version 2. Earth System Science Data, 8(2), 325–340. https://doi.org/10.5194/essd-8-325-2016

Lee, R. F., Nevenzel, J. C., & Paffenhöfer, G. A. (1971). Importance of wax esters and other lipids in the marine food chain: phytoplankton and copepods. Marine Biology, 9(2), 99-108.

Legrand, T., Di Franco, A., Ser-Giacomi, E., Caló, A., & Rossi, V. (2019). A multidisciplinary analytical framework to delineate spawning areas and quantify larval dispersal in coastal fish. Marine Environmental Research, 151, 104761. https://doi.org/10.1016/j.marenvres.2019.104761

Lester, S., Halpern, B., Grorud-Colvert, K., Lubchenco, J., Ruttenberg, B., Gaines, S., Airamé, S., & Warner, R. (2009). Biological effects within no-take marine reserves: A global synthesis. Marine Ecology Progress Series, 384, 33–46. https://doi.org/10.3354/meps08029

Locarnini, R. A., A. V. Mishonov, J. I. Antonov, T. P. Boyer, H. E. Garcia, O. K. Baranova, M. M. Zweng, C. R. Paver, J. R. Reagan, D. R. Johnson, M. Hamilton, and D. Seidov, (2013). World Ocean Atlas 2013, Volume 1: Temperature. S. Levitus, Ed., A. Mishonov Technical Ed.; NOAA Atlas NESDIS 73, 40 pp. Lynnes AS, Reid K, Croxall JP (2004) Diet and reproductive success of Ade´lie and chinstrap penguins: linking response of predators to prey population dynamics. Polar Biology 27: 544–554.

Lynnes, A. S., Reid, K., & Croxall, J. P. (2004). Diet and reproductive success of Adélie and chinstrap penguins: linking response of predators to prey population dynamics. Polar Biology, 27(9), 544-554.

Marr, J. W. S. (1962). The natural history and geography of the Antarctic krill (Euphausia superba Dana). Discovery Rep., 32, 33-464.

Marschall, H. P. (1988). The overwintering strategy of Antarctic krill under the pack-ice of the Weddell Sea. Polar biology, 9(2), 129-135.

Mazloff, M. R., Heimbach, P., & Wunsch, C. (2010). An eddy-permitting Southern Ocean State Estimate. Journal of Physical Oceanography, 40(5), 880–899. https://doi.org/10.1175/2009jpo4236.1

McBride, M., Schram Stokke, O., Renner, A., Krafft, B., Bergstad, O., Biuw, M., Lowther, A., & Stiansen, J. (2021). Antarctic krill Euphausia superba: Spatial distribution, abundance, and management of fisheries in a changing climate. Marine Ecology Progress Series, 668, 185–214. https://doi.org/10.3354/meps13705

Meiners, K. M., et al. (2012), Chlorophyll a in Antarctic sea ice from historical ice core data, Geophys. Res. Lett., 39, L21602, doi:10.1029/2012GL053478.

Melbourne-Thomas, J., S. P. Corney, R. Trebilco, K. M. Meiners, R. P. Stevens, S. Kawaguchi, M. D. Sumner, and A. J. Constable (2016), Under ice habitats for Antarctic krill larvae: Could less mean more under climate warming?, Geophys. Res. Lett., 43, 10,322–10,327, doi:10.1002/2016GL070846.

Meyer, B. Ulrich Freier, Volker Grimm, Jürgen Groeneveld, Brian P V Hunt, Sven Kerwath, Rob King, Christine Klaas, Evgeny Pakhomov, Klaus M Meiners, Jessica Melbourne-Thomas, Eugene J Murphy, Sally E Thorpe, Sharon Stammerjohn, Dieter Wolf-Gladrow, Lutz Auerswald, Albrecht Götz, Laura Halbach, Simon Jarman, So Kawaguchi, Thomas Krumpen, Gernot Nehrke, Robert Ricker, Michael Sumner, Mathias Teschke, Rowan Trebilco, and Noyan I Yilmaz (2017) The winter pack-ice zone provides a sheltered but food-poor habitat for larval Antarctic krill, Nature Ecology & Evolution vol. 1 (12) pp. 1853-1861

Meyer, B., & Oettl, B. (2005). Effects of short-term starvation on composition and metabolism of larval Antarctic krillEuphausia superba. Marine Ecology Progress Series, 292, 263-270.

Meyer, B., A. Atkinson, B. Blume, and U. V. Bathmann (2002), Feeding and energy budgets of Antarctic krill Euphausia superba at the onset of winter–I–Furcilia III larvae, Limnol. Oceanogr., 47, 943–952.Miller, D.G.M., Hampton, I., 1989. Krill

aggregation characteristics: spatial distribution patterns from hydro-acoustic observations. Polar Biology 10, 125-134.

Meyer, B., Auerswald, L., Siegel, V., Spahic, c, Pape, C., Fach, B., Teschke, M., Lopata, A., & Fuentes, V. (2010). Seasonal variation in body composition, metabolic activity, feeding, and growth of adult Krill Euphausia superba in the Lazarev Sea. Marine Ecology Progress Series, 398, 1–18. https://doi.org/10.3354/meps08371

Meyer, Bettina, Atkinson, A., Bernard, K. S., Brierley, A. S., Driscoll, R., Hill, S. L., Marschoff, E., Maschette, D., Perry, F. A., Reiss, C. S., Rombolá, E., Tarling, G. A., Thorpe, S. E., Trathan, P. N., Zhu, G., & Kawaguchi, S. (2020). Successful ecosystem-based management of Antarctic krill should address uncertainties in krill recruitment, behaviour and ecological adaptation. Communications Earth & Environment, 1(1). https://doi.org/10.1038/s43247-020-00026-1

Meyer, Bettina. (2011). The overwintering of Antarctic krill, Euphausia superba, from an ecophysiological perspective. Polar Biology, 35(1), 15–37. https://doi.org/10.1007/s00300-011-1120-0

Moffitt, E. A., Wilson White, J., & Botsford, L. W. (2011). The utility and limitations of size and spacing guidelines for designing Marine Protected Area (MPA) networks. Biological Conservation, 144(1), 306–318. https://doi.org/10.1016/j.biocon.2010.09.008

Moffitt, E.A., Botsford, L.W., Kaplan, D.M. and O'Farrell, M.R. (2009). Marine reserve networks for species that move within a home range. Ecological Applications, 19: 1835–1847.

Morgan-Kiss, R. M., J. C. Priscu, T. Pocock, L. Gudynaite-Savitch, and N. P. Huner (2006), Adaptation and acclimation of photosynthetic microorganisms to permanently cold environments, Microbiol. Mol. Biol. Rev., 70(1), 222–252, doi:10.1128/MMBR.70.1.222-252.2006.

Mueller, R. D., & Timmermann, R. (2017). Weddell Sea Circulation. Journal of Atmospheric and Solar-Terrestrial Physics, 161, 105-117.

Muench, R. D., & Gordon, A. L. (1995). Circulation and transport of water along the western Weddell Sea margin. Journal of Geophysical Research: Oceans, 100(C9), 18503-18515.

Murphy, E. J., Thorpe, S. E., Tarling, G. A., Watkins, J. L., Fielding, S., & Underwood, P. (2017). Restricted regions of enhanced growth of Antarctic krill in the circumpolar Southern Ocean. Scientific Reports, 7(1). https://doi.org/10.1038/s41598-017-07205-9

Murphy, E.J., Thorpe, S. E., Watkins, J. L., & Hewitt, R. (2004). Modeling the krill transport pathways in the Scotia Sea: Spatial and environmental connections generating the seasonal distribution of Krill. Deep Sea Research Part II: Topical Studies in Oceanography, 51(12–13), 1435–1456. https://doi.org/10.1016/j.dsr2.2004.06.019

Nast, F. (1978). The vertical distribution of larval and adult krill (Euphausia superba Dana) on a time station south of Elephant Island, South Shetlands.

Naughten, K. A., Meissner, K. J., Galton-Fenzi, B. K., England, M. H., Timmermann, R., Hellmer, H. H., Hattermann, T., & Debernard, J. B. (2018). Intercomparison of Antarctic Ice-shelf, ocean, and sea-ice interactions simulated by metroms-iceshelf and Fesom 1.4. Geoscientific Model Development, 11(4), 1257–1292. https://doi.org/10.5194/gmd-11-1257-2018

Neumann, T., & Fennel, W. (2006). A method to represent seasonal vertical migration of zooplankton in 3D-eulerian models. Ocean Modelling, 12(1–2), 188–204. https://doi.org/10.1016/j.ocemod.2005.05.007

Nicol S, Foster J, Kawaguchi S (2011) The fishery for Antarctic krill – recent developments. Fish and Fisheries. no–no. doi:10.1111/j.1467- 2979.2011.00406.x.

Nicol, S., & Foster, J. (2016). The fishery for Antarctic Krill: Its current status and management regime. Advances in Polar Ecology, 387–421. https://doi.org/10.1007/978-3-319-29279-3_11

Nicol, S., Stolp, M., Cochran, T., Geijsel, P., & Marshall, J. (1992). Growth and shrinkage of Antarctic krill Euphausia superba from the Indian Ocean sector of the Southern Ocean during summer. Marine Ecology Progress Series, 89, 175-181.

Nicol, S., William, K., & Stolp, M. (1995). The energetic cost of egg production in Antarctic krill (Euphausia superba Dana). Antarctic Science, 7(1), 25-30.

Nordhausen, W., Huntley, M., Lopez, M.D.G., (1992). RACER: Carnivory by Euphausia superba during the Antarctic winter, Antarctic Journal of the United States 27(5), 181-183.

Orr, J. C. (1999). On Ocean Carbon-cycle model comparison. Tellus B: Chemical and Physical Meteorology, 51(2), 509. https://doi.org/10.3402/tellusb.v51i2.16334

Orsi, A. H., Whitworth, T., & Nowlin, W. D. (1995). On the meridional extent and fronts of the Antarctic Circumpolar Current. Deep Sea Research Part I: Oceanographic Research Papers, 42(5), 641–673. https://doi.org/10.1016/0967-0637(95)00021-w

Osman LP, Hucke-Gaete R, Moreno CA, Torres D (2004) Feeding ecology of Antarctic fur seals at Cape Shirreff, South Shetlands, Antarctica. Polar Biology 27: 92–98.

Parkinson, C. L., & Washington, W. M. (1979). A large-scale numerical model of Sea Ice. Journal of Geophysical Research: Oceans, 84(C1), 311–337. https://doi.org/10.1029/jc084ic01p00311

Patti, B., Torri, M., & Cuttitta, A. (2020). General surface circulation controls the interannual fluctuations of anchovy stock biomass in the central Mediterranean Sea. Scientific Reports, 10(1). https://doi.org/10.1038/s41598-020-58028-0

Perovich, D. K. (1993). A theoretical model of ultraviolet light transmission through Antarctic Sea Ice. Journal of Geophysical Research: Oceans, 98(C12), 22579–22587. https://doi.org/10.1029/93jc02563

Pinkerton, M. H., Boyd, P. W., Deppeler, S., Hayward, A., Höfer, J., & Moreau, S. (2021). Evidence for the impact of climate change on primary producers in the Southern Ocean. Frontiers in Ecology and Evolution, 9, 592027.

Pinones, A., and A. V. Fedorov (2016), Projected changes of Antarctic krill habitat by the end of the 21st century, Geophys. Res. Lett., 43, 8580–8589, doi:10.1002/2016GL069656.

Pinones, A., E. E. Hofmann, K. L. Daly, M. S. Dinniman, and J. M. Klinck (2013), Modeling the remote and local connectivity of Antarctic krill populations along the western Antarctic Peninsula, Mar. Ecol. Prog. Ser., 481, 69–92.

Pinones, A., E. E. Hofmann, M. S. Dinniman, and L.B. Davis (2016) Modeling the transport and fate of euphausiids in the Ross Sea. Polar Biol, 39:177–187 DOI 10.1007/s00300-015-1798-5

Piñones, Andrea, Hofmann, E. E., Daly, K. L., Dinniman, M. S., & Klinck, J. M. (2013). Modeling Environmental Controls on the transport and fate of early life stages of Antarctic Krill (euphausia superba) on the western Antarctic Peninsula continental shelf. Deep Sea Research Part I: Oceanographic Research Papers, 82, 17–31. https://doi.org/10.1016/j.dsr.2013.08.001

Quetin, L. B., & Ross, R. M. (1991). Behavioral and physiological characteristics of the Antarctic krill, Euphausia superba. American Zoologist, 31(1), 49-63. https://doi.org/10.1093/icb/31.1.49

Quetin, L. B., & Ross, R. M. (1991). Behavioral and physiological characteristics of the Antarctic krill,euphausia superba. American Zoologist, 31(1), 49–63. https://doi.org/10.1093/icb/31.1.49

Quetin, L.B., Ross, R.M., Clarke, A., 1994. Krill energetics: seasonal and environmental aspects of the physiology of it Euphausia superba. In: El-Sayed, S.Z. (Ed.) Southern Ocean ecology: the BIOMASS perspective. Cambridge University Press, Cambridge, pp. 165-184.

Rackow, T., Wesche, C., Timmermann, R., Hellmer, H. H., Juricke, S., & Jung, T. (2017). A simulation of small to giant antarctic iceberg evolution: Differential Impact on Climatology estimates. Journal of Geophysical Research: Oceans, 122(4), 3170–3190. https://doi.org/10.1002/2016jc012513

Roman, M. R. (1983). NITROGENOUS NUTRITION OF MARINE. Nitrogen in the marine environment, 347.

Ross, R. M., & Quetin, L. B. (1989). Energetic cost to develop to the first feeding stage of Euphausia superba Dana and the effect of delays in food availability. Journal of Experimental Marine Biology and Ecology, 133(1–2), 103–127. https://doi.org/10.1016/0022-0981(89)90161-5

Ross, R. M., and L. B. Quetin (1989), Energetic cost to develop to the first feeding stage of Euphausia superba Dana and the effect of delays in food availability, J. Exp. Mar. Biol. Ecol., 133, 103–127.

Rossi, V., Ser-Giacomi, E., López, C., & Hernández-García, E. (2014). Hydrodynamic provinces and oceanic connectivity from a transport network help designing marine reserves. Geophysical Research Letters, 41(8), 2883–2891. https://doi.org/10.1002/2014gl059540

Ryabov, A., Berger, U., Blasius, B., & Meyer, B. (2023). Driving forces of Antarctic Krill Abundance. Science Advances, 9(50). https://doi.org/10.1126/sciadv.adh4584

Schnack, S. B. (1985). Feeding by Euphausia superba and copepod species in response to varying concentrations of phytoplankton. In Antarctic nutrient cycles and food webs (pp. 311-323). Berlin, Heidelberg: Springer Berlin Heidelberg.

Schneider, B., Bopp, L., Gehlen, M., Segschneider, J., Frölicher, T. L., Cadule, P., Friedlingstein, P., Doney, S. C., Behrenfeld, M. J., & Joos, F. (2008). Climate-induced interannual variability of marine primary and export production in three global coupled climate carbon cycle models. Biogeosciences, 5(2), 597–614. https://doi.org/10.5194/bg-5-597-2008

Schourup-Kristensen, V., Sidorenko, D., Wolf-Gladrow, D. A., & Völker, C. (2014). A skill assessment of the biogeochemical model RECOM2 coupled to the finite element sea ice–ocean model (FESOM 1.3). Geoscientific Model Development, 7(6), 2769–2802. https://doi.org/10.5194/gmd-7-2769-2014

Schourup-Kristensen, Vibe, Wekerle, C., Wolf-Gladrow, D. A., & Völker, C. (2018). Arctic Ocean Biogeochemistry in the high resolution FESOM 1.4-RECOM2 model. Progress in Oceanography, 168, 65–81. https://doi.org/10.1016/j.pocean.2018.09.006

Schröder, M., & Fahrbach, E. (1999). On the structure and the transport of the eastern Weddell Gyre. Deep Sea Research Part II: Topical Studies in Oceanography, 46(1–2), 501–527. https://doi.org/10.1016/s0967-0645(98)00112-x

Sein, D. V., Danilov, S., Biastoch, A., Durgadoo, J. V., Sidorenko, D., Harig, S., & Wang, Q. (2016). Designing variable ocean model resolution based on the observed ocean variability. Journal of Advances in Modeling Earth Systems, 8(2), 904-916.

Sein, D. V., Koldunov, N. V., Danilov, S., Wang, Q., Sidorenko, D., Fast, I., Rackow, T., Cabos, W., & Jung, T. (2017). Ocean modeling on a mesh with resolution following the local Rossby radius. Journal of Advances in Modeling Earth Systems, 9(7), 2601–2614. https://doi.org/10.1002/2017ms001099

Shao, C., Sun, S., Liu, K., Wang, J., Li, S., Liu, Q., Deagle, B. E., Seim, I., Biscontin, A., Wang, Q., Liu, X., Kawaguchi, S., Liu, Y., Jarman, S., Wang, Y., Wang, H.-Y., Huang, G., Hu, J., Feng, B., … Fan, G. (2023). The enormous repetitive Antarctic krill genome reveals environmental adaptations and population insights. Cell, 186(6). https://doi.org/10.1016/j.cell.2023.02.005

Sidorenko, D., T. Rackow, T. Jung, T. Semmler, D. Barbi, S. Danilov, K. Dethloff, W. Dorn, K. Fieg, H. F. Gößling, et al. (2015), Towards multi-resolution global climate modeling with ECHAM6–FESOM. Part I: model formulation and mean climate, Climate Dynamics, 44(3-4), 757–780, doi:10.1007/s00382-014-2290-6.

Sidorenko, D., Wang, Q., Danilov, S., & Schröter, J. (2011). FESOM under coordinated ocean-ice reference experiment forcing. Ocean Dynamics, 61(7), 881–890. https://doi.org/10.1007/s10236-011-0406-7

Siegel V (2005) Distribution and population dynamics of Euphausia superba: summary of recent findings. Polar Biology 29: 1–22.

Siegel, V. (2012). Krill stocks in high latitudes of the Antarctic Lazarev Sea: Seasonal and interannual variation in distribution, abundance and demography. Polar Biology, 35(8), 1151–1177. https://doi.org/10.1007/s00300-012-1162-y

Siegel, V., Driscoll, R., MühlernhardtSiegel, U., Elsheimer, A., & Fromm, C. (2013). 5. ANTARCTIC KRILL POPULATION DYNAMICS IN THE NORTH-WESTERN WEDDELL SEA (CCAMLR). The Expedition of the Research Vessel" Polarstern" to the Antarctic in 2013 (ANT-XXIX/3), 106.

Siegel, V., Reiss, C. S., Dietrich, K. S., Haraldsson, M., & Rohardt, G. (2013). Distribution and abundance of Antarctic krill (Euphausia superba) along the Antarctic Peninsula. Deep Sea Research Part I: Oceanographic Research Papers, 77, 63–74. https://doi.org/10.1016/j.dsr.2013.02.005

Smith, A. J., Wotherspoon, S., Ratnarajah, L., Cutter, G. R., Macaulay, G. J., Hutton, B., King, R., Kawaguchi, S., & Cox, M. J. (2025). Antarctic krill vertical migrations modulate seasonal carbon export. Science, 387(6732). https://doi.org/10.1126/science.adq5564

Sylvester, Z. T., Veytia, D., Bahl, A. A., Bahlburg, D., Benkort, D., Bestley, S., Cagdas, B., Cleary, A. C., Constable, A., Corney, S., Fach, B. A., Hellessey, N., Hill, S. L., Johnston, N. M., Labrousse, S., Merkel, B., Murphy, E. J., Subramaniam, R. C., Thorpe, S., & Raymond, B. (2025). Untangling the complexities of larval Antarctic krill overwintering success under climate change. ICES Journal of Marine Science, 82(4). https://doi.org/10.1093/icesjms/fsaf049

Tarling, G. A., & Thorpe, S. E. (2014). Instantaneous movement of krill swarms in the Antarctic Circumpolar Current. Limnology and Oceanography, 59(3), 872-886.

Teschke, K., Brtnik, P., Hain, S., Herata, H., Liebschner, A., Pehlke, H., Brey T. (2021) Planning marine protected areas under the CCAMLR regime – The case of the Weddell Sea (Antarctica), Marine Policy, 124:104370, doi: 10.1016/j.marpol.2020.104370

Teschke, K., Pehlke, H., Deininger, M., Jerosch, K., & Brey, T. (2016). Scientific background document in support of the development of a CCAMLR MPA in the Weddell Sea (Antarctica)–Version 2016-Part C: Data analysis and MPA scenario development. CCAMLR WG-EMM-16, (WG-EMM).

Thorpe, S. E., Murphy, E. J., & Watkins, J. L. (2007). Circumpolar connections between Antarctic Krill (Euphausia superba Dana) populations: Investigating the roles of Ocean and Sea Ice Transport. Deep Sea Research Part I: Oceanographic Research Papers, 54(5), 792–810. https://doi.org/10.1016/j.dsr.2007.01.008

Timmermann, R., Le Brocq, A. M., Deen, T., J., Domack, E. W., Dutrieux, P., Galton-Fenzi, B., Hellmer, H. H., Humbert, A., Jansen, D., Jenkins, A., Lambrecht, A., Makinson, K., Niederjasper, F., Nitsche, F.-O., Nøst, O. A., Smedsrud, L. H., and Smith, W. (2010) Antarctic ice sheet topography, cavity geometry, and global bathymetry (RTopo 1.0.5-beta), doi:10.1594/PANGAEA.741917.

Timmermann, R., Wang, Q., & Hellmer, H. H. (2012). Ice-shelf basal melting in a global finite-element sea-ice/ice-shelf/ocean model. Annals of Glaciology, 53(60), 303–314. https://doi.org/10.3189/2012aog60a156

Timmermann, Ralph, & Hellmer, H. H. (2013). Southern Ocean warming and increased ice shelf basal melting in the twenty-first and twenty-second centuries based on coupled ice-ocean finite-element modelling. Ocean Dynamics, 63(9–10), 1011–1026. https://doi.org/10.1007/s10236-013-0642-0

Timmermann, Ralph, Danilov, S., Schröter, J., Böning, C., Sidorenko, D., & Rollenhagen, K. (2009). Ocean circulation and sea ice distribution in a finite element global sea ice–ocean model. Ocean Modelling, 27(3–4), 114–129. https://doi.org/10.1016/j.ocemod.2008.10.009

Torres, J. J., Aarset, A. V., Donnelly, J., Hopkins, T. L., Lancraft, T. M., & Ainley, D. G. (1994). Metabolism of Antarctic micronektonic Crustacea as a function of depth of occurrence and season. Marine Ecology Progress Series, 113, 207-219.

Torri, M., Corrado, R., Falcini, F., Cuttitta, A., Palatella, L., Lacorata, G., Patti, B., Arculeo, M., Mifsud, R., Mazzola, S., & Santoleri, R. (2018). Planktonic stages of small pelagic fishes (sardinella aurita and engraulis encrasicolus) in the central Mediterranean Sea: The key role of physical forcings and implications for fisheries management. Progress in Oceanography, 162, 25–39. https://doi.org/10.1016/j.pocean.2018.02.009

Trathan, P. N. (2023). What is needed to implement a sustainable expansion of the Antarctic krill fishery in the Southern Ocean? Marine Policy, 155, 105770. https://doi.org/10.1016/j.marpol.2023.105770

Trathan, P. N., & Hill, S. L. (2016). The importance of krill predation in the Southern Ocean. Advances in Polar Ecology, 321–350. https://doi.org/10.1007/978-3-319-29279-3_9

TÜBİTAK. (2022). Küresel anlamda önemli bir tür olan Antartika Krili'nin (Euphausia superba) üzerindeki çevresel etkilerin ve biyolojik şartların modelleme ile değerlendirilmesi

Våge, K., Spall, M. A., & Lee, C. M. (2020). Topographic control of ocean circulation around Maud Rise. Journal of Physical Oceanography, 50(7), 1909–1925. https://doi.org/10.1175/JPO-D-19-0278.1

Veytia, D., Corney, S., Meiners, K. M., Kawaguchi, S., Murphy, E. J., & Bestley, S. (2020). Circumpolar projections of Antarctic krill growth potential. Nature Climate Change, 10(6), 568–575. https://doi.org/10.1038/s41558-020-0758-4

Vogt, M., Hashioka, T., Payne, M. R., Buitenhuis, E. T., Quéré, C. L., Alvain, S., Aita, M. N., Bopp, L., Doney, S. C., Hirata, T., Lima, I., Sailley, S., & Yamanaka, Y. (2013). The Distribution, Dominance Patterns and Ecological Niches of Plankton

Functional Types in Dynamic Green Ocean Models and Satellite Estimates. https://doi.org/10.5194/bgd-10-17193-2013

Walsh, J., Reiss, C., & Watters, G. (2020). Flexibility in Antarctic Krill Euphausia superba decouples diet and recruitment from overwinter sea-ice conditions in the northern Antarctic Peninsula. Marine Ecology Progress Series, 642, 1–19. https://doi.org/10.3354/meps13325

Wang, Q., Danilov, S., & Schröter, J. (2008). Finite element ocean circulation model based on triangular prismatic elements, with application in studying the effect of topography representation. Journal of Geophysical Research: Oceans, 113(C5). https://doi.org/10.1029/2007jc004482

Wang, Q., S. Danilov, D. Sidorenko, R. Timmermann, C. Wekerle, X. Wang, T. Jung, and J. Schröter (2014), The Finite Element Sea Ice-Ocean Model (FESOM) v.1.4: formulation of an ocean general circulation model, Geoscientific Model Development, 7(2), 663–693, doi:10.5194/gmd-7-663-2014.

Wang, Qiang, Wekerle, C., Danilov, S., Wang, X., & Jung, T. (2018). A 4.5 km resolution Arctic Ocean simulation with the global multi-resolution model fesom 1.4. Geoscientific Model Development, 11(4), 1229–1255. https://doi.org/10.5194/gmd-11-1229-2018

Wang, S., Wang, Q., Shu, Q., Scholz, P., Lohmann, G., & Qiao, F. (2019). Improving the upper-ocean temperature in an ocean climate model (fesom 1.4): Shortwave penetration versus mixing induced by nonbreaking surface waves. Journal of Advances in Modeling Earth Systems, 11(2), 545–557. https://doi.org/10.1029/2018ms001494

Wanninkhof, R. (1992). Relationship between wind speed and gas exchange over the Ocean. Journal of Geophysical Research: Oceans, 97(C5), 7373–7382. https://doi.org/10.1029/92jc00188

Wekerle, C., Krumpen, T., Dinter, T., von Appen, W.-J., Iversen, M. H., & Salter, I. (2018). Properties of sediment trap catchment areas in Fram Strait: Results from

lagrangian modeling and remote sensing. Frontiers in Marine Science, 5. https://doi.org/10.3389/fmars.2018.00407

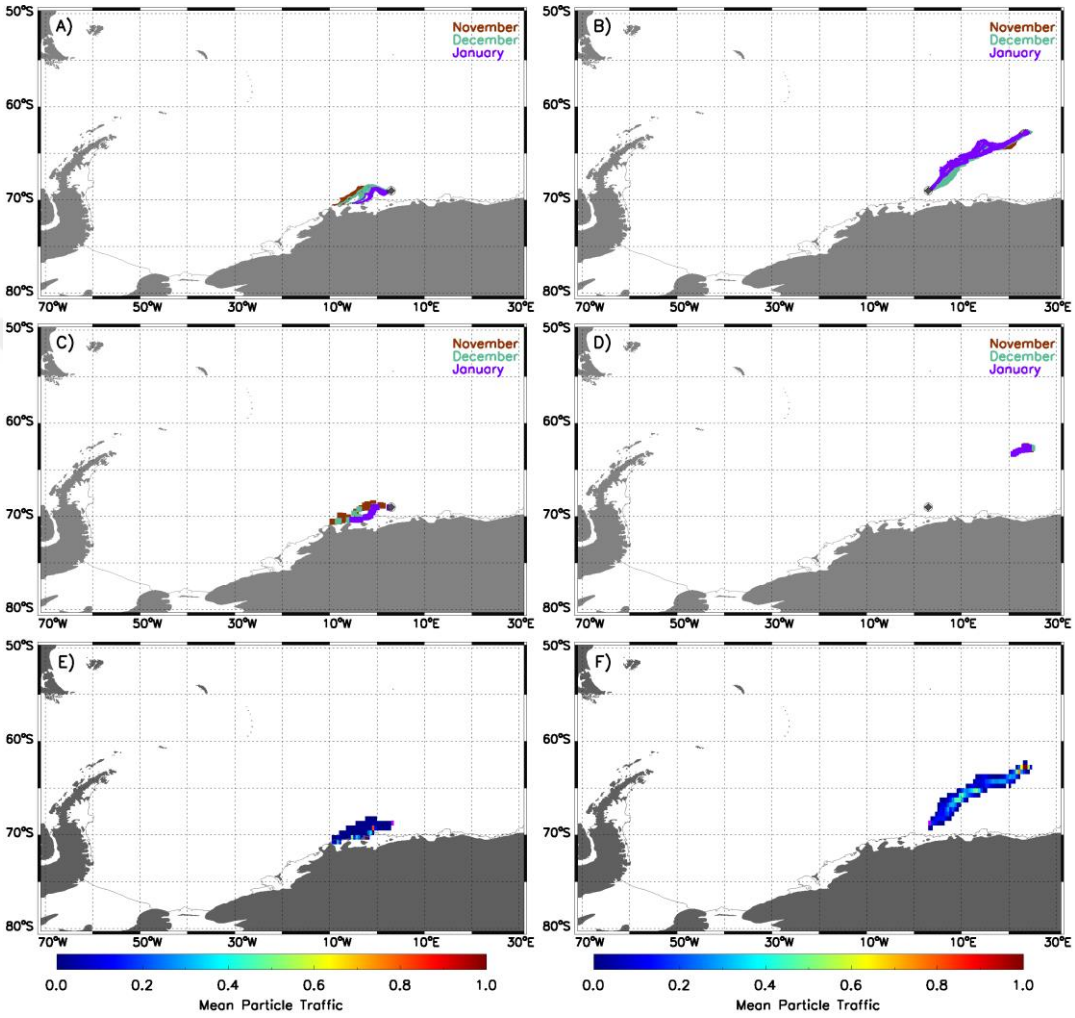
Westberry, T., Behrenfeld, M. J., Siegel, D. A., & Boss, E. (2008). Carbon-based primary productivity modeling with vertically resolved photoacclimation. Global Biogeochemical Cycles, 22(2). https://doi.org/10.1029/2007gb003078

Wood, S., Paris, C. B., Ridgwell, A., & Hendy, E. J. (2014). Modelling dispersal and connectivity of broadcast spawning corals at the global scale. Global Ecology and Biogeography, 23(1), 1-11.

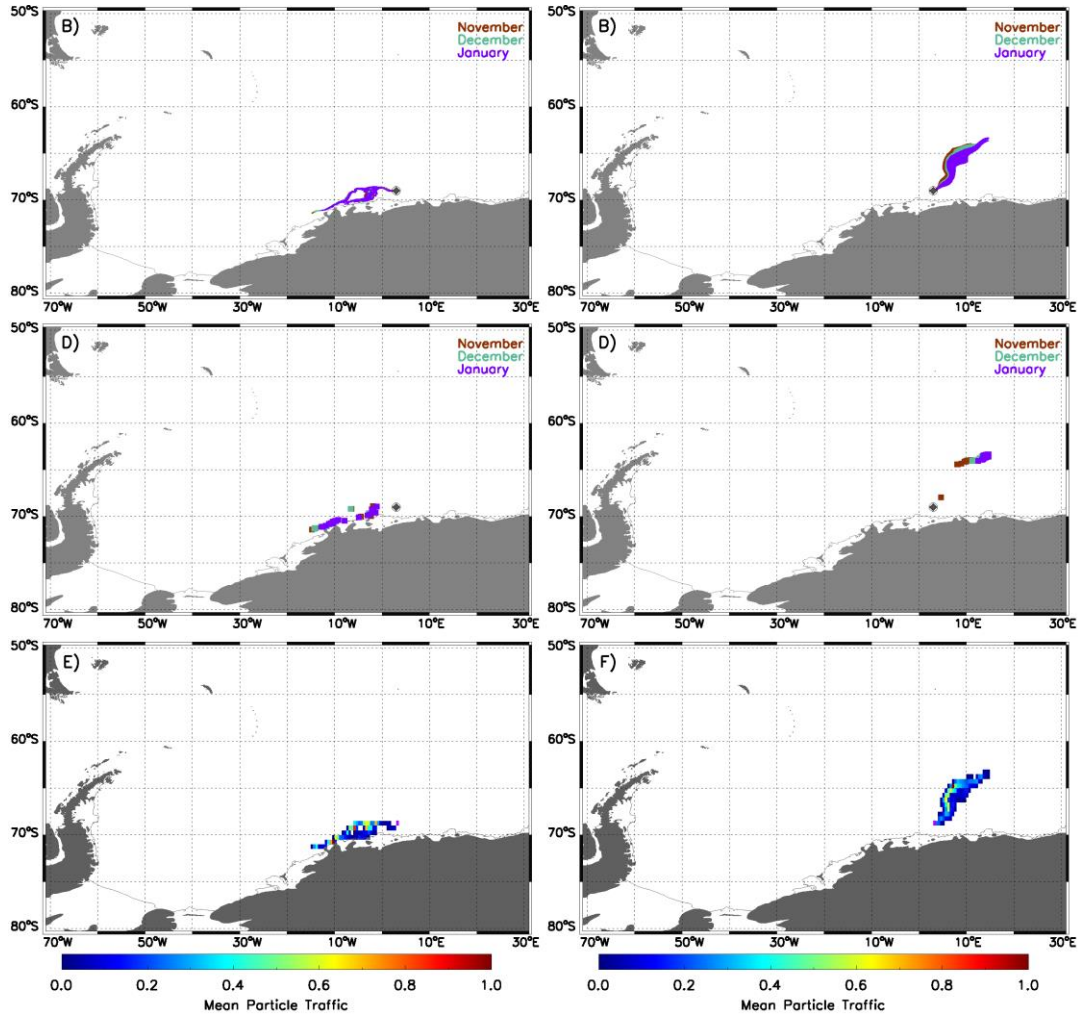
Zweng, M.M, J.R. Reagan, J.I. Antonov, R.A. Locarnini, A.V. Mishonov, T.P. Boyer, H.E. Garcia, O.K. Baranova, D.R. Johnson, D.Seidov, M.M. Biddle, (2013). World Ocean Atlas 2013, Volume 2: Salinity. S. Levitus, Ed., A. Mishonov Technical Ed.; NOAA Atlas NESDIS 74, 39 pp.

APPENDICES

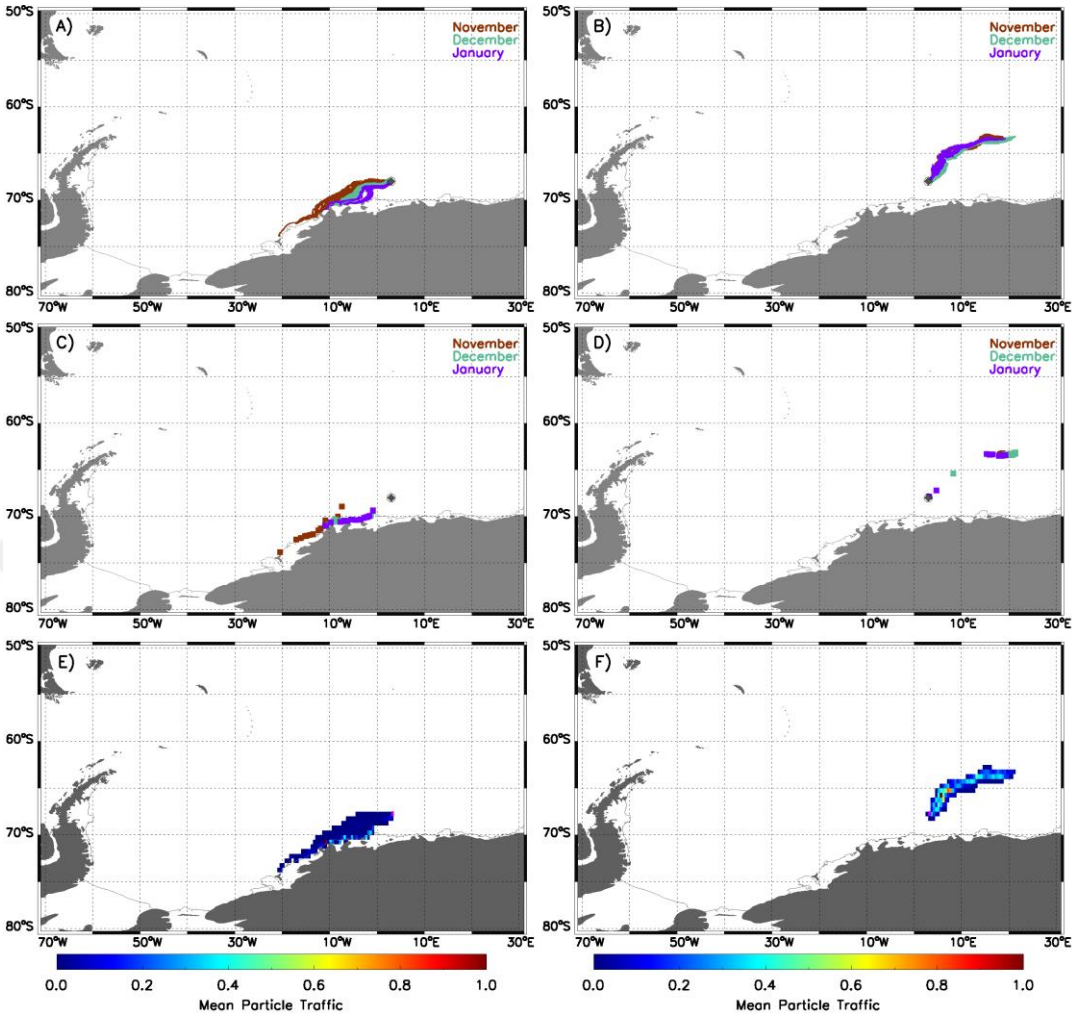
A. Lagrangian particle tracking results



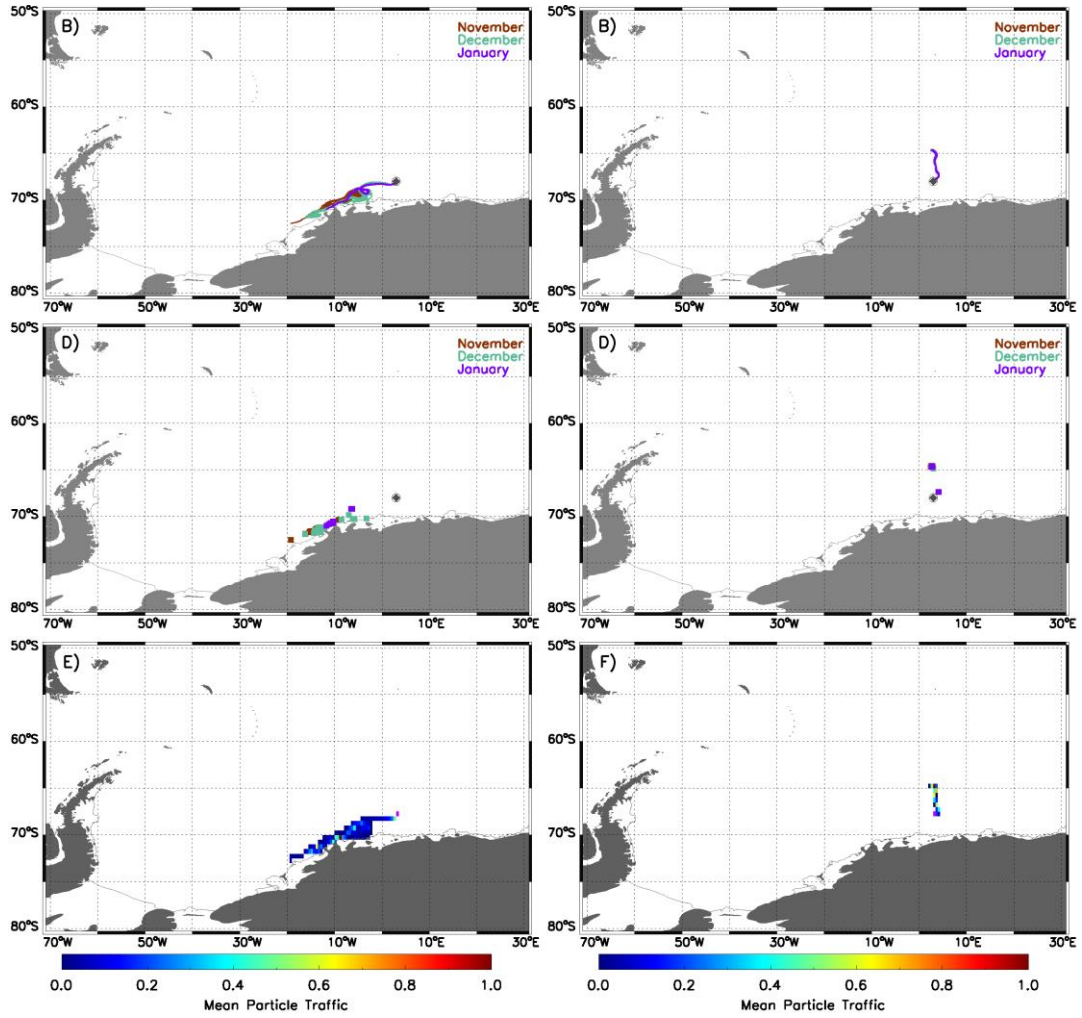
Appendix A 1 Lagrangian Particle tracking results of 92 particles released at station 44 in austral spring and summer 2005. A) Trajectory of all particles tracked forward in time from 2005 to 2006, black diamond denotes the release point of particles. B) Trajectory of all particles tracked backwards in time from 2005 to 2004, black diamond denotes the release point of particles. C) End points of particles tracked forwards in time are denoted by squares, black diamond inside the circle denotes the release point of particles. D) End points of particles tracked backwards in time are denoted by squares, black diamond inside the circle denotes the release point of particles. E) Mean particle traffic map of particles tracked forwards in time, purple rectangle denotes the release cell. F) Mean particle traffic map of particles tracked backwards in time, purple rectangle denotes the release cell.



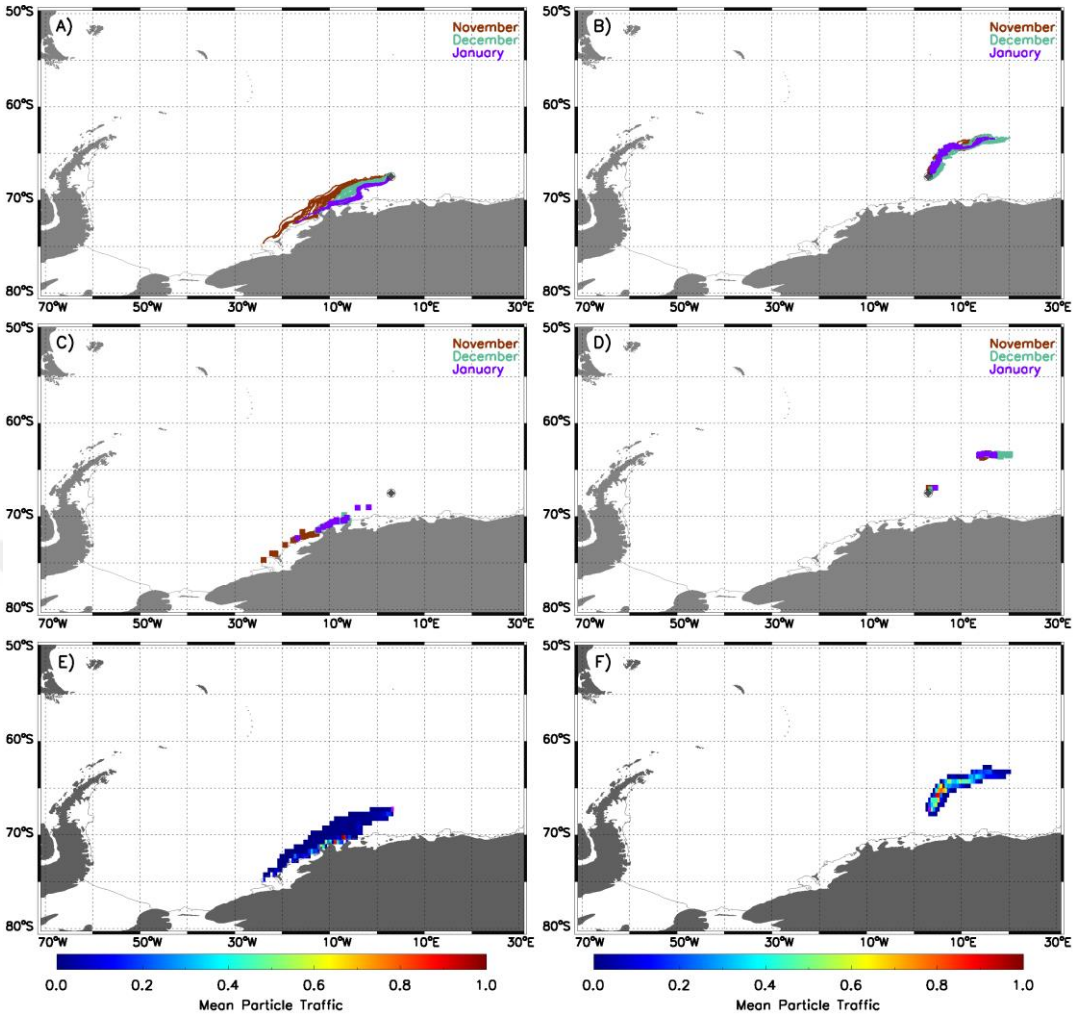
Appendix A 2 Lagrangian Particle tracking results of 92 particles released at station 44 at 200 m depth in austral spring and summer 2005. A) Trajectory of all particles tracked forward in time from 2005 to 2006, black diamond denotes the release point of particles. B) Trajectory of all particles tracked backwards in time from 2005 to 2004, black diamond denotes the release point of particles. C) End points of particles tracked forwards in time are denoted by squares, black diamond inside the circle denotes the release point of particles. D) End points of particles tracked backwards in time are denoted by squares, black diamond inside the circle denotes the release point of particles. E) Mean particle traffic map of particles tracked forwards in time, purple rectangle denotes the release cell. F) Mean particle traffic map of particles tracked backwards in time, purple rectangle denotes the release cell.



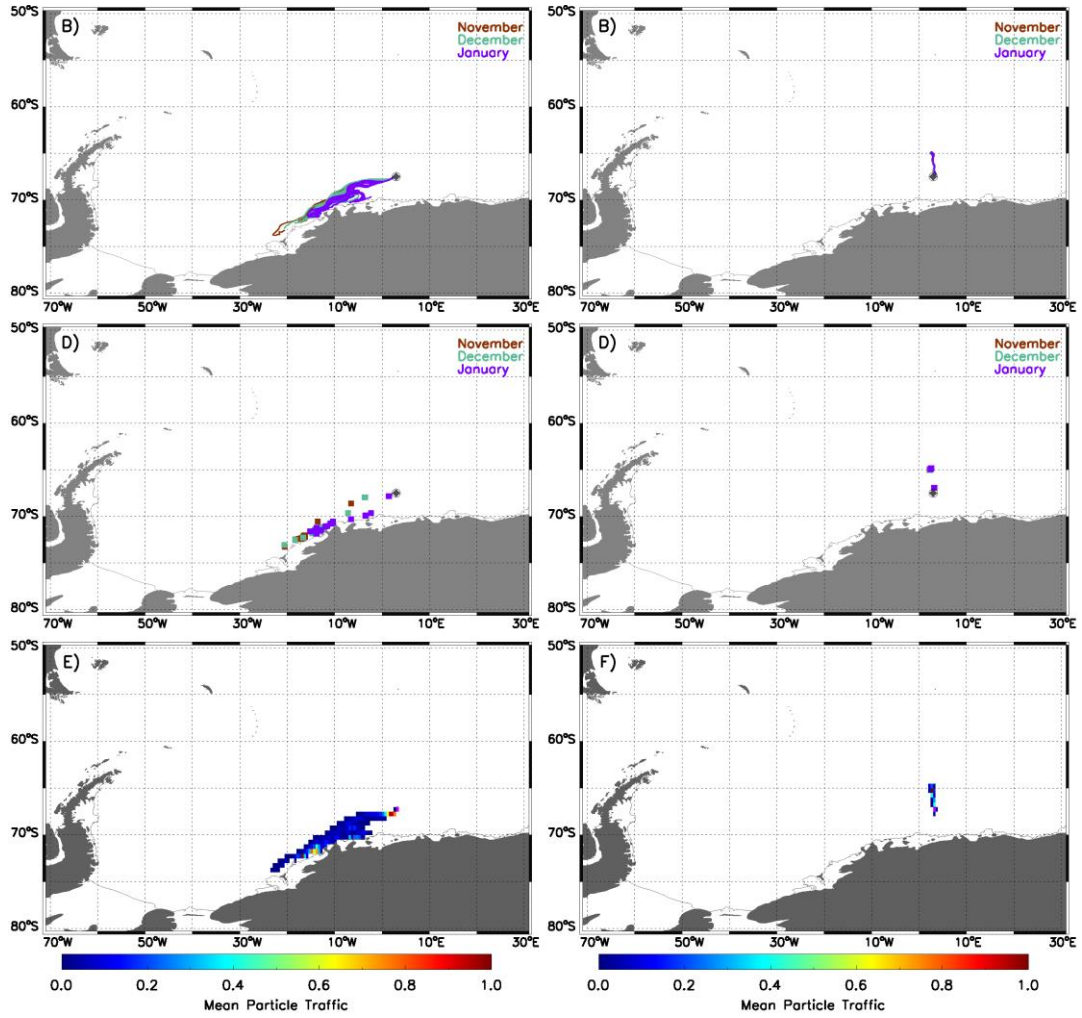
Appendix A 3 Lagrangian Particle tracking results of 92 particles released at station 46 in austral spring and summer 2005. A) Trajectory of all particles tracked forward in time from 2005 to 2006, black diamond denotes the release point of particles. B) Trajectory of all particles tracked backwards in time from 2005 to 2004, black diamond denotes the release point of particles. C) End points of particles tracked forwards in time are denoted by squares, black diamond inside the circle denotes the release point of particles. D) End points of particles tracked backwards in time are denoted by squares, black diamond inside the circle denotes the release point of particles. E) Mean particle traffic map of particles tracked forwards in time, purple rectangle denotes the release cell. F) Mean particle traffic map of particles tracked backwards in time, purple rectangle denotes the release cell.



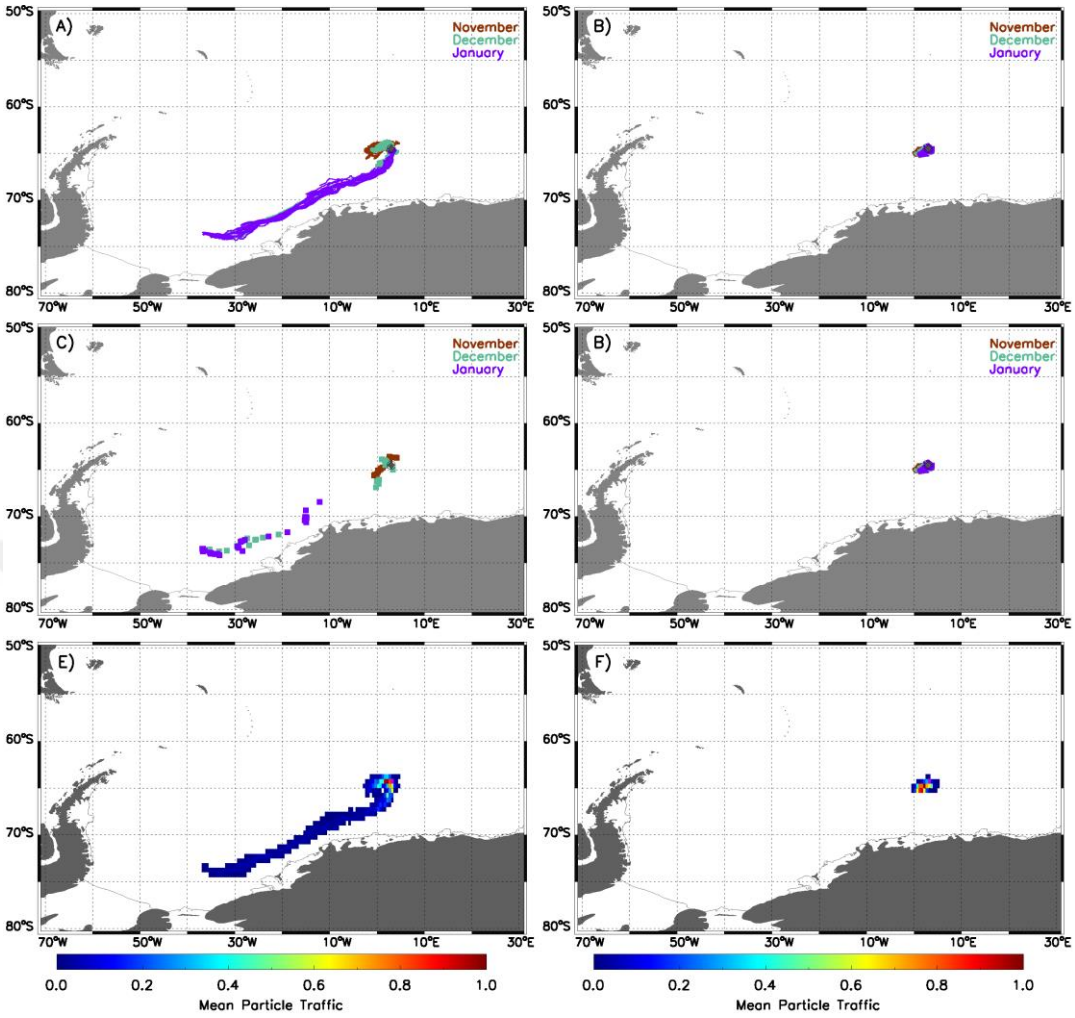
Appendix A 4 Lagrangian Particle tracking results of 92 particles released at station 46 at 200 m depth in austral spring and summer 2005. A) Trajectory of all particles tracked forward in time from 2005 to 2006, black diamond denotes the release point of particles. B) Trajectory of all particles tracked backwards in time from 2005 to 2004, black diamond denotes the release point of particles. C) End points of particles tracked forwards in time are denoted by squares, black diamond inside the circle denotes the release point of particles. D) End points of particles tracked backwards in time are denoted by squares, black diamond inside the circle denotes the release point of particles. E) Mean particle traffic map of particles tracked forwards in time, purple rectangle denotes the release cell. F) Mean particle traffic map of particles tracked backwards in time, purple rectangle denotes the release cell.



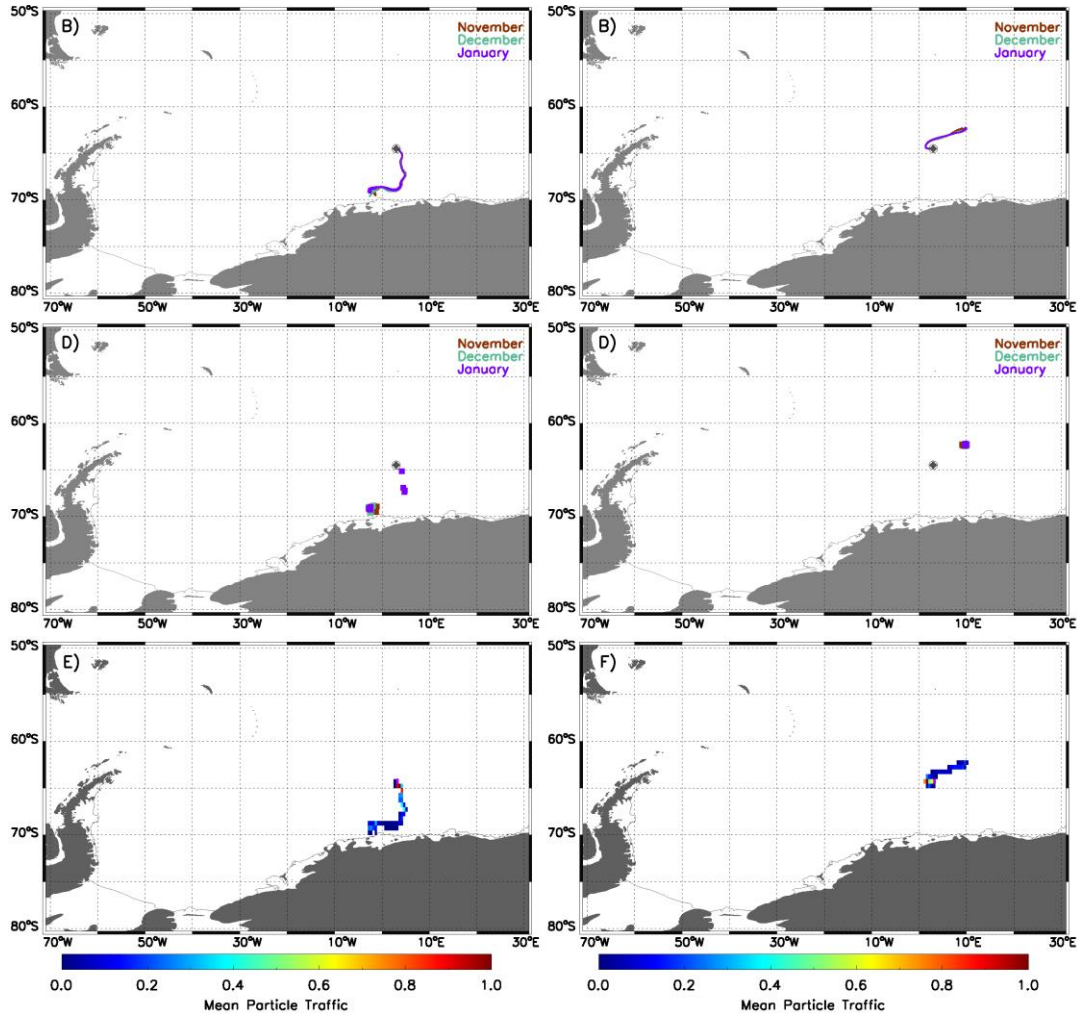
Appendix A 5 Lagrangian Particle tracking results of 92 particles released at station 47 in austral spring and summer 2005. A) Trajectory of all particles tracked forward in time from 2005 to 2006, black diamond denotes the release point of particles. B) Trajectory of all particles tracked backwards in time from 2005 to 2004, black diamond denotes the release point of particles. C) End points of particles tracked forwards in time are denoted by squares, black diamond inside the circle denotes the release point of particles. D) End points of particles tracked backwards in time are denoted by squares, black diamond inside the circle denotes the release point of particles. E) Mean particle traffic map of particles tracked forwards in time, purple rectangle denotes the release cell. F) Mean particle traffic map of particles tracked backwards in time, purple rectangle denotes the release cell.



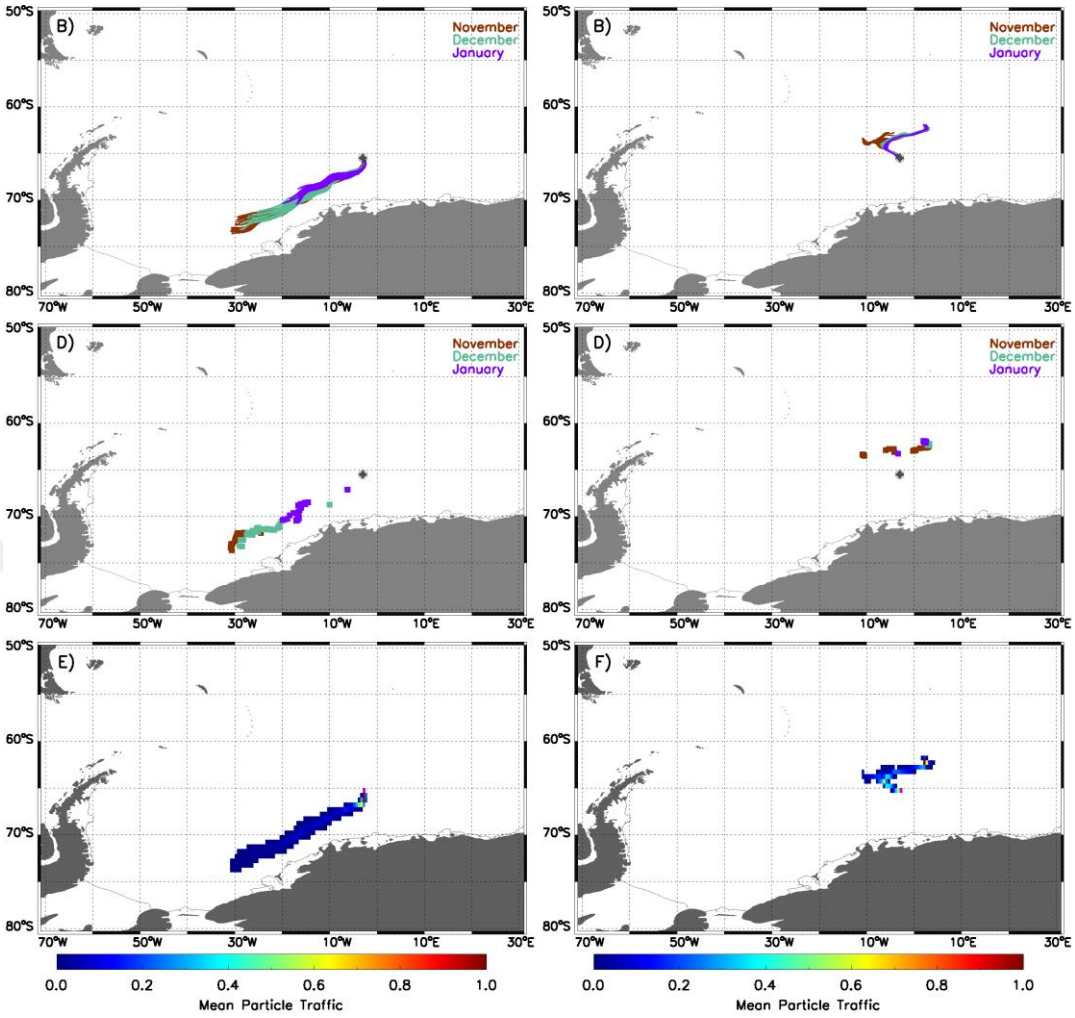
Appendix A 6 Lagrangian Particle tracking results of 92 particles released at station 47 at 200 m in austral spring and summer 2005. A) Trajectory of all particles tracked forward in time from 2005 to 2006, black diamond denotes the release point of particles. B) Trajectory of all particles tracked backwards in time from 2005 to 2004, black diamond denotes the release point of particles. C) End points of particles tracked forwards in time are denoted by squares, black diamond inside the circle denotes the release point of particles. D) End points of particles tracked backwards in time are denoted by squares, black diamond inside the circle denotes the release point of particles. E) Mean particle traffic map of particles tracked forwards in time, purple rectangle denotes the release cell. F) Mean particle traffic map of particles tracked backwards in time, purple rectangle denotes the release cell.



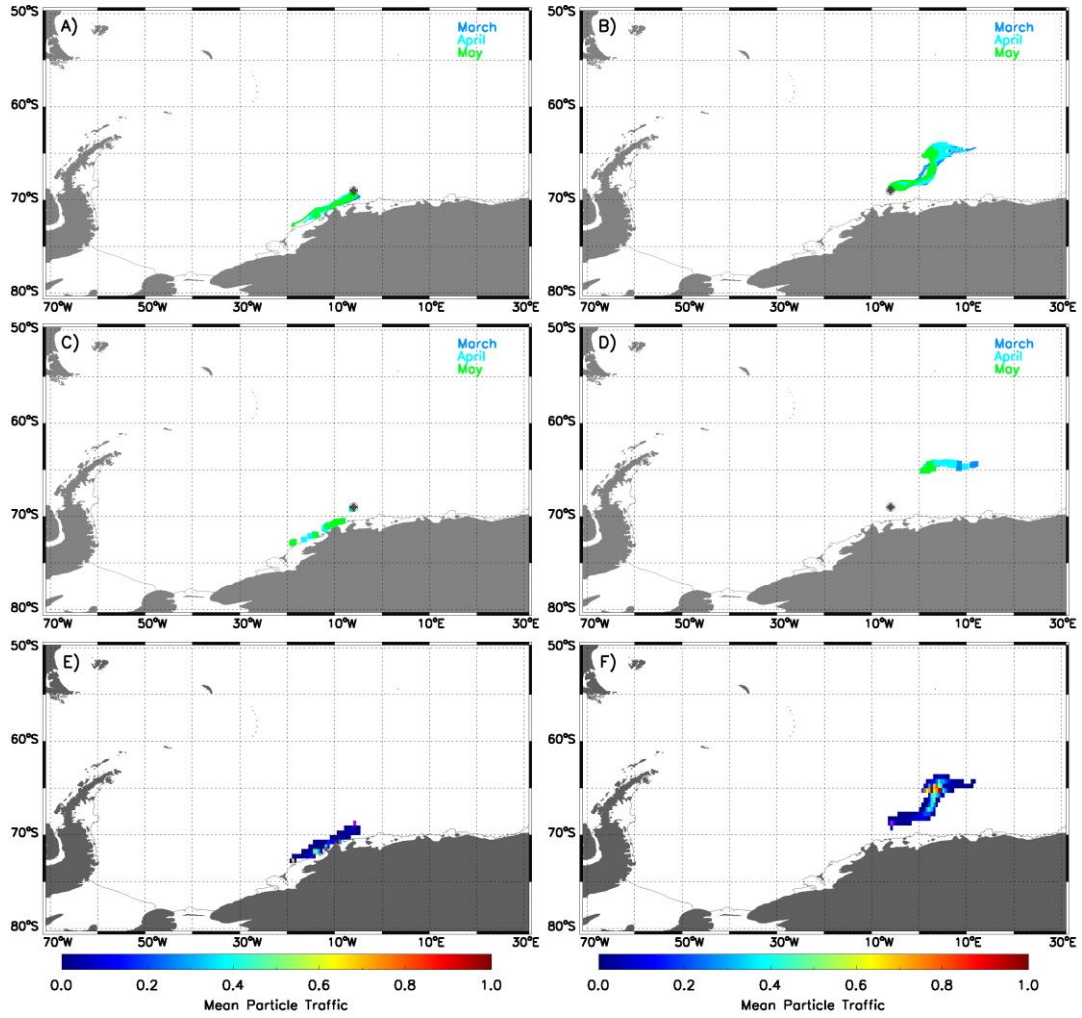
Appendix A 7 Lagrangian Particle tracking results of 92 particles released at station 53 in austral spring and summer 2005. A) Trajectory of all particles tracked forward in time from 2005 to 2006, black diamond denotes the release point of particles. B) Trajectory of all particles tracked backwards in time from 2005 to 2004, black diamond denotes the release point of particles. C) End points of particles tracked forwards in time are denoted by squares, black diamond inside the circle denotes the release point of particles. D) End points of particles tracked backwards in time are denoted by squares, black diamond inside the circle denotes the release point of particles. E) Mean particle traffic map of particles tracked forwards in time, purple rectangle denotes the release cell. F) Mean particle traffic map of particles tracked backwards in time, purple rectangle denotes the release cell.



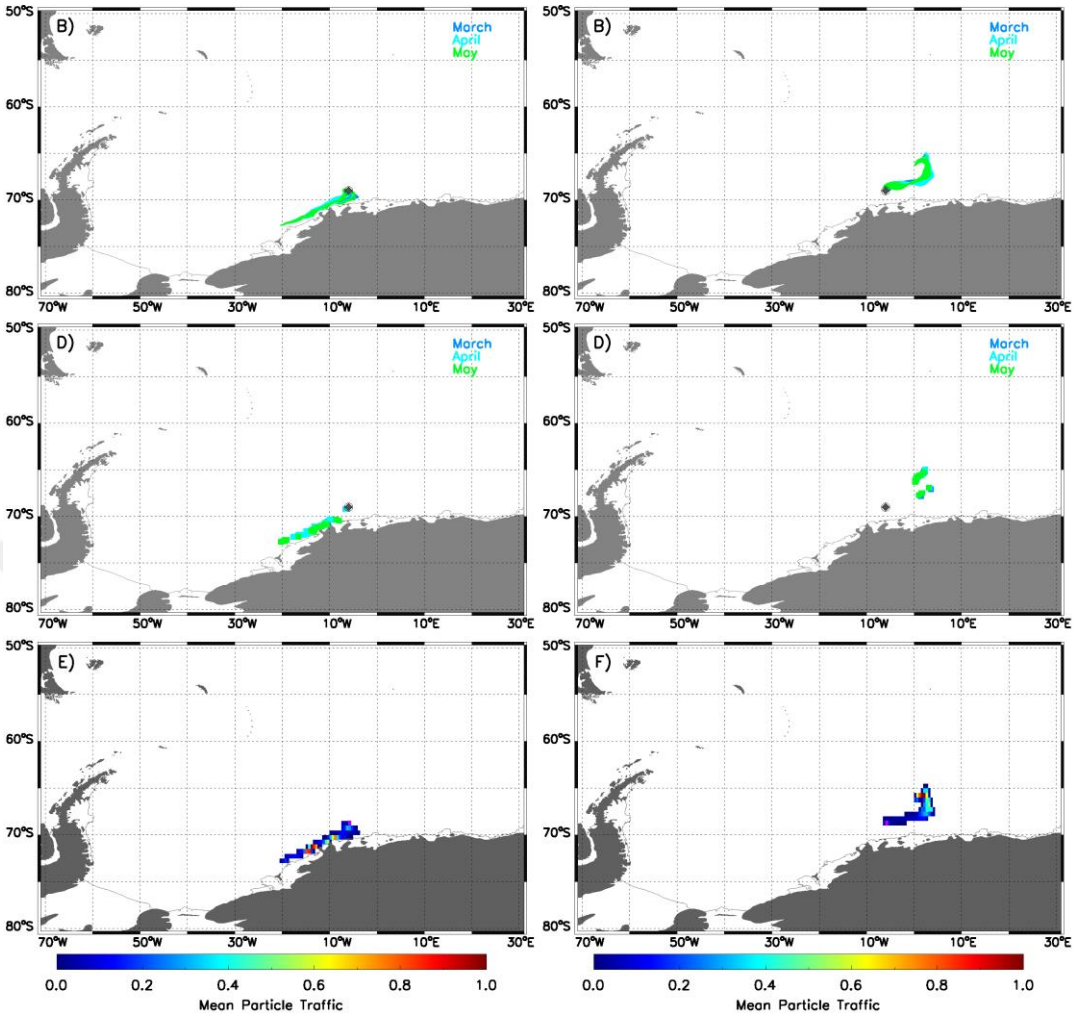
Appendix A 8 Lagrangian Particle tracking results of 92 particles released at station 53 at 200 m in austral spring and summer 2005. A) Trajectory of all particles tracked forward in time from 2005 to 2006, black diamond denotes the release point of particles. B) Trajectory of all particles tracked backwards in time from 2005 to 2004, black diamond denotes the release point of particles. C) End points of particles tracked forwards in time are denoted by squares, black diamond inside the circle denotes the release point of particles. D) End points of particles tracked backwards in time are denoted by squares, black diamond inside the circle denotes the release point of particles. E) Mean particle traffic map of particles tracked forwards in time, purple rectangle denotes the release cell. F) Mean particle traffic map of particles tracked backwards in time, purple rectangle denotes the release cell.



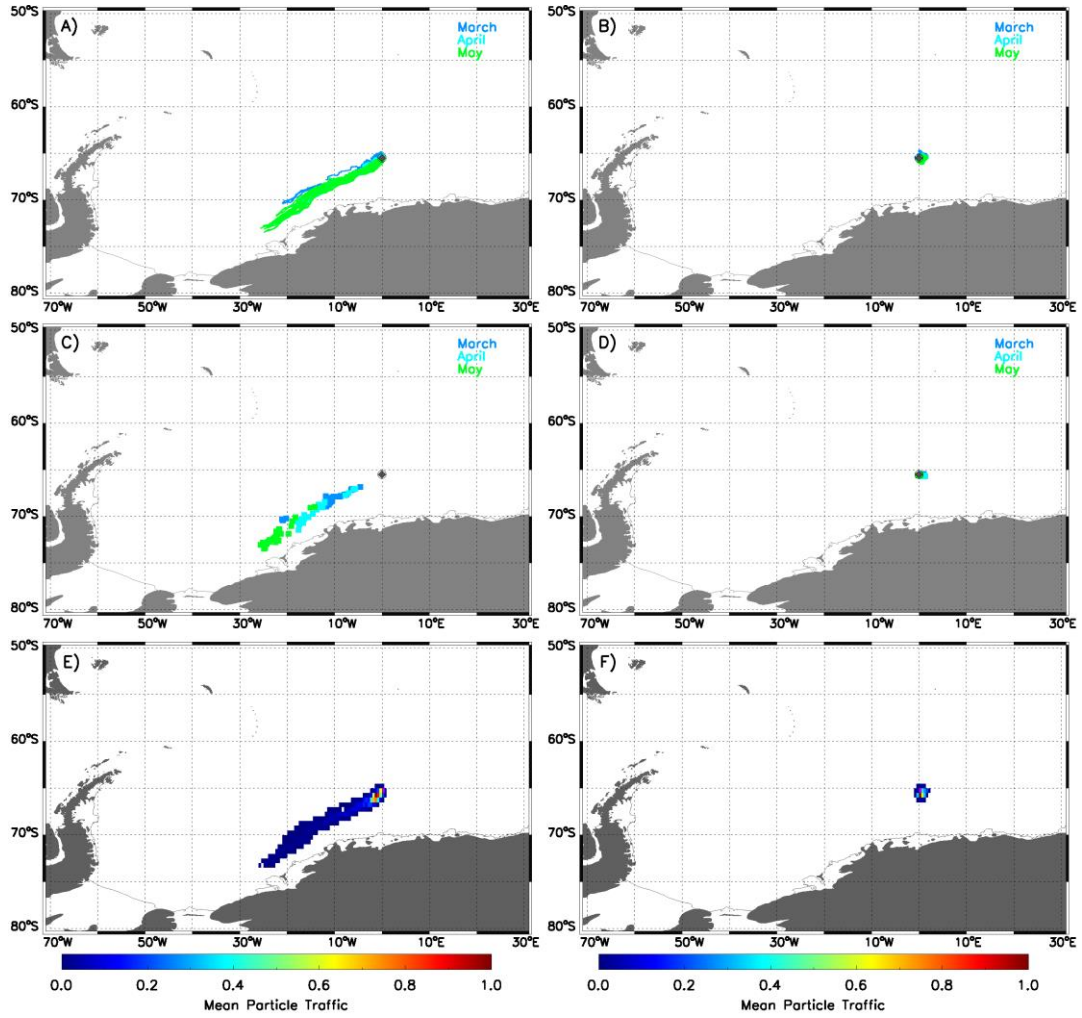
Appendix A 9 Lagrangian Particle tracking results of 92 particles released at station 92 at 200 m in austral spring and summer 2005. A) Trajectory of all particles tracked forward in time from 2005 to 2006, black diamond denotes the release point of particles. B) Trajectory of all particles tracked backwards in time from 2005 to 2004, black diamond denotes the release point of particles. C) End points of particles tracked forwards in time are denoted by squares, black diamond inside the circle denotes the release point of particles. D) End points of particles tracked backwards in time are denoted by squares, black diamond inside the circle denotes the release point of particles. E) Mean particle traffic map of particles tracked forwards in time, purple rectangle denotes the release cell. F) Mean particle traffic map of particles tracked backwards in time, purple rectangle denotes the release cell.



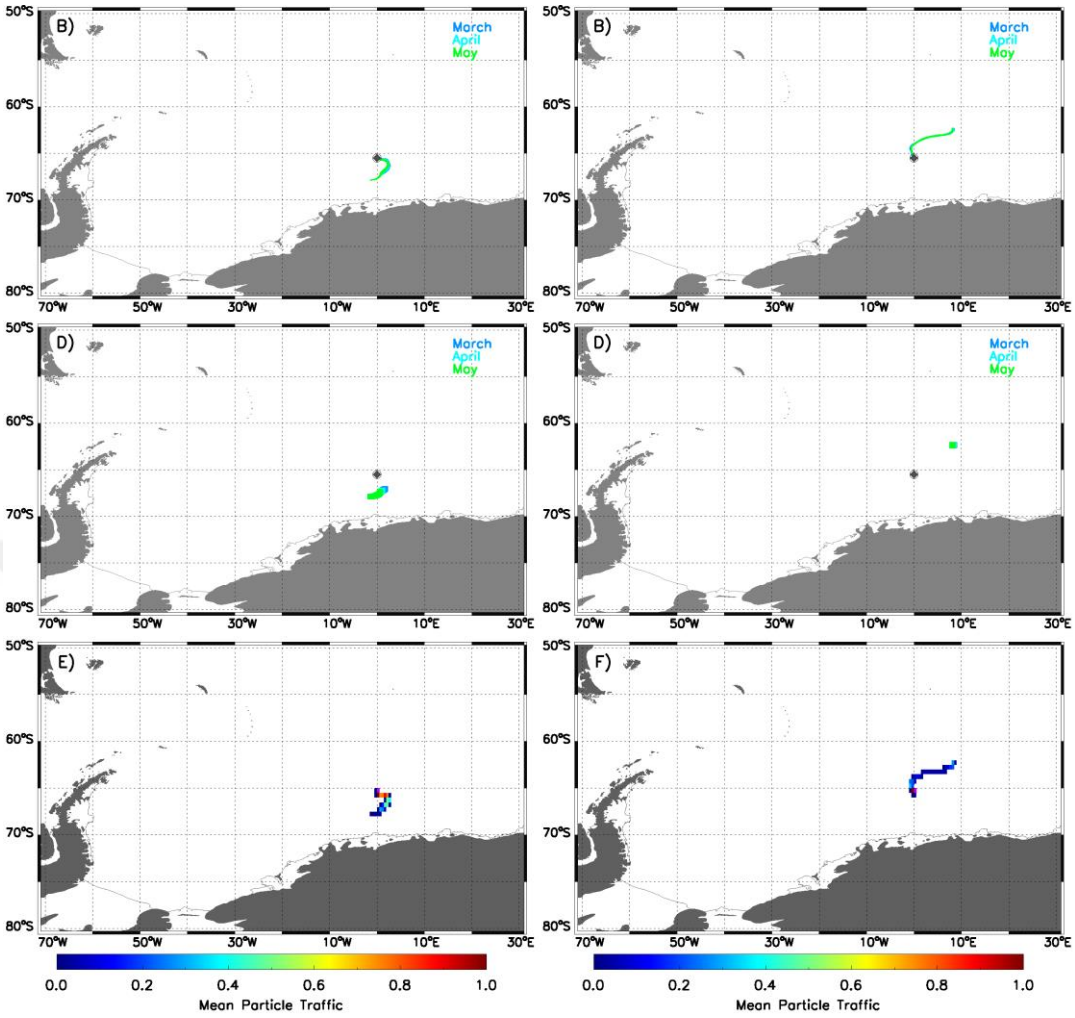
Appendix A 10 Lagrangian Particle tracking results of 92 particles released at station 621 in austral fall 2004. A) Trajectory of all particles tracked forward in time from 2004 to 2005, black diamond denotes the release point of particles. B) Trajectory of all particles tracked backwards in time from 2004 to 2003, black diamond denotes the release point of particles. C) End points of particles tracked forwards in time are denoted by squares, black diamond inside the circle denotes the release point of particles. D) End points of particles tracked backwards in time are denoted by squares, black diamond inside the circle denotes the release point of particles. E) Mean particle traffic map of particles tracked forwards in time, purple rectangle denotes the release cell. F) Mean particle traffic map of particles tracked backwards in time, purple rectangle denotes the release cell.



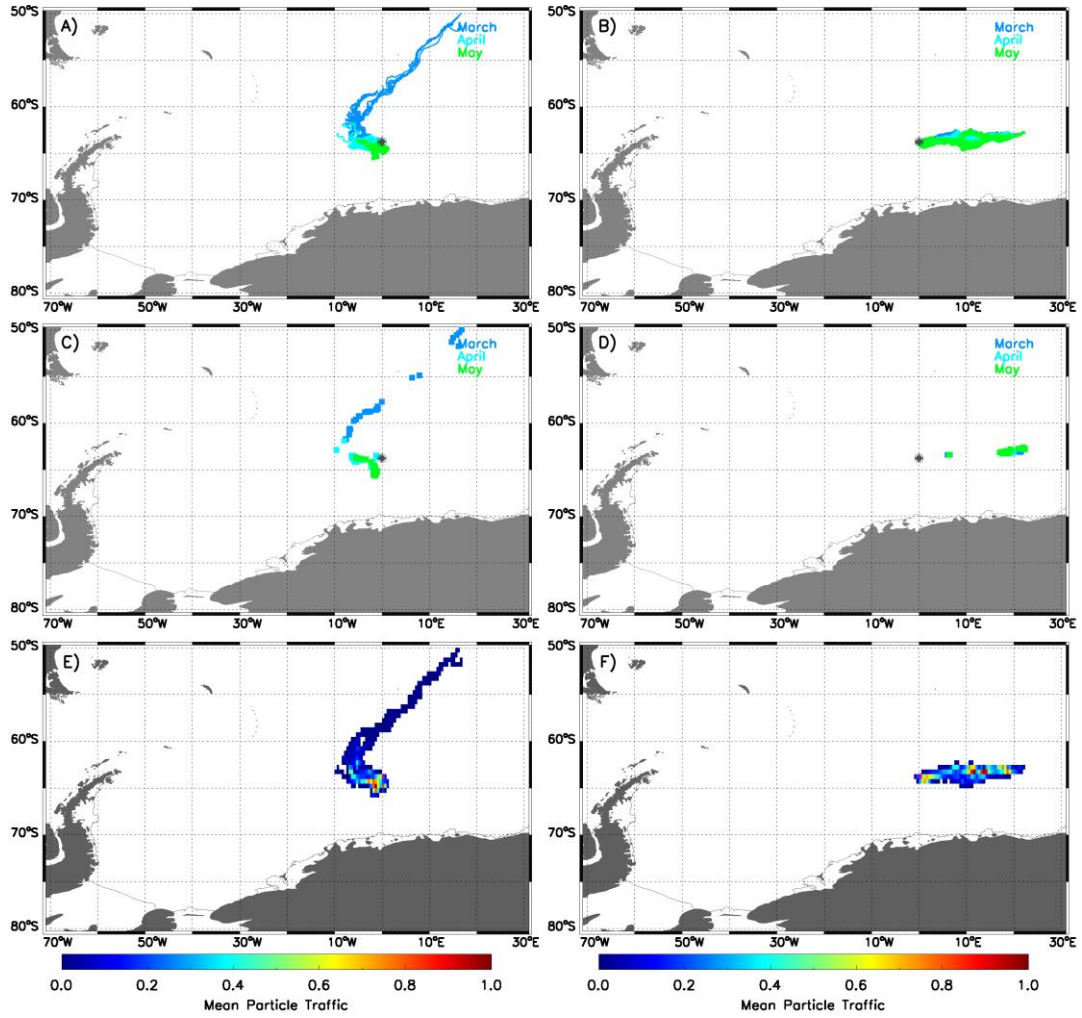
Appendix A 11 Lagrangian Particle tracking results of 92 particles released at station 621 at 200 m in austral fall 2004. A) Trajectory of all particles tracked forward in time from 2004 to 2005, black diamond denotes the release point of particles. B) Trajectory of all particles tracked backwards in time from 2004 to 2003, black diamond denotes the release point of particles. C) End points of particles tracked forwards in time are denoted by squares, black diamond inside the circle denotes the release point of particles. D) End points of particles tracked backwards in time are denoted by squares, black diamond inside the circle denotes the release point of particles. E) Mean particle traffic map of particles tracked forwards in time, purple rectangle denotes the release cell. F) Mean particle traffic map of particles tracked backwards in time, purple rectangle denotes the release cell.



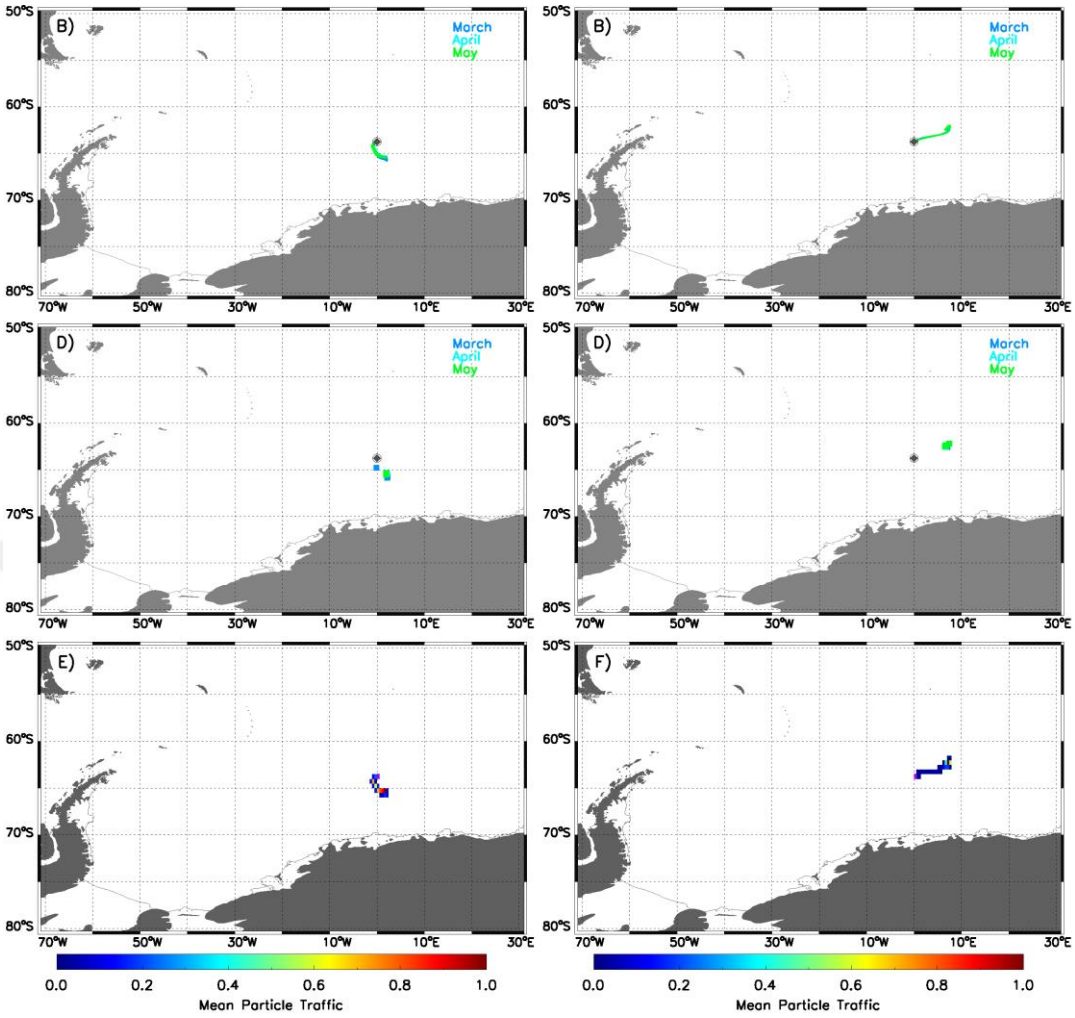
Appendix A 12 Lagrangian Particle tracking results of 92 particles released at station 678 in austral fall 2004. A) Trajectory of all particles tracked forward in time from 2004 to 2005, black diamond denotes the release point of particles. B) Trajectory of all particles tracked backwards in time from 2004 to 2003, black diamond denotes the release point of particles. C) End points of particles tracked forwards in time are denoted by squares, black diamond inside the circle denotes the release point of particles. D) End points of particles tracked backwards in time are denoted by squares, black diamond inside the circle denotes the release point of particles. E) Mean particle traffic map of particles tracked forwards in time, purple rectangle denotes the release cell. F) Mean particle traffic map of particles tracked backwards in time, purple rectangle denotes the release cell.



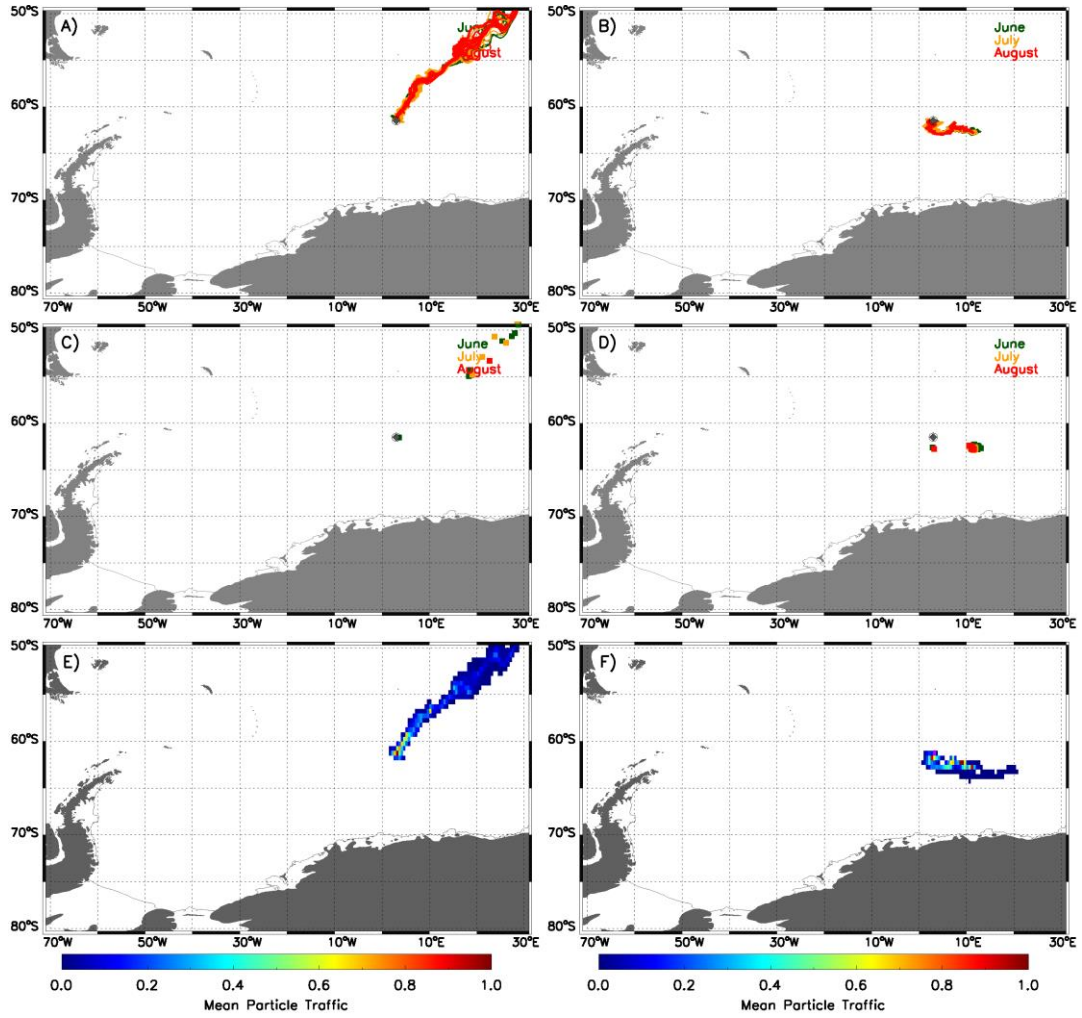
Appendix A 13 Lagrangian Particle tracking results of 92 particles released at station 678 at 200 m in austral fall 2004. A) Trajectory of all particles tracked forward in time from 2004 to 2005, black diamond denotes the release point of particles. B) Trajectory of all particles tracked backwards in time from 2004 to 2003, black diamond denotes the release point of particles. C) End points of particles tracked forwards in time are denoted by squares, black diamond inside the circle denotes the release point of particles. D) End points of particles tracked backwards in time are denoted by squares, black diamond inside the circle denotes the release point of particles. E) Mean particle traffic map of particles tracked forwards in time, purple rectangle denotes the release cell. F) Mean particle traffic map of particles tracked backwards in time, purple rectangle denotes the release cell.



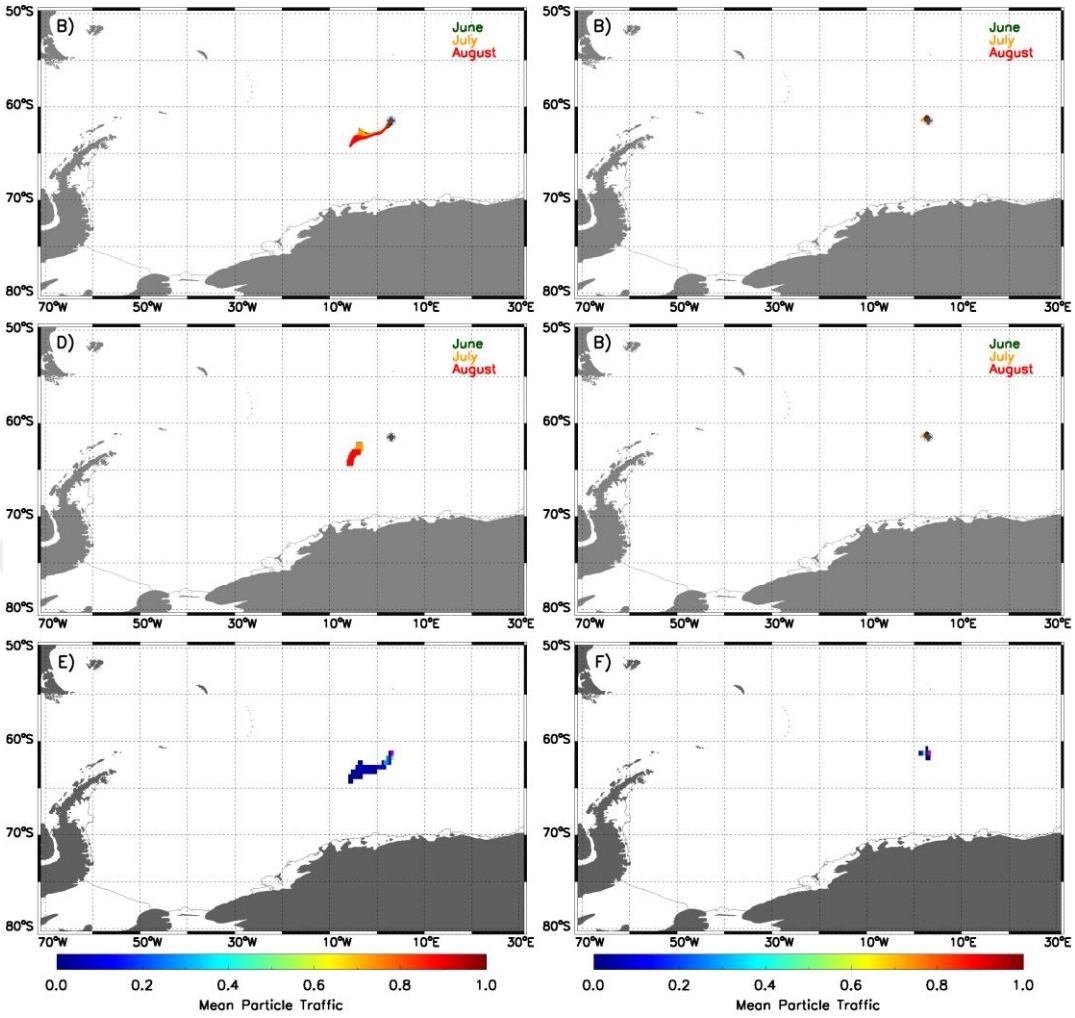
Appendix A 14 Lagrangian Particle tracking results of 92 particles released at station 683 in austral fall 2004. A) Trajectory of all particles tracked forward in time from 2004 to 2005, black diamond denotes the release point of particles. B) Trajectory of all particles tracked backwards in time from 2004 to 2003, black diamond denotes the release point of particles. C) End points of particles tracked forwards in time are denoted by squares, black diamond inside the circle denotes the release point of particles. D) End points of particles tracked backwards in time are denoted by squares, black diamond inside the circle denotes the release point of particles. E) Mean particle traffic map of particles tracked forwards in time, purple rectangle denotes the release cell. F) Mean particle traffic map of particles tracked backwards in time, purple rectangle denotes the release cell.



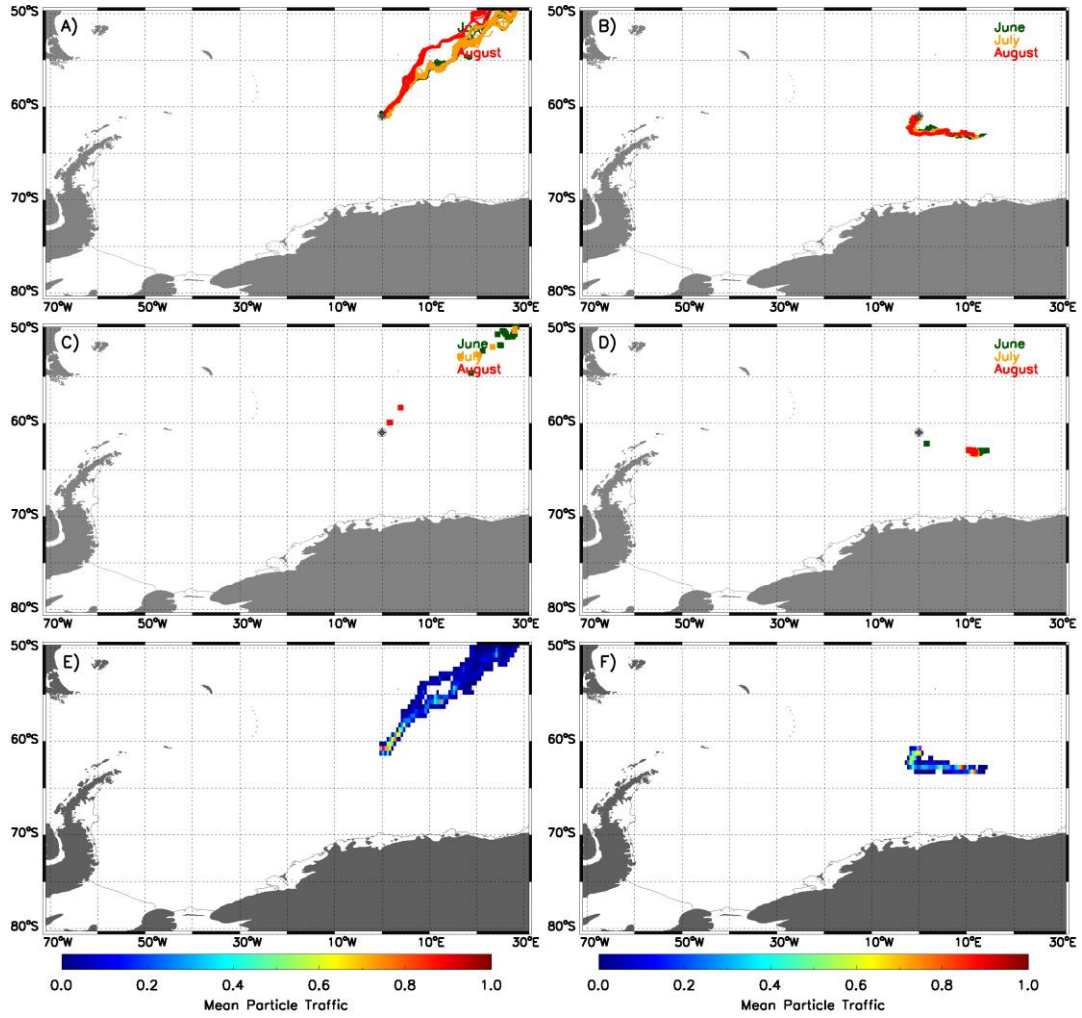
Appendix A 15 Lagrangian Particle tracking results of 92 particles released at station 683 at 200 m in austral fall 2004. A) Trajectory of all particles tracked forward in time from 2004 to 2005, black diamond denotes the release point of particles. B) Trajectory of all particles tracked backwards in time from 2004 to 2003, black diamond denotes the release point of particles. C) End points of particles tracked forwards in time are denoted by squares, black diamond inside the circle denotes the release point of particles. D) End points of particles tracked backwards in time are denoted by squares, black diamond inside the circle denotes the release point of particles. E) Mean particle traffic map of particles tracked forwards in time, purple rectangle denotes the release cell. F) Mean particle traffic map of particles tracked backwards in time, purple rectangle denotes the release cell.



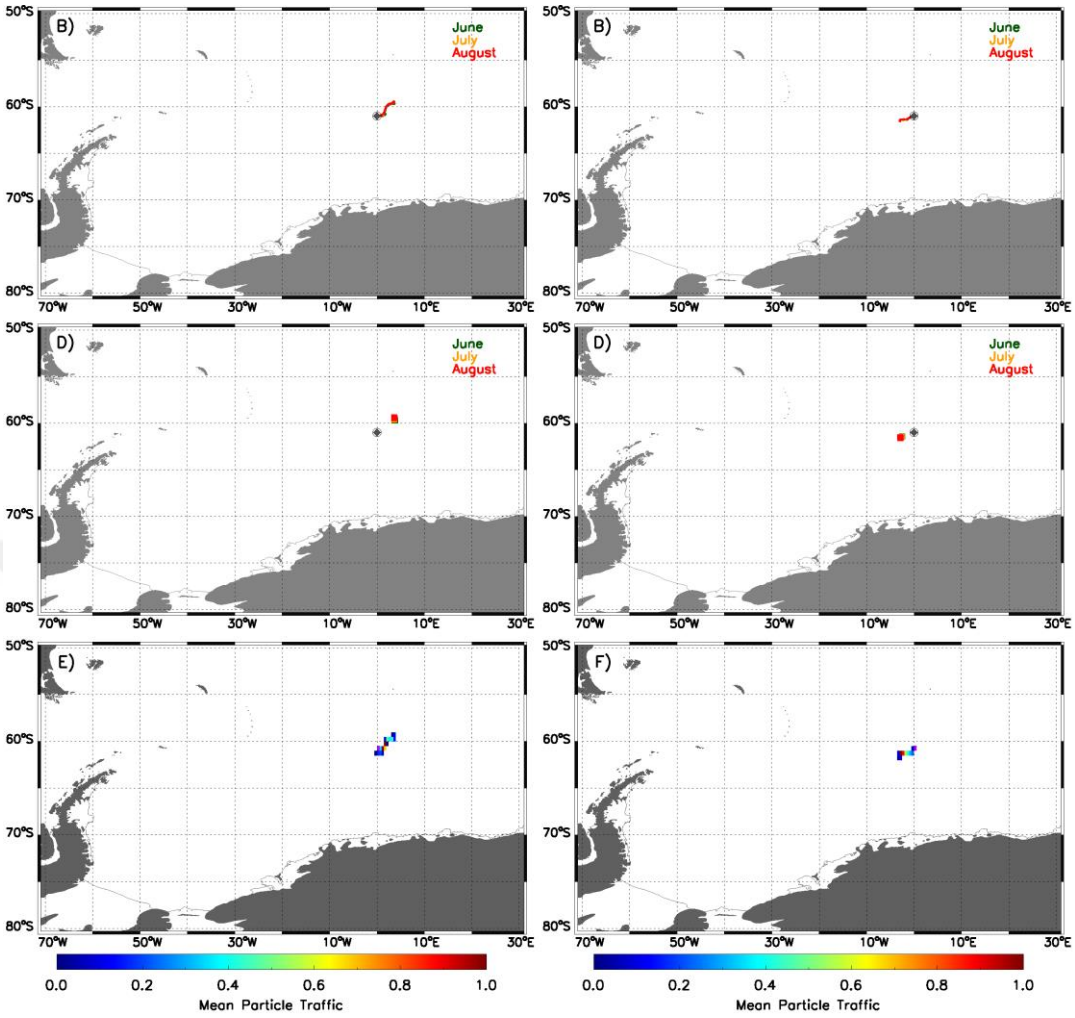
Appendix A 16 Lagrangian Particle tracking results of 92 particles released at station 474 in austral winter 2006. A) Trajectory of all particles tracked forward in time from 2006 to 2007, black diamond denotes the release point of particles. B) Trajectory of all particles tracked backwards in time from 2006 to 2005, black diamond denotes the release point of particles. C) End points of particles tracked forwards in time are denoted by squares, black diamond inside the circle denotes the release point of particles. D) End points of particles tracked backwards in time are denoted by squares, black diamond inside the circle denotes the release point of particles. E) Mean particle traffic map of particles tracked forwards in time, purple rectangle denotes the release cell. F) Mean particle traffic map of particles tracked backwards in time, purple rectangle denotes the release cell.



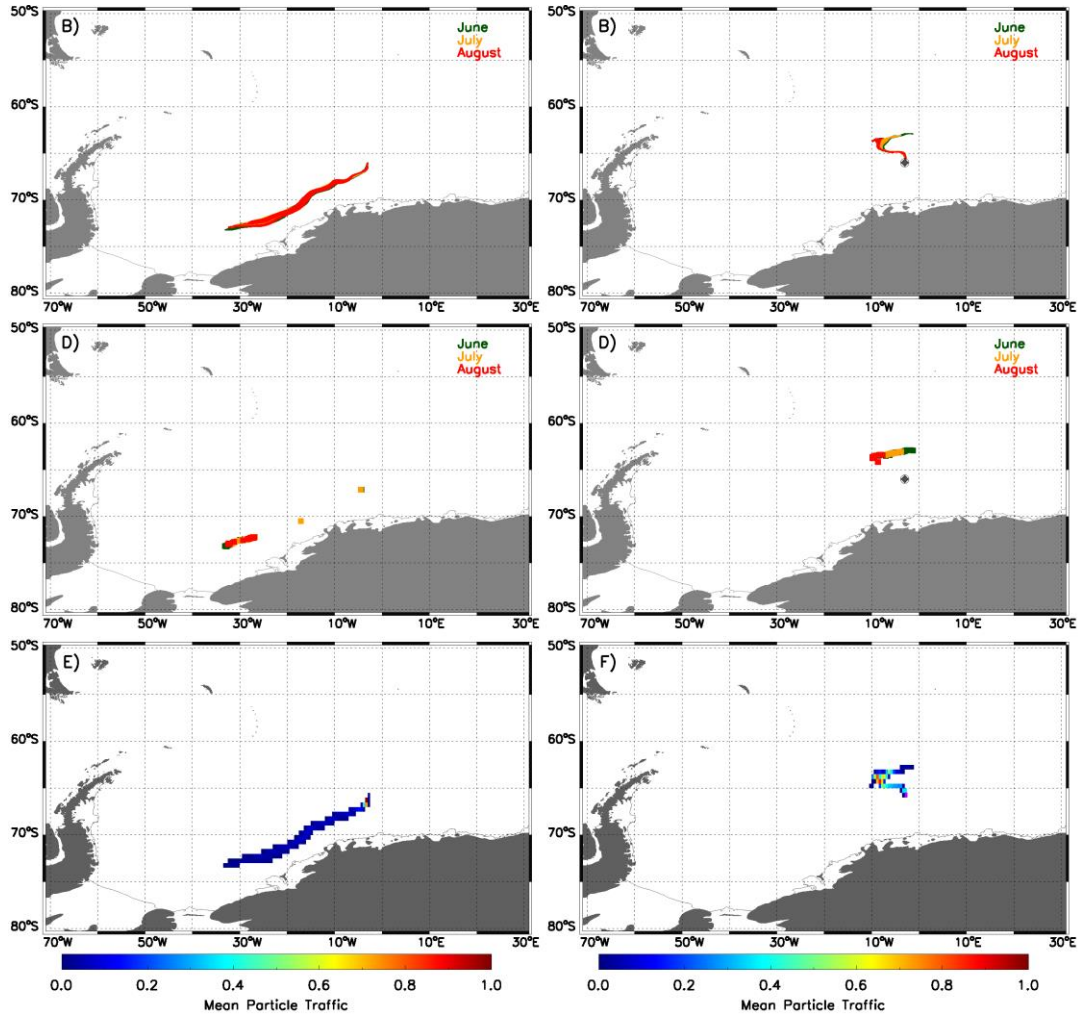
Appendix A 17 Lagrangian Particle tracking results of 92 particles released at station 474 at 200 m in austral winter 2006. A) Trajectory of all particles tracked forward in time from 2006 to 2007, black diamond denotes the release point of particles. B) Trajectory of all particles tracked backwards in time from 2006 to 2005, black diamond denotes the release point of particles. C) End points of particles tracked forwards in time are denoted by squares, black diamond inside the circle denotes the release point of particles. D) End points of particles tracked backwards in time are denoted by squares, black diamond inside the circle denotes the release point of particles. E) Mean particle traffic map of particles tracked forwards in time, purple rectangle denotes the release cell. F) Mean particle traffic map of particles tracked backwards in time, purple rectangle denotes the release cell.



Appendix A 18 Lagrangian Particle tracking results of 92 particles released at station 508 in austral winter 2006. A) Trajectory of all particles tracked forward in time from 2006 to 2007, black diamond denotes the release point of particles. B) Trajectory of all particles tracked backwards in time from 2006 to 2005, black diamond denotes the release point of particles. C) End points of particles tracked forwards in time are denoted by squares, black diamond inside the circle denotes the release point of particles. D) End points of particles tracked backwards in time are denoted by squares, black diamond inside the circle denotes the release point of particles. E) Mean particle traffic map of particles tracked forwards in time, purple rectangle denotes the release cell. F) Mean particle traffic map of particles tracked backwards in time, purple rectangle denotes the release cell.

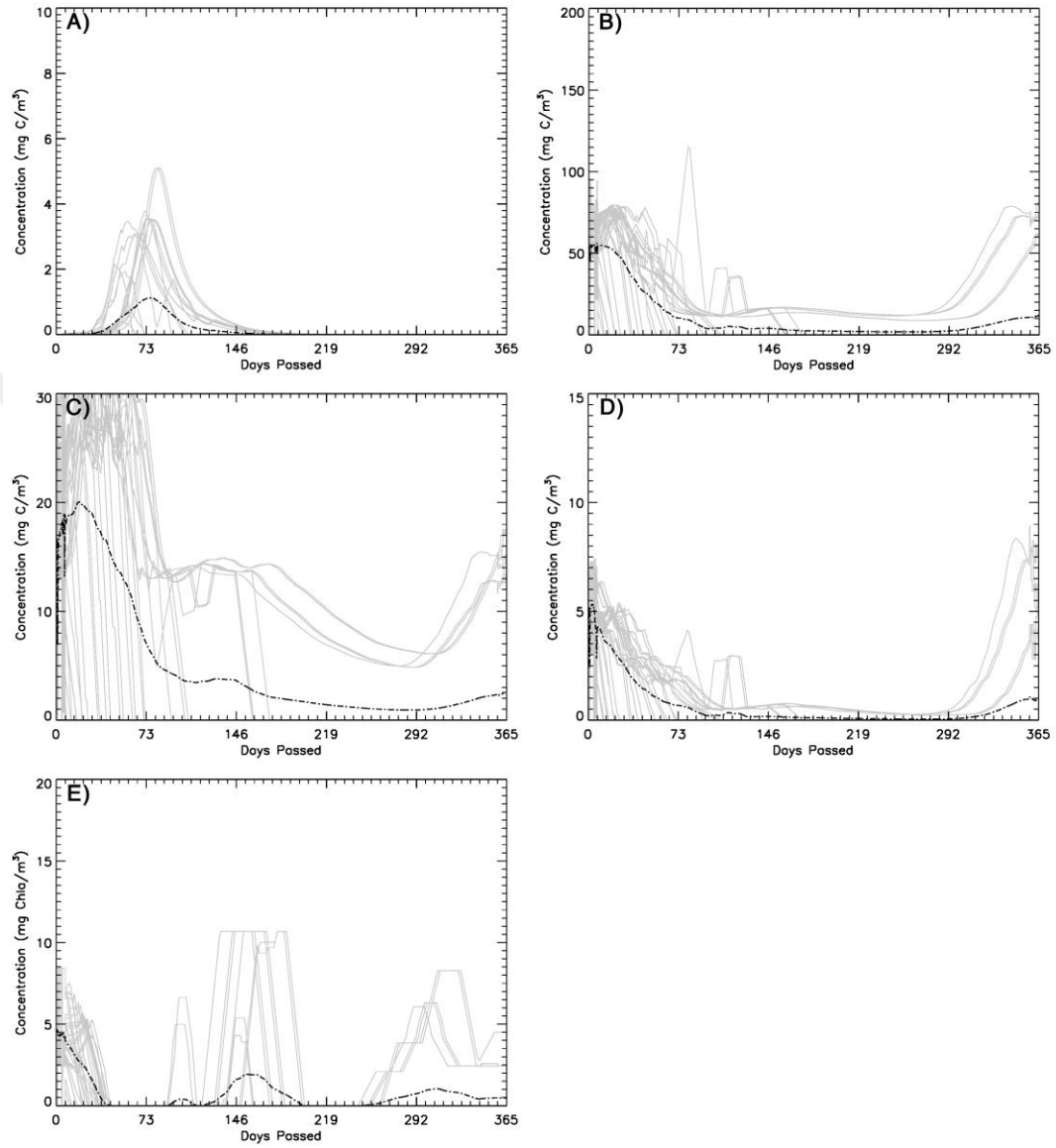


Appendix A 19 Lagrangian Particle tracking results of 92 particles released at station 508 at 200 m in austral winter 2006. A) Trajectory of all particles tracked forward in time from 2006 to 2007, black diamond denotes the release point of particles. B) Trajectory of all particles tracked backwards in time from 2006 to 2005, black diamond denotes the release point of particles. C) End points of particles tracked forwards in time are denoted by squares, black diamond inside the circle denotes the release point of particles. D) End points of particles tracked backwards in time are denoted by squares, black diamond inside the circle denotes the release point of particles. E) Mean particle traffic map of particles tracked forwards in time, purple rectangle denotes the release cell. F) Mean particle traffic map of particles tracked backwards in time, purple rectangle denotes the release cell.

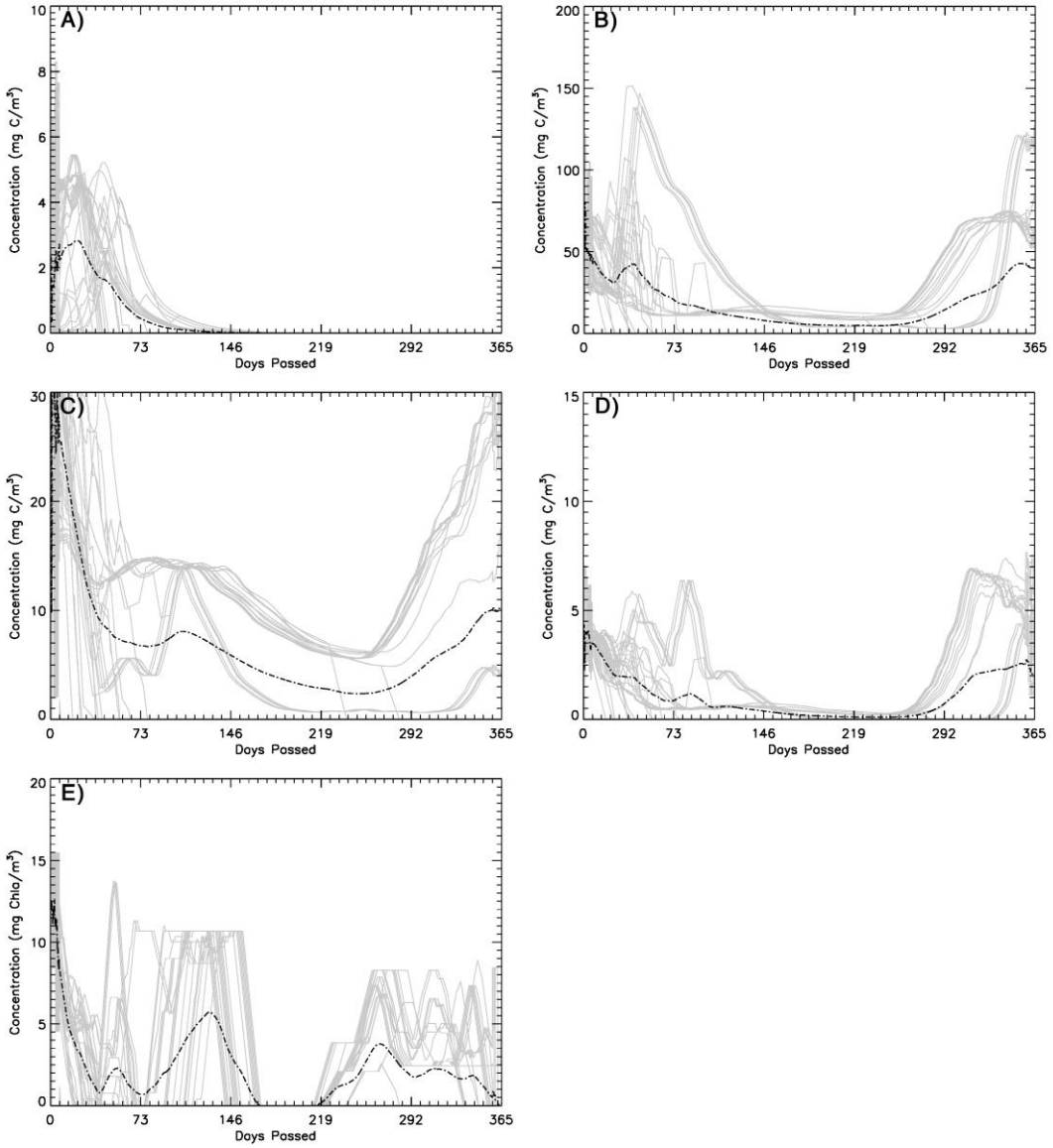


Appendix A 20 Lagrangian Particle tracking results of 92 particles released at station 516 at 200 m in austral winter 2006. A) Trajectory of all particles tracked forward in time from 2006 to 2007, black diamond denotes the release point of particles. B) Trajectory of all particles tracked backwards in time from 2006 to 2005, black diamond denotes the release point of particles. C) End points of particles tracked forwards in time are denoted by squares, black diamond inside the circle denotes the release point of particles. D) End points of particles tracked backwards in time are denoted by squares, black diamond inside the circle denotes the release point of particles. E) Mean particle traffic map of particles tracked forwards in time, purple rectangle denotes the release cell. F) Mean particle traffic map of particles tracked backwards in time, purple rectangle denotes the release cell.

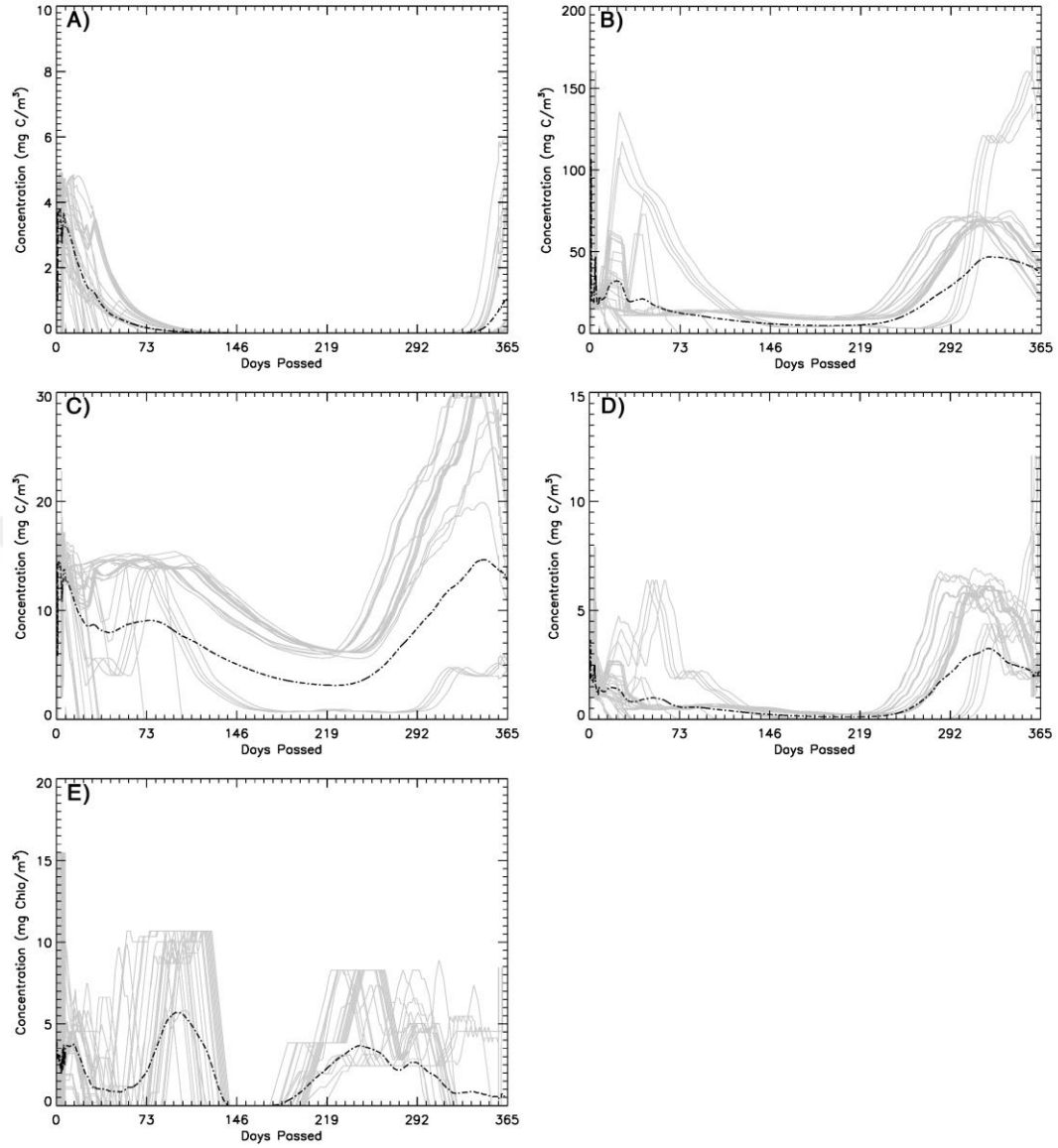
B. Larvae and juvenile IBM results



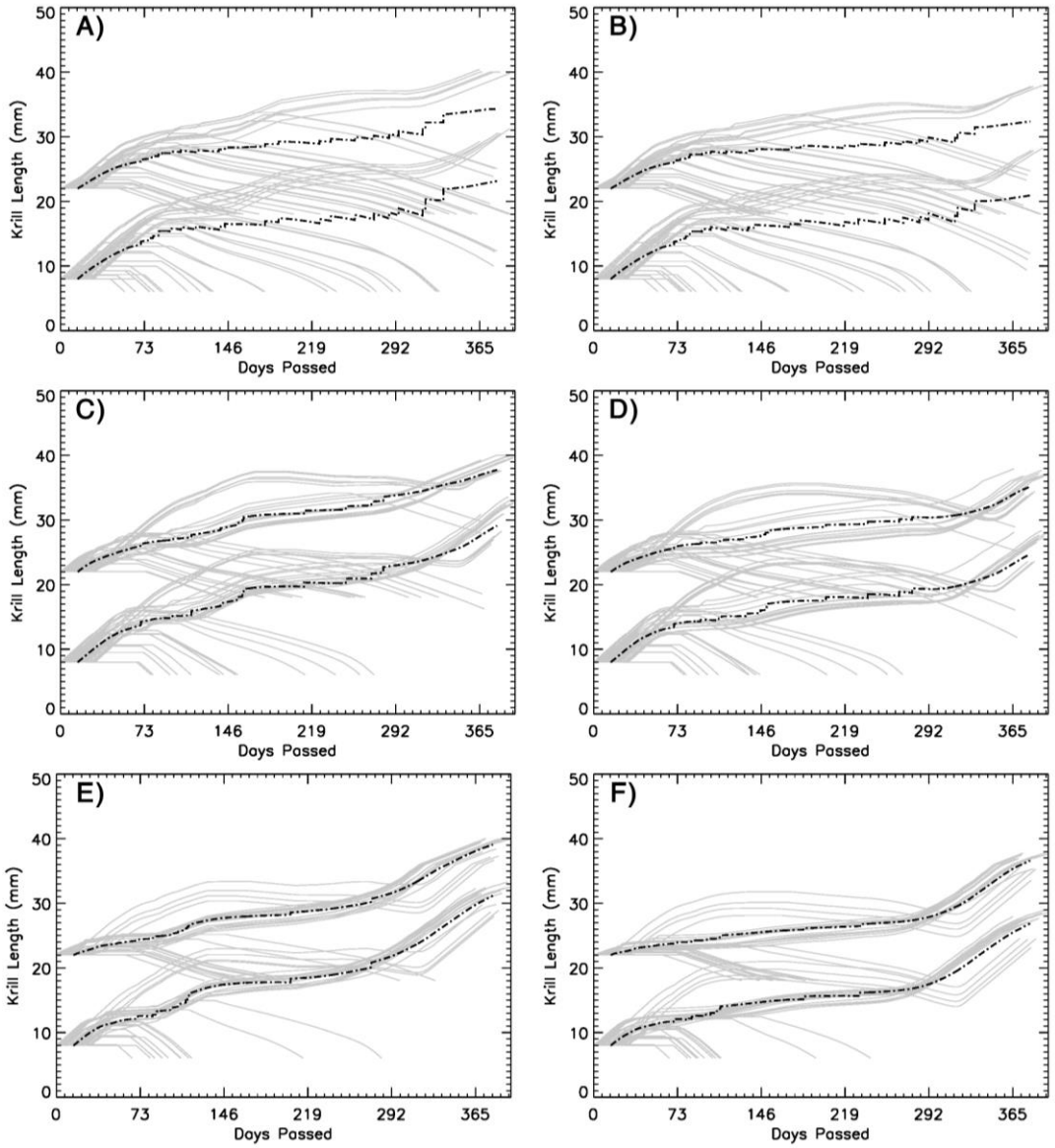
Appendix B 1 Concentrations of food for krill encountered by all drifters released from station 44 in November 2005. A) Copepod concentration (mgC m^{-3}), B) Diatom concentration (mgC m^{-3}), C) Nanophytoplankton concentration (mgC m^{-3}), D) Detritus concentration (mgC m^{-3}), E) Sea ice algae concentration (mg Chla m^{-3}). The black dash dot dash line is the average value of all particles.



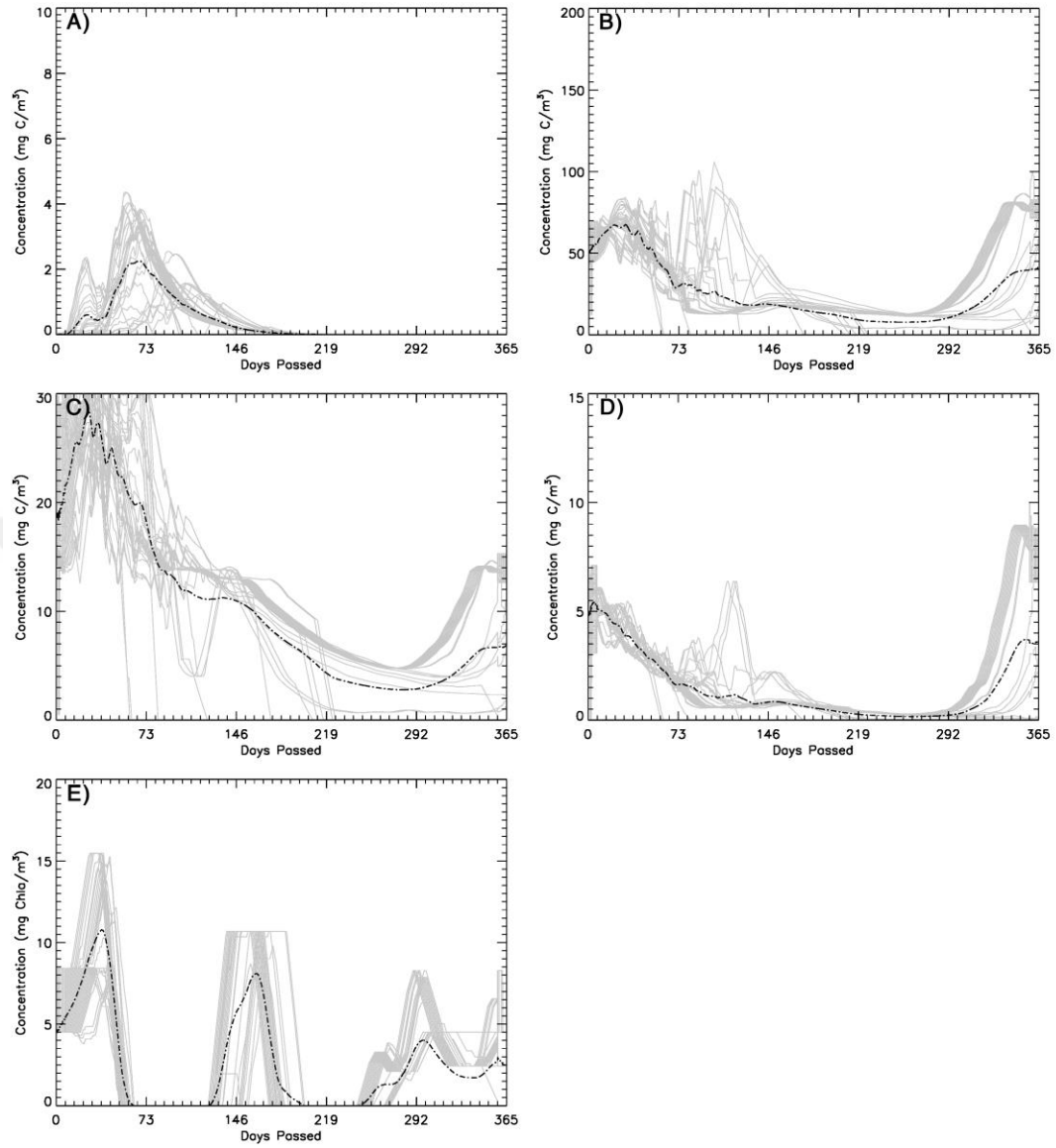
Appendix B 2 Concentrations of food for krill encountered by all drifters released from station 44 in December 2005. A) Copepod concentration (mgC m^{-3}), B) Diatom concentration (mgC m^{-3}), C) Nanophytoplankton concentration (mgC m^{-3}), D) Detritus concentration (mgC m^{-3}), E) Sea ice algae concentration (mg Chla m^{-3}). The black dash dot dash line is the average value of all particles.



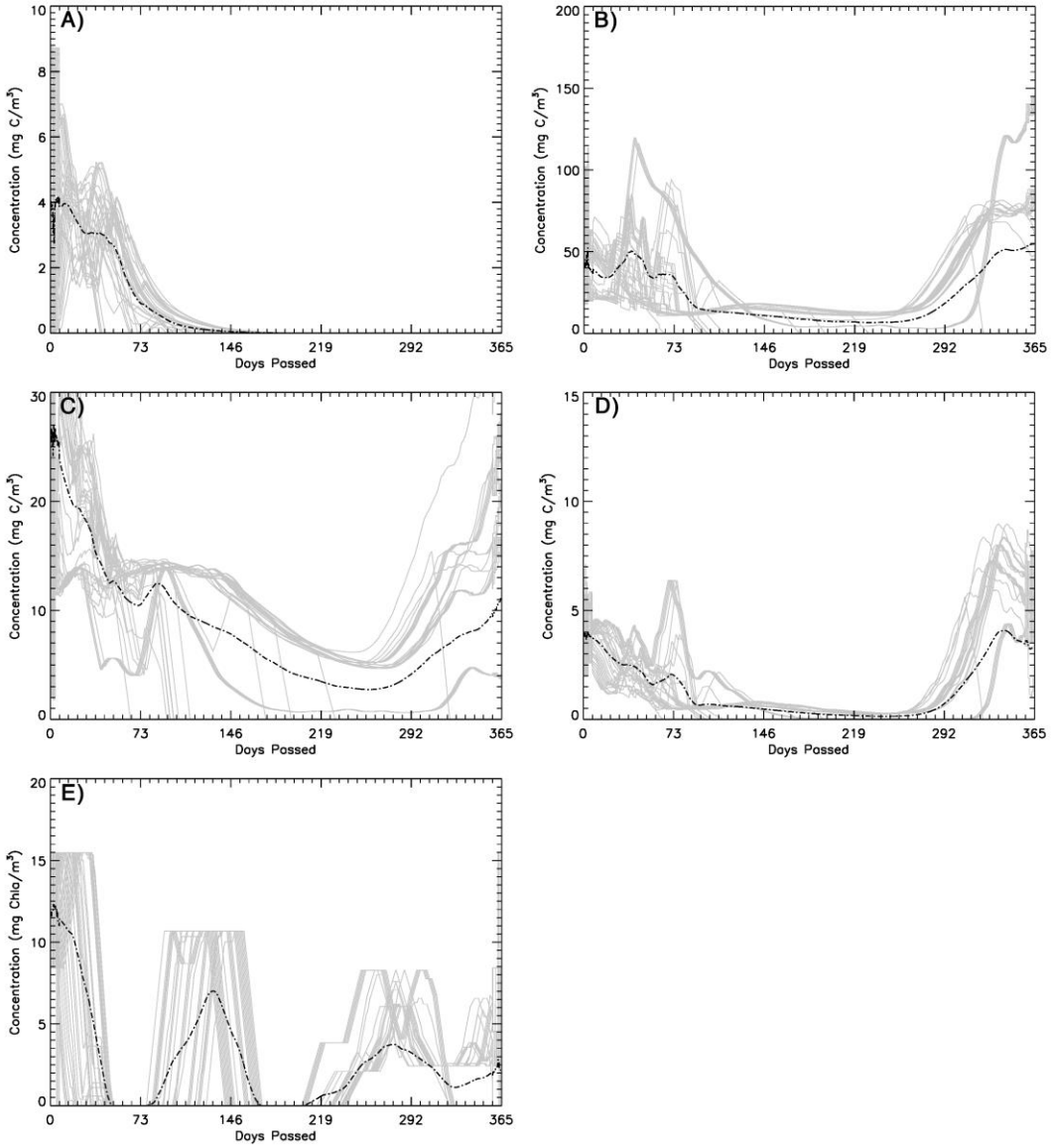
Appendix B 3 Concentrations of food for krill encountered by all drifters released from station 44 in January 2006. A) Copepod concentration (mgC m^{-3}), B) Diatom concentration (mgC m^{-3}), C) Nanophytoplankton concentration (mgC m^{-3}), D) Detritus concentration (mgC m^{-3}), E) Sea ice algae concentration (mg Chla m^{-3}). The black dash dot dash line is the average value of all particles.



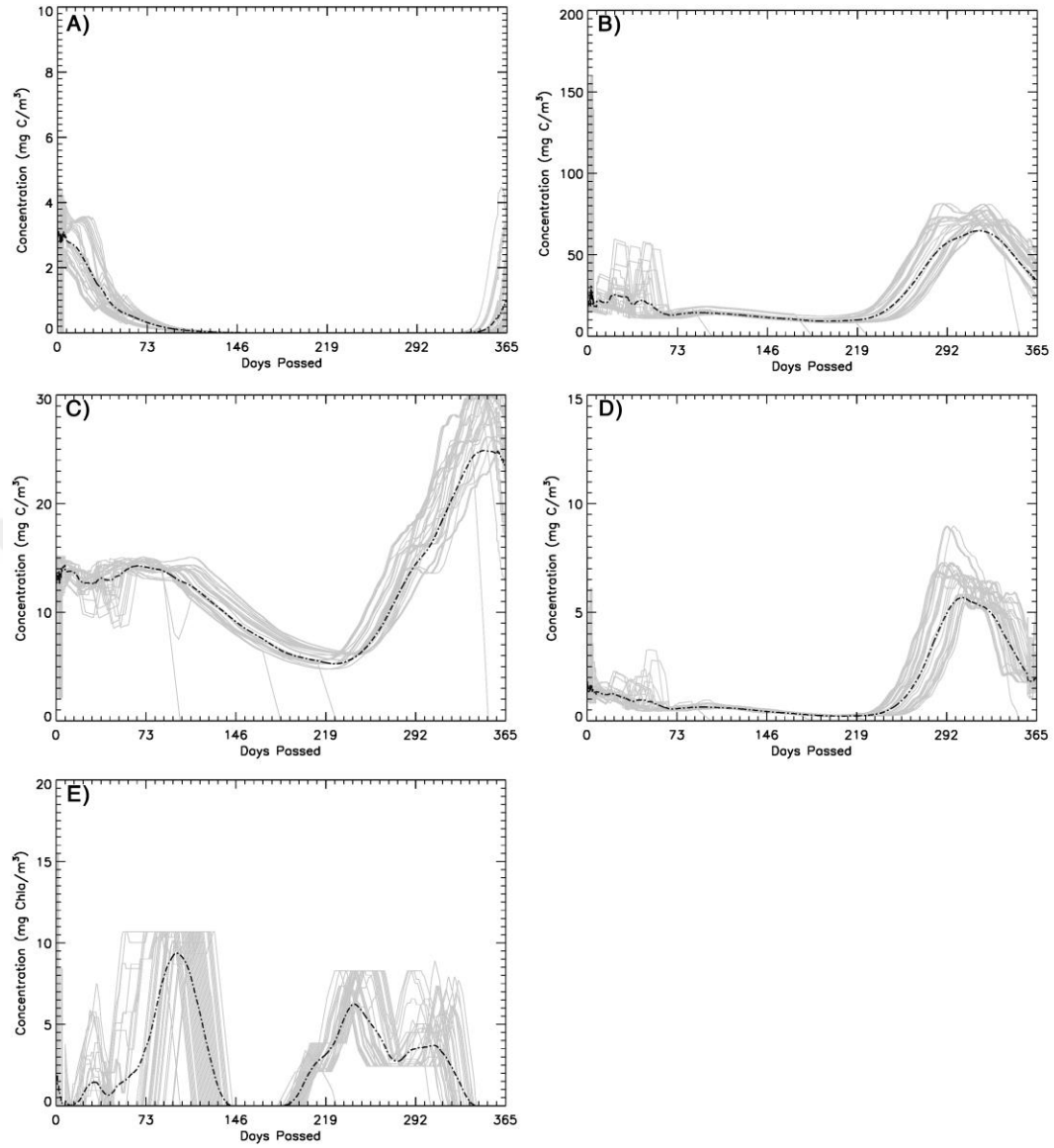
Appendix B 4 Krill growth over time for krill originating at station 44 starting A) November of 2005 feeding on sea ice algae, B) November of 2005 without feeding on sea ice algae, C) December of 2005 feeding on sea ice algae, D) December of 2005 without feeding sea ice algae, E) January of 2006 feeding on sea ice algae, F) January of 2006 without feeding sea ice algae. Juveniles start at 22mm, larvae start at 8mm. The black dash dot dash line indicates the average of all the surviving krill. Particles representing krill were released on consecutive days seen by the offset on the x-axis month and the average growth line corresponds to day 15 day.



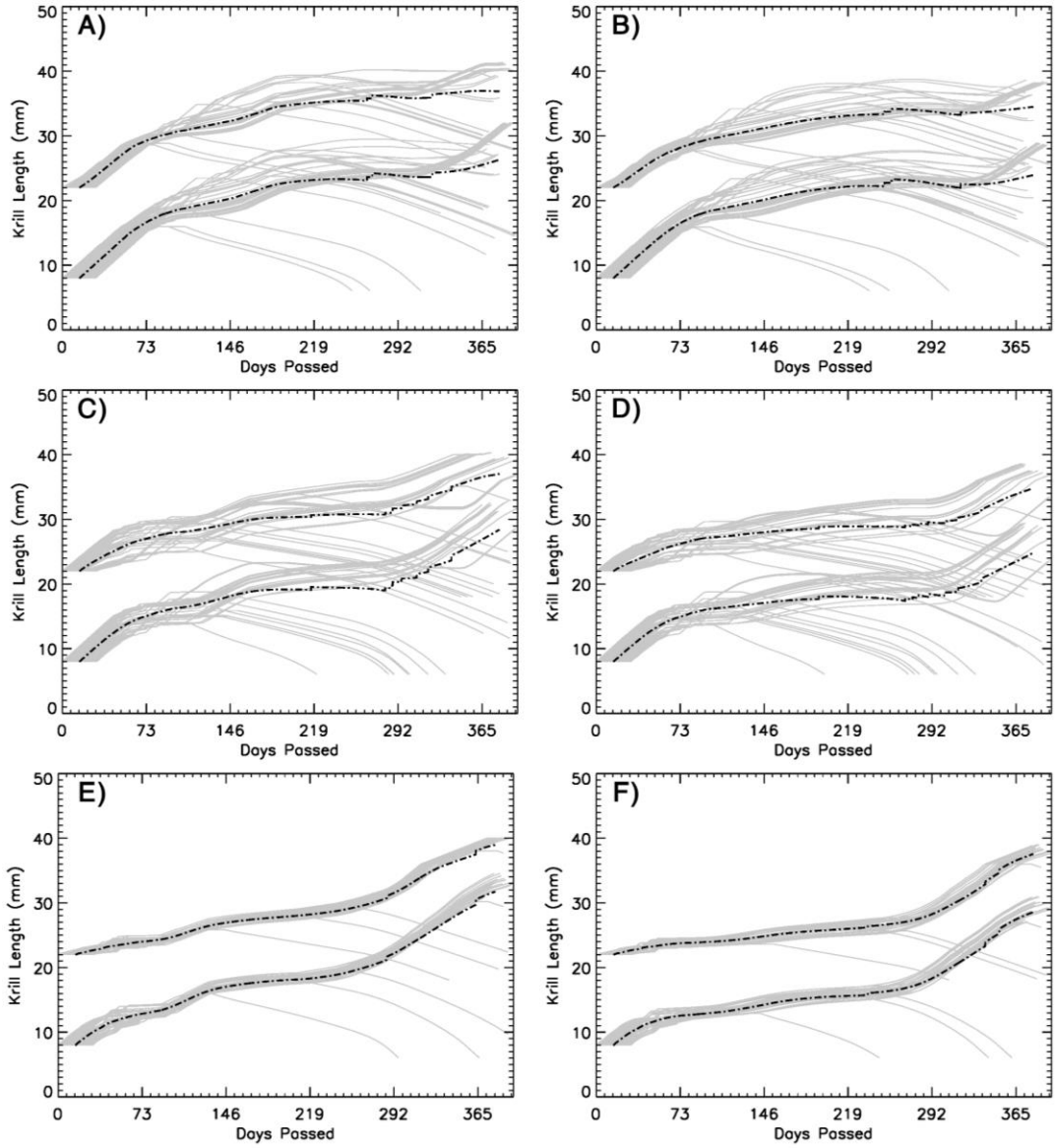
Appendix B 5 Concentrations of food for krill encountered by all drifters released from station 46 in November 2005. A) Copepod concentration (mgC m^{-3}), B) Diatom concentration (mgC m^{-3}), C) Nanophytoplankton concentration (mgC m^{-3}), D) Detritus concentration (mgC m^{-3}), E) Sea ice algae concentration (mg Chla m^{-3}). The black dash dot dash line is the average value of all particles.



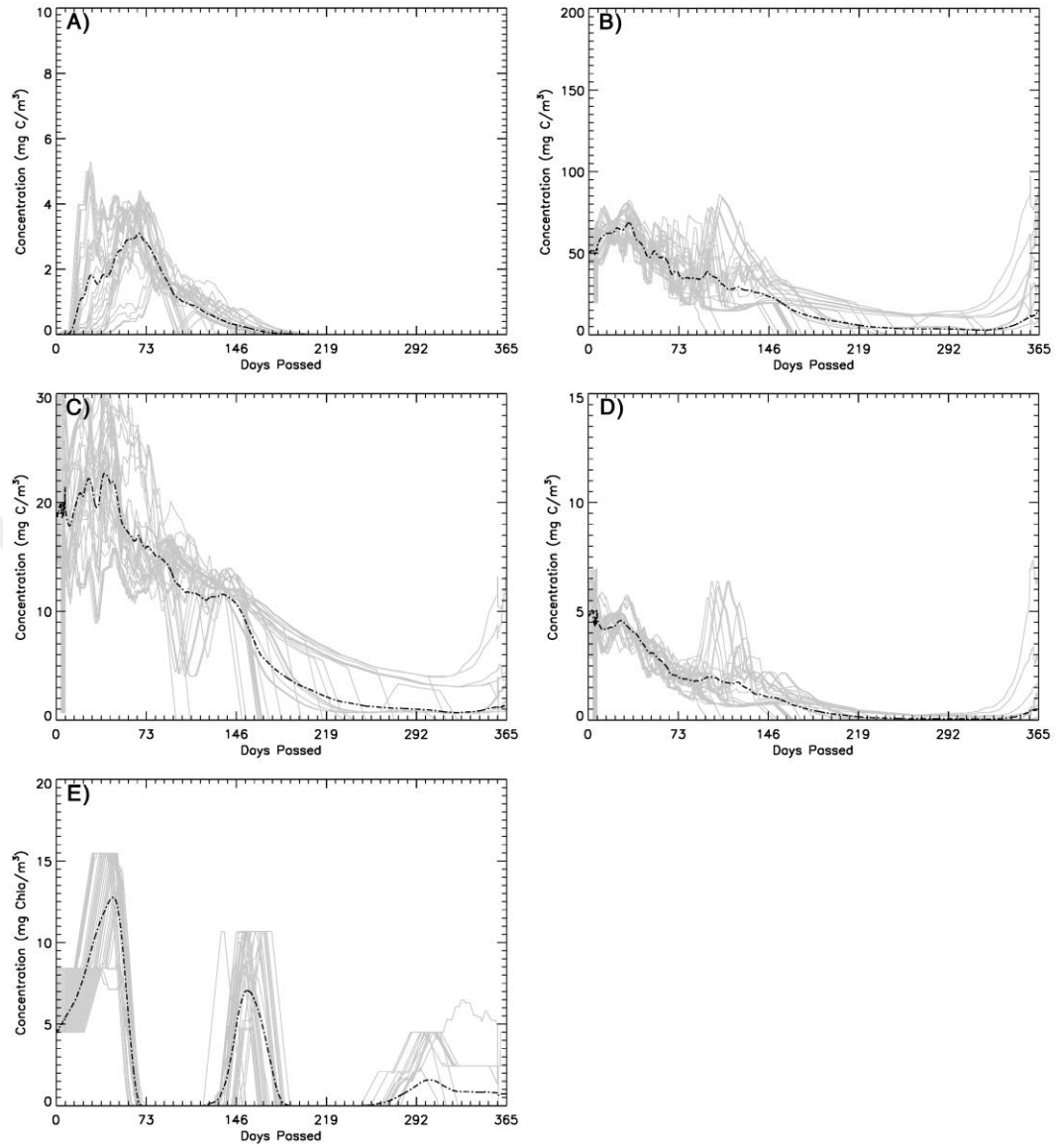
Appendix B 6 Concentrations of food for krill encountered by all drifters released from station 46 in December 2005. A) Copepod concentration (mgC m^{-3}), B) Diatom concentration (mgC m^{-3}), C) Nanophytoplankton concentration (mgC m^{-3}), D) Detritus concentration (mgC m^{-3}), E) Sea ice algae concentration (mg Chla m^{-3}). The black dash dot dash line is the average value of all particles.



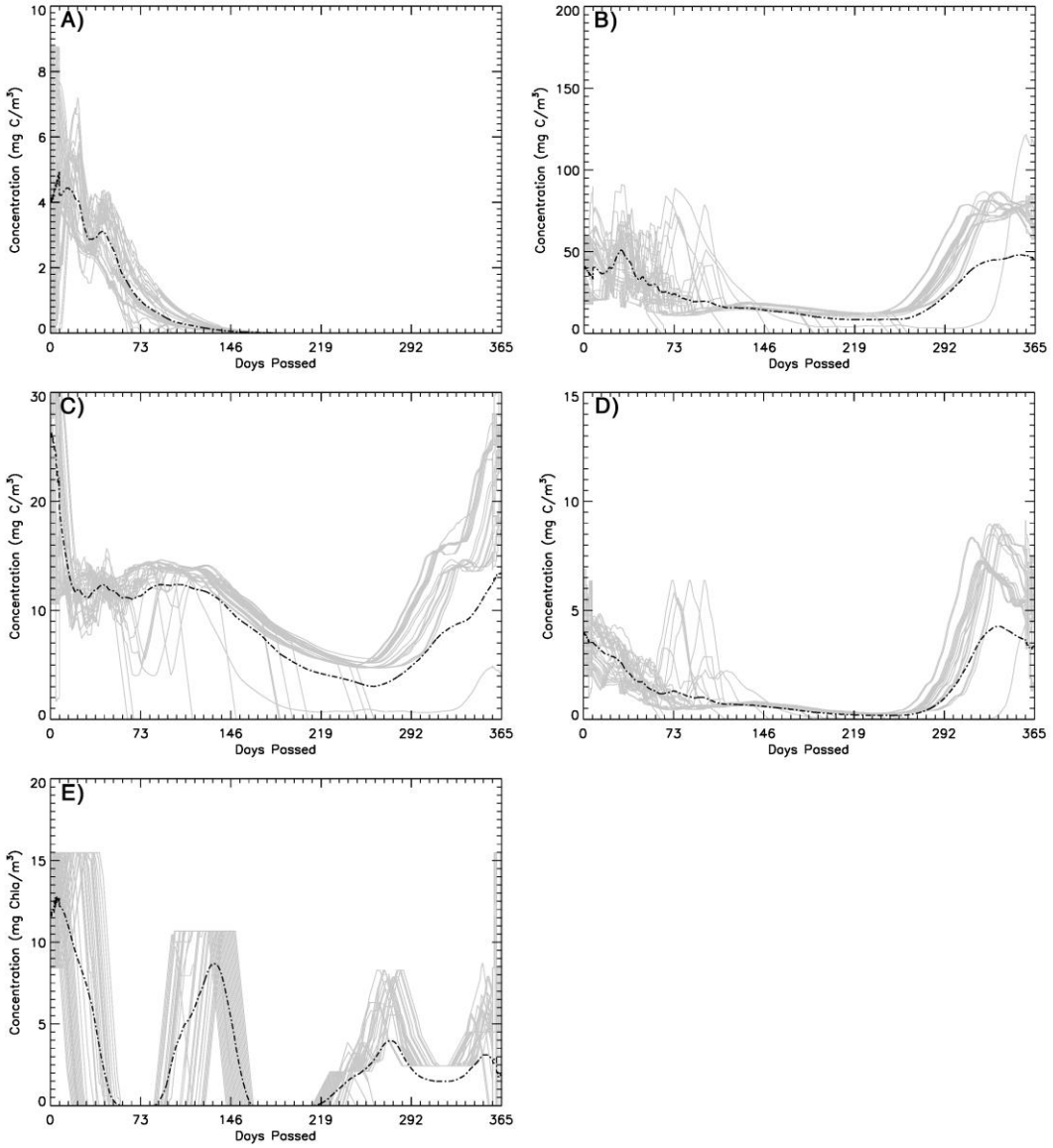
Appendix B 7 Concentrations of food for krill encountered by all drifters released from station 46 in January 2006. A) Copepod concentration (mgC m^{-3}), B) Diatom concentration (mgC m^{-3}), C) Nanophytoplankton concentration (mgC m^{-3}), D) Detritus concentration (mgC m^{-3}), E) Sea ice algae concentration (mg Chla m^{-3}). The black dash dot dash line is the average value of all particles.



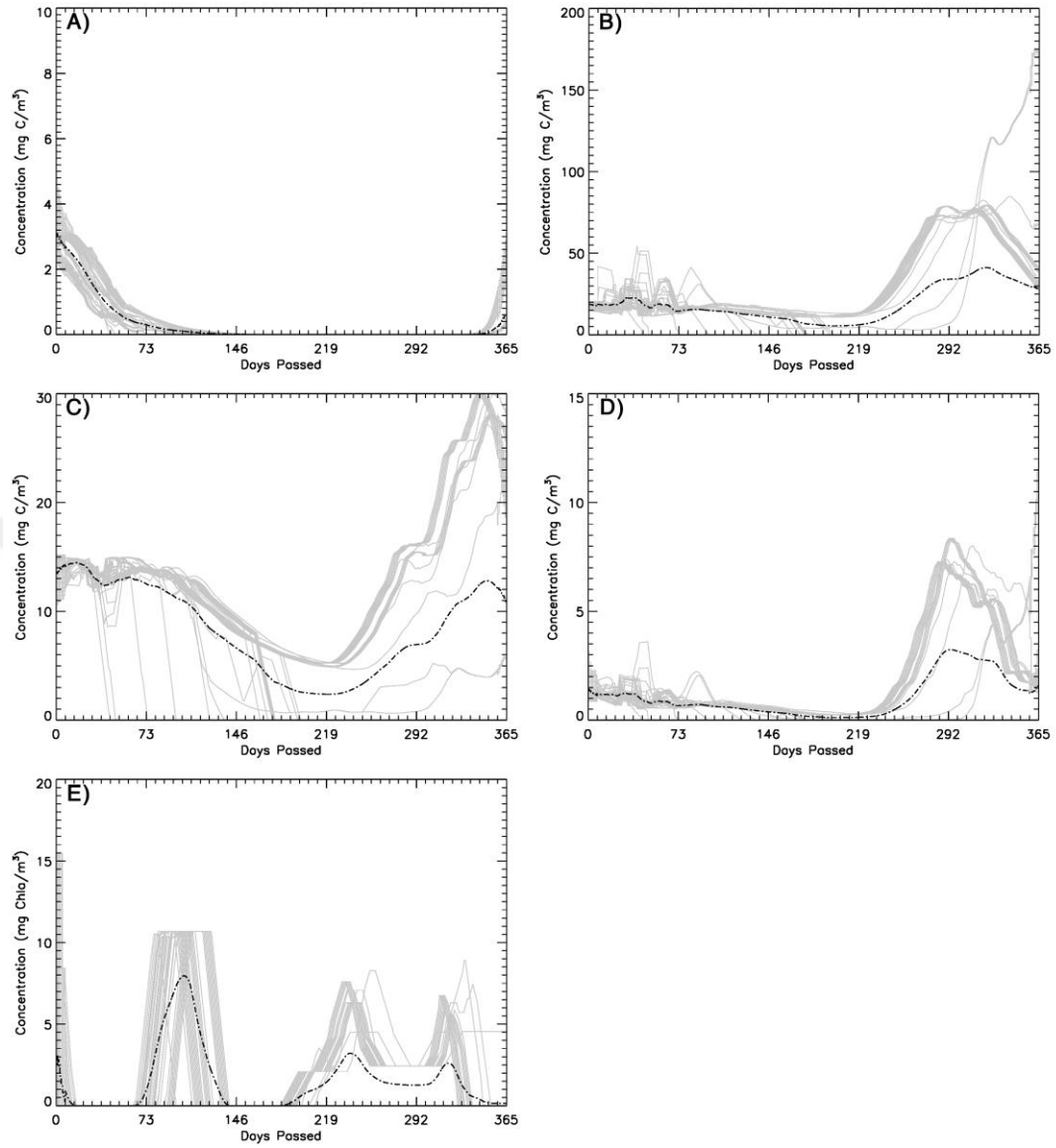
Appendix B 8 Krill growth over time for krill originating at station 46 starting A) November of 2005 feeding on sea ice algae, B) November of 2005 without feeding on sea ice algae, C) December of 2005 feeding on sea ice algae, D) December of 2005 without feeding sea ice algae, E) January of 2006 feeding on sea ice algae, F) January of 2006 without feeding sea ice algae. Juveniles start at 22mm, larvae start at 8mm. The black dash dot dash line indicates the average of all the surviving krill. Particles representing krill were released on consecutive days seen by the offset on the x-axis month and the average growth line corresponds to day 15 day.



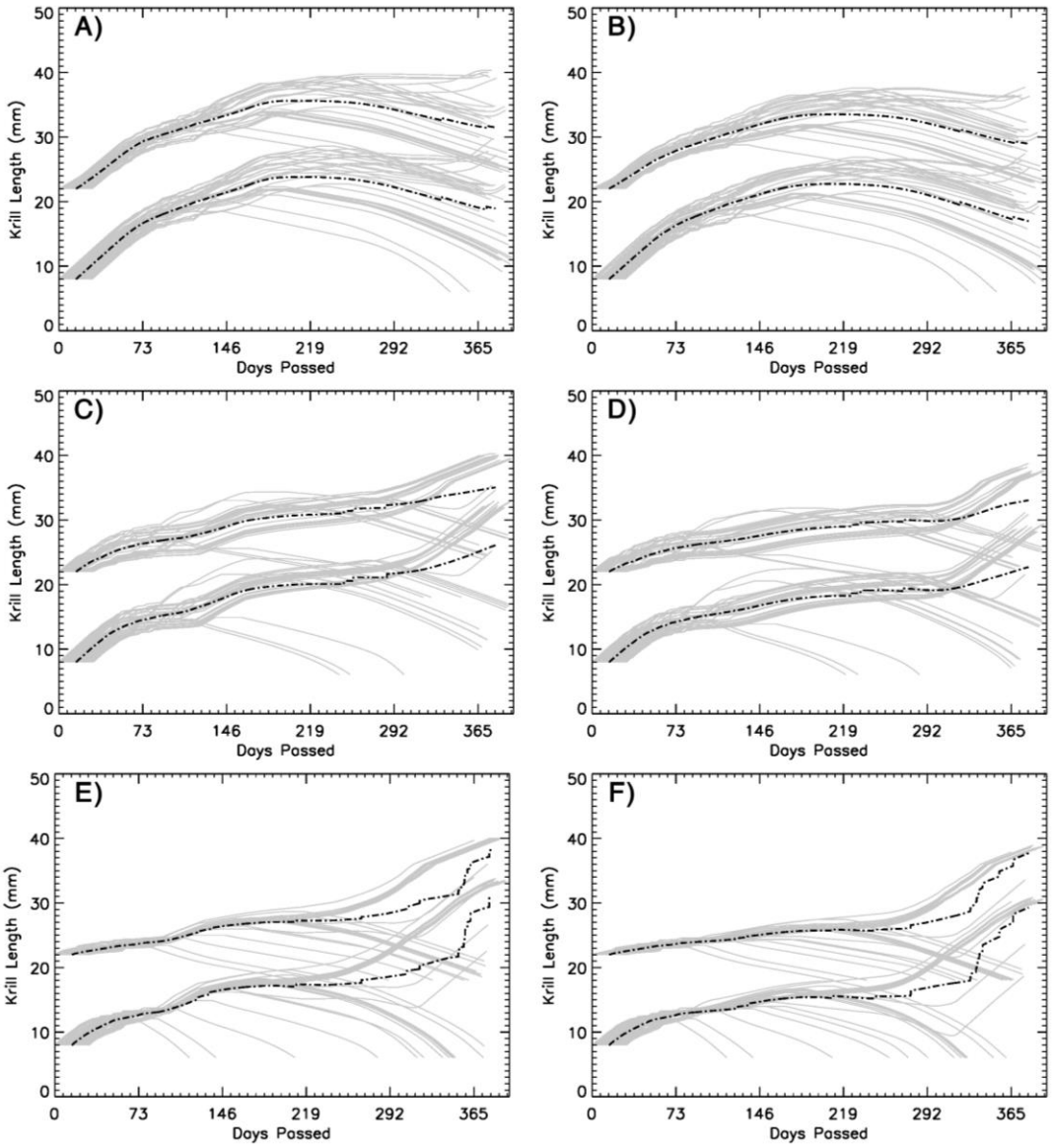
Appendix B 9 Concentrations of food for krill encountered by all drifters released from station 47 in November 2005. A) Copepod concentration (mgC m^{-3}), B) Diatom concentration (mgC m^{-3}), C) Nanophytoplankton concentration (mgC m^{-3}), D) Detritus concentration (mgC m^{-3}), E) Sea ice algae concentration (mg Chla m^{-3}). The black dash dot dash line is the average value of all particles.



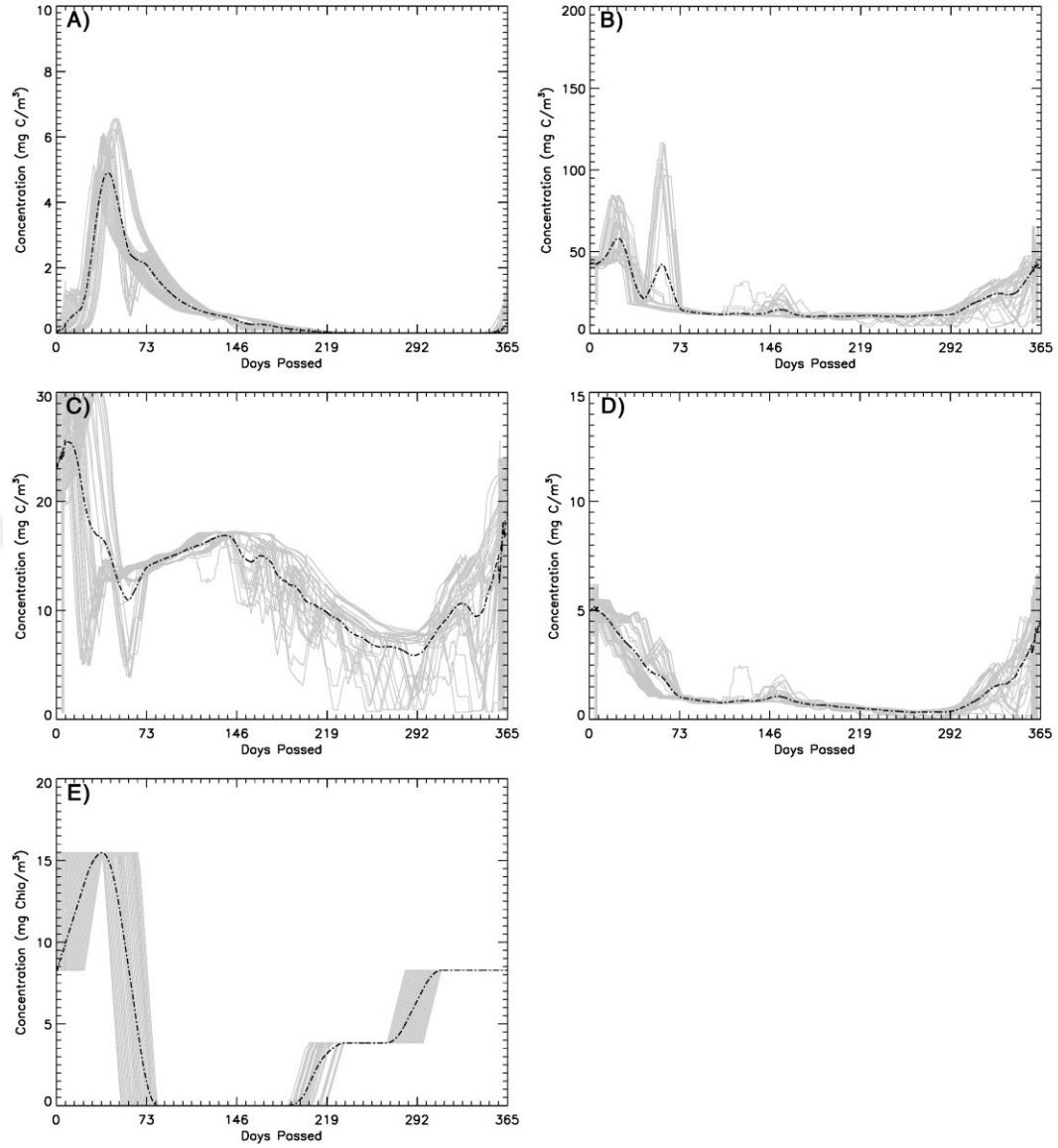
Appendix B 10 Concentrations of food for krill encountered by all drifters released from station 47 in December 2005. A) Copepod concentration (mgC m^{-3}), B) Diatom concentration (mgC m^{-3}), C) Nanophytoplankton concentration (mgC m^{-3}), D) Detritus concentration (mgC m^{-3}), E) Sea ice algae concentration (mg Chla m^{-3}). The black dash dot dash line is the average value of all particles.



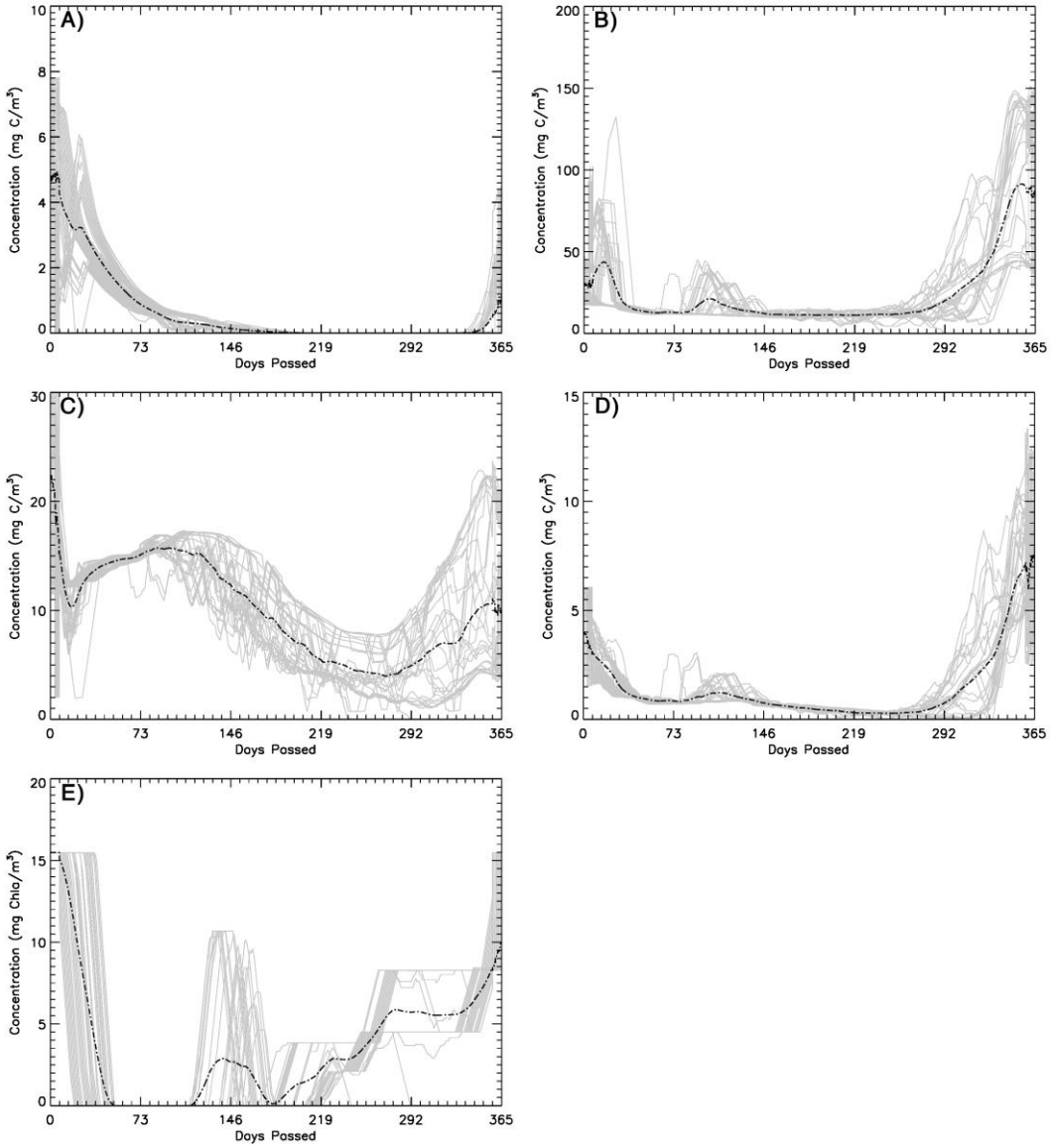
Appendix B 11 Concentrations of food for krill encountered by all drifters released from station 47 in January 2006. A) Copepod concentration (mgC m^{-3}), B) Diatom concentration (mgC m^{-3}), C) Nanophytoplankton concentration (mgC m^{-3}), D) Detritus concentration (mgC m^{-3}), E) Sea ice algae concentration (mg Chla m^{-3}). The black dash dot dash line is the average value of all particles.



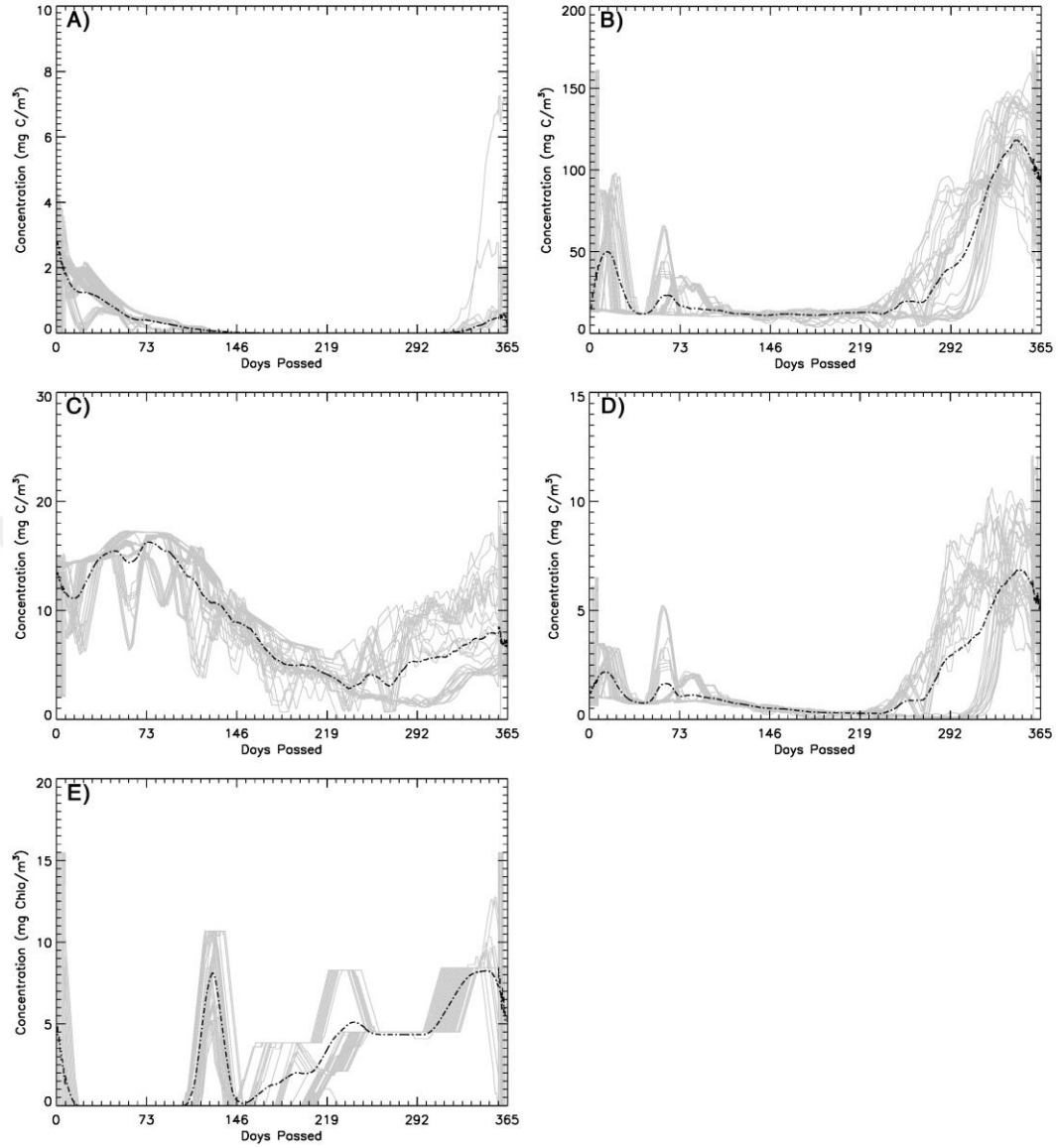
Appendix B 12 Krill growth over time for krill originating at station 47 starting A) November of 2005 feeding on sea ice algae, B) November of 2005 without feeding on sea ice algae, C) December of 2005 feeding on sea ice algae, D) December of 2005 without feeding sea ice algae, E) January of 2006 feeding on sea ice algae, F) January of 2006 without feeding sea ice algae. Juveniles start at 22mm, larvae start at 8mm. The black dash dot dash line indicates the average of all the surviving krill. Particles representing krill were released on consecutive days seen by the offset on the x-axis month and the average growth line corresponds to day 15 day.



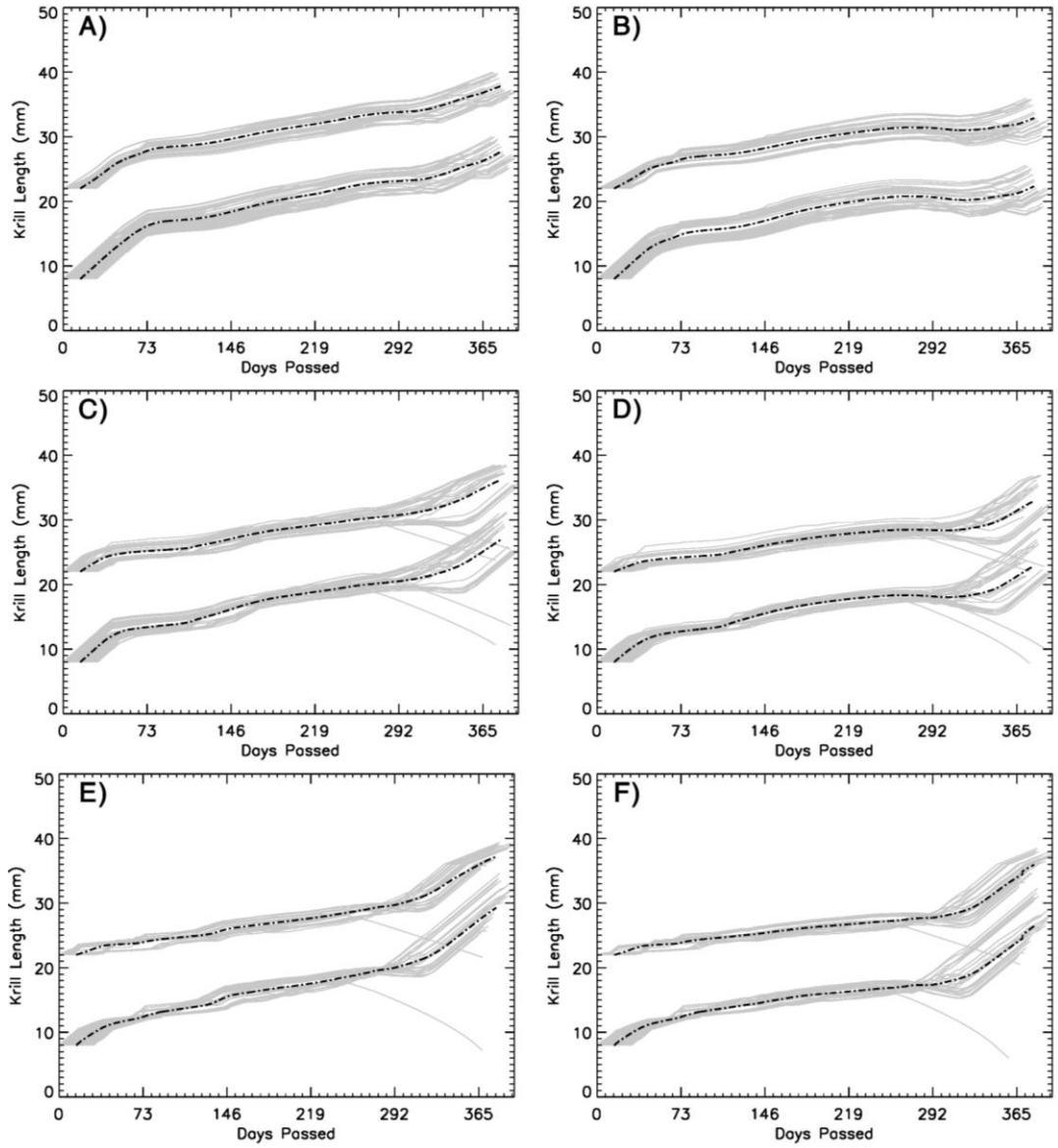
Appendix B 13 Concentrations of food for krill encountered by all drifters released from station 53 in November 2005. A) Copepod concentration (mgC m^{-3}), B) Diatom concentration (mgC m^{-3}), C) Nanophytoplankton concentration (mgC m^{-3}), D) Detritus concentration (mgC m^{-3}), E) Sea ice algae concentration (mg Chla m^{-3}). The black dash dot dash line is the average value of all particles.



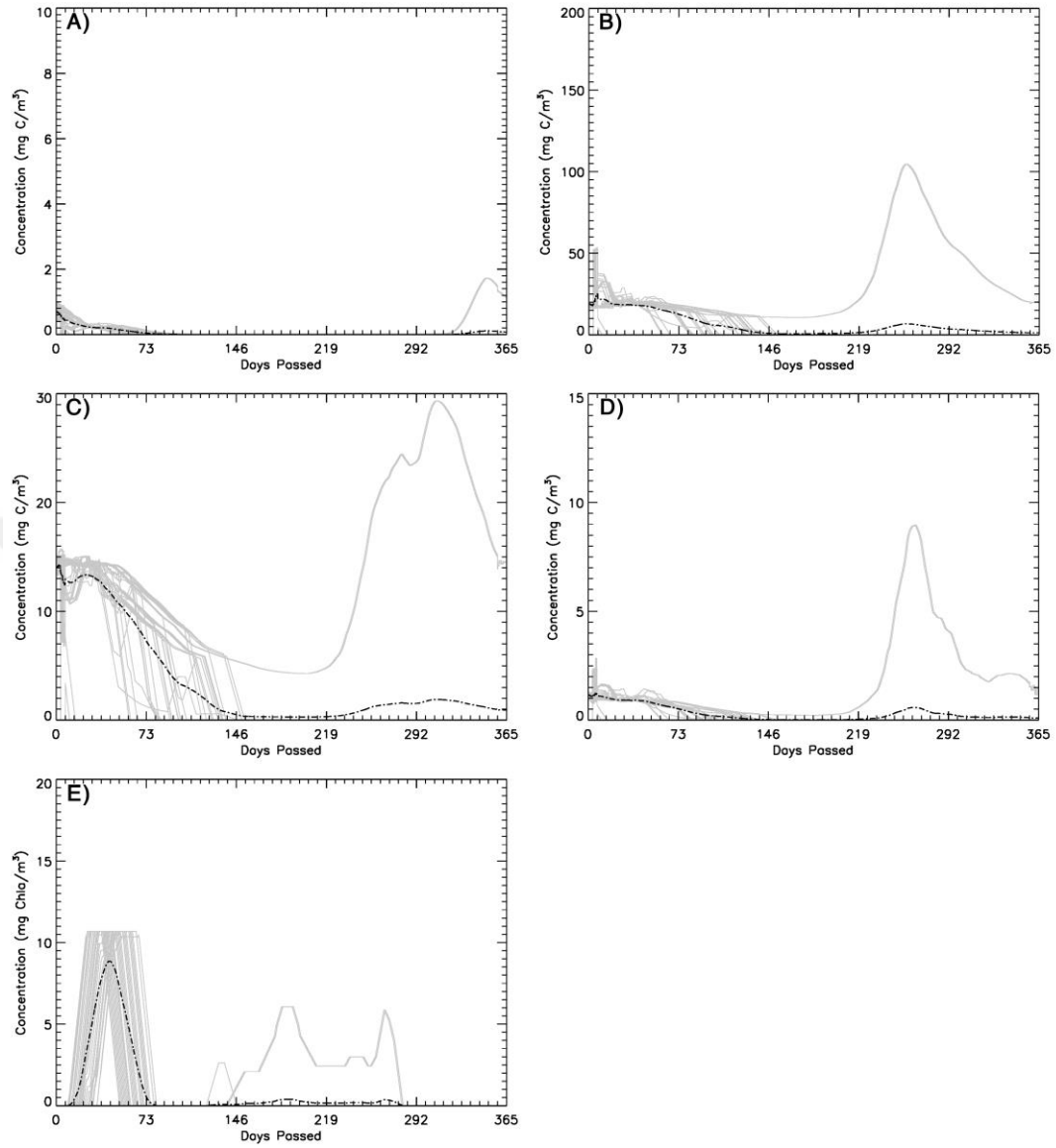
Appendix B 14 Concentrations of food for krill encountered by all drifters released from station 53 in December 2005. A) Copepod concentration (mgC m^{-3}), B) Diatom concentration (mgC m^{-3}), C) Nanophytoplankton concentration (mgC m^{-3}), D) Detritus concentration (mgC m^{-3}), E) Sea ice algae concentration (mg Chla m^{-3}). The black dash dot dash line is the average value of all particles.



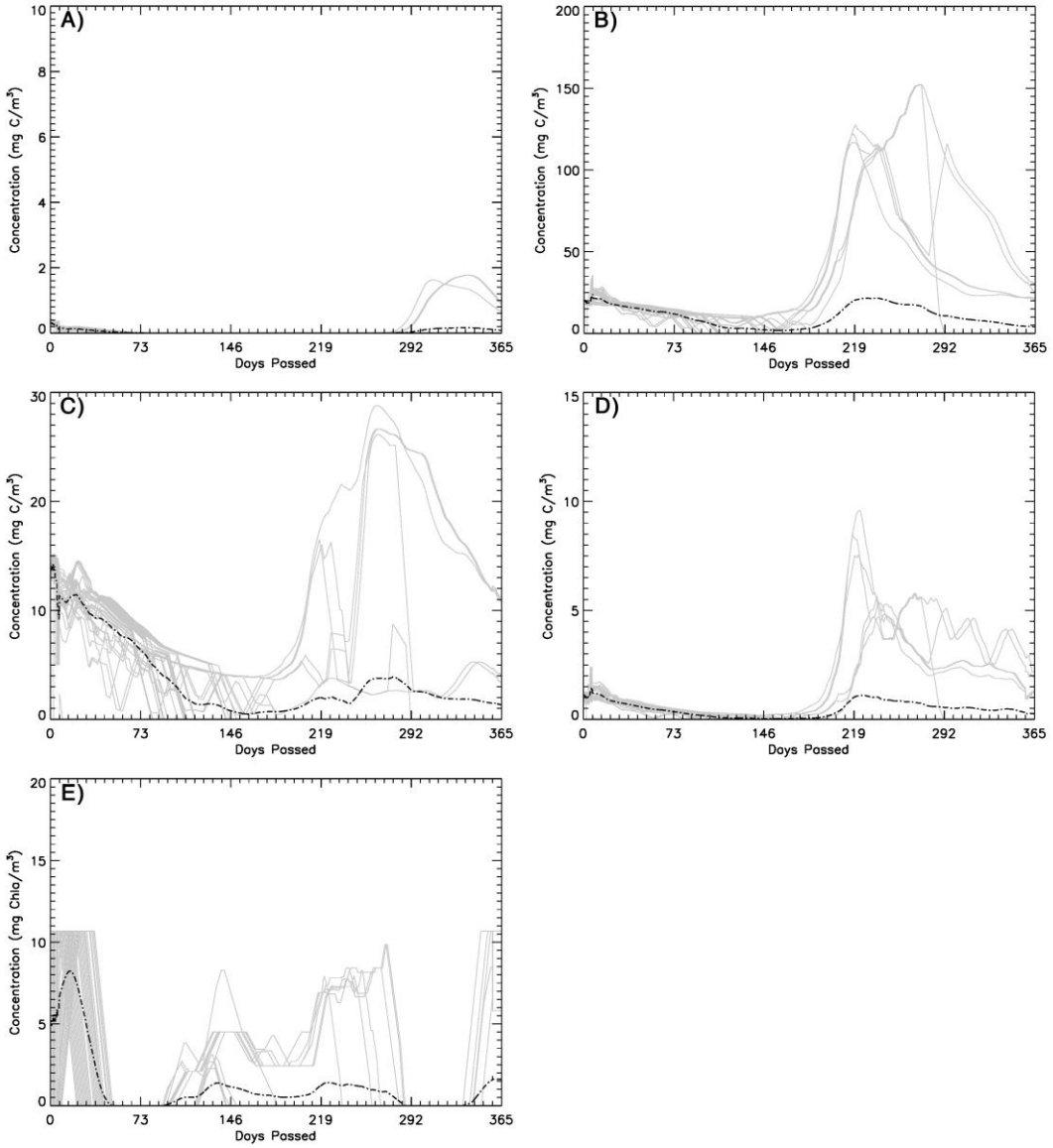
Appendix B 15 Concentrations of food for krill encountered by all drifters released from station 53 in January 2006. A) Copepod concentration (mgC m^{-3}), B) Diatom concentration (mgC m^{-3}), C) Nanophytoplankton concentration (mgC m^{-3}), D) Detritus concentration (mgC m^{-3}), E) Sea ice algae concentration (mg Chla m^{-3}). The black dash dot dash line is the average value of all particles.



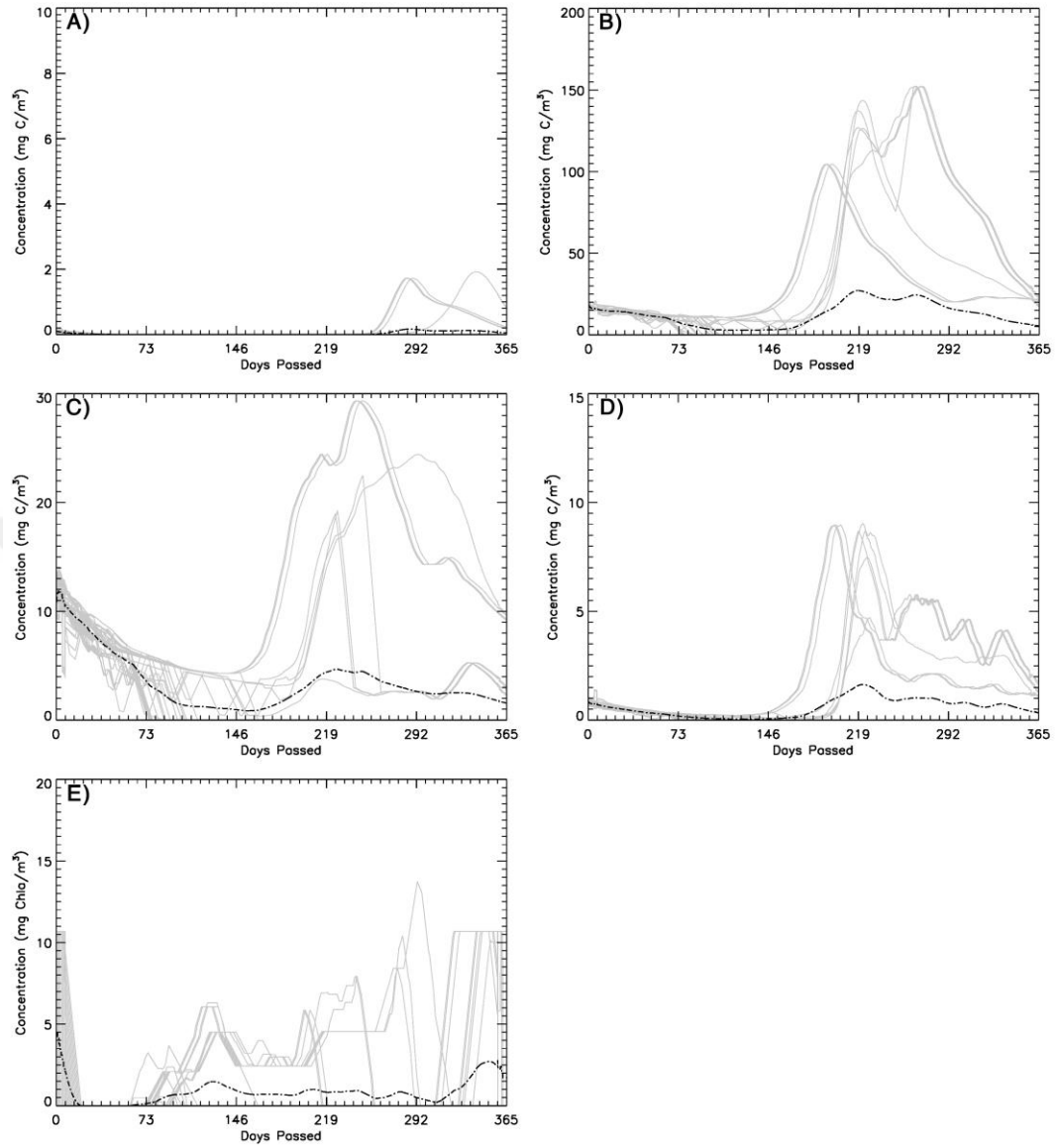
Appendix B 16 Krill growth over time for krill originating at station 53 starting A) November of 2005 feeding on sea ice algae, B) November of 2005 without feeding on sea ice algae, C) December of 2005 feeding on sea ice algae, D) December of 2005 without feeding sea ice algae, E) January of 2006 feeding on sea ice algae, F) January of 2006 without feeding sea ice algae. Juveniles start at 22mm, larvae start at 8mm. The black dash dot dash line indicates the average of all the surviving krill. Particles representing krill were released on consecutive days seen by the offset on the x-axis month and the average growth line corresponds to day 15 day.



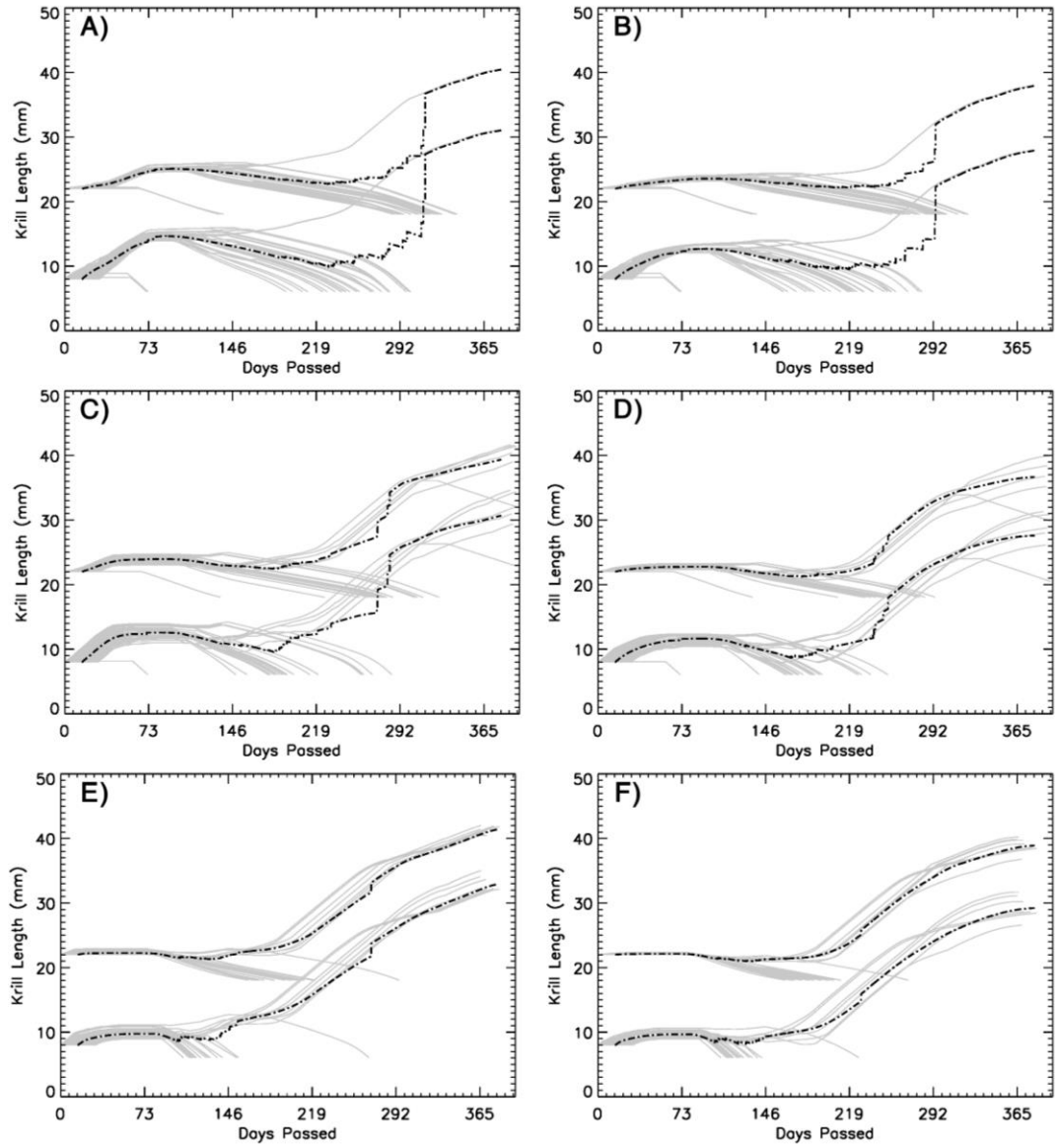
Appendix B 17 Concentrations of food for krill encountered by all drifters released from station 621 in March 2004. A) Copepod concentration (mgC m^{-3}), B) Diatom concentration (mgC m^{-3}), C) Nanophytoplankton concentration (mgC m^{-3}), D) Detritus concentration (mgC m^{-3}), E) Sea ice algae concentration (mg Chla m^{-3}). The black dash dot dash line is the average value of all particles.



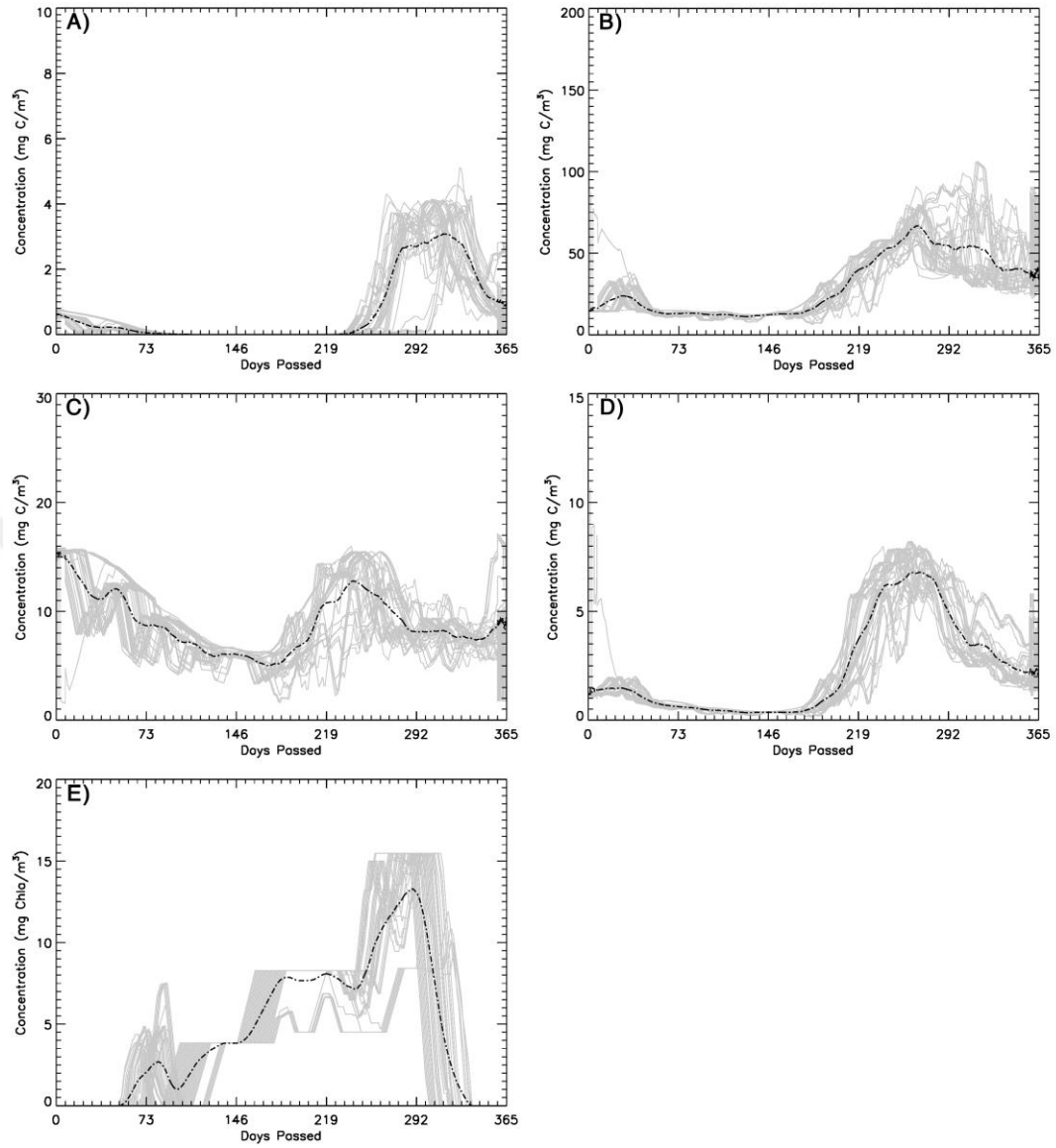
Appendix B 18 Concentrations of food for krill encountered by all drifters released from station 621 in April 2004. A) Copepod concentration (mgC m^{-3}), B) Diatom concentration (mgC m^{-3}), C) Nanophytoplankton concentration (mgC m^{-3}), D) Detritus concentration (mgC m^{-3}), E) Sea ice algae concentration (mg Chla m^{-3}). The black dash dot dash line is the average value of all particles.



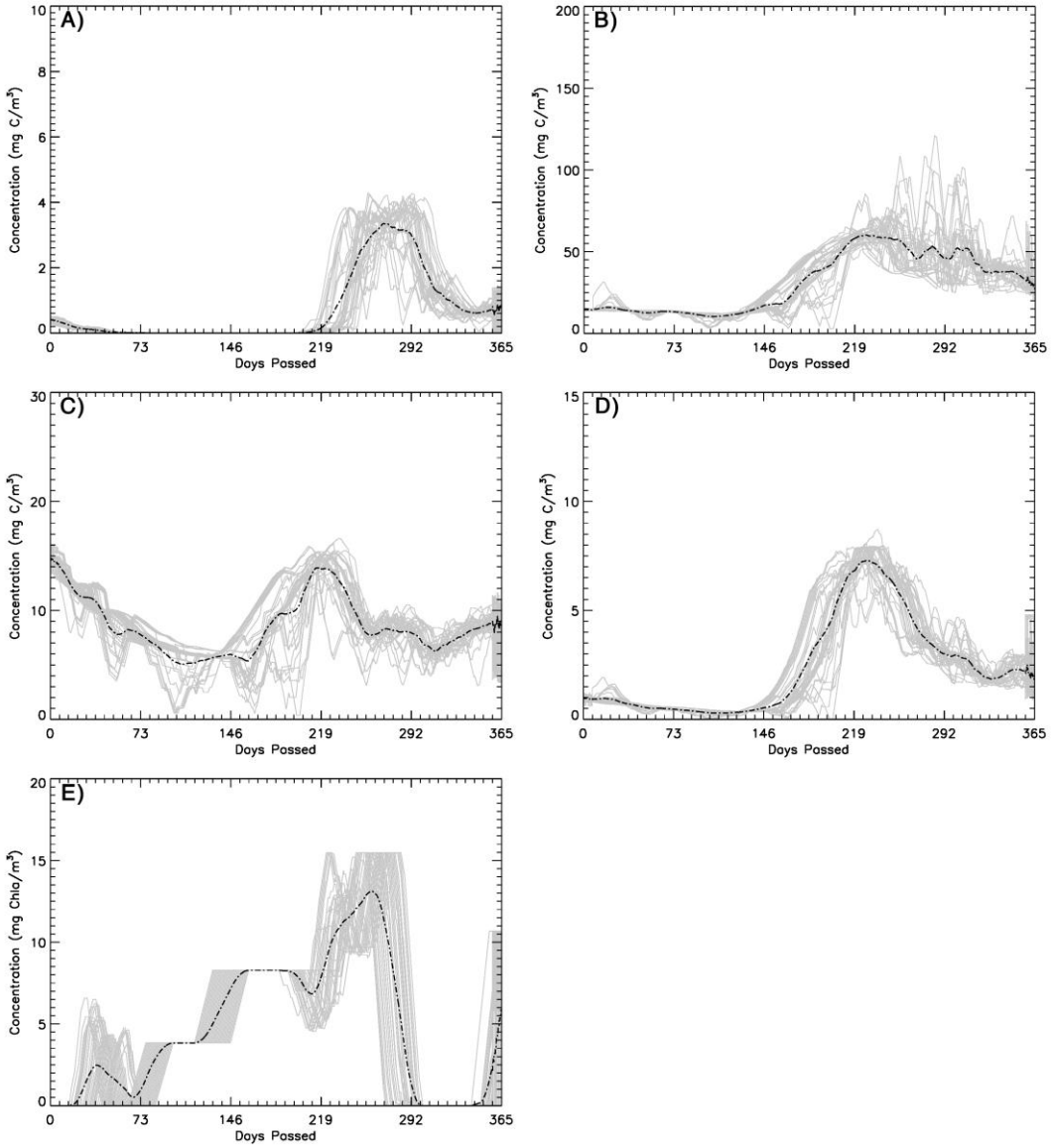
Appendix B 19 Concentrations of food for krill encountered by all drifters released from station 621 in May 2004. A) Copepod concentration (mgC m^{-3}), B) Diatom concentration (mgC m^{-3}), C) Nanophytoplankton concentration (mgC m^{-3}), D) Detritus concentration (mgC m^{-3}), E) Sea ice algae concentration (mg Chla m^{-3}). The black dash dot dash line is the average value of all particles.



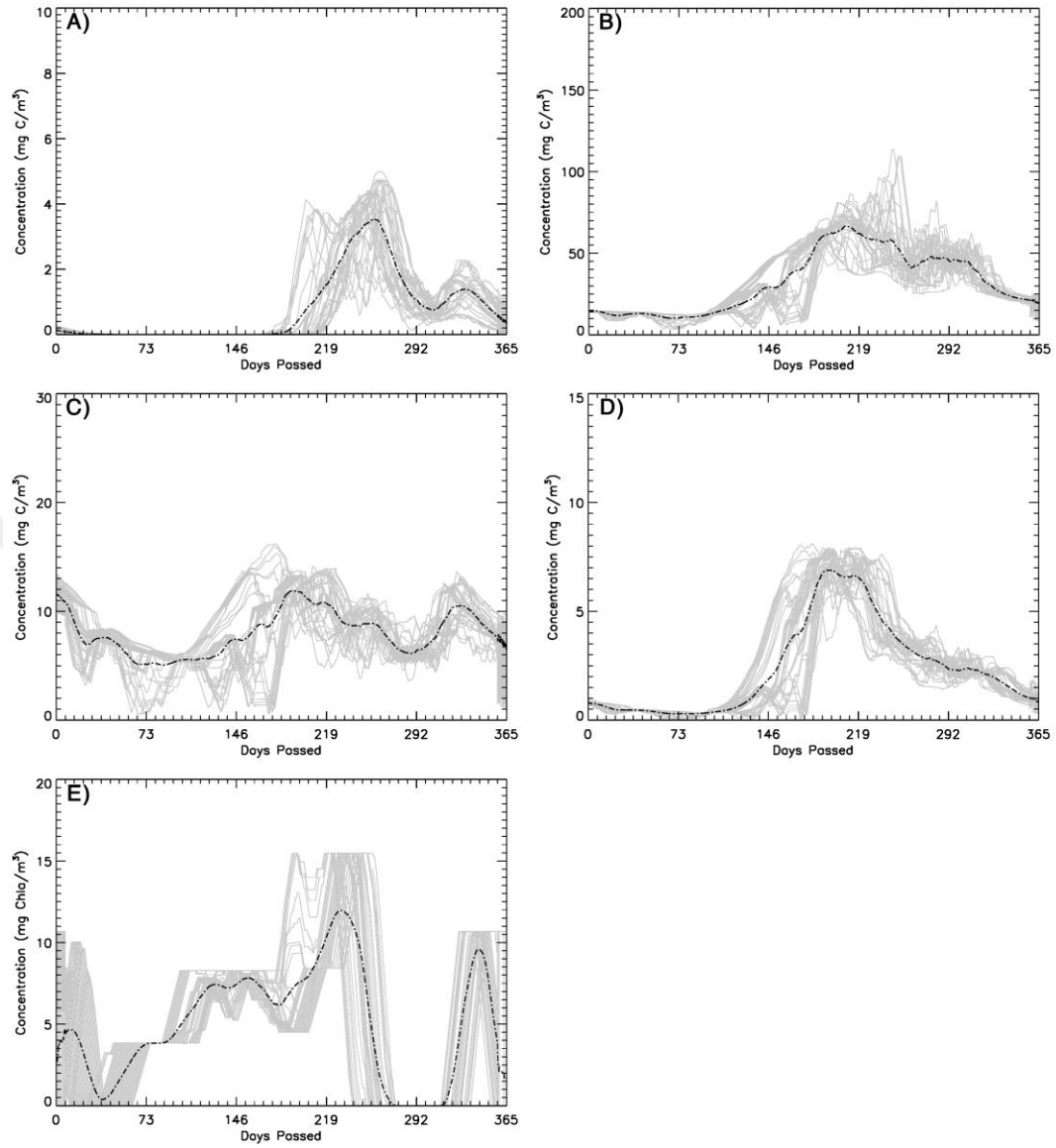
Appendix B 20 Krill growth over time for krill originating at station 621 starting A) March of 2004 with feeding on sea ice algae, B) March of 2004 without sea ice algae, C) April of 2004 with sea ice algae, D) April of 2004 without sea ice algae, E) May of 2004 with sea ice algae, F) May of 2004 without sea ice algae. Juveniles start at 22mm, larvae start at 8mm. The black dash dot dash line indicates the average of all the surviving krill. Particles representing krill were released on consecutive days seen by the offset on the x-axis month and the average growth line corresponds to day 15 day.



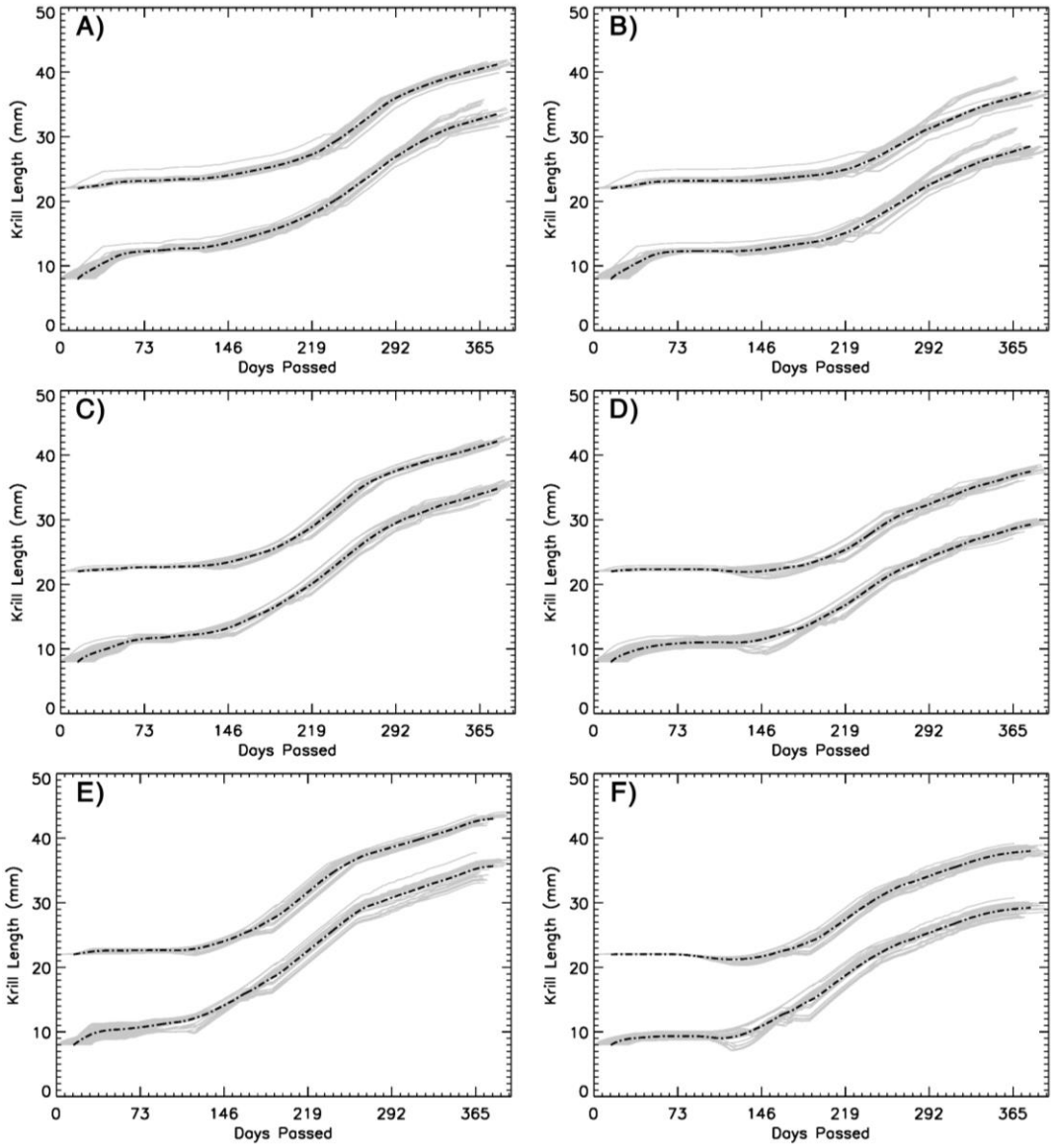
Appendix B 21 Concentrations of food for krill encountered by all drifters released from station 678 in March 2004. A) Copepod concentration (mgC m^{-3}), B) Diatom concentration (mgC m^{-3}), C) Nanophytoplankton concentration (mgC m^{-3}), D) Detritus concentration (mgC m^{-3}), E) Sea ice algae concentration (mg Chla m^{-3}). The black dash dot dash line is the average value of all particles.



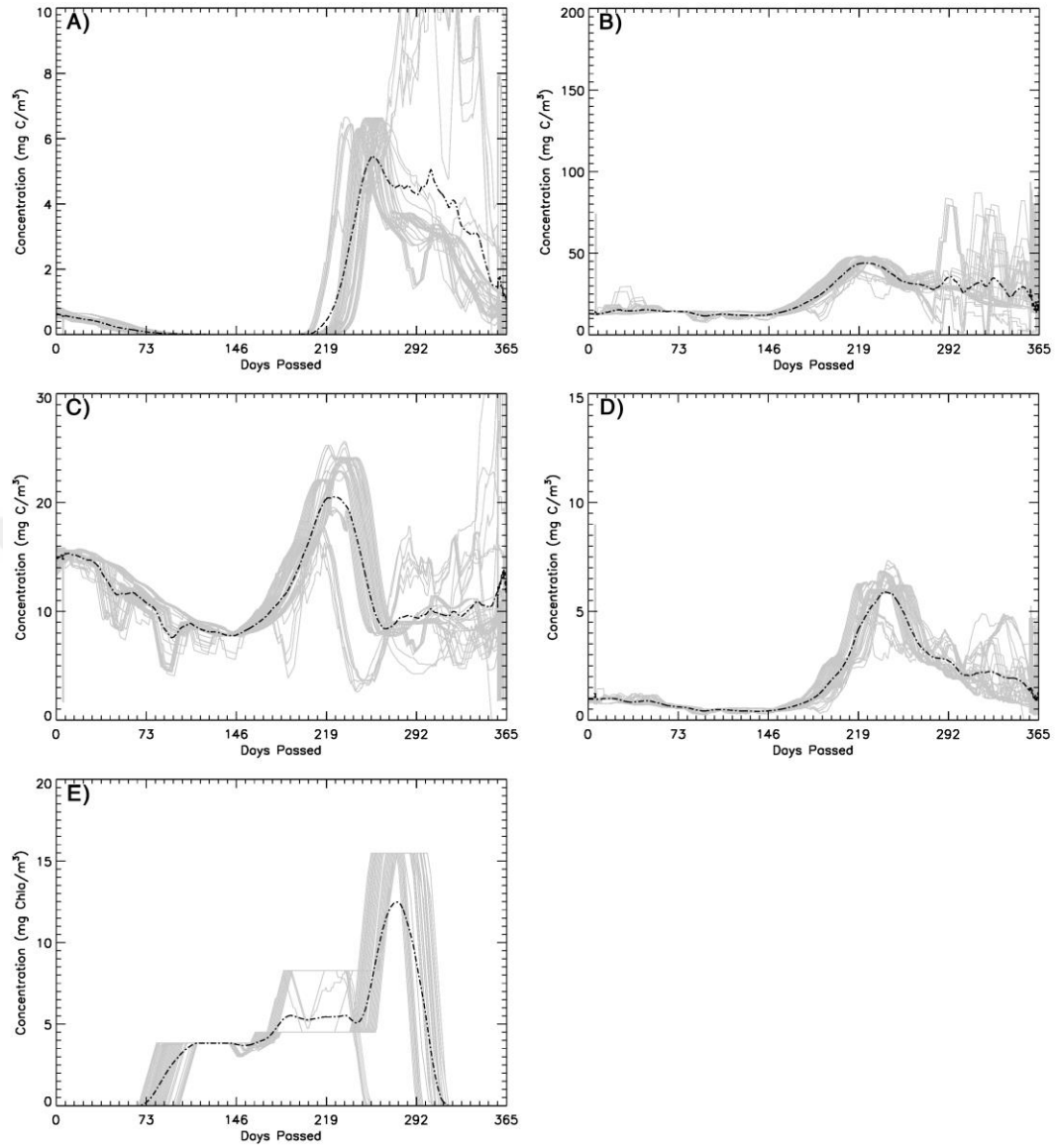
Appendix B 22 Concentrations of food for krill encountered by all drifters released from station 678 in April 2004. A) Copepod concentration (mgC m^{-3}), B) Diatom concentration (mgC m^{-3}), C) Nanophytoplankton concentration (mgC m^{-3}), D) Detritus concentration (mgC m^{-3}), E) Sea ice algae concentration (mg Chla m^{-3}). The black dash dot dash line is the average value of all particles.



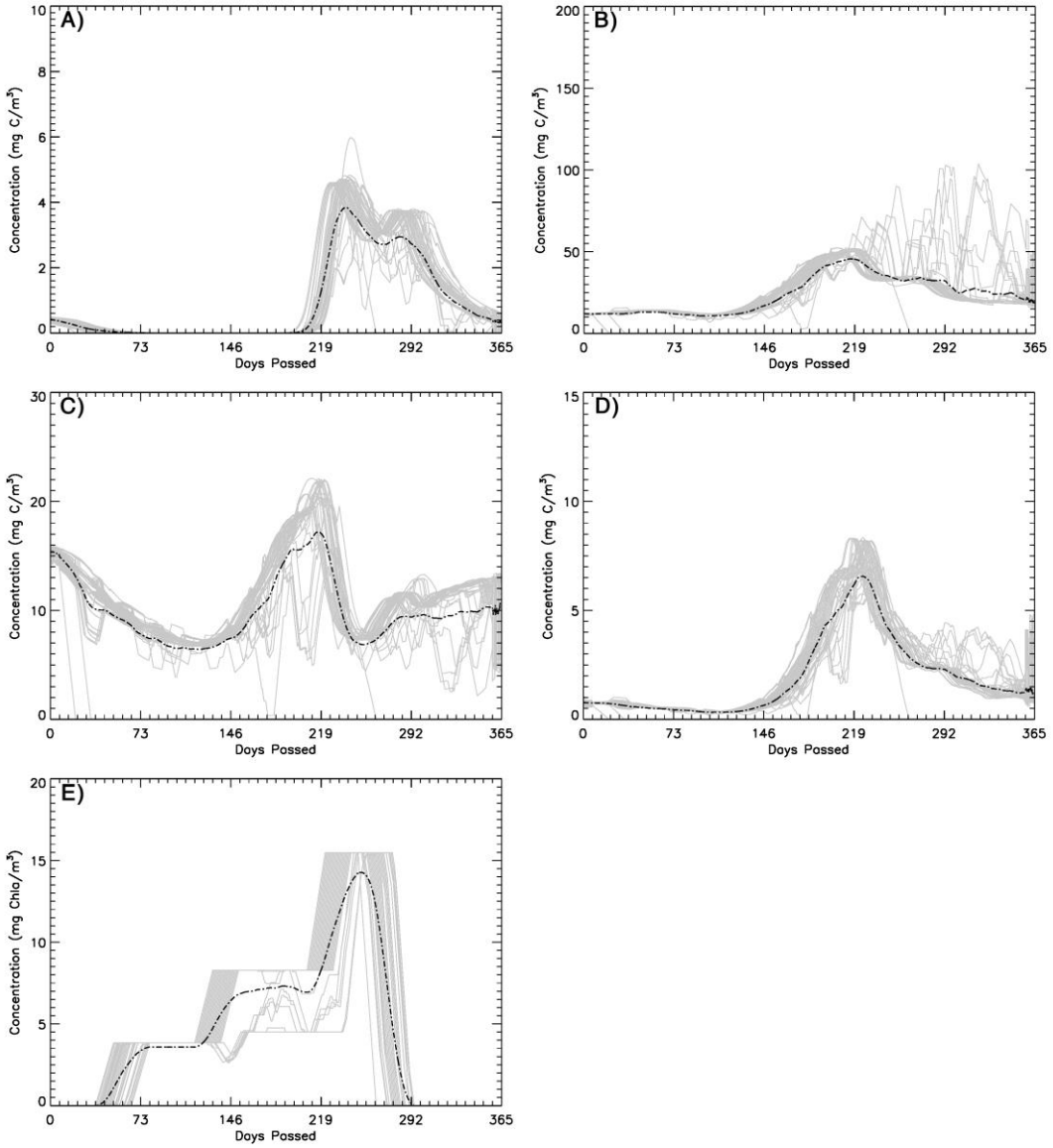
Appendix B 23 Concentrations of food for krill encountered by all drifters released from station 678 in May 2004. A) Copepod concentration (mgC m^{-3}), B) Diatom concentration (mgC m^{-3}), C) Nanophytoplankton concentration (mgC m^{-3}), D) Detritus concentration (mgC m^{-3}), E) Sea ice algae concentration (mg Chla m^{-3}). The black dash dot dash line is the average value of all particles.



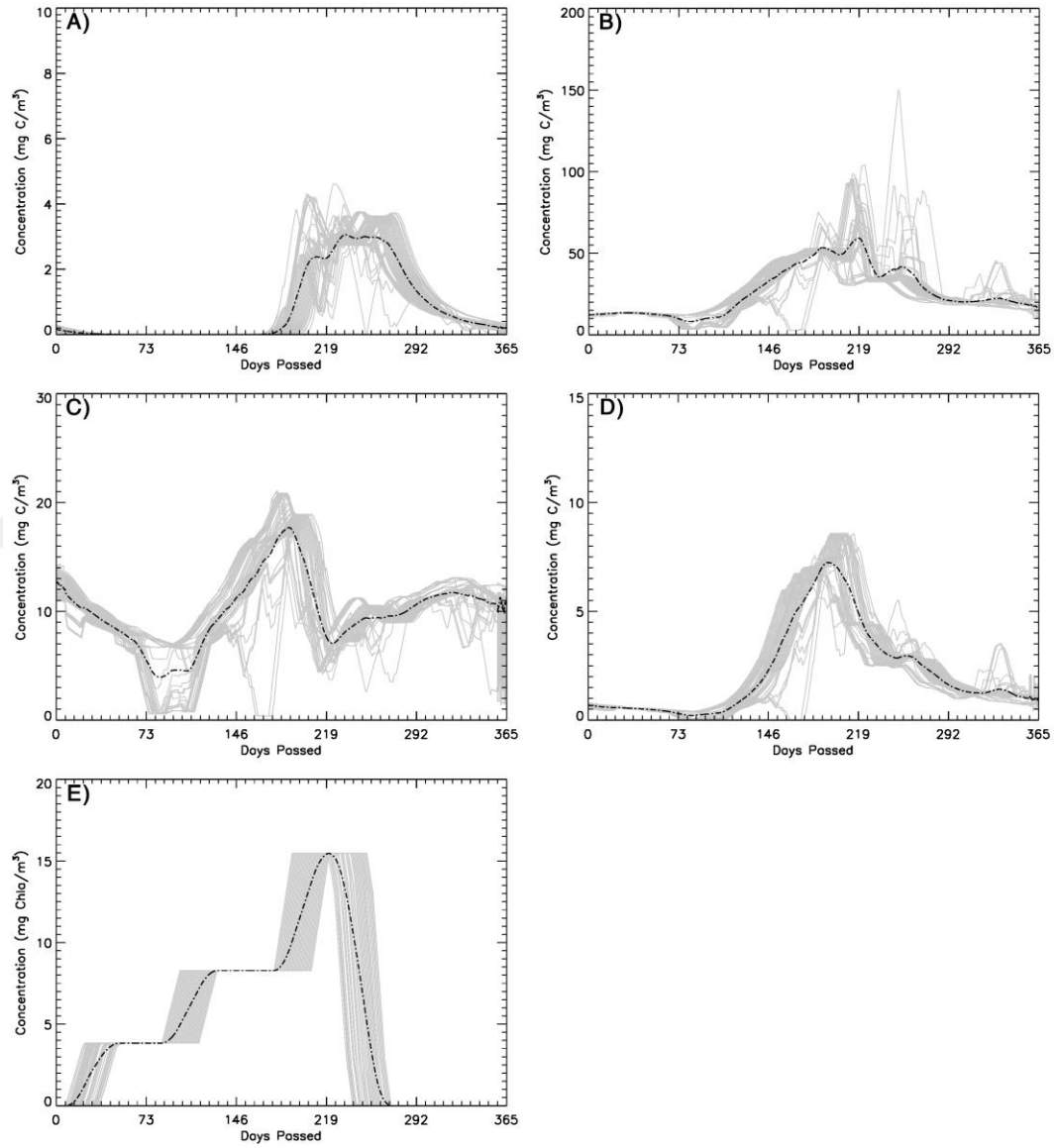
Appendix B 24 Krill growth over time for krill originating at station 678 starting A) March of 2004 with feeding on sea ice algae, B) March of 2004 without sea ice algae, C) April of 2004 with sea ice algae, D) April of 2004 without sea ice algae, E) May of 2004 with sea ice algae, F) May of 2004 without sea ice algae. Juveniles start at 22mm, larvae start at 8mm. The black dash dot dash line indicates the average of all the surviving krill. Particles representing krill were released on consecutive days seen by the offset on the x-axis month and the average growth line corresponds to day 15 day.



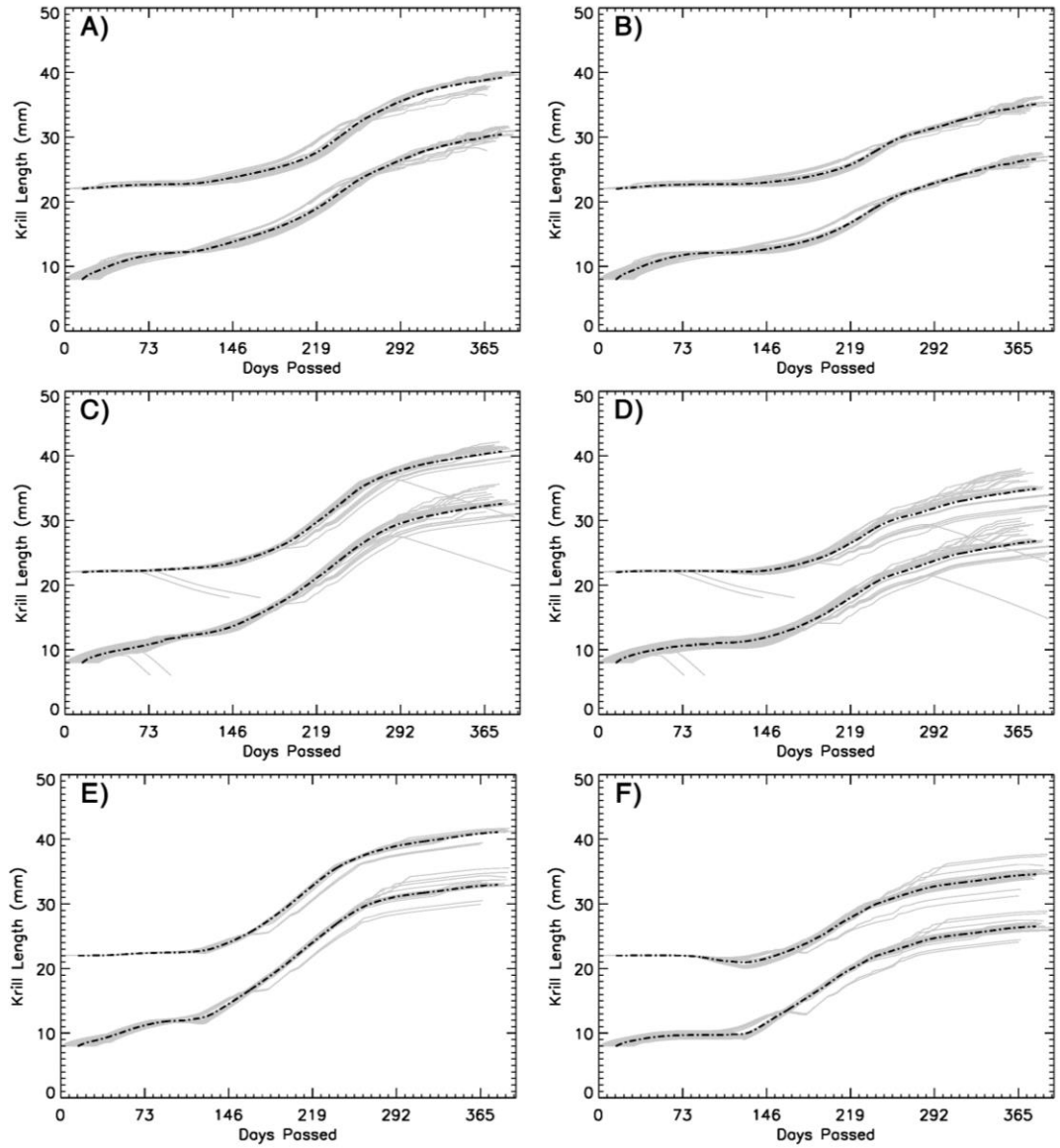
Appendix B 25 Concentrations of food for krill encountered by all drifters released from station 683 in March 2004. A) Copepod concentration (mgC m^{-3}), B) Diatom concentration (mgC m^{-3}), C) Nanophytoplankton concentration (mgC m^{-3}), D) Detritus concentration (mgC m^{-3}), E) Sea ice algae concentration (mg Chla m^{-3}). The black dash dot dash line is the average value of all particles.



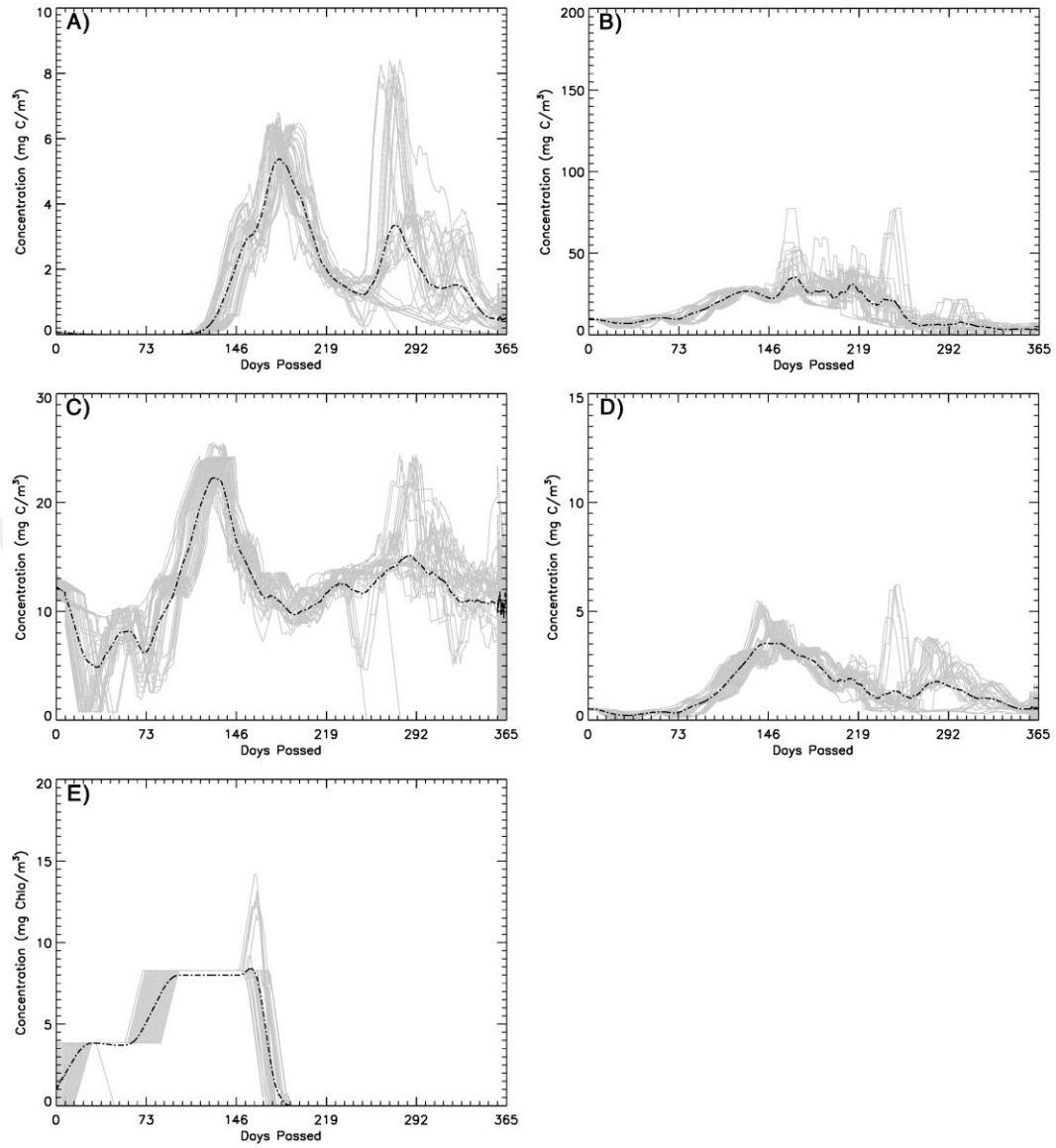
Appendix B 26 Concentrations of food for krill encountered by all drifters released from station 683 in April 2004. A) Copepod concentration (mgC m^{-3}), B) Diatom concentration (mgC m^{-3}), C) Nanophytoplankton concentration (mgC m^{-3}), D) Detritus concentration (mgC m^{-3}), E) Sea ice algae concentration (mg Chla m^{-3}). The black dash dot dash line is the average value of all particles.



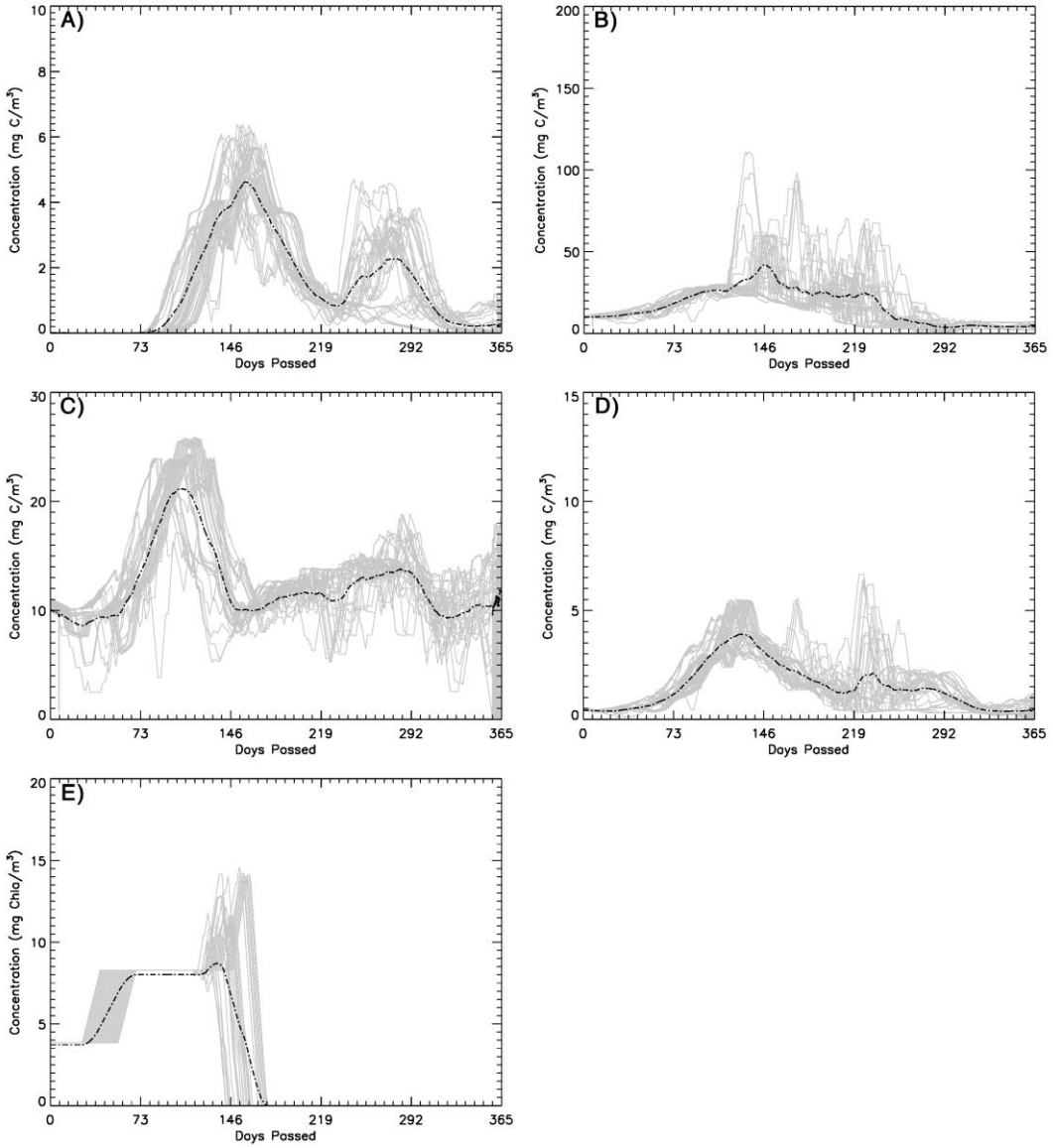
Appendix B 27 Concentrations of food for krill encountered by all drifters released from station 683 in May 2004. A) Copepod concentration (mgC m^{-3}), B) Diatom concentration (mgC m^{-3}), C) Nanophytoplankton concentration (mgC m^{-3}), D) Detritus concentration (mgC m^{-3}), E) Sea ice algae concentration (mg Chla m^{-3}). The black dash dot dash line is the average value of all particles.



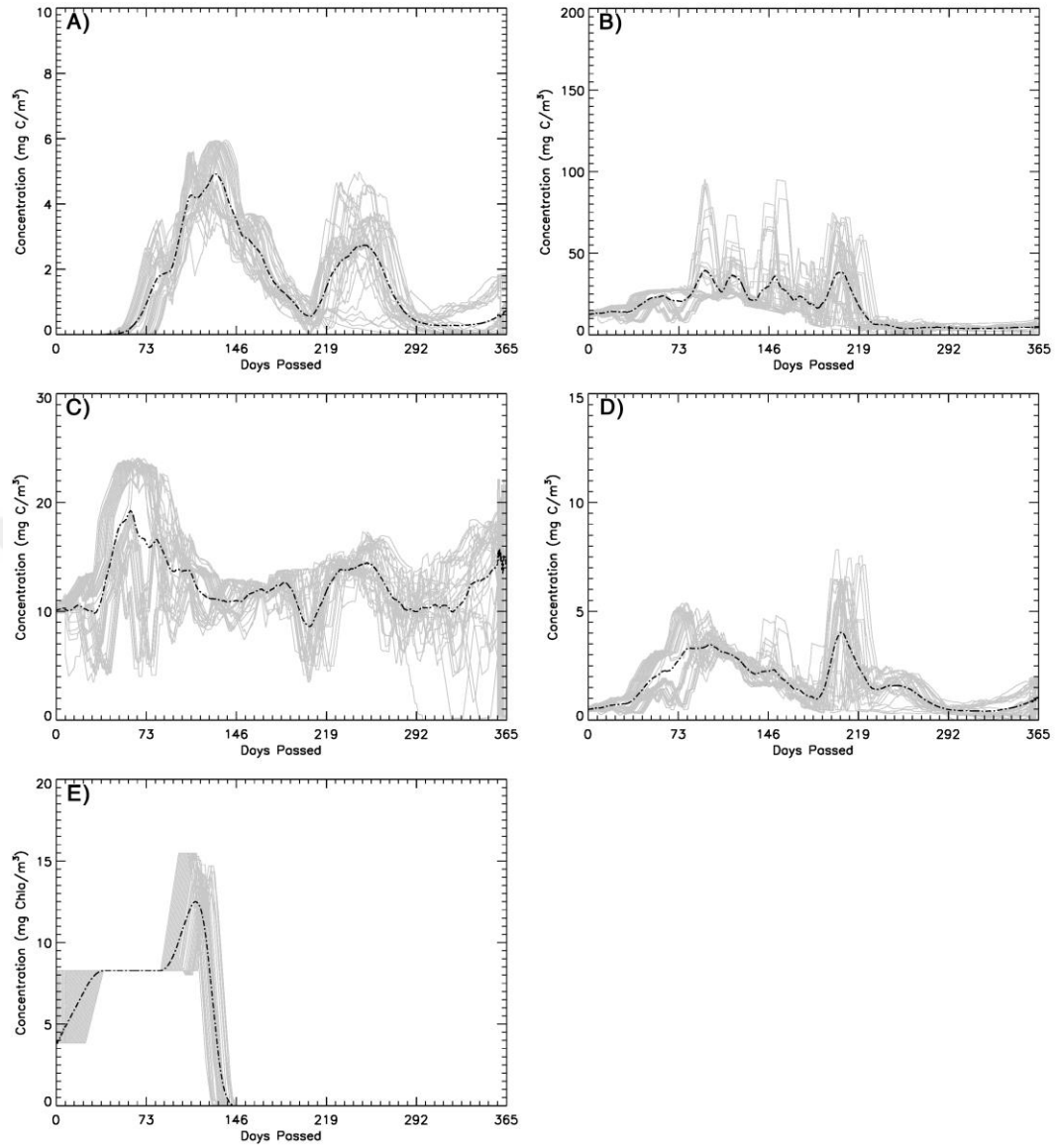
Appendix B 28 Krill growth over time for krill originating at station 683 starting A) March of 2004 with feeding on sea ice algae, B) March of 2004 without sea ice algae, C) April of 2004 with sea ice algae, D) April of 2004 without sea ice algae, E) May of 2004 with sea ice algae, F) May of 2004 without sea ice algae. Juveniles start at 22mm, larvae start at 8mm. The black dash dot dash line indicates the average of all the surviving krill. Particles representing krill were released on consecutive days seen by the offset on the x-axis month and the average growth line corresponds to day 15 day.



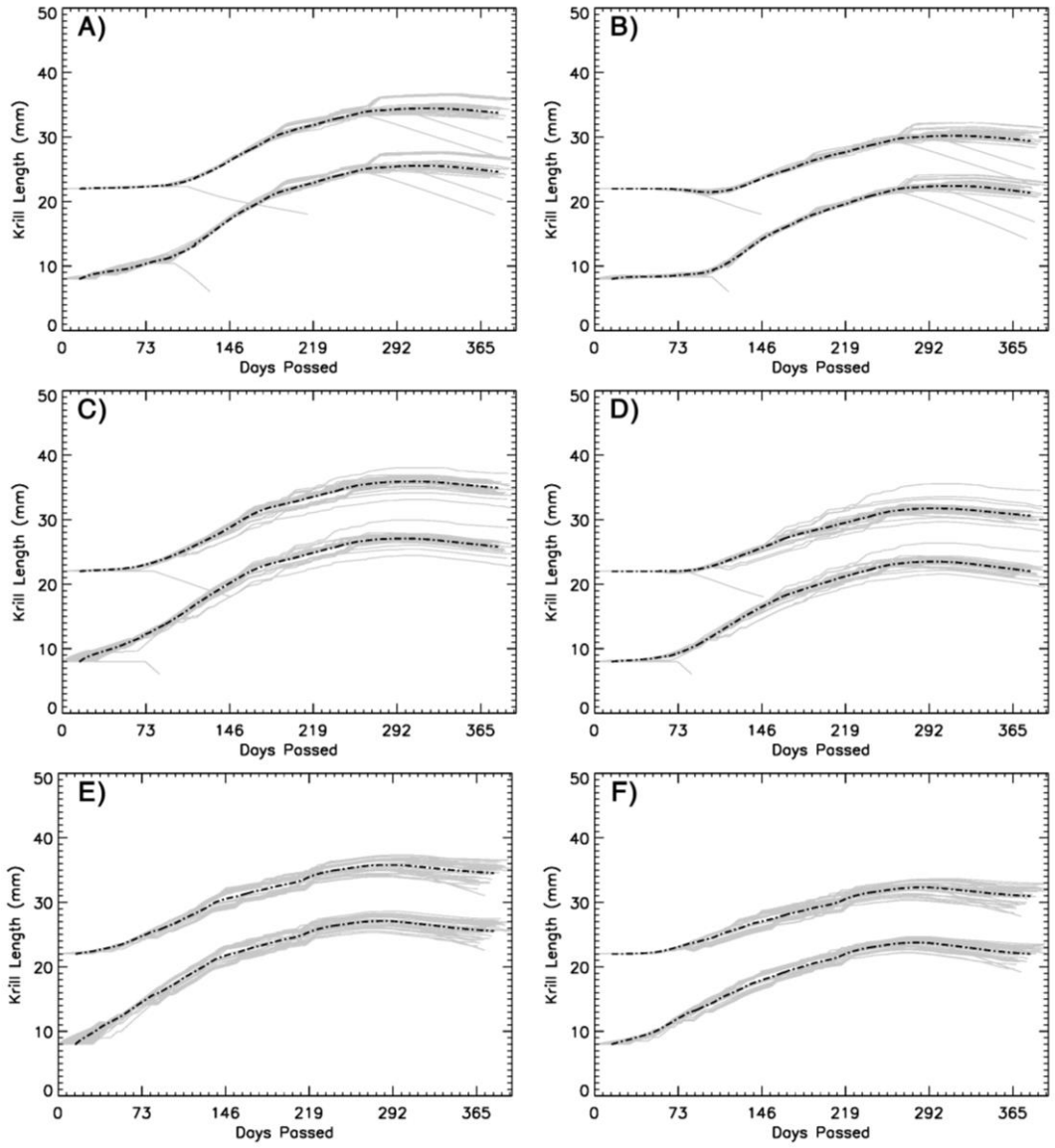
Appendix B 29 Concentrations of food for krill encountered by all drifters released from station 474 in June 2006. A) Copepod concentration (mgC m^{-3}), B) Diatom concentration (mgC m^{-3}), C) Nanophytoplankton concentration (mgC m^{-3}), D) Detritus concentration (mgC m^{-3}), E) Sea ice algae concentration (mg Chla m^{-3}). The black dash dot dash line is the average value of all particles.



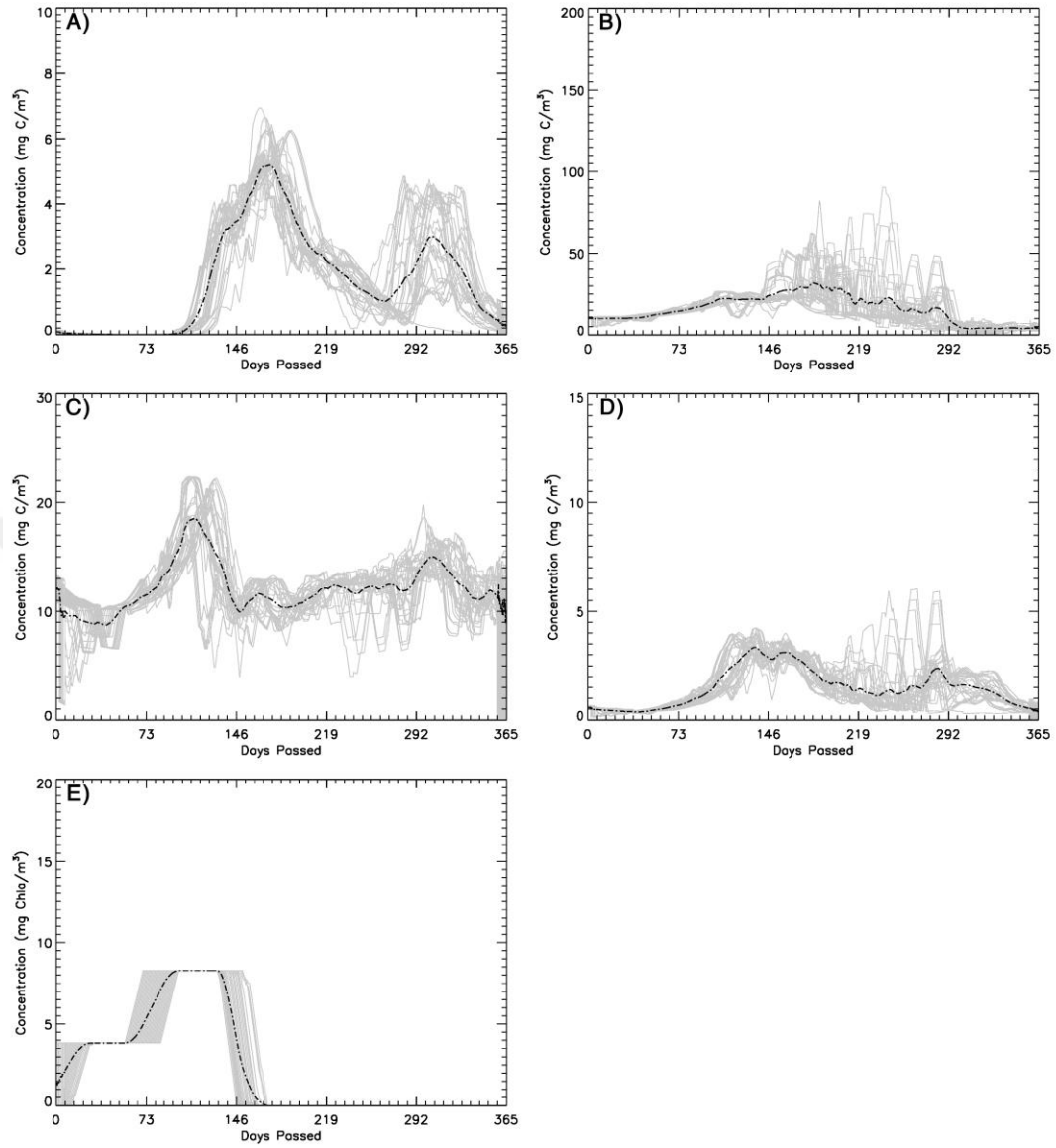
Appendix B 30 Concentrations of food for krill encountered by all drifters released from station 474 in July 2006. A) Copepod concentration (mgC m^{-3}), B) Diatom concentration (mgC m^{-3}), C) Nanophytoplankton concentration (mgC m^{-3}), D) Detritus concentration (mgC m^{-3}), E) Sea ice algae concentration (mg Chla m^{-3}). The black dash dot dash line is the average value of all particles.



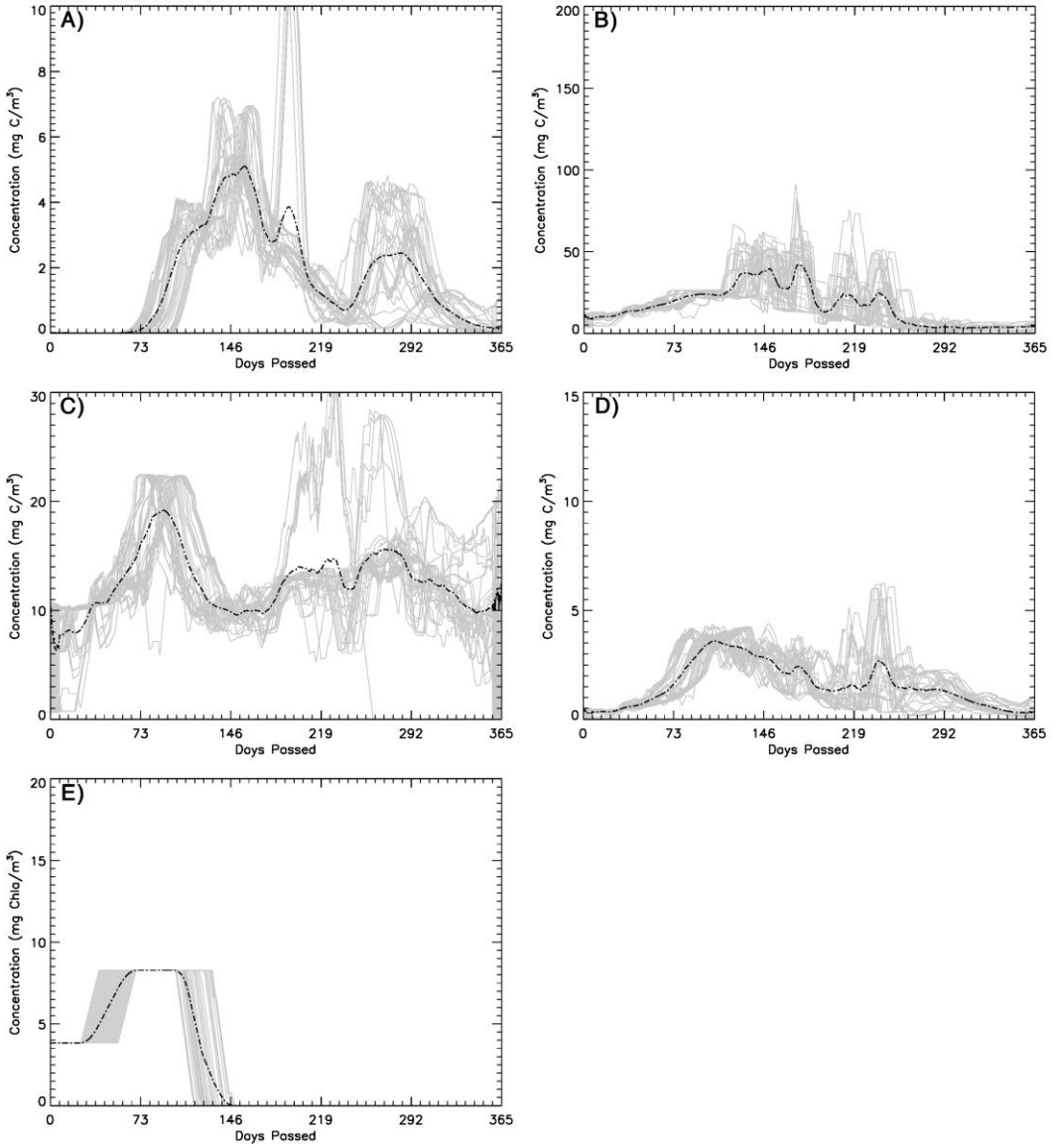
Appendix B 31 Concentrations of food for krill encountered by all drifters released from station 474 in August 2006. A) Copepod concentration (mgC m^{-3}), B) Diatom concentration (mgC m^{-3}), C) Nanophytoplankton concentration (mgC m^{-3}), D) Detritus concentration (mgC m^{-3}), E) Sea ice algae concentration (mg Chla m^{-3}). The black dash dot dash line is the average value of all particles.



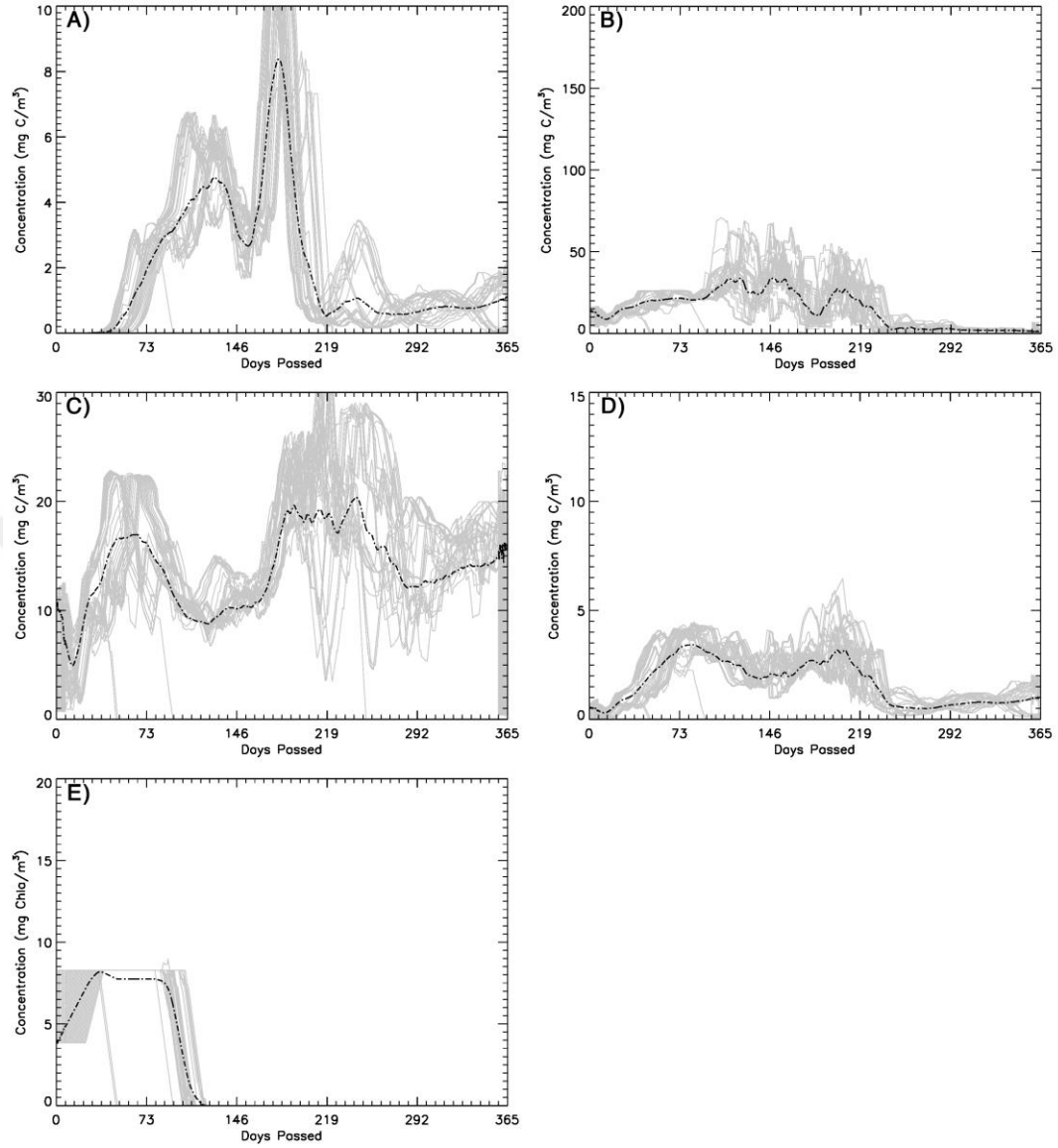
Appendix B 32 Krill growth figures for station 474 A) June of 2006 with sea ice algae, B) June of 2006 without sea ice algae, C) July of 2006 with sea ice algae, D) July of 2006 without sea ice algae, E) August of 2006 with sea ice algae, F) August of 2006 without sea ice algae. Juveniles start growth from 22mm, larvae start growth from 8mm. The black dash dot dash line indicates the average of all the surviving particles. Every particle has been given the day offset on the x-axis to their respective starting date on the month and the average line has been given a 15 day offset.



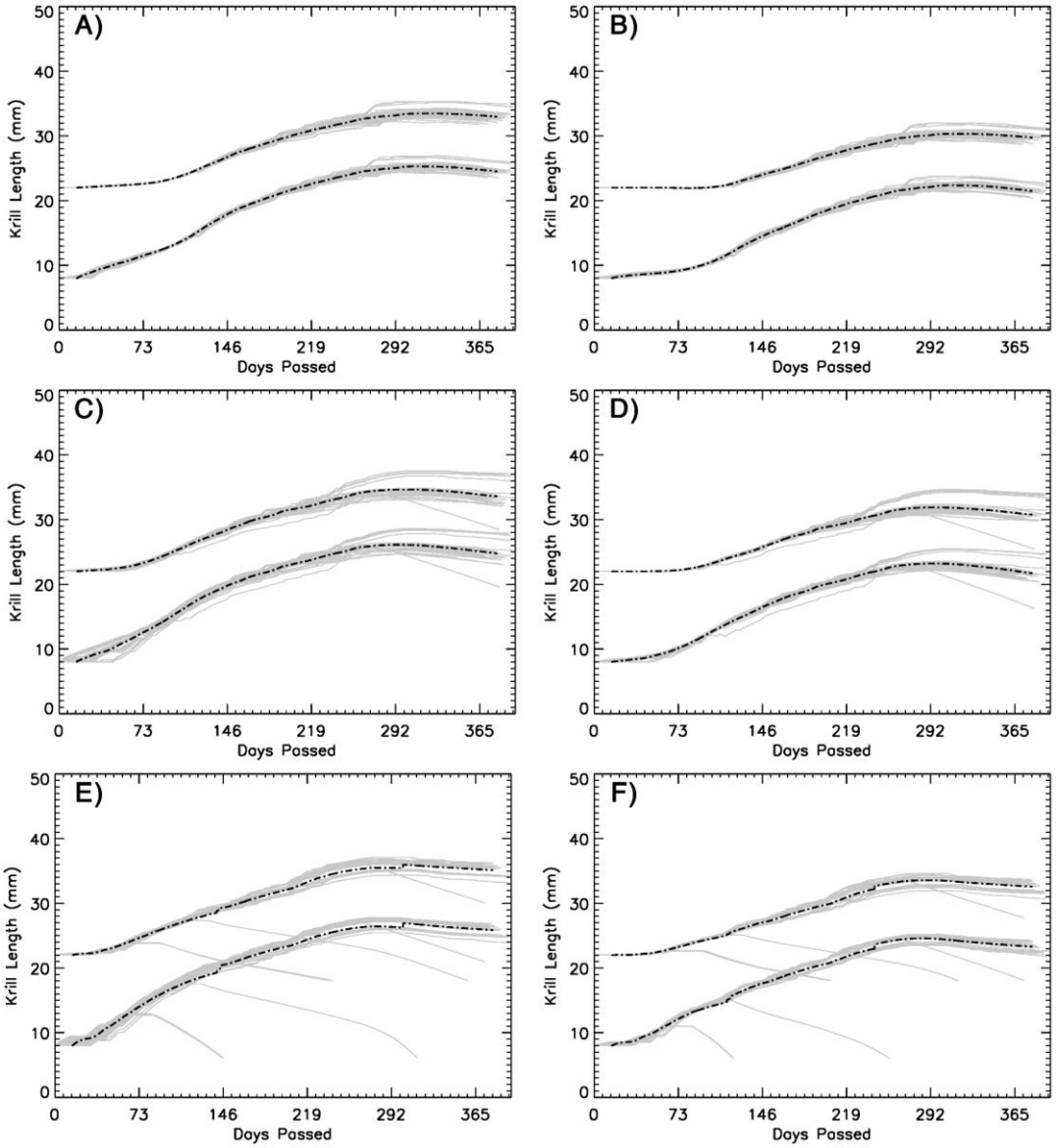
Appendix B 33 Concentrations of food for krill encountered by all drifters released from station 508 in June 2006. A) Copepod concentration (mgC m^{-3}), B) Diatom concentration (mgC m^{-3}), C) Nanophytoplankton concentration (mgC m^{-3}), D) Detritus concentration (mgC m^{-3}), E) Sea ice algae concentration (mg Chla m^{-3}). The black dash dot dash line is the average value of all particles.



Appendix B 34 Concentrations of food for krill encountered by all drifters released from station 508 in July 2006. A) Copepod concentration (mgC m^{-3}), B) Diatom concentration (mgC m^{-3}), C) Nanophytoplankton concentration (mgC m^{-3}), D) Detritus concentration (mgC m^{-3}), E) Sea ice algae concentration (mg Chla m^{-3}). The black dash dot dash line is the average value of all particles.



Appendix B 35 Concentrations of food for krill encountered by all drifters released from station 508 in August 2006. A) Copepod concentration (mgC m^{-3}), B) Diatom concentration (mgC m^{-3}), C) Nanophytoplankton concentration (mgC m^{-3}), D) Detritus concentration (mgC m^{-3}), E) Sea ice algae concentration (mg Chla m^{-3}). The black dash dot dash line is the average value of all particles.



Appendix B 36 Krill growth figures for station 508 A) June of 2006 with sea ice algae, B) June of 2006 without sea ice algae, C) July of 2006 with sea ice algae, D) July of 2006 without sea ice algae, E) August of 2006 with sea ice algae, F) August of 2006 without sea ice algae. Juveniles start growth from 22mm, larvae start growth from 8mm. The black dash dot dash line indicates the average of all the surviving particles. Every particle has been given the day offset on the x-axis to their respective starting date on the month and the average line has been given a 15 day offset.

Appendix B 37 Krill Recruitment numbers of Austral spring stations

Station Name	% Larvae Recruited Without Sea Ice Algae	% Juveniles Recruited Without Sea Ice Algae	% Larvae Recruited With Sea Ice Algae	% Juveniles Recruited With Sea Ice Algae
St 44 November	26.7	30.0	26.7	30.0
St 44 December	58.1	58.1	58.1	58.1
St 44 January	61.3	61.3	61.3	61.3
St 46 November	90.0	93.3	90.0	93.3
St 46 December	74.2	77.4	74.2	87.1
St 46 January	90.3	96.8	93.5	96.8
St 47 November	93.3	96.7	93.3	100.0
St 47 December	90.3	90.3	90.3	90.3
St 47 January	51.6	61.3	54.8	80.6
St 53 November	100.0	100.0	100.0	100.0
St 53 December	100.0	100.0	100.0	100.0
St 53 January	96.8	100.0	100.0	100.0
St 92 November	100.0	100.0	100.0	100.0
St 92 December	100.0	100.0	100.0	100.0
St 92 January	100.0	100.0	100.0	100.0

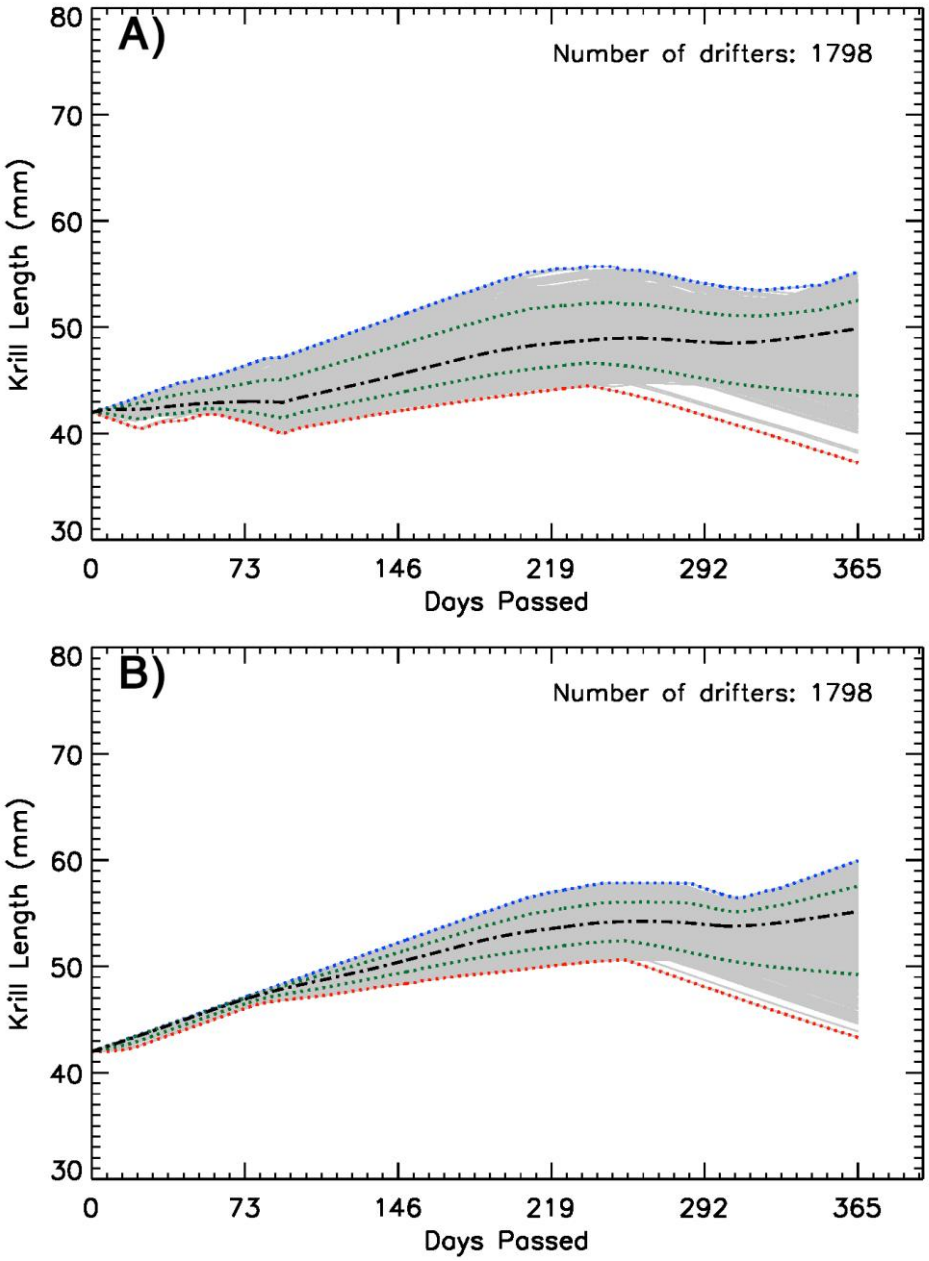
Appendix B 38 Krill Recruitment numbers of Austral fall stations

Station Name	% Larvae Recruited Without Sea Ice Algae	% Juveniles Recruited Without Sea Ice Algae	% Larvae Recruited With Sea Ice Algae	% Juveniles Recruited With Sea Ice Algae
St 621 March	6.4	6.4	6.4	6.4
St 621 April	20.0	20.0	20.0	20.0
St 621 May	25.8	25.8	25.8	25.8
St 634 March	64.5	67.7	64.5	74.2
St 634 April	53.3	56.7	53.3	56.7
St 634 May	90.3	90.3	90.3	90.3
St 678 March	100.0	100.0	100.0	100.0
St 678 April	100.0	100.0	100.0	100.0
St 678 May	100.0	100.0	100.0	100.0
St 683 March	100.0	100.0	100.0	100.0
St 683 April	93.3	93.3	93.3	93.3
St 683 May	100.0	100.0	100.0	100.0

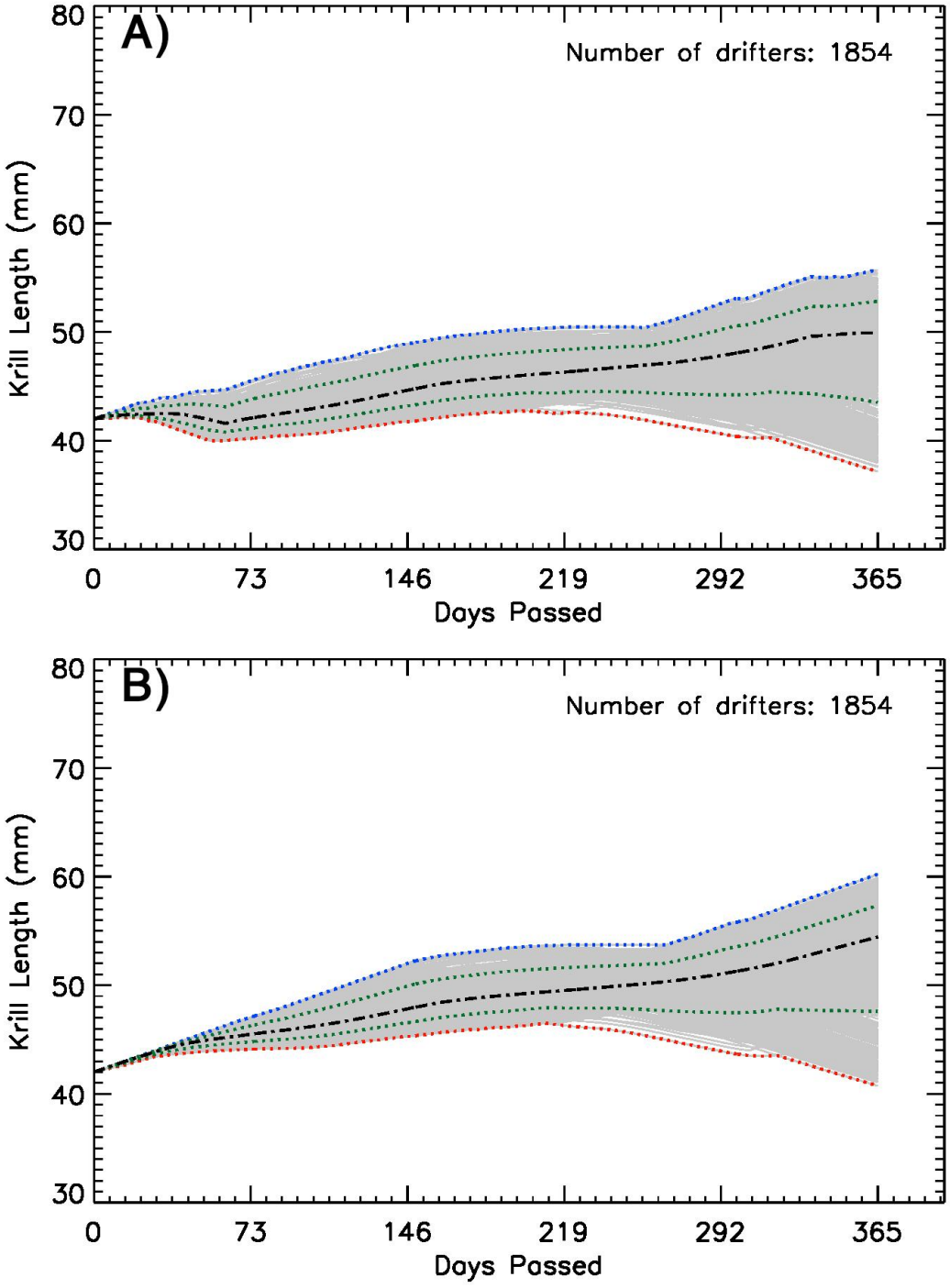
Appendix B 39 Krill Recruitment numbers of Austral winter stations

Station Name	% Larvae Recruited Without Sea Ice Algae	% Juveniles Recruited Without Sea Ice Algae	% Larvae Recruited With Sea Ice Algae	% Juveniles Recruited With Sea Ice Algae
St 474 June	96.7	96.7	96.7	96.7
St 474 July	96.8	96.8	96.8	96.8
St 474 August	100.0	100.0	100.0	100.0
St 508 June	100.0	100.0	100.0	100.0
St 508 July	100.0	100.0	100.0	100.0
St 508 August	90.3	90.3	90.3	90.3
St 516 June	96.7	96.7	96.7	96.7
St 516 July	100.0	100.0	100.0	100.0
St 516 August	96.8	96.8	100.0	100.0

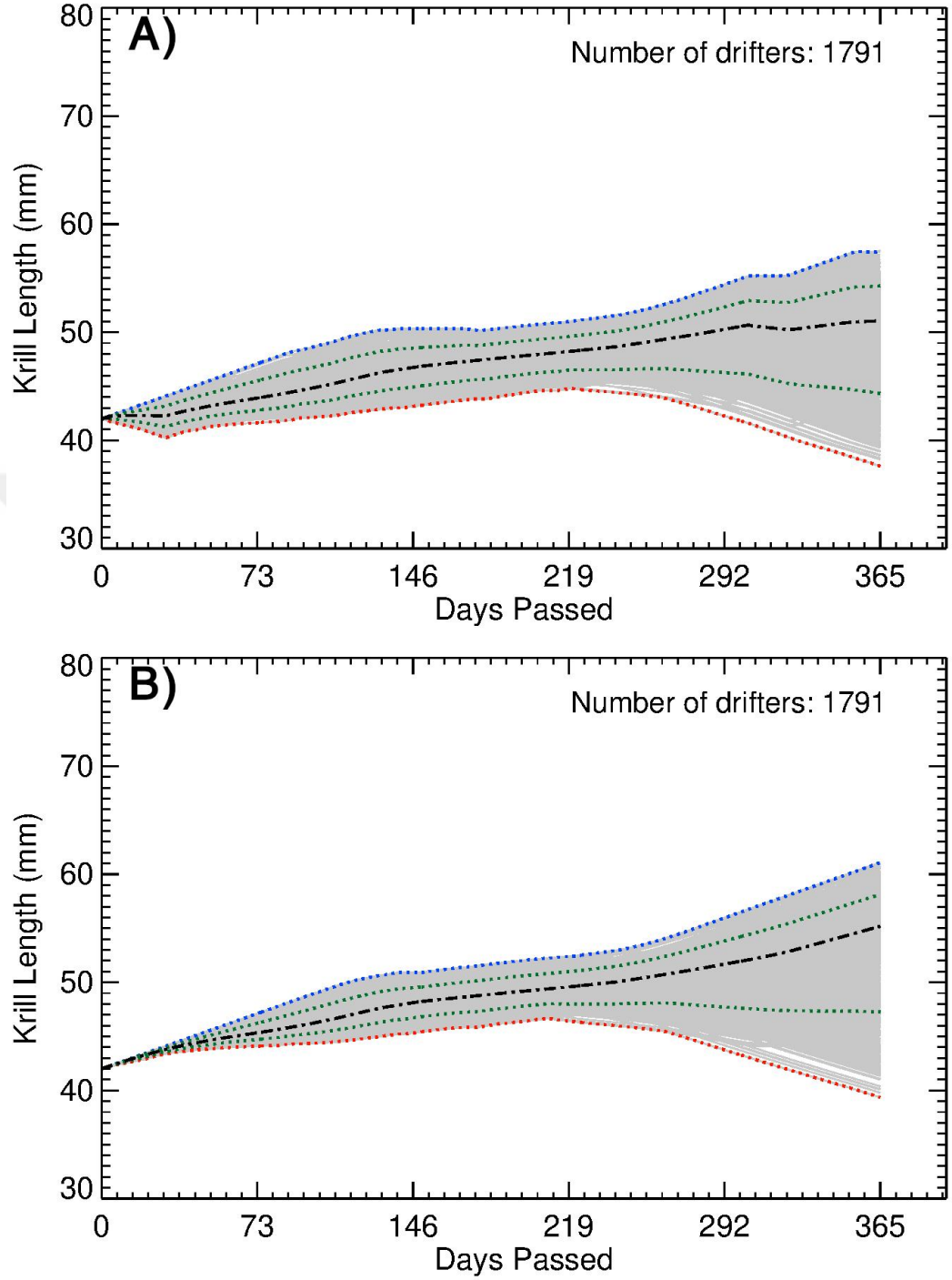
C. Adult krill IBM results



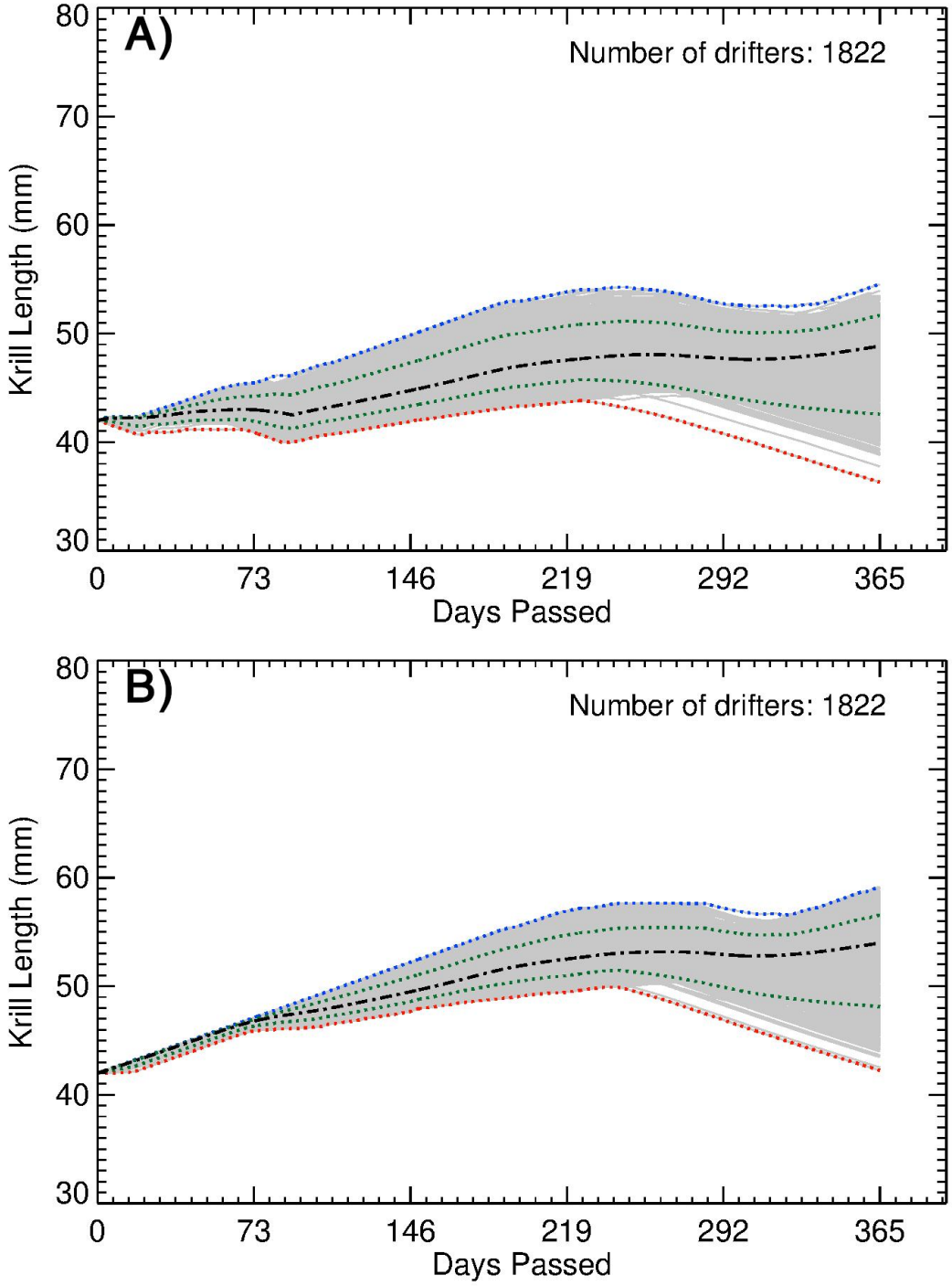
Appendix C 1 Adult krill growth (mm) of particles released on November 1, 2004. A) Simulation with reproduction enabled and B) with reproduction disabled. Black dash dot dash line represents the total average length of all krill, red dotted line represents the minimum length at a given timestep, blue dotted line represents the maximum length at a given timestep, green dotted lines are the middle point between the average and the maximum/minimum length at a given timestep.



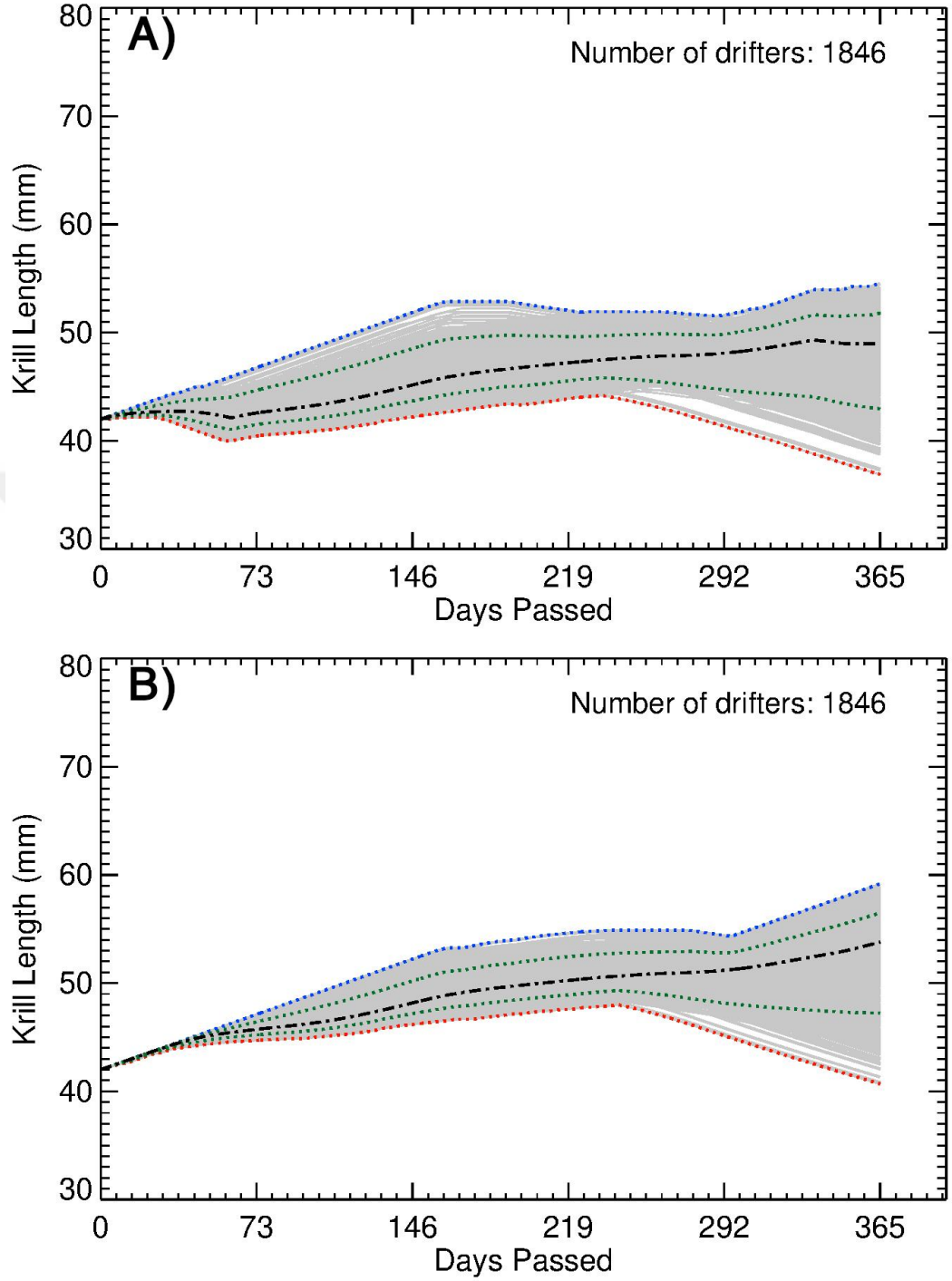
Appendix C 2 Adult krill growth (mm) of particles released on December 1, 2004. A) Simulation with reproduction enabled and B) with reproduction disabled. Black dash dot dash line represents the total average length of all krill, red dotted line represents the minimum length at a given timestep, blue dotted line represents the maximum length at a given timestep, green dotted lines are the middle point between the average and the maximum/minimum length at a given timestep.



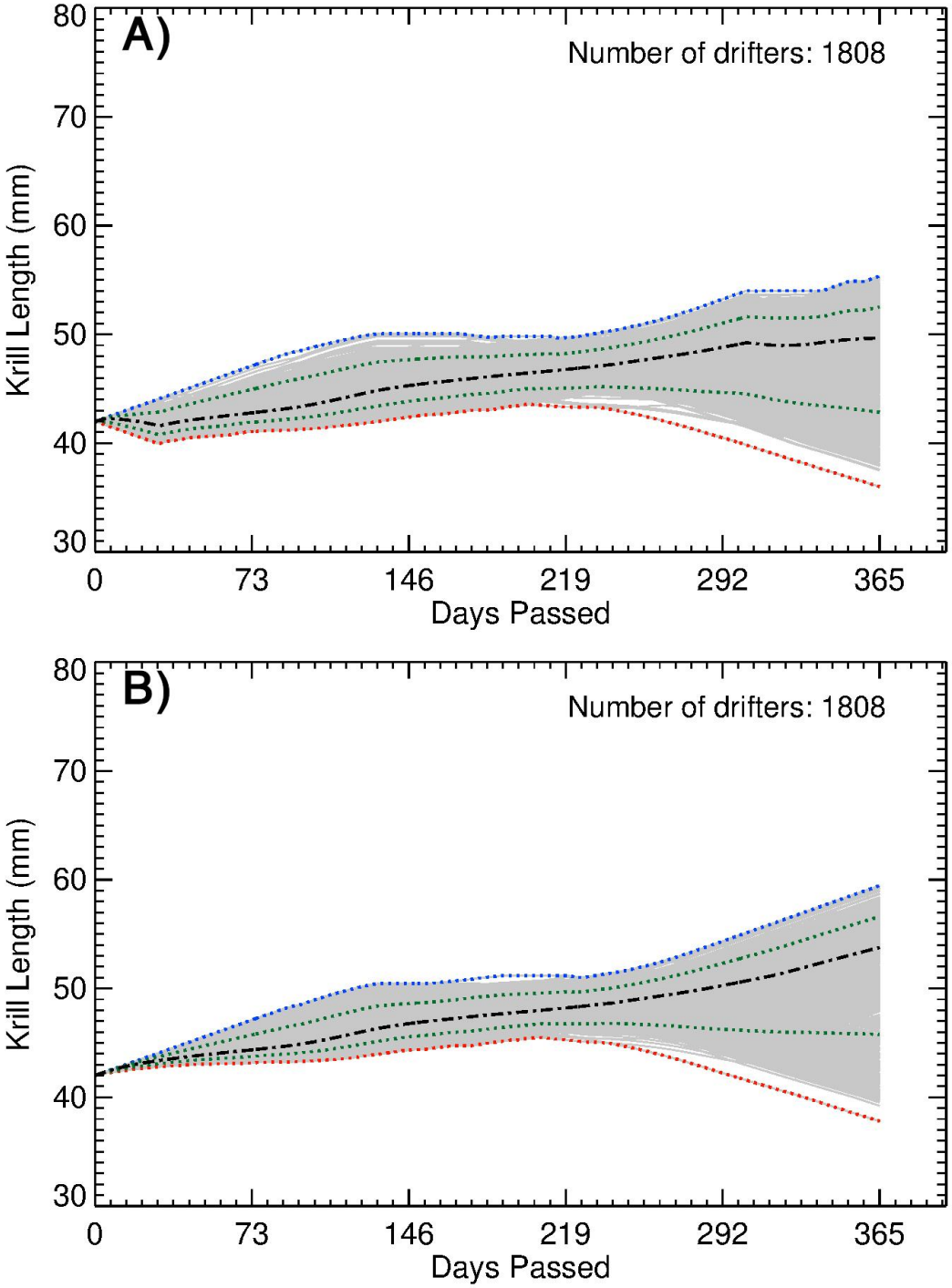
Appendix C 3 Adult krill growth (mm) of particles released on January 1, 2005. A) Simulation with reproduction enabled and B) with reproduction disabled. Black dash dot dash line represents the total average length of all krill, red dotted line represents the minimum length at a given timestep, blue dotted line represents the maximum length at a given timestep, green dotted lines are the middle point between the average and the maximum/minimum length at a given timestep.



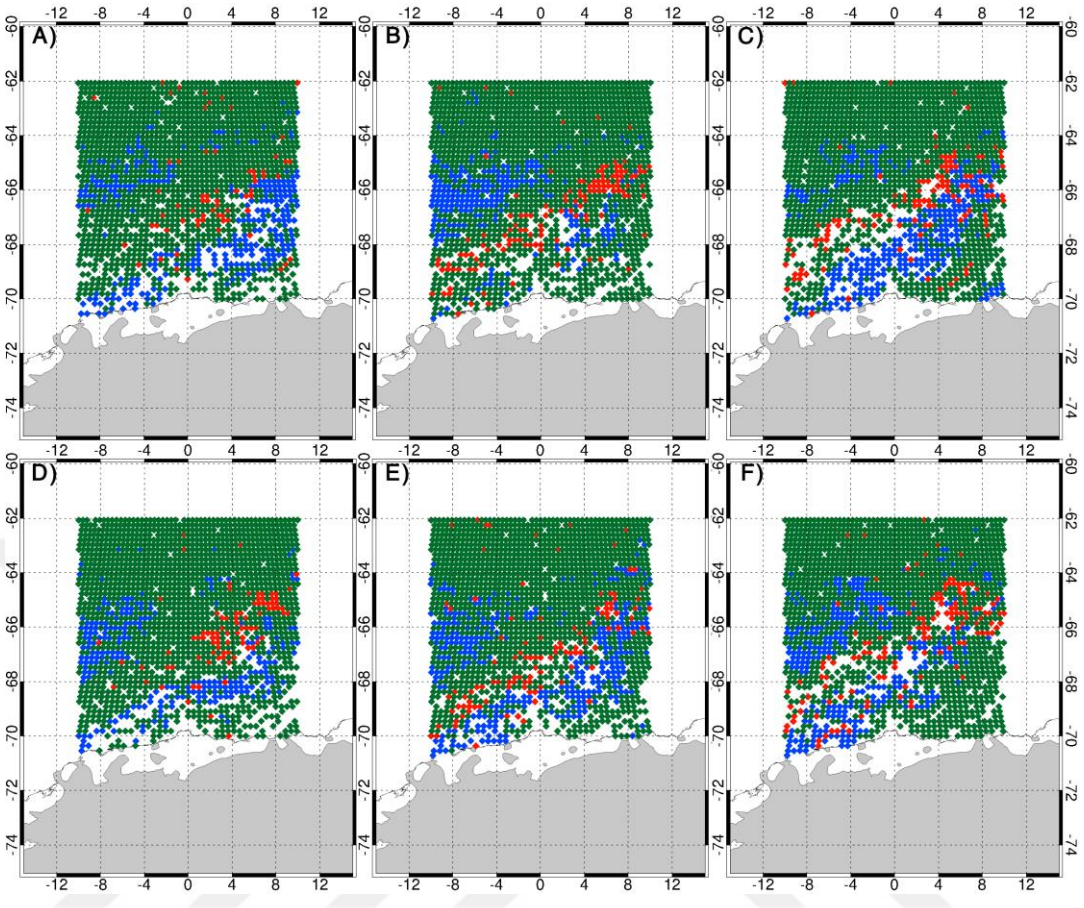
Appendix C 4 Adult krill growth (mm) of particles released on November 1, 2005. A) Simulation with reproduction enabled and B) with reproduction disabled. Black dash dot dash line represents the total average length of all krill, red dotted line represents the minimum length at a given timestep, blue dotted line represents the maximum length at a given timestep, green dotted lines are the middle point between the average and the maximum/minimum length at a given timestep.



Appendix C 5 Adult krill growth (mm) of particles released on December 1, 2005. A) Simulation with reproduction enabled and B) with reproduction disabled. Black dash dot dash line represents the total average length of all krill, red dotted line represents the minimum length at a given timestep, blue dotted line represents the maximum length at a given timestep, green dotted lines are the middle point between the average and the maximum/minimum length at a given timestep.



Appendix C 6 Adult krill growth (mm) of particles released on January 1, 2006. A) Simulation with reproduction enabled and B) with reproduction disabled. Black dash dot dash line represents the total average length of all krill, red dotted line represents the minimum length at a given timestep, blue dotted line represents the maximum length at a given timestep, green dotted lines are the middle point between the average and the maximum/minimum length at a given timestep.



Appendix C 7 Starting locations of krill experiencing above average growth in length (blue), average growth (green) and below average growth (red) in simulations starting in A) November 1 2004, B) December 1 2004, C) January 1 2005, D) November 1 2005, E) December 1 2005, and F) January 1 2006

CURRICULUM VITAE

Surname, Name: Çağdaş,Bulut

EDUCATION

Degree	Institution	Year of Graduation
MS	METU Oceanography	2019
BS	METU Physics	2016
High School	Ayrancı High School, Ankara	2010

FOREIGN LANGUAGES

Fluent English, Elementary German

PUBLICATIONS

1. Sylvester, Z. T., Veytia, D., Bahl, A. A., Bahlburg, D., Benkort, D., Bestley, S., Cagdas, B., Cleary, A. C., Constable, A., Corney, S., Fach, B. A., Hellessey, N., Hill, S. L., Johnston, N. M., Labrousse, S., Merkel, B., Murphy, E. J., Subramaniam, R. C., Thorpe, S., & Raymond, B. (2025). Untangling the complexities of larval Antarctic krill overwintering success under climate change. ICES Journal of Marine Science, 82(4). https://doi.org/10.1093/icesjms/fsaf049

2. Fach, B. A., Cagdas, B., Arkin, S. S., Salihoglu, B., & Tezcan, D. (2024). Investigating the impact of cross-shelf transport and local retention in the Black Sea rim current system on small pelagic fishes. Frontiers in Marine Science, 11. https://doi.org/10.3389/fmars.2024.1435556

Fencing, Trekking, Computer Technologies, Hobby Electronics, Video and Audio Editing